UNIVERSITY OF NAPLES FEDERICO II
DEPARTMENT OF MATERIALS AND PRODUCTION ENGINEERING

DOCTORATE PROGRAMMES IN CHEMICAL, MATERIALS AND PRODUCTION ENGINEERING

PhD Projects on

Intelligent Technologies and Systems for Production Automation

XIX CYCLE

PhD THESIS

Advanced Methods for Product Control and Process Monitoring

SUPERVISOR
PROF. ROBERTO TETI

PHD CANDIDATE
ING. IOAN LIVIU BACIU

CO-SUPERVISOR
PROF. LARS MATTSSON

PHD PROGRAMME COORDINATOR
PROF. NINO GRIZZUTI

ACADEMIC YEAR 2005-2006

UNIVERSITÀ DEGLI STUDI DI NAPOLI FEDERICO II
DIPARTIMENTO DI INGEGNERIA DEI MATERIALI E DELLA PRODUZIONE

DOTTORATO DI RICERCA IN INGEGNERIA CHIMICA,
DEI MATERIALI E DELLA PRODUZIONE

Indirizzo in

Tecnologie e Sistemi Intelligenti per l'Automazione della Produzione

XIX CICLO

TESI DI DOTTORATO

Metodi Avanzati di Controllo di Prodotto e Monitoraggio di Processo

TUTOR
PROF. ROBERTO TETI

DOTTORANDO
ING. IOAN LIVIU BACIU

CO-TUTOR
PROF. LARS MATTSSON

COORDINATORE
PROF. NINO GRIZZUTI

ANNO ACCADEMICO 2005-2006

Acknowledgments

The present PhD thesis work was carried out with support by the following projects:

- EC FP6 Network of Excellence on Innovative Production Machines and Systems (I*PROMS)

- EC FP6 Network of Excellence on Multi-Material micro Manufacture (4M)

- Campania Region, Centre of Competence on Transportation (CRdC Trasporti)

- AnsaldoBreda Project on Quality Assessment of IGBT Devices through Advanced Nondestructive Evaluation Techniques

- Europea Microfusioni Aerospaziali Project on Development of Advanced Products Technologies for Net Shape Microcasting with High Geometrical Complexity

Table of Contents

Chapter I

Introduction to Nondestructive Methods for Product Control

I.1. Guide to nondestructive testing techniques

Nondestructive Evaluation (NDE) comprises many terms used to describe various activities within the field. Some of this terms are Nondestructive Testing (NDT), Nondestructive Inspection (NDI) and Nondestructive Examination (NDE, but should be probably called NDEx). These activities include testing, inspection and examination, which are similar in that they primarily involve looking at/through or measuring something about an object in order to determine some characteristic of the object or to determine whether the object contains irregularities, discontinuities, or flaws.

The terms irregularity, discontinuity, and flaw can be used interchangeably to mean something that is questionable in the part or assembly, but specifications, codes, and local usage can result in different conditions for these terms. Because these terms describe what is being sought through testing, inspection or examination, the term NDE (Nondestructive Evaluation) has come to include all the activities of NDT, NDI and NDEx used to find, locate, size, or determine something about the object or flaws are acceptable. A flaw that has been evaluated as rejectable is usually termed a defect.

Several different ways of NDE methods are presented in this article, but there is no completely acceptable system of comparison, because the results are highly dependent on the applications. Therefore, is recommended that a comparison be developed specifically for each NDE area and application type.

NDE is vital for constructing and maintaining all types of components and structures. To detect different defects such as cracking and corrosion, there are different methods of testing available, such as X-ray (where cracks show up on the film) and/or ultrasound (where cracks show up as an echo blip on the screen). These methods are aimed mainly for industrial NDT, but many of the described ones can be used to test the human body. In fact methods from the medical field, where there tends to be more development funding available, have often been adapted for industrial use, as was the case with Phased Array Ultrasonics (PAU) and Computed Radiography(CR).

While destructive testing usually provides a more reliable assessment of the state of the test object, destruction of the test object usually makes this type of test more costly to the test object's owner than nondestructive testing. Destructive testing is also inappropriate in many circumstances, such as forensic investigation. That there is a tradeoff between the cost of the test and its reliability favors a strategy in which most test objects are inspected nondestructively.

Destructive testing is performed on a sampling of test objects that is drawn randomly for the purpose of characterizing the testing reliability of the nondestructive test.

I.1.1 The need for NDT

It is actually very difficult to weld, bond, braze or mold a solid object that has no risk of breaking in service, so testing at manufacture and during use is often essential. During the process of molding a metal object, for example, the metal may shrink as it cools, and crack or introduce voids inside the structure. Even the best welders (and welding machines) do not make 100% perfect welds. Some typical weld defects that need to be found and repaired are lack of fusion of the weld to the metal and porous bubbles inside the weld, both of which could cause a structure to break or a pipeline to rupture.

During their service lives, many industrial components need regular nondestructive tests to detect damage that may be difficult or expensive to find by everyday methods.

For example:

- aircraft skins need regular checking to detect cracks;
- underground pipelines are subject to corrosion and stress corrosion cracking;
- pipes in industrial plants may be subject to erosion and corrosion from the products they carry;
- concrete structures may be weakened if the inner reinforcing steel is corroded;
- pressure vessels may develop cracks in welds;
- wire ropes in suspension bridges are subject to weather, vibration, and high loads, so testing for broken wires and other damage is important.
- over the past centuries, swordsmiths, blacksmiths, and bell-makers would listen to the ring of the objects they were creating to get an indication of the soundness of the material — a function that is now carried out by instrumentation and referred to as acoustic emission.
- notable events in early industrial NDT – Hellier, 2001
- 1854 Hartford, Connecticut: a boiler at the Fales and Gay Gray Car works explodes, killing 21 people and seriously injuring 50. Within a decade, the State of Connecticut passes a law requiring annual inspection (in this case visual) of boilers.
- 1895 Wilhelm Conrad Röntgen discovers what are now known as X-rays. In his first paper he discusses the possibility of flaw detection.
- 1880 - 1920 The "Oil and Whiting" method of crack detection is used in the railroad industry to find cracks in heavy steel parts. (A part is soaked in thinned oil, and then painted with a white coating that dries to a powder. Oil seeping out from cracks turns the white powder brown, allowing the cracks to be detected.) This was the precursor to modern liquid penetrant tests.
- 1920 Dr. H. H. Lester begins development of industrial radiography for metals. 1924 — Lester uses radiography to examine castings to be installed in a Boston Edison Company steam pressure power plant (source).
- 1926 The first electromagnetic eddy current instrument is available to measure material thicknesses.
- 1927 - 1928 Magnetic induction system to detect flaws in railroad track developed by Dr. Elmer Sperry and H.C. Drake.
- 1929 Magnetic particle methods and equipment pioneered (A.V. DeForest and F.B. Doane.)
- 1930s Robert F. Mehl demonstrates radiographic imaging using gamma radiation from Radium, which can examine thicker components than the low-energy X-ray machines available at the time.

- 1935 - 1940 Liquid penetrant tests developed (Betz, Doane, and DeForest)
- 1935 - 1940s Eddy current instruments developed (H.C. Knerr, C. Farrow, Theo Zuschlag, and Fr. F. Foerster).
- 1940 - 1944 Ultrasonic test method developed in USA by Dr. Floyd Firestone.
- 1950 J. Kaiser introduces acoustic emission as an NDT method.

I.1.2 Applications

NDT is used in a variety of settings that covers a wide range of industrial activity.

- Automotive
  - ✓ Engine parts
  - ✓ Frame
- Aviation / Aerospace
  - ✓ Airframes
  - ✓ Spaceframes
  - ✓ Power plants
    - Reciprocating Engines
    - Jet Engines
    - Rocketry
- Construction
  - ✓ Structures
  - ✓ Bridges
- Manufacturing
  - ✓ Machine parts
  - ✓ Castings and Forgings
- Industrial plants such as Nuclear, Petrochemical, Power, Refineries, Pulp and Paper, Fabrication shops, and Mine processing.
  - ✓ Pressure vessels
  - ✓ Storage tanks
  - ✓ Welds
  - ✓ Boilers
  - ✓ Heat exchangers
  - ✓ Turbine bores
  - ✓ In-plant Piping
- Miscellaneous
  - ✓ Pipelines
    - In-line Inspection using "pigs"
    - Pipeline integrity
  - ✓ Railways
    - Rail Inspection
    - Wheel Inspection
  - ✓ Tubular NDT, for Tubing material
  - ✓ Corrosion Under Insulation (CUI)
  - ✓ Amusement park rides
  - ✓ Medical imaging applications

I.1.3 Methods and techniques

NDT is divided into various methods of nondestructive testing, each based on a particular scientific principle. These methods may be further subdivided into various techniques. The various methods and techniques, due to their particular natures, may lend themselves especially well to certain applications and be of little or no value at all in other applications. Therefore choosing the right method and technique is an important part of the performance of NDT.

I.2 Liquid penetrant testing/inspection (PT or LPI)

Liquid penetrant examination (LPE) is a nondestructive method of revealing discontinuities that are open to the surfaces of solid and essentially nonporous materials. Indications of a wide spectrum of flaw sizes can be found regardless of the configuration of the workpiece and regardless of the configuration of the flaw orientation. Liquid penetrants seep into various types of minute surface openings by capillary action as showed in Figure I.1. Because of this, the process is well suited to the detection of all types of surface cracks, laps, porosity, shrinkage areas, laminations, and similar discontinuities. It is extensively used for inspection of wrought and cast products of ferrous or nonferrous metals, powder metallurgy parts, ceramic, plastics, and glass objects.

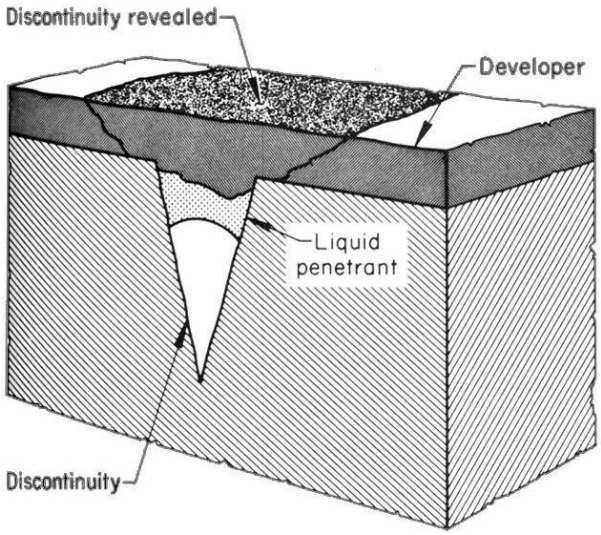

Figure I.1: Crack detection through liquid penetrant testing.

Liquid penetrant inspection (LPI) method does not depend on ferromagnetism, and the arrangement of the discontinuities is not a factor. LPI is also used to inspect items made from ferromagnetic steels; generally, its sensitivity is greater than that of magnetic particle inspection.

The major limitation of LPI method is that it can detect only imperfections that are open to the surface; some other NDE methods must be used for detecting subsurface flaws. Surface roughness and porosity are other factors that can limit the use of LPI method, by producing excessive background and interfere with inspection.

Because of the vast differences among applications for penetrant inspection, it has been necessary to refine and develop the two types of penetrants (type I, fluorescent, and

type II, visible) into four basic methods to accommodate the wide variations in the following principal factors:

- Surface condition of the workpiece being inspected
- Characteristics of the flaws to be detected
- Time and place of inspection
- Size of the workpiece
- Sensitivity required.

Type I penetrants are available in different sensitivity levels classified as follows:

- Level ½: Ultralow
- Level 1: Low
- Level 2: Medium
- Level 3: High
- Level 4: Ultrahigh

The four LPI methods are broadly classified as:

- Water washable, method A
- Postemulsifiable lipophilic, method B
- Solvent removable, method C
- Postemulsifiable hydrophilic, method D.

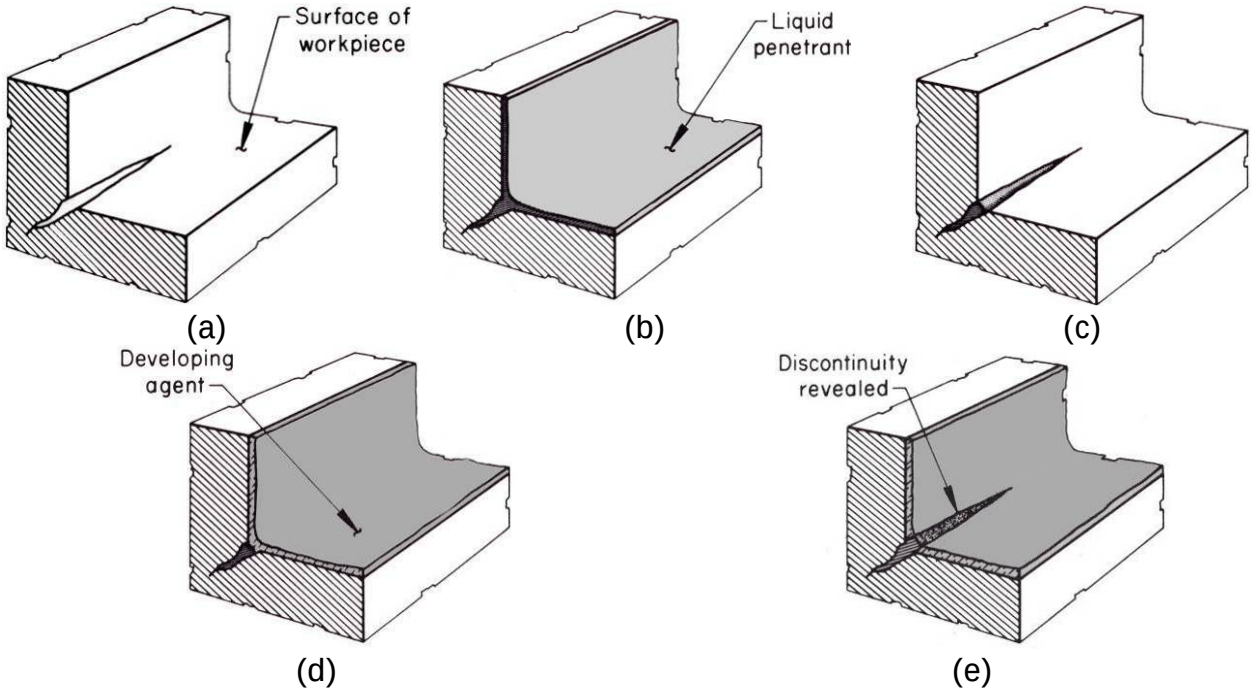

Figure I.2: Essential operations for LPI using method A (water washable system): (a) Cleaning and drying of surface, (b) Application of liquid penetrant to surface, (c) Water-wash removal of liquid penetrant from surface, (d) Application of developing agent, (e) final LIP inspection.

Method A (water washable) is designed so that the penetrant is directly water washable from the surface of the workpiece; it does not require a separate emulsification step, as does the postemulsifiable penetrant methods (method B and D). Water washable can be used to process workpieces quickly and efficiently. It is important, however, that the washing operation be carefully controlled because water-washable penetrants are susceptible to overwashing. The essential operations involved in this method are illustrated in Figure I.2.

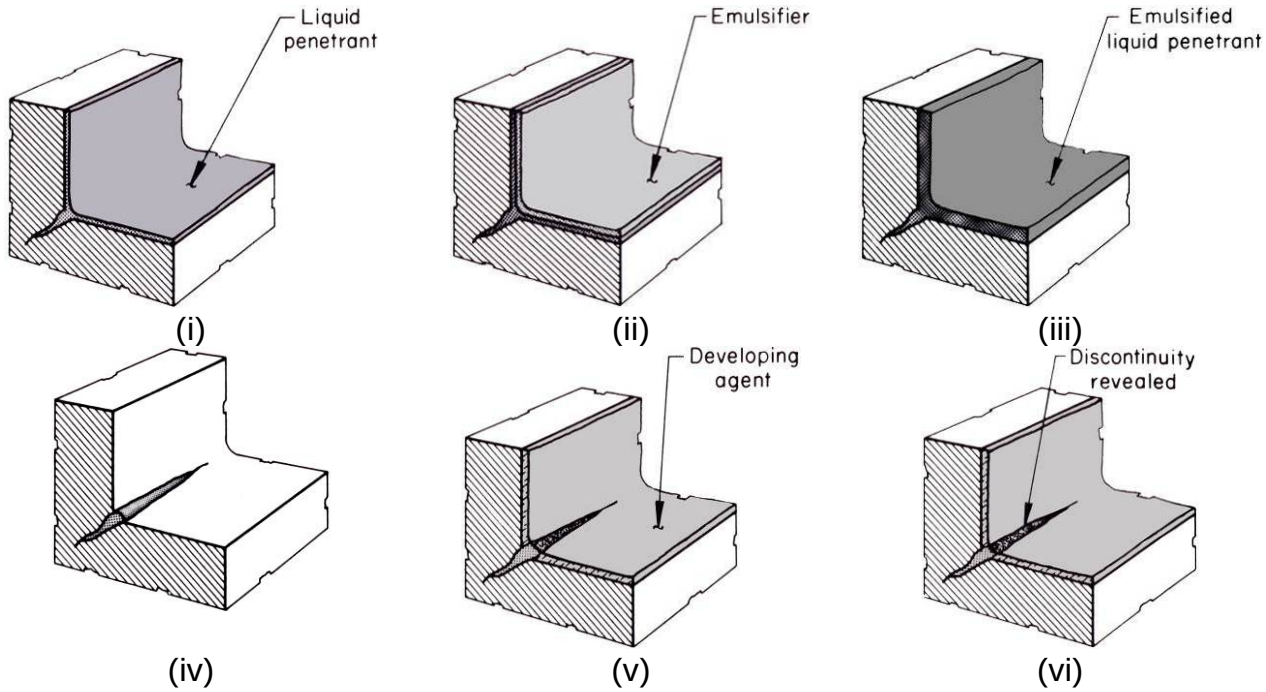

Figure I.3: Essential operations for LPI using method B (postemulsifiable lipophilic penetrant system): (i) application of liquid penetrant to surface, (ii) application of emulsifier to liquid penetrant, (iii) combination of emulsifier and liquid penetrant, (iv) Water-wash removal of liquid penetrant from surface, (v) Application of developing agent, (vi) final LIP inspection.

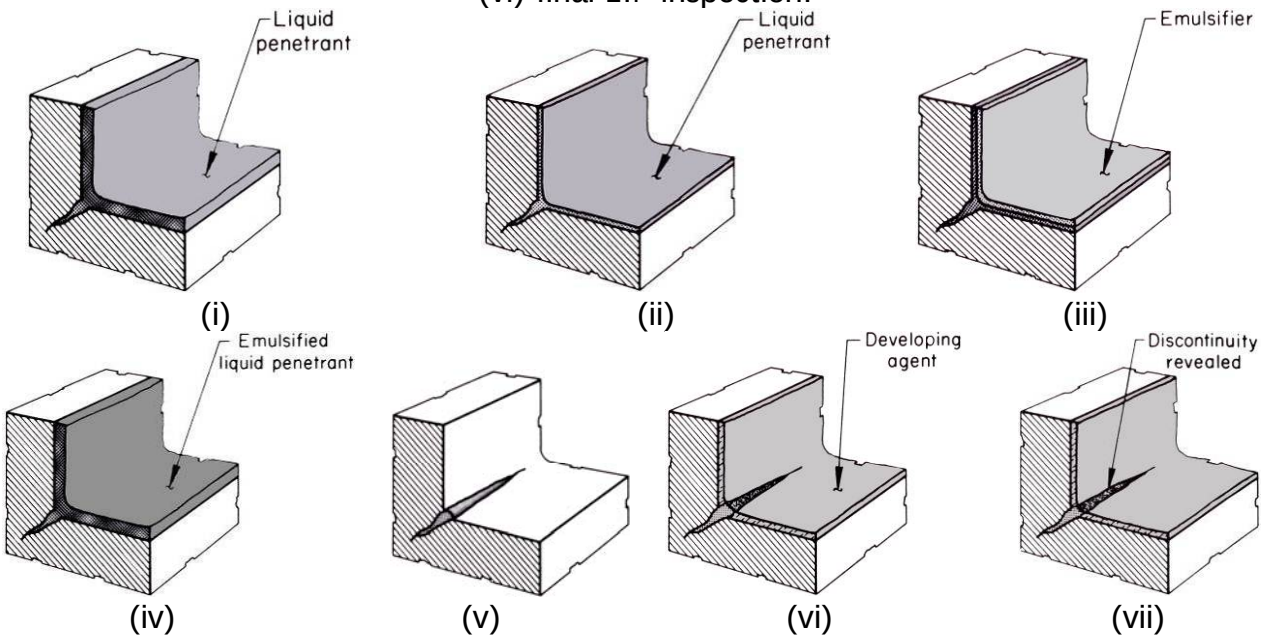

Figure I.4: Essential operations for LPI using method B (postemulsifiable hydrophilic penetrant system): (i) application of liquid penetrant to surface, (ii) prerinse, water-wash to assist liquid penetrant removal from surface and to reduce emulsifier contamination, (iii) application of emulsifier to liquid penetrant, (iv) combination of emulsifier and liquid penetrant, (v) Water-wash removal of liquid penetrant from surface, (vi) Application of developing agent, (vii) final LIP inspection.

Methods B and D (postemulsifiable penetrants) are designed to ensure the detection of minute flaws in some materials. These penetrants are not directly water washable, and because of this characteristic, the danger of overwashing the penetrant out

of the flaws is reduced. The difference between methods B and D and method A lies in the use of an emulsifier prior to the final rinsing. The emulsifier makes the residual surface penetrant soluble in water so that the excess surface penetrant can be removed by the water rinse. A special care is regarding the emulsification time that must be carefully controlled so that the surface penetrant becomes water soluble but the penetrant in the flaws does not. These methods are the most reliable for detecting minute flaws, and the methods are illustrated schematically in Figure I.3 and I.4.

Method C (solvent-removal) is available for use when it is necessary to inspect a workpiece at the site rather than on a production inspection basis. Normally, the same type of solvent is used for precleaning and for removing excess penetrant. The operations for this process are illustrated schematically in Figure I.4.

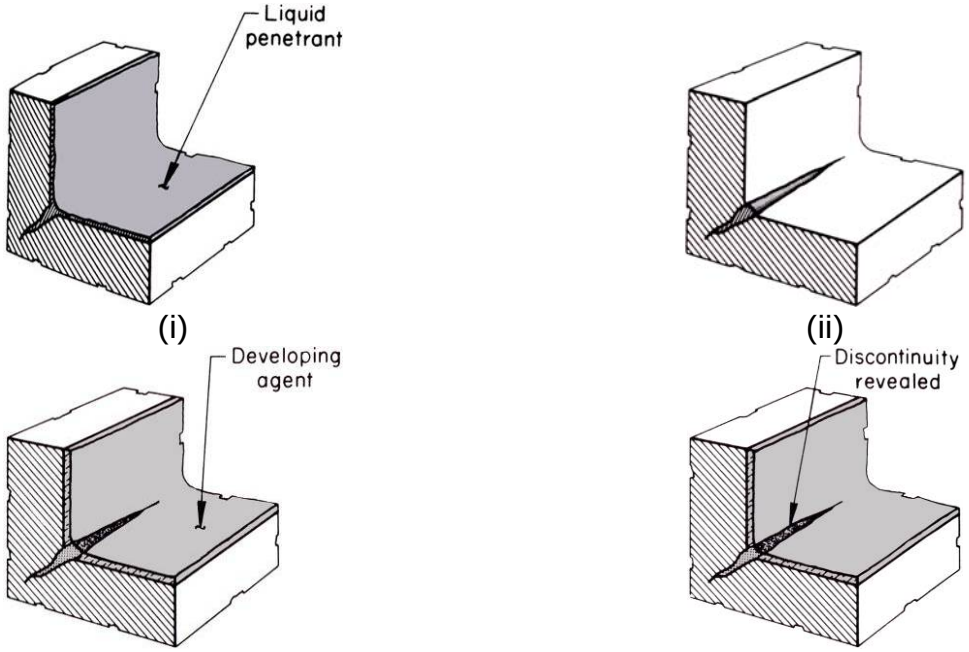

Figure I.5: Essential operations for LPI using method C (solvent-removal): (i) Application of liquid penetrant to surface, (ii) solvent-cleaner removal of liquid penetrant from surface, (iii) Application of developing agent, (iv) final LIP inspection.

Regardless the type of penetrant used, penetrant LPI requires at least 5 steps, ass follows:

- Pre-cleaning (surface preparation): The test surface is cleaned to remove any dirt, paint, oil, grease or any loose scale, etc;
- Application of Penetrant: The penetrant is then applied to the surface of the part being tested. The dye is allowed time to soak into any flaws (generally 10 to 30 minutes). The soak time mainly depends upon the material being testing and the type of flaws;
- Excess Penetrant Removal: The excess penetrant is the removed from the surface by using a lint (free cloth soaked with solvent remover is normally used for this purpose in case of solvent removable penetrant inspections). It is important to not spray the solvent remover on the test surface directly, because this can remove the penetrant from the flaws;
- Application of Developer: After the removal of excess penetrant, a white developer is sprayed in a thin, even coating on the surface. This is to draw

any dye which has entered defects to the surface, a process similar to the action of blotting paper. Any colored stains indicate the positions and types of defects on the surface under inspection. The penetrants are usually red, purple or sometimes orange, to give a good contrast against the white developer used in the process;

- Inspection: The inspection of the test surface is carried out immediately after the application of the developer and 15 minutes after the immediate inspection;
- Post Cleaning: After the inspection and recording of defects if found, the test surface should be cleaned.

The equipment used in the LPI process varies from spray/aerosol cans to complex, automated, computer-driven processing systems. The type of equipment most frequently used in fixed installations consists of a series of modular subunits. Each subunit is performing a special task. These subunits are:

- Drain and/or dwell stations
- Penetrant and emulsifier stations
- Pre- and post-wash stations
- Drying station
- Developer station
- Inspection station
- Cleaning station.

In the Figure I.6 is presented an inspection station installation used for different castings control. Many of the castings to be controlled are requiring handling by crane or by roller conveyor.

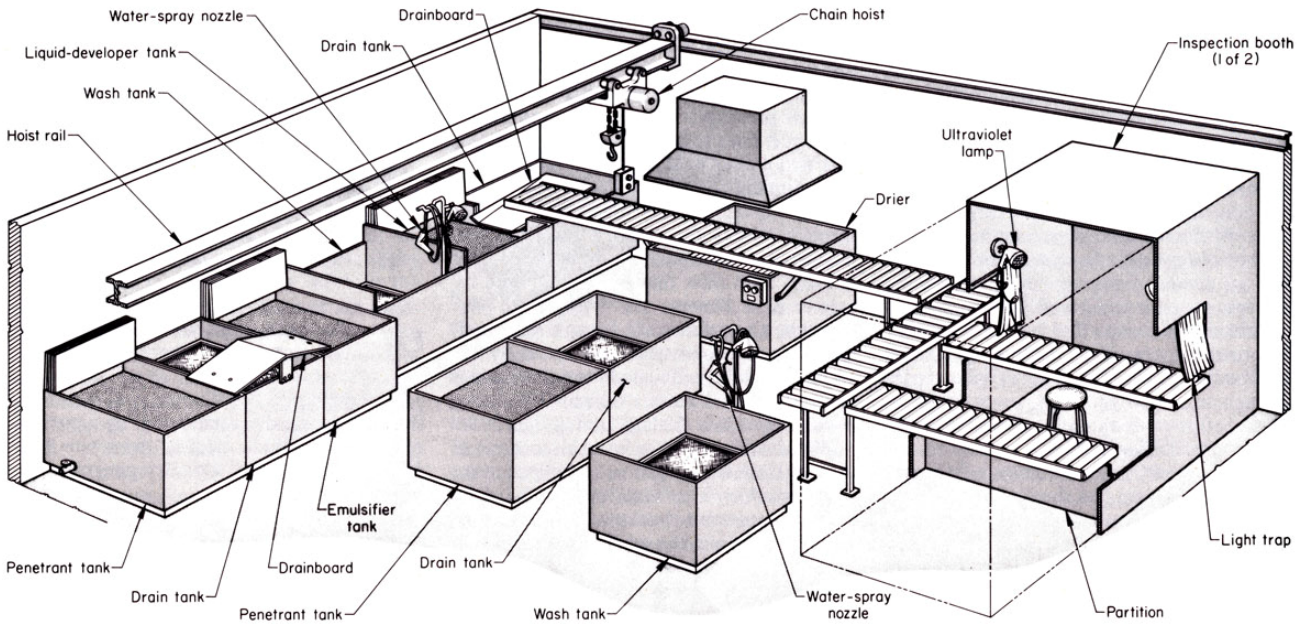

Figure I.6: Arrangement of equipment used in casting part control by means of liquid penetrant inspection in a foundry plant.

In the case of LPT it is possible to observe different method advantages and disadvantages:

- The flaws are more visible, because the colour of the penetrant and the developer (e.g. red dye with a white developer, or a fluorescent penetrant and illumination by ultraviolet light) presents a high contrast (see Figure I.7);

- The developer tears the penetrant out of the flaw over a wider area than the real flaw, so it looks wider;
- Limited training required for the operator (but experience is valuable);
- Low testing costs.
- Correct cleaning is needed; rusty parts have to be smoothed;
- Penetrant, developer and cleaner are polluting. The penetrant requires special care in handling it.

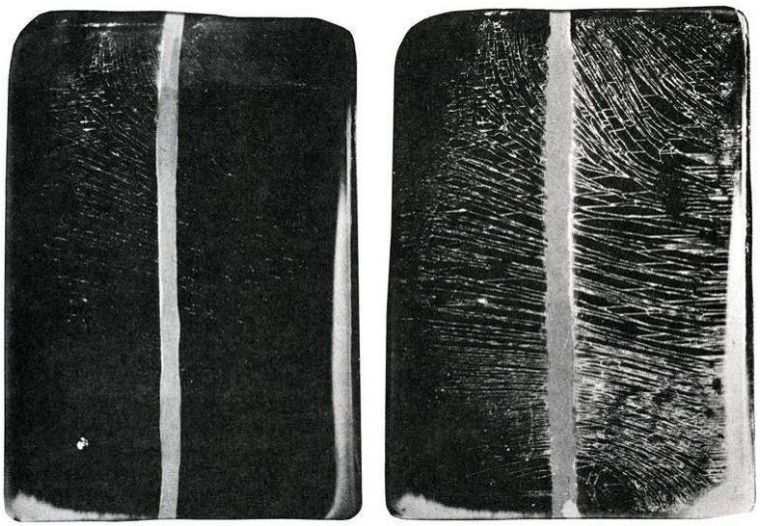

Figure I.7: Comparison of indications on chromium-cracked panels for different penetrant sensitivities levels (Level 1 sensitivity – right panel and Level 3 sensitivity – left panel).

I.3 Radiographic testing (X-Ray)

I.3.1 Real-time radiography

Radiology is the general term given to material inspection methods that are based on the differential absorption of penetrating radiation - either electromagnetic radiation of very short wavelength or particulate radiation - by the part or testpiece (object) being inspected. Because of the difference in density and variations in thickness of the art or differences in absorption characteristics caused by variations in composition, different portions of a testpiece absorb different amounts o penetration radiation. These variations in the absorption of penetrating radiation can be monitored by detecting the unabsorbed radiation that passes through the testpiece.

The term radiography often refers to the specific radiogical method the produces a permanent image on film (conventional radiography) or paper (paper radiography or xeroradiography). In a broad sense, however, radiography can also refer to other radiological techniques that can produce bi-dimensional (2D), plane-views images from the unabsorbed radiation.

There are considered the following two techniques as part of the radiographic inspection methods (with x-rays or γ-rays):

- *Film or paper radiography:* A 2D latent image from the projected radiation is produced on a sheet of film or paper that has been exposed to the unabsorbed radiation passing through the testpiece. This technique requires

subsequent development of the exposed film or paper so that the latent image becomes visible for viewing.

- *Real-time radiography (radioscopy):* A 2D image can be immediately displayed on a viewing screen or television monitor. This technique does not involve the creation of a latent image; instead, the unabsorbed radiation is converted into an optical or electronic signal, which can be viewed immediately or can be processed in near real time with electronic and video equipment.

The principal advantage of real-time radiography over film radiography is the opportunity to manipulate the testpiece during radiographic inspection. This capability allows the inspection of internal mechanism and enhances the detection of cracks and planar defects by manipulating the part to achieve the proper orientation for flaw detection.

Moreover, part manipulation in real-time radiography simplifies three-dimensional dynamic imaging and the determination of flaw location and size. In film radiography, however, the position of a flaw within the volume of a testpiece cannot be determined exactly with a single radiograph; depth parallel to the radiation beam is not recorded.

Consequently, other film techniques, such as stereoradiography, triangulation, or simply by making two or more film exposures (with the radiation beam being directed at the testpiece from different angle for each exposure), must be used to locate flaws more accurately within the testpiece volume.

Although real-time radiography enhances the detection and location of flaws by allowing the manipulation of testpiece during inspection, another important radiological technique with enhanced flaw detection and location capabilities is Computed Tomography (CT).

Unlike film and real-time radiography, computed tomography (CT) involves the generation of cross-sectional views instead of a planar projection. The CT image is comparable to that obtained by making a radiograph of a physically sectioned thin planar slab from an object. This cross-sectional image is not obscured by overlying structures and is highly sensitive to small differences in relative density. Moreover, CT images are easier to interpret than radiographies.

Other forms of radiation (except x-rays or γ-rays) include subatomic particles that are generated during nuclear decay. The most commonly known subatomic particles are α particles, β particles and neutrons, all which are emitted from the nuclei of various atoms during radioactive decay.

Beta particles and neutrons are sufficiently penetrating to be useful for radiography, but neutrons are more widely used (see neutron radiography paragraph).

Radiography is used to detect the features of a component or assembly that exhibit a difference in thickness or physical density as compared to surrounding material. Large differences are more easily detected than small ones. In general, radiography can detect only those features that have an appreciable thickness in a direction parallel to the radiation beam. This means that the ability of the process to detect planar discontinuities such as cracks depends on proper orientation of the testpiece during inspection. Discontinuities such as voids and inclusions, which have measurable thickness in all directions, can be detected as long as they are not too small in relation to section thickness. In general, features that exhibit a 1% or more difference in absorption compared to the surrounding material can be detected.

Although neither is limited to the detection of internal flaws, radiography and ultrasonics are the two generally used nondestructive inspection methods that can

satisfactorily detect flaws that are completely internal and located well below the surface of the part. Neither method is limited to the detection of specific types of internal flaws, but radiography is more effective when the flaws are not planar, while ultrasonics is more effective when the flaws are planar. In comparison to other generally used nondestructive methods (for example, magnetic particle, liquid penetrant, and eddy current inspection), radiography has three main advantages:

- The ability to detect internal flaws
- The ability to detect significant variations in composition
- Permanent recording of raw inspection data

Radiographic inspection is extensively used on castings and weldments, particularly where there is a critical need to ensure freedom from internal flaws.

For example, radiography is often specified for the inspection of thick-wall castings and weldments for steam-power equipment (boiler and turbine components and assemblies) and other high-pressure systems. Radiography can also be used on forgings and mechanical assemblies, although with mechanical assemblies radiography is usually limited to inspection for condition and proper placement of components or for proper liquid-fill level in sealed systems.

Certain special devices are more satisfactorily inspected by radiography than by other methods. For example, radiography is well suited to the inspection of semiconductor devices for voids in the element mount area, in the case seal area, and in plastic molding compounds used to encapsulate some devices. Radiography is also used to inspect for cracks, broken wires, foreign material, and misplaced and misaligned elements. High-resolution real-time imaging with microfocus x-ray sources has made it possible to use radiography as a failure analysis tool for semiconductors and other electronic components. Real-time imaging allows analysis from a variety of angles, while microfocus adds the capability of detecting flaws as small as 0.025 mm in the major dimension.

New uses of radiography have also occurred with the inspection of composites. In such applications, the sensitivity is maximized with the use of high-intensity, low-energy radiation.

The sensitivity of x-ray and γ-ray radiography to various types of flaws depends on many factors, including type of material, type of flaw, and product form. The type of material in this context is usually expressed in terms of atomic number - for example, metals having low atomic numbers are classified as light metals, and those having high atomic numbers are heavy metals. Table I.1 indicates the general degree of suitability of the three main radiographic methods for the detection of discontinuities in various product forms and applications.

Radiography can be used to inspect most types of solid material, with the possible exception of materials of very high or very low density. Neutron radiography, however, can often be used in such cases. Both ferrous and nonferrous alloys can be radiographed, as can non-metallic materials and composites.

There is wide latitude both in the material thickness that can be inspected and in the techniques that can be used.

In some cases, radiography cannot be used even though it appears suitable from Table I.1, because the part is accessible from one side only. Radiography typically involves the transmission of radiation through the testpiece, in which case both sides of the part must be accessible. However, radiographic and radiometric inspection can also be performed with Compton scattering, in which the scattered photons are used for imaging.

Table I.1:
Comparison of suitability of three radiographic methods for the inspection of light and heavy metals

Inspection Application	Suitability for light metals[a]			Suitability for heavy metals[a]		
	Film with x-rays	Real-time radiography	Film with γ -rays	Film with x-rays	Real-time radiography	Film with γ -rays
General						
Surface cracks[b]	F[c]	F	F[c]	F[c]	F	**F[c]**
Internal cracks	F[c]	F	F[c]	F[c]	F	F[c]
Voids	G	G	G	G	G	**G**
Thickness	F	G	F	F	G	**F**
Metallurgical variations	F	F	F	F	F	**F**
Sheet and plate						
Thickness	G[d]	G	G[d]	G[d]	G	G[d]
Laminations	U	U	U	U	U	U
Voids	G	G	G	G	G	G
Bars and Tubes						
Seams	P	P	P	P	P	P
Pipe	G	G	G	G	G	F
Cupping	G	G	G	G	G	F
Inclusions	F	F	F	F	F	F
Castings						
Cold shuts	G	G	G	G	G	G
Surface cracks	F[c]	F	F[c]	F[c]	F	F[c]
Internal shrinkage	G	G	G	G	G	G
Voids, pores	G	G	G	G	G	G
Core shift	G	G	G	G	G	G
Forgings						
Laps	P[c]	P[c]	P[c]	P	P	U
Inclusions	F	F	F	F	F	U
Internal bursts	G	G	G	F	F	G
Internal flakes	P[c]	P	U	P[c]	P	U
Cracks and tears	F[c]	F	F[c]	F[c]	F	F[c]
Welds						
Shrinkage cracks	G[c]	G	G[c]	G[c]	G	G[c]
Slag inclusions	G	G	G	G	G	G
Incomplete fusion	G	G	G	G	G	G
Pores	G	G	G	G	G	G
Incomplete penetration	G	G	G	G	G	G
Processing						
Heat-treat cracks	U	U	U	P	U	U
Grinding cracks	U	U	U	U	U	U
Service						
Fatigue and heat cracks	F[c]	F	P[c]	P	P	P
Stress corrosion	F	F	P	F	F	P
Blistering	P	P	P	P	P	P
Thinning	F	F	F	F	F	F
Corrosion pits	F	F	P	G	G	P

(a) G - good; F - fair; P - poor; U – unsatisfactory; (b) Includes only visible cracks. Minute surface cracks are undetectable by radiographic inspection methods; (c) Radiation beam must be parallel to the cracks, laps, or flakes. In real-time radiography, the testpiece can be manipulated for proper orientation; (d) When calibrated using special thickness gages.

With Compton scattering, inspection can be performed when only one side is accessible. Another method of inspecting a region having one inaccessible side is to use probes with a microfocus x-ray tube.

Compared to other nondestructive methods of inspection, radiography is expensive. Relatively large capital costs and space allocations are required for a radiographic laboratory, although costs can be reduced when portable x-ray or γ-ray sources are used in film radiography. Capital costs can be relatively low with portable units, and space is required only for film processing and interpretation. Operating costs can be high; sometimes as much as 60% of the total inspection time is spent in setting up for radiography. With real-time radiography, operating costs are usually much lower, because setup times are shorter and there are no extra costs for processing or interpretation of film.

The field inspection of thick sections can be a time-consuming process because the effective radiation output of portable sources may require long exposure times of the radiographic film. Radioactive (γ-ray) sources are limited in their output primarily because high-activity sources require heavy shielding for the protection of personnel. This limits field usage to sources of lower activity that can be transported. The output of portable x-ray sources may also limit the field inspection of thick sections, particularly if a portable x-ray tube is used. Portable x-ray tubes emit relatively low-energy (300 keV) radiation and are limited in the radiation output. Both of these characteristics of portable x-ray tubes combine to limit their application to the inspection of sections having the absorption equivalent of 75 mm of steel. Instead of portable x-ray tubes, portable linear accelerators and betatrons provide high-energy (>1 MeV) x-rays for the radiographic field inspection of thicker sections.

Certain types of flaws are difficult to detect by radiography. Cracks cannot be detected unless they are essentially parallel to the radiation beam. Tight cracks in thick sections may not be detected at all, even when properly oriented. Minute discontinuities such as inclusions in wrought material, flakes, microporosity, and microfissures may not be detected unless they are sufficiently segregated to yield a detectable gross effect. Laminations are nearly impossible to detect with radiography; because of their unfavourable orientation, delamination do not yield differences in absorption that enable laminated areas to be distinguished from delaminated areas.

It is well known that large doses of x-rays or γ-rays can kill human cells, and in massive doses can cause severe disability or death. Protection of personnel - not only those engaged in radiographic work but also those in the vicinity of radiographic inspection - is of major importance. Safety requirements impose both economic and operational constraints on the use of radiography for inspection.

Three basic elements of radiography include a radiation source, the testpiece or object being evaluated, and a sensing material. These elements are shown schematically in Figure I.8.

The testpiece (see Figure I.8) is a plate of uniform thickness containing an internal flaw that has absorption characteristics different from those of the surrounding material. Radiation from the source is absorbed by the testpiece as the radiation passes through it; the flaw and surrounding material absorb different amounts of radiation. Thus, the intensity of radiation that impinges on the sensing material in the area beneath the flaw is different from the amount that impinges on adjacent areas. This produces an image, or shadow, of the flaw on the sensing material. This section briefly reviews the general characteristics and safety principles associated with radiography.

Two types of electromagnetic radiation are used in radiographic inspection: x-rays and γ- rays. X-rays and γ- rays differ from other types of electromagnetic radiation (such as visible light, microwaves, and radio waves) only in their wavelengths, although there is not always a distinct transition from one type of electromagnetic radiation to another (Figure I.9). Only x-rays and γ- rays, because of their relatively short wavelengths (high energies), have the capability of penetrating opaque materials to reveal internal flaws.

X-rays and γ- rays are physically indistinguishable; they differ only in the manner in which they are produced. X-rays result from the interaction between a rapidly moving stream of electrons and atoms in a solid target material, while γ - rays are emitted during the radioactive decay of unstable atomic nuclei.

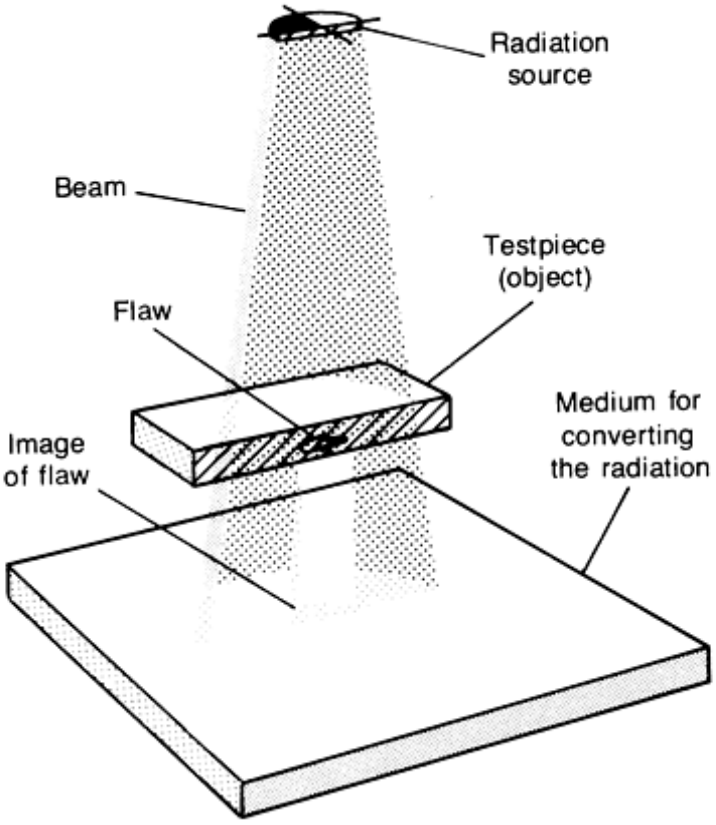

Figure I.8: Schematic of the basic elements of a radiographic system showing the method of sensing the image of an internal flaw in a plate of uniform thickness

The amount of exposure from x-rays or -rays is measured in roentgens (R), where 1 R is the amount of radiation exposure that produces one electrostatic unit (3.33564×10^{-10} C) of charge from 1.293 mg (45.61×10^{-6} oz) of air. The intensity of an x-ray or -ray radiation is measured in roentgens per unit time.

Although the intensity of x-ray or γ- ray radiation is measured in the same units, the strengths of x-ray and γ- ray sources are usually given in different units. The strength of an x-ray source is typically given in roentgens per minute at one meter (RMM) from the source or in some other suitable combination of time or distance units (such as roentgens per hour at one meter, or RHM). The strength of a γ- ray source is usually given in terms of the radioactive decay rate, which has the traditional unit of a curie (1 Ci = 37×10^9

disintegrations per second). The corresponding unit in the Système International d'Unités (SI) system is a gigabecquerel (1 GBq = 1 × 10^9 disintegrations per second).

The spectrum of radiation is often expressed in terms of photon energy rather than as a wavelength. Photon energy is measured in electron volts, with 1 eV being the energy imparted to an electron by an accelerating potential of 1 V. Figure I.9 shows the radiation spectrum in terms of both wavelength and photon energy.

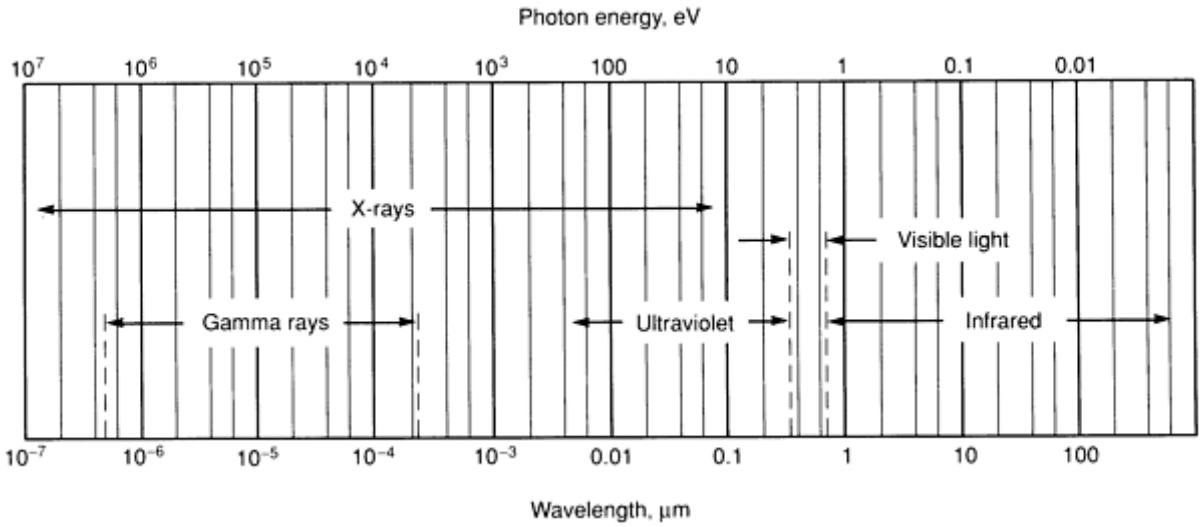

Figure I.9: Schematic of the portion of electromagnetic spectrum that includes x-rays, γ-rays, ultraviolet and visible light, and infrared radiation showing their relationship with wavelength and proton.

When x-rays are produced from the collision of fast-moving electrons with a target material, two types of x-rays are generated. The first type of x-ray is generated when the electrons are rapidly decelerated during collisions with atoms in the target material. These x-rays have a broad spectrum of many wavelengths (or energies) and are referred to as continuous x-rays or by the German word bremsstrahlung, which means braking radiation. The second type of x-ray occurs when the collision of an electron with an atom of the target material causes a transition of an orbital electron in the atom, thus leaving the atom in an excited state. When the orbital electrons in the excited atom rearrange themselves, x-rays are emitted that have specific wavelengths (or energies) characteristic of the particular electron rearrangements taking place. These characteristic x-rays usually have much higher intensities than the background of bremsstrahlung having the same wavelengths.

Gamma rays are generated during the radioactive decay of both naturally occurring and artificially produced unstable isotopes. In all respects other than their origin, γ- rays and x-rays are identical. Unlike the broad-spectrum radiation produced by x-ray sources, γ- ray sources emit one or more discrete wavelengths of radiation, each having its own characteristic photon energy (or wavelength).

Many of the elements in the periodic table have either naturally occurring radioactive isotopes or isotopes that can be made radioactive by irradiation with a stream of neutrons in the core of the nuclear reactor. However, only certain isotopes are extensively used for radiography.

I.3.2 Digital radiography

Various types of image conversion techniques allow the viewing of radiographic images while the testpiece is being irradiated and moved with respect to the radiation source and the radiation detector. These radioscopic techniques can be classified as real-time radiography (also known as real-time radioscopy) and near real-time radiography (or near real-time radioscopy). The distinction between these two classifications is that the formation of near real-time images occurs after a time delay, and this requires limitation of the test object motion. An example of near real-time radiographic imaging involves the use of discrete detectors (primarily linear arrays) that scan the area being irradiated. The outputs are then processed digitally to form images in near real time. This technique is often referred to as digital radiography.

The predecessor of the modern methods of real-time radiography is fluoroscopy. This technique, which is now largely obsolete, involves the projection of radiographic images on a fluorescent screen (Figure I.10). The screen consists of fluorescent crystals, which emit light in proportion to the intensity of the impinging radiation. The radiographic image can then be viewed, with appropriate measures taken to protect the viewer from radiation.

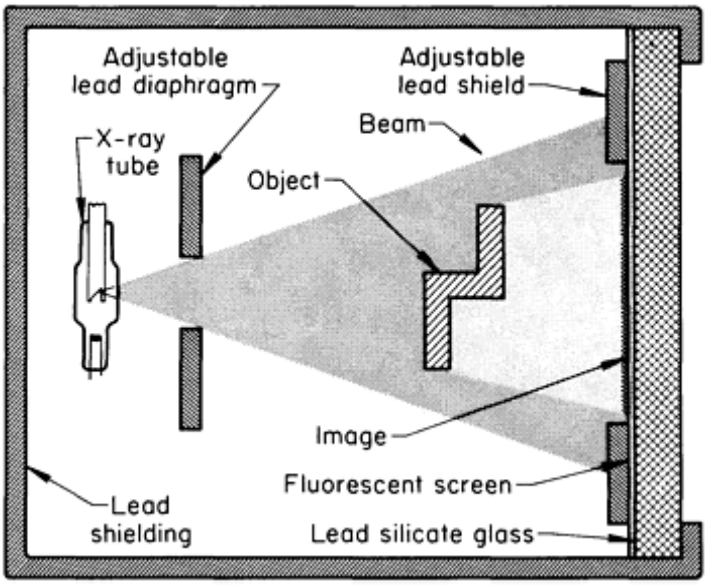

Figure I.10: Diagram of the components and principles of operation of a fluoroscope.

The main problem with fluoroscopes is the low level of light output from the fluorescent screen. This requires the suppression of background light and about 30 min. for the viewer's eyes to become acclimated. Moreover, radiation safety dictates viewing through leaded glass or indirectly by mirrors. Because of these limitations, other methods have been developed to improve safety and to amplify the images from fluorescent screens.

One of the early systems (1950's) involved the development of image-intensifier tubes. Image-intensifier tubes (Figure I.11) are glass-enclosed vacuum devices that convert a low-intensity x-ray image or a low-brightness fluorescent-screen image into a high-brightness visible-light image. Image intensification is achieved by a combination of electronic amplification and image minification. The image brightness at the output

window of an image-intensifier tube is 0.3 × 10^3 cd/m2 (10^{-1} Lambert) compared to 0.3 cd/m^2 (10^{-4} Lambert) for conventional fluoroscopic screen.

These early image intensifiers were originally developed for medical purposes and were limited to applications with low energy radiation (because of low detection efficiencies at high energies). Consequently, industrial radiography with these devices was restricted to aluminium, plastics, or thin sections of steel.

By the mid-1970s, other technological developments led to further improvements in real-time radiography. These advances included high-energy x-ray sensitivity for image intensifiers, improved screen materials, digital video processing for image enhancement, and high-definition imaging with microfocus x-ray generators.

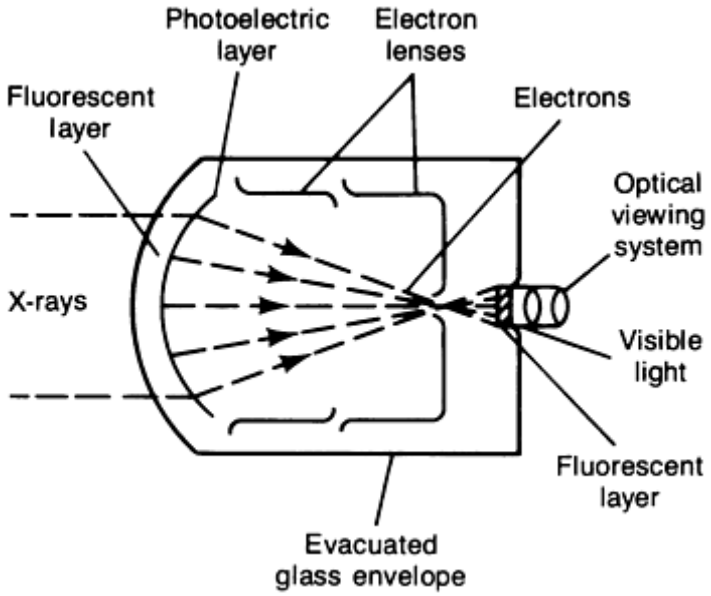

Figure I.11: Schematic of an image – intensifier tube.

Although the early image intensifiers were suitable for medical applications and the inspection of light materials and thin sections of steel, the image quality was not sufficient for general use in radiography. Therefore, image intensifiers had to be redesigned for industrial material testing. The modern image intensifier is a very practical imaging device for radiographic inspection with radiation energies up to 10 MeV. With the image intensifier, a 2% difference in absorption can be routinely achieved in production inspection applications. The typical dynamic range of an image intensifier before image processing is about 2000:1.

A schematic of a modern x-ray image intensifier is shown in Figure I.12, along with a graph indicating the level of signal strength as the radiation passes through a sample and impinges on the entrance screen of the image-intensifier tube. These screens are usually made of a scintillating material, such as cesium iodide (CsI), and fixed to a photocathode. The energy of the incident radiation quanta generates electrons that produce light in the CsI entrance screen (approximately 150 photons per absorbed gamma quantum). To avoid degradation of the image quality by lateral dispersion of the light in the conversion screen, the CsI scintillating material, with a cubic crystalline structure, is grown under controlled conditions, resulting in small, needle-shaped elements. This structure causes the scintillating screen to act as a fiber-optical faceplate.

Light generated in one crystal needle does not spread laterally, but is confined to the needle in a direction parallel to the incident radiation. Therefore, the thickness of the

conversion screen does not cause appreciable deterioration in the spatial resolution of the system.

The light from the scintillating screen then impinges on a photocathode in contact with the entrance screen. The photocathode emits photoelectrons. The electron image produced at the cathode is reduced by a factor of ten and is intensified by means of an accelerating voltage. The final phosphor screen presents a relatively bright image (approximately 5 million photons per second per square millimetre), caused by the impinging electrons. The image then passes through an optical system, which directs the image to a television camera tube, such as a vidicon or plumbicon tube. Vidicons have a dynamic range of 70:1; plumbicons, 200:1.

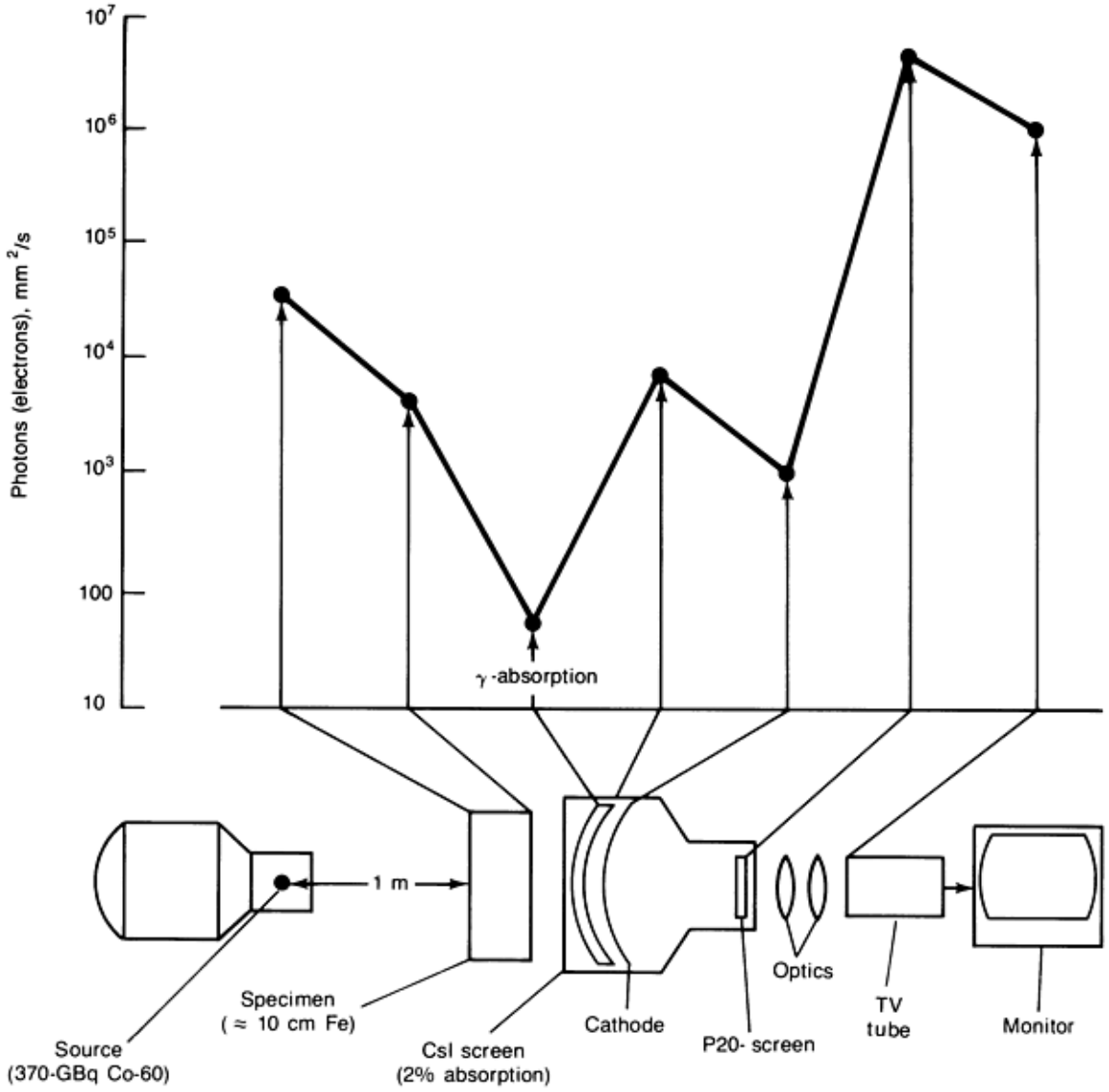

Figure I.12: Schematic of a typical radioscopic system using an x-ray image intensifier.

Real-time radiography is often applied to objects on assembly lines for rapid inspection. Digital radiography with discrete detectors, in particular, is being more widely used because it provides an unlimited field of view and the largest dynamic range of all the radiographic methods. Because a larger dynamic range allows the inspection of parts having a wider range of thicknesses, digital radiography has found application in the inspection of castings (see Figure I.13).

Radiography is also an accepted method of detecting internal discontinuities in welds. Image intensifiers are the most widely used system for the real-time radiographic inspection of welds, although digital radiography with discrete detectors is also used. Projective magnification with microfocus x-ray sources is also useful in weld and diffusion bond inspection.

Real-time radiography provides immediate information without the delay and expense of film development. Real-time systems also allow the manipulation of the testpiece during inspection and the improvement of resolution and dynamic range by digital image enhancement. Real-time radiography with discrete detectors (that is, digital radiography) also provides good scatter rejection.

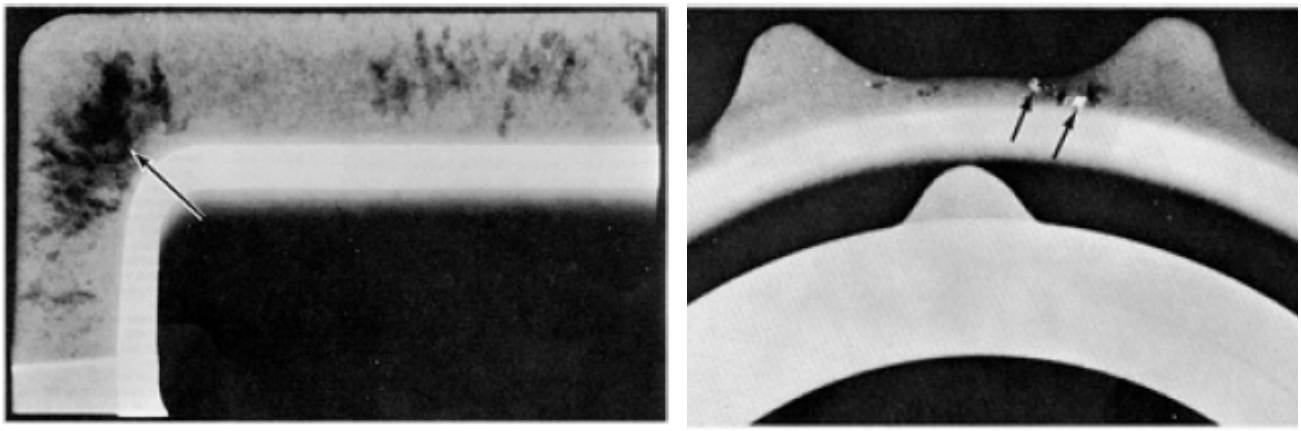

(a) (b)

Figure I.13: Radiographic appearance of:
(a) gross porosity (see arrow) in Al alloy 319 manifold casting, (b) dross inclusions (arrows) in the outer flange of a cast aluminium alloy 355 housing body

Nevertheless, film radiography is a simpler technique that represents less of a capital investment. The sensitivity and resolution of real-time systems are usually not as good as those of film, although real-time radiography can approach the sensitivity and resolution of film radiography when good inspection techniques are used. Good technique is often more important than the details of the imaging system itself.

I.3.3 Industrial computed tomography (CT)

Computed tomography (CT), in a general sense, is an imaging technique that generates an image of a thin, cross-sectional slice of a testpiece (Figure I.14.a). The CT imaging technique differs from other imaging methods in that the energy beam and the detector array in CT systems lie in the same plane as the surface being imaged. This is unlike typical imaging techniques, in which the energy beam path is perpendicular to the surface being imaged. Moreover, because the plane of a CT image is parallel with the energy beam and detector scan path, CT systems require a computing procedure to calculate, locate, and display the point-by-point relative attenuation of the energy beam passing through the structures within the thin, cross-sectional slice of the testpiece.

Computed tomography has been demonstrated with a number of different types of energy beams, such as ultrasound, electrons, protons, particles, lasers, and microwaves.

In industrial nondestructive evaluations (NDE), however, only x-ray computed tomography is considered to have widespread value. X-ray computed tomography collects

and reconstructs the data of x-ray transmission through a two-dimensional slice of an object to form a cross-sectional image without interference from overlying and underlying areas of the object. The CT image represents the point-by-point linear attenuation coefficients in the slice, which depend on the physical density of the material, the effective atomic number of the material, and the x-ray beam energy.

The CT image is unobscured by other regions of the testpiece and is highly sensitive to small density differences (<1%) between structures. Computed tomography systems can also produce digital radiography (DR) images, and the DR and CT images can be further processed or analyzed within the computer. A series of CT images can be used to characterize the object volume, with the data reformatted to display alternate planes through the component or to present three-dimensional surfaces of structures within the object.

Computed tomography provides a unique means of obtaining very specific information on the interior structure of components. Computed tomography technology is very versatile and is not restricted by the shape or composition of the object being inspected. Also, CT systems can be configured to inspect objects of greatly varying sizes, weights, and densities. Generally, systems designed to accommodate large objects do not provide spatial resolution as high as systems designed for the inspection of smaller objects.

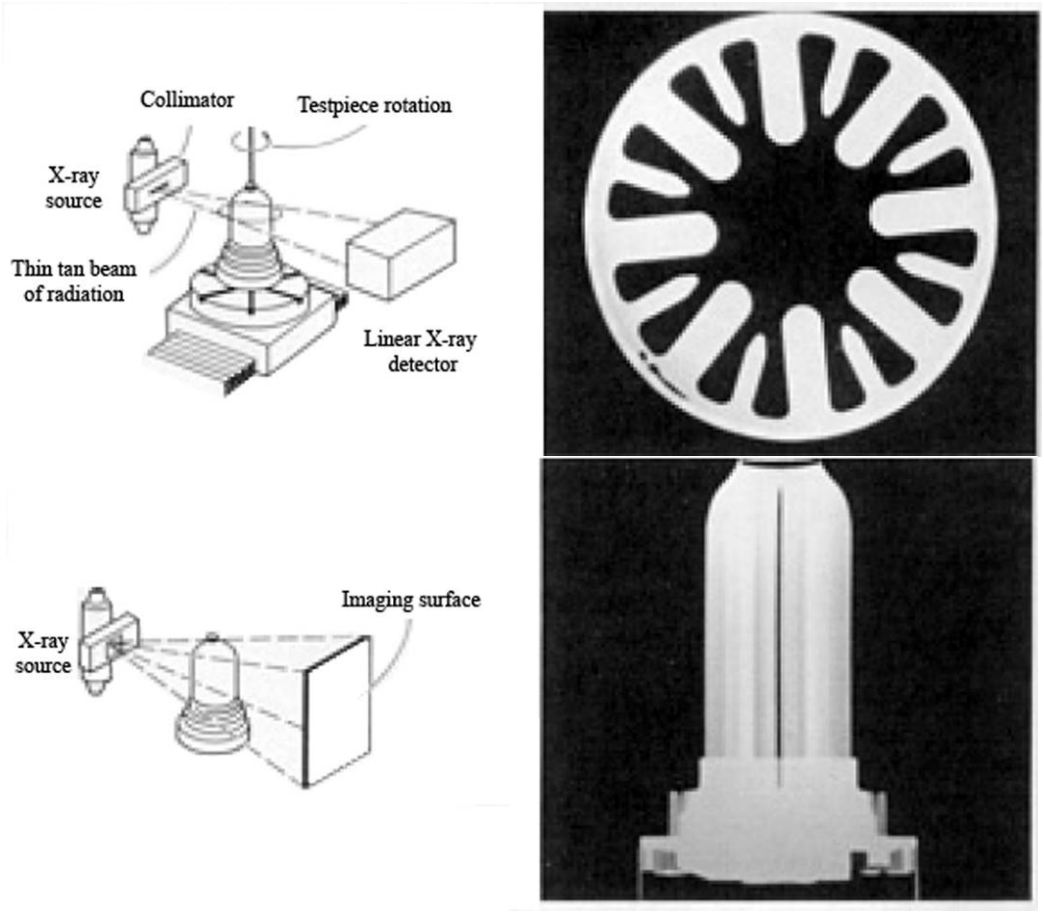

Figure I.14: Comparison of computed tomography (a) and radiography (b). A high-quality digital radiograph (b) of solid rocket motor igniters shows a serious flaw in a carefully oriented tangential shot. A CT image (a) at the height of the flaw shows the flaw in more detail and in a form an inexperienced viewer can readily recognize.

The major limitations of computed tomography are the relatively high equipment costs and the limited throughput for evaluating large volumes. Although CT systems improve sensitivity by generating images of a thin cross section, this procedure also produces throughput difficulties if information is required over a large volume. Many thin CT slices are required for the full characterization of an entire component. Typically, full-volume CT scanning is limited to certain low volume, high-value components or to the engineering evaluation of prototype or test specimens. In higher-volume production, CT images are often taken at specific critical positions for flaw detection or dimensional analysis. The digital radiography mode of CT systems or some other conventional inspection technique is often used to identify suspicious indications. The CT imaging mode is then used to characterize the structure or flaw to provide more information for the accept/reject/repair decision on the component.

Composite structures, by their nature are complex materials that can pose challenges in design, fabrication, and inspection. Because of the high strength-to-weight ratio of these materials, composite usage is increasing, especially in the weight-sensitive aerospace industry. Computed tomography imaging has found considerable use in assisting the engineering development, problem solving, and production of composite components (particularly carbon composite components). The ability to track the integrity of individual components can greatly simplify process analysis relative to a sampled destructive study.

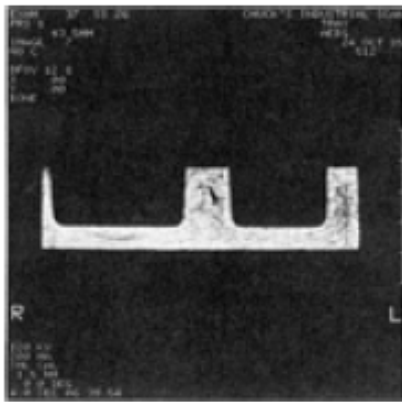

Figure I.15: CT image of a molded chopped-fiber carbon composite showing a resin flow (left) and a void in the center rib.

Computed tomography has been used to evaluate the fabrication process for certain composite components, including molded chopped-fiber components, as shown in Figure I.15. Resin flow patterns (Figure I.15) can be seen, and an individual component can be evaluated at different stages of curing to determine the point at which processing defects are created in the component. Resin flows in composite materials are generally visible, assuming a difference in the linear attenuation coefficient between the fiber and resin material. Low-density resin flows with widths near the image resolution may appear similar to a crack with sub resolution separation. The use of dual energy techniques may help in distinguishing between similar indications. Fiber orientation in composite materials is sometimes seen, especially with chopped-fiber molded components. The ability to discriminate individual fiber bundles is highly dependent on fiber bundle size and system resolution. Computed tomography can detect indications of waviness in composite layers and porpoising (out-of-plane waviness). Radiographic tracer fibres appear with very high contrast.

Operational tests and tests to failure can also benefit from detailed data obtained at various stages of the test. One example of this type of use is the evaluation of rocket motor nozzles before and after firing tests. In this case, the degree and depth of charring were evaluated and compared with theoretical models. Computed tomography has been used in a number of situations to assist in the evaluation of valuable prototype components.

Some of the highest interest in the use of new techniques occurs with engineering problem solving. An example is the failure of the space shuttle launched communication satellites to obtain proper orbit in February 1984. In this case, computed tomography demonstrated interlaminar density variations (see Figure I.16.b) in some of the rocket motor exit cones of the type used with the satellites. These variations had not been detected by routine inspection of the components.

Computed tomography provided a mechanism to evaluate the existing inventories, permitting judgments to be made on the flight-worthiness of the remaining hardware

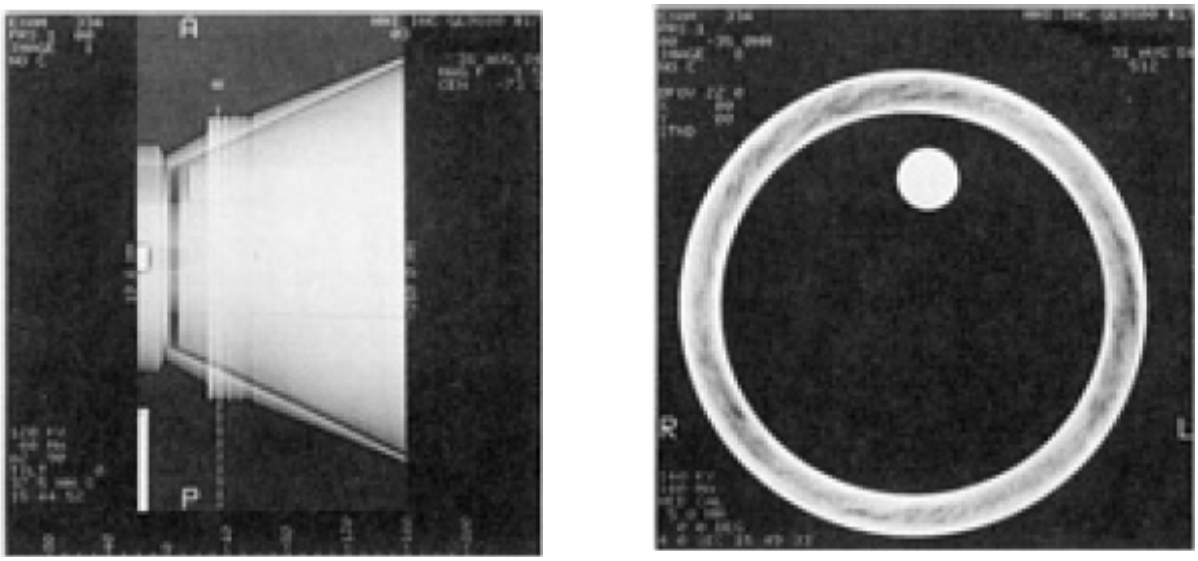

Figure I.16: Digital radiograph (a) of rocket exit cone showing the position for CT scanning through the thread portion of the component. (b) CT image through threaded area of rocket exit cone. CT revealed the extent of interply density variations.

Computed tomography is also used in the production inspection of certain composite hardware. This is particularly true in the case of composite rocket motor hardware because of the experiences discussed above and the active role governmental agencies have played in driving this capability. The increased use of composite materials in critical structures is increasing the role of computed tomography in the production inspection of composite components.

In addition to individual rocket motor composite components, CT systems are used to scan full rocket motors. Some of these systems use linear accelerator x-ray sources up to 25 MV and are designed to inspect solid propellant rockets in excess of 3 m in diameter. These systems can be used to evaluate the assembly of the various motor components and to evaluate the integrity and fit of the casing, liners, and propellant.

Computed tomography systems are used for the production inspection of small, complex precision castings and forgings, especially turbine blades and vanes used in aircraft engines and liquid propellant rocket motor pumps. The ability to localize material flaws and passage dimensions has also permitted the reworking of complex castings and fabrications. In the aircraft engine industry, computed tomography is considered an

enabling technology that will allow large, complex structural castings to replace fabricated components, reducing both component weight and manufacturing costs. Computed tomography is also used to analyze the wall thickness of certain used blades to evaluate if sufficient material remains for refurbishing the component. This has permitted the overhaul and reuse of components that would otherwise be questionable.

Because of throughput considerations for production, casting flaws are generally detected in the digital radiography mode.

Computed tomography is used to detect flaws in critical areas and to further evaluate flaw indications detected by digital radiography or other methods. The specific data provided by computed tomography for the evaluation of flaw indications allow for a more informed accept/reject decision. Porosity and micro shrink reduce the density of the material and are usually visible if distributed over a multipixel area (Figure I.17). The percentage of porosity can be quantified with properly controlled procedures. Other detectable conditions include casting bridges or fins, residual core material in the casting (Figure I.18.a), and machining defects (Figure I.18.b).

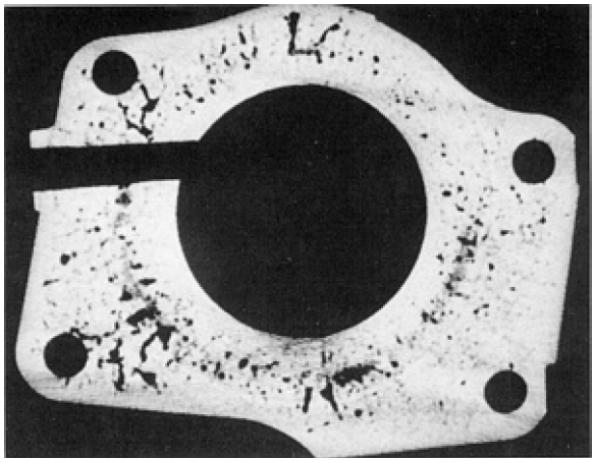

Figure I.17: CT image of cast housing showing severe shrinkage and porosity

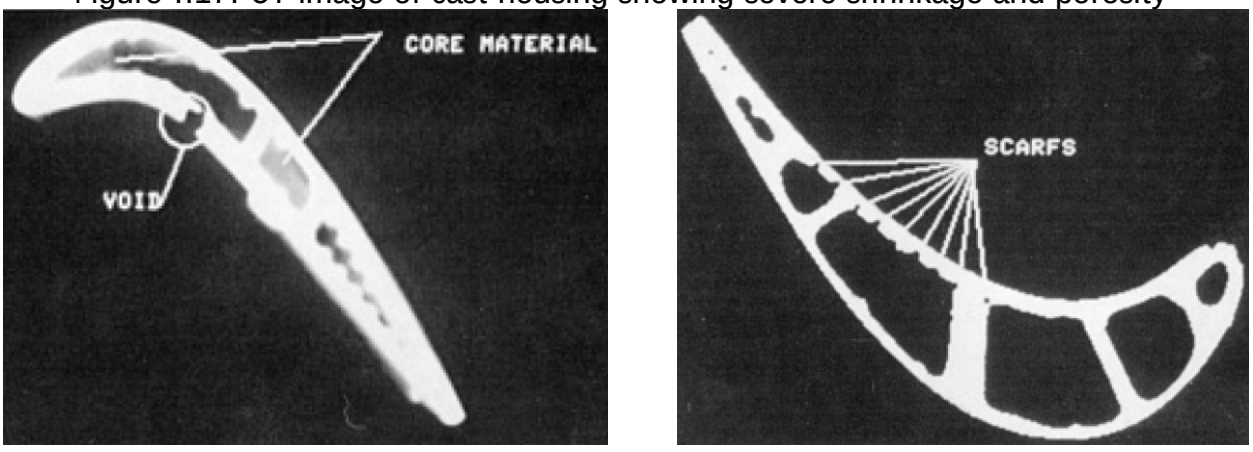

(a) (b)

Figure I.18: CT images of a turbine blade: (a) Residual core from the casting process, (b) scarfing caused by near-tangential drilling of nearby walls.

Because of the density sensitivity of the CT data and the averaging of the density values within a measured voxel, dimensional measurements can be made with better precision than the resolution of the image. The use of computed tomography for wall thickness gaging has advantages over other gaging techniques in that the measurements

are not operator dependent, and precise information can be obtained from regions with internal walls and sharp curvatures.

Figure I.19 shows a typical CT image of a turbine blade with the measured wall thickness information displayed. In this case, the wall thicknesses were measured with automated software, which makes many measurements along each wall segment (between ribs), marks the location of the thinnest portion, and posts the measured data in a table. The quantitative data can also be passed to a statistical software package for process control analysis. Applications are being pursued for using this dimensional information for subsequent machining operations, such as adjusting power levels for laser drilling. The ability to provide spatially specific structure and density information also opens up the opportunity to obtain three-dimensional (3D) data representations (Figure I.23) of physical components for computer-aided design documentation and computer-aided engineering analysis.

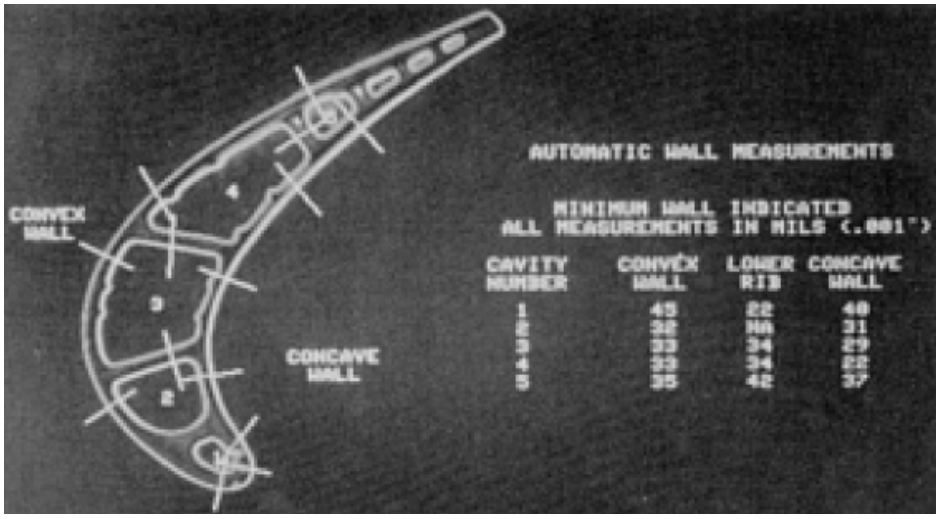

Figure I.19: Cross sectional CT image through a turbine blade with wall thickness measurement locations and values determined with automated software.

The sensitivity of computed tomography to density differences of a fraction of 1% can be applied to a number of material characterization problems. Materials that vary in density or composition because of the fabrication process may benefit from this capability. Injection-molded powder metal components have been scanned with the potential of better density characterization and process control in the green state to produce an improved sintered product. The computed tomography of advanced ceramic materials is also increasing, especially for high-stress and complex-shaped components.

In general, the advantages of computed tomography over alternative inspection methods increase with the complexity of the structure. The ability of computed tomography to image the components in an assembly does not reduce the need for component inspection prior to assembly. This ability can be a valuable tool, however, when quality questions arise regarding the assembled product. Computed tomography can also be used to verify proper assembly or help evaluate damage or distortion in components caused by the fabrication process.

Examples and potential applications for computed tomography cover a wide range. They include the evaluation of composite spars in helicopter rotor blades, detonators and arming devices, thermal batteries, and a variety of electronic assemblies. The major limitation is the capacity of the system and economic considerations, especially for large production volume items. Computed tomography can provide worthwhile capabilities even

for low-cost, high-volume components by assisting engineering development and problem solving.

The components that constitute a CT system often allow for additional flexibility and capabilities beyond providing the cross-sectional CT images. The x-ray source, detector, and manipulation system provide the ability to acquire conventional radiographic images. The acquisition of digital images along with the computer system facilitates the use of image processing and automated analysis. In addition, the availability of the cross-sectional data permits 3D data processing, image generation, and analysis.

One of the limitations of CT inspection is that the CT image provides detailed information only over the limited volume of the cross-sectional slice. Full inspection of the entire volume of a component with computed tomography requires many slices, limiting the inspection throughput of the system. Therefore, CT equipment is often used in a digital radiography (DR) mode during production operations, with the CT imaging mode used for specific critical areas or to obtain more detailed information on indications found in the DR image. DR capabilities and throughput can be significant operational considerations for the overall system usage.

Computed tomography systems generally provide a DR imaging mode, producing a two-dimensional radiographic image of the overall testpiece. The high-resolution detector of the rotate-only systems normally requires a single z-axis translation (Figure I.21) to produce a high-quality DR image. For even higher resolution, interleaved data can be obtained by repeating with a shift of a fraction of the detector spacing. For large objects, a scan-shift-scan approach can be used. The translate-rotate systems are typically less efficient at acquiring DR data because the wider detector spacing requires multiple scans, with shifts to provide adequate interleaving of data. If the width of the radiographic field does not cover the full width of the object, the object can be translated and the sequence repeated.

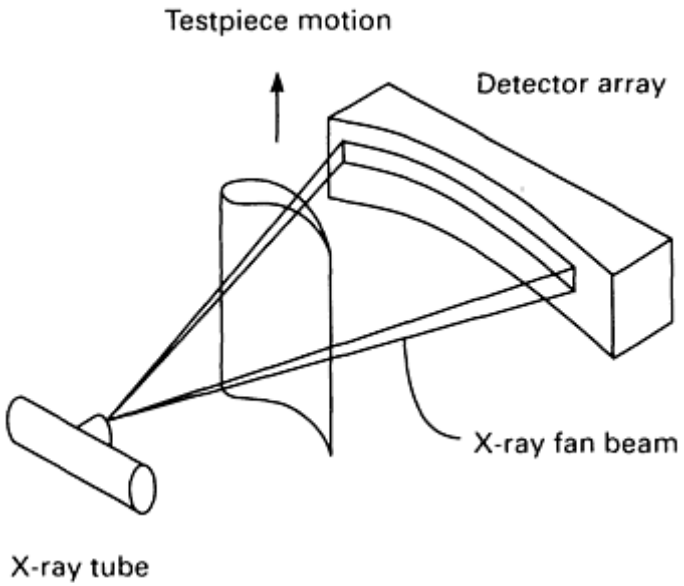

Figure I.21: Digital radiography mode. The component moves perpendicular to the fan beam, and the radiographic data are acquired line-by-line..

The capabilities and use of these DR images are generally the same as discussed for radiographic inspection. The method of data acquisition is different on the CT systems; the data are acquired as a sequence of lines or line segments. The use of a thin fan beam with a slit-scan data acquisition is a very effective method of reducing the relative amount

of measured scatter radiation. This can significantly improve the overall image contrast (Figure I.22). In addition, the data acquisition requirements for CT systems provide for a high sensitivity and very wide dynamic range detector system.

Because the DR and CT images are stored as a matrix of numbers, the computer can be used as a tool to obtain specific image information, to enhance images, or to assist in analyzing image data (see Figure I.23).

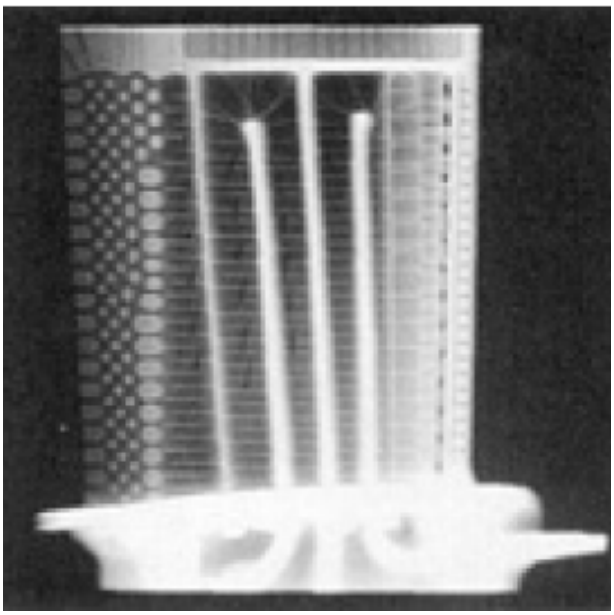

Figure I.22: Digital radiograph of an aircraft engine turbine blade (nickel alloy precision casting) from an industrial CT system.

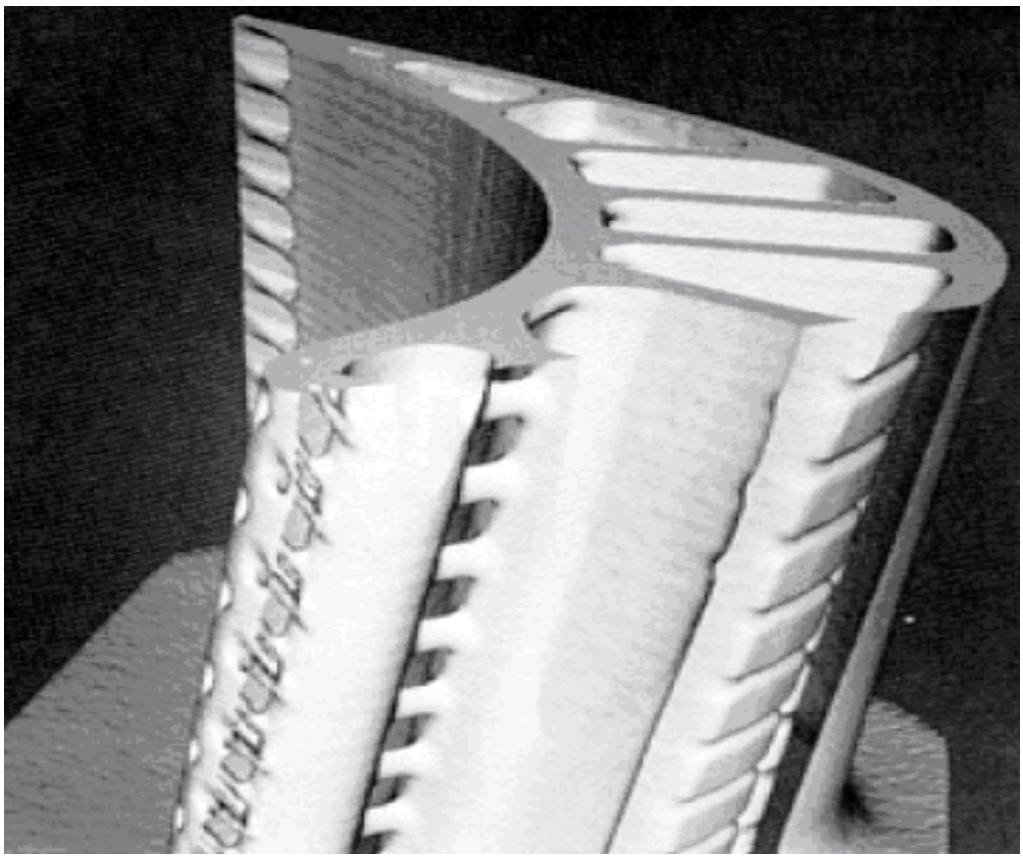

Figure I.23: Complete 3D surface image of a turbine blade based on a CT data scan.

I.3.4 Neutron radiographic testing (NR)

Neutron radiography (NR) is a form of nondestructive inspection that uses a specific type of particulate radiation, called neutrons, to form a radiographic image of a testpiece. The geometric principles of shadow formation, the variation of attenuation with testpiece thickness, and many other factors that govern the exposure and processing of a neutron radiograph are similar to those for radiography using x-rays or γ - rays.

Neutron radiography is similar to conventional radiography in that both techniques employ radiation beam intensity modulation by an object to image macroscopic object details. X-rays or γ - rays are replaced by neutrons as the penetrating radiation in a through-transmission inspection. The absorption characteristics of matter for x-rays and neutrons differ drastically; the two techniques in general serve to complement one another.

Neutrons are subatomic particles that are characterized by relatively large mass and a neutral electric charge. The attenuation of neutrons differs from the attenuation of x-rays in that the processes of attenuation are nuclear rather than ones that depend on interaction with the electron shells surrounding the nucleus.

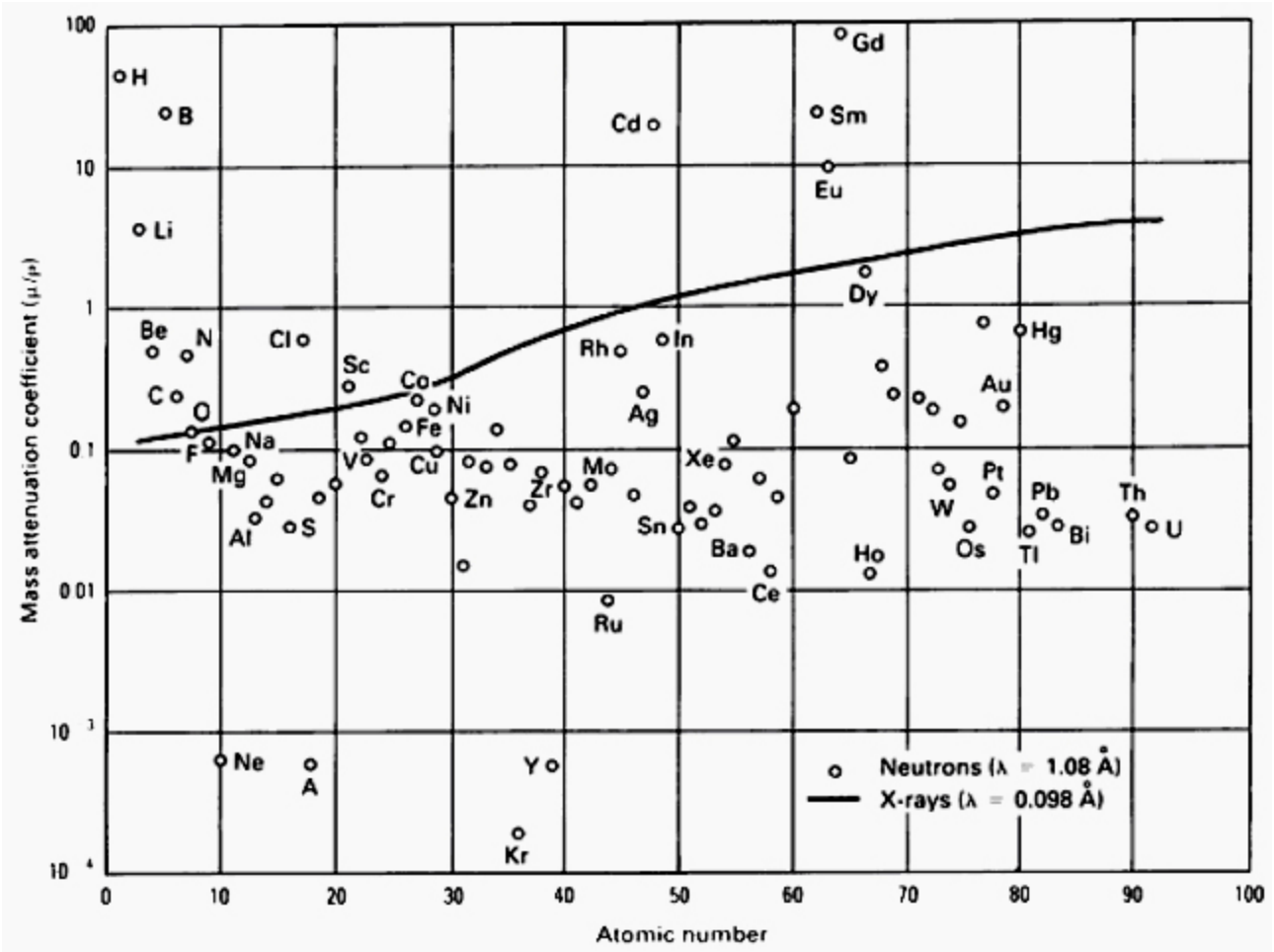

Figure I.24: Mass attenuation coefficients for the elements as a function of atomic number for thermal (4.0 × 10-21 J, or 0.025 eV) neutrons and x-rays (energy 125 kV).

Neutrons are produced by nuclear reactors, accelerators, and certain radioactive isotopes, all of which emit neutrons of relatively high energy (fast neutrons). Because

most neutron radiography is performed with neutrons of lower energy (thermal neutrons), the sources are usually surrounded by a moderator, which is a material that reduces the kinetic energy of the neutrons.

Neutron radiography is not accomplished by direct imaging on film, because neutrons do not expose x-ray emulsions efficiently. In one form of neutron radiography, the beam of neutrons impinges on a conversion screen or detector made of a material such as dysprosium or indium, which absorbs the neutrons and becomes radioactive, decaying with a short half-life. In this method, the conversion screen alone is exposed in the neutron beam, then immediately placed in contact with film to expose it by autoradiography. In another common form of imaging, a conversion screen that immediately emits secondary radiation is used with film directly in the neutron beam.

Neutron radiography differs from conventional radiography in that the attenuation of neutrons as they pass through the testpiece is more related to the specific isotope present than to density or atomic number. X-rays are attenuated more by elements of high atomic number than by elements of low atomic number, and this effect varies relatively smoothly with atomic number. Thus, x-rays are generally attenuated more by materials of high density than by materials of low density.

For thermal neutrons, attenuation generally tends to decrease with increasing atomic number, although the trend is not a smooth relationship. In addition, certain light elements (hydrogen, lithium, and boron), certain medium-to-heavy elements (especially cadmium, samarium, europium, gadolinium, and dysprosium), and certain specific isotopes have an exceptionally high capability of attenuating thermal neutrons (Figure I.24). This means that neutron radiography can detect these highly attenuating elements or isotopes when they are present in a structure of lower attenuation.

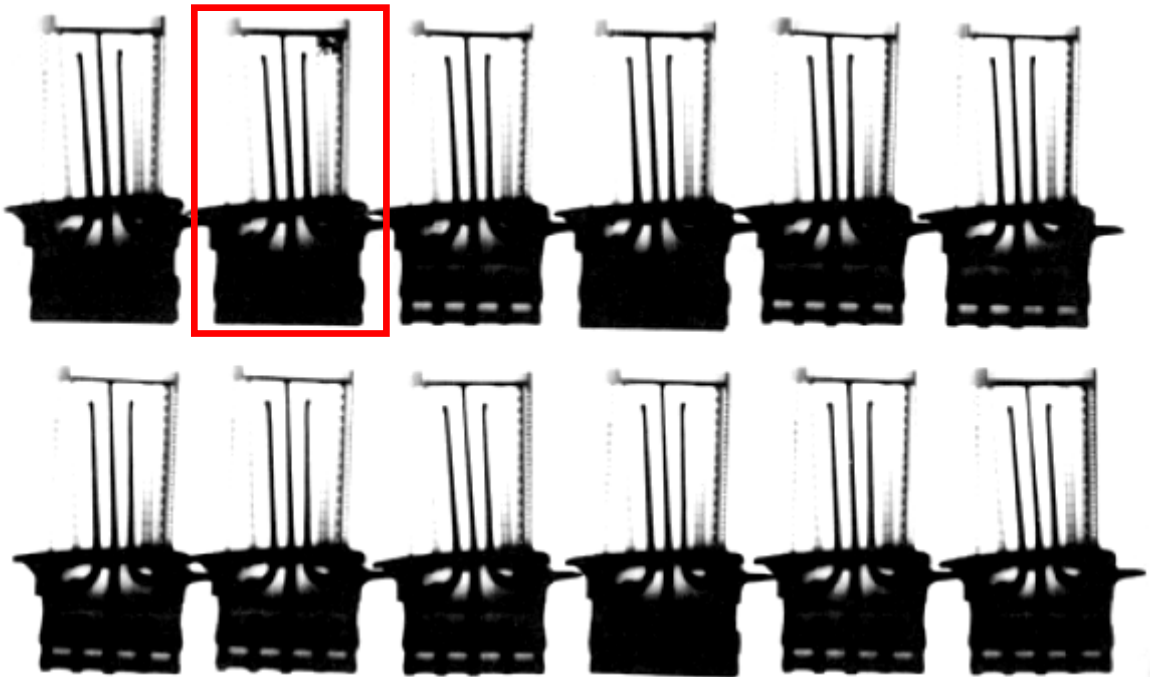

Figure I.25: Thermal neutron radiograph of 12 turbine blades tagged with Gd_2O_3 solution. One of the 12 blades (located in the top row and second from the left) contains residual core material, > 0.38 mm in diameter, in its upper right-hand corner cooling passage.

Thermal (slow) neutrons permit the radiographic visualization of low atomic number elements even when they are present in assemblies with high atomic number elements

such as iron, lead, or uranium. Although the presence of the heavy metals would make detection of the light elements virtually impossible with x-rays, the attenuation characteristics of the elements for slow neutrons are different, which makes detection of light elements feasible. Practical applications of neutron radiography include the inspection of metal-jacketed explosives, rubber O-ring assemblies, investment cast turbine blades (see Figure I.25) to detect residual ceramic core, and the detection of corrosion in metallic assemblies.

Using neutrons, it is possible to detect radiographically certain isotopes - for example, certain isotopes of hydrogen, cadmium, or uranium. Some neutron image detection methods are insensitive to background γ- rays or x-rays and can be used to inspect radioactive materials such as reactor fuel elements.

In the nuclear field, these capabilities have been used to image highly radioactive materials and to show radiographic differences between different isotopes in reactor fuel and control materials. The characteristics of neutron radiography complement those of conventional radiography; one radiation provides a capability lacking or difficult for the other.

I.4 Ultrasonic inspection (UT)

I.4.1 Generalities

Ultrasonic inspection is a nondestructive method in which beams of high-frequency sound waves are introduced into materials for the detection of surface and subsurface flaws in the material. The sound waves travel through the material with some attendant loss of energy (attenuation) and are reflected at interfaces. The reflected beam is displayed and then analyzed to define the presence and location of flaws or discontinuities.

The degree of reflection depends largely on the physical state of the materials forming the interface and to a lesser extent on the specific physical properties of the material. For example, sound waves are almost completely reflected at metal/gas interfaces. Partial reflection occurs at metal/liquid or metal/solid interfaces, with the specific percentage of reflected energy depending mainly on the ratios of certain properties of the material on opposing sides of the interface.

Cracks, laminations, shrinkage cavities, bursts, flakes, pores, disbonds, and other discontinuities that produce reflective interfaces can be easily detected. Inclusions and other inhomogeneities can also be detected by causing partial reflection or scattering of the ultrasonic waves or by producing some other detectable effect on the ultrasonic waves.

Most ultrasonic inspection instruments detect flaws by monitoring one or more of the following:

- Reflection of sound from interfaces consisting of material boundaries or discontinuities within the metal itself
- Time of transit of a sound wave through the testpiece from the entrance point at the transducer to the exit point at the transducer
- Attenuation of sound waves by absorption and scattering within the testpiece
- Features in the spectral response for either a transmitted or a reflected signal

Most ultrasonic inspection is done at frequencies between 0.1 and 25 MHz--well above the range of human hearing, which is about 20 Hz to 20 kHz. Ultrasonic waves are

mechanical vibrations; the amplitudes of vibrations in metal parts being ultrasonically inspected impose stresses well below the elastic limit, thus preventing permanent effects on the parts.

Many of the characteristics for ultrasonic waves also apply to audible sound waves and to wave motion in general.

Ultrasonic inspection is one of the most widely used methods of nondestructive inspection. Its primary application in the inspection of metals is the detection and characterization of internal flaws; it is also used to detect surface flaws, to define bond characteristics, to measure the thickness and extent of corrosion, and (much less frequently) to determine physical properties, structure, grain size, and elastic constants.

Most ultrasonic inspection systems include the following basic equipment:

- An electronic signal generator that produces bursts of alternating voltage (a negative spike or a square wave) when electronically triggered
- A transducer (probe or search unit) that emits a beam of ultrasonic waves when bursts of alternating voltage are applied to it
- A couplant to transfer energy in the beam of ultrasonic waves to the testpiece
- A couplant to transfer the output of ultrasonic waves (acoustic energy) from the testpiece to the transducer
- A transducer (can be the same as the transducer initiating the sound or it can be a separate one) to accept and convert the output of ultrasonic waves from the testpiece to corresponding bursts of alternating voltage. In most systems, a single transducer alternately acts as sender and receiver
- An electronic device to amplify and, if necessary, demodulate or otherwise modify the signals from the transducer
- A display or indicating device to characterize or record the output from the testpiece. The display device may be a CRT, sometimes referred to as an oscilloscope; a chart or strip recorder; a marker, indicator, or alarm device; or a computer printout
- An electronic clock, or timer, to control the operation of the various components of the system, to serve as a primary reference point, and to provide coordination for the entire system

The principal advantages of ultrasonic inspection as compared to other methods for nondestructive inspection of metal parts are:

- Superior penetrating power, which allows the detection of flaws deep in the part. Ultrasonic inspection is done routinely to thicknesses of a few meters on many types of parts and to thicknesses of about 6 m in the axial inspection of parts such as long steel shafts or rotor forgings
- High sensitivity, permitting the detection of extremely small flaws
- Greater accuracy than other nondestructive methods in determining the position of internal flaws, estimating their size, and characterizing their orientation, shape, and nature
- Only one surface needs to be accessible
- Operation is electronic, which provides almost instantaneous indications of flaws. This makes the method suitable for immediate interpretation, automation, rapid scanning, in-line production monitoring, and process control. With most systems, a permanent record of inspection results can be made for future reference

- Volumetric scanning ability, enabling the inspection of a volume of metal extending from front surface to back surface of a part
- Non-hazardous to operations or to nearby personnel and has no effect on equipment and materials in the vicinity
- Portability
- Provides an output that can be processed digitally by a computer to characterize defects and to determine material properties

The disadvantages of ultrasonic inspection include the following:

- Manual operation requires careful attention by experienced technicians
- Extensive technical knowledge is required for the development of inspection procedures
- Parts that are rough, irregular in shape, very small or thin, or not homogeneous are difficult to inspect
- Discontinuities that are present in a shallow layer immediately beneath the surface may not be detectable
- Couplants are needed to provide effective transfer of ultrasonic wave energy between transducers and parts being inspected
- Reference standards are needed, both for calibrating the equipment and for characterizing flaws

The ultrasonic inspection of metals is principally conducted for the detection of discontinuities. This method can be used to detect internal flaws in most engineering metals and alloys. Bonds produced by welding, brazing, soldering, and adhesive bonding can also be ultrasonically inspected. In-line techniques have been developed for monitoring and classifying material as acceptable, salvageable, or scrap and for process control. Both line-powered and battery-operated commercial equipment is available, permitting inspection in shop, laboratory, warehouse, or field.

Ultrasonic inspection is used for quality control and materials inspection in all major industries. This includes electrical and electronic component manufacturing; production of metallic and composite materials; and fabrication of structures such as airframes, piping and pressure vessels, ships, bridges, motor vehicles, machinery, and jet engines. In-service ultrasonic inspection for preventive maintenance is used for detecting the impending failure of railroad-rolling-stock axles, press columns, earthmoving equipment, mill rolls, mining equipment, nuclear systems, and other machines and components.

Some of the major types of equipment that are ultrasonically inspected for the presence of flaws are:

- Mill components: Rolls, shafts, drives, and press columns
- Power equipment: Turbine forgings, generator rotors, pressure piping, weldments, pressure vessels, nuclear fuel elements, and other reactor components
- Jet engine parts: Turbine and compressor forgings, and gear blanks
- Aircraft components: Forging stock, frame sections, and honeycomb sandwich assemblies
- Machinery materials: Die blocks, tool steels, and drill pipe
- Railroad parts: Axles, wheels, track, and welded rail
- Automotive parts: Forgings, ductile castings, and brazed and/or welded components

The flaws to be detected include voids, cracks, inclusions, pipe, laminations, debonding, bursts, and flakes. They may be inherent in the raw material, may result from fabrication and heat treatment, or may occur in service from fatigue, impact, abrasion, corrosion, or other causes.

Government agencies and standards-making organizations have issued inspection procedures, acceptance standards, and related documentation. These documents are mainly concerned with the detection of flaws in specific manufactured products, but they also can serve as the basis for characterizing flaws in many other applications.

Ultrasonic inspection can also be used to measure the thickness of metal sections. Thickness measurements are made on refinery and chemical-processing equipment, shop plate, steel castings, submarine hulls, aircraft sections, and pressure vessels. A variety of ultrasonic techniques are available for thickness measurements; several use instruments with digital readout. Structural material ranging in thickness from a few thousandths of an inch to several feet can be measured with accuracies of better than 1%. Ultrasonic inspection methods are particularly well suited to the assessment of loss of thickness from corrosion inside closed systems, such as chemical-processing equipment. Such measurements can often be made without shutting down the process. Special ultrasonic techniques and equipment have been used on such diverse problems as the rate of growth of fatigue cracks, detection of borehole eccentricity, measurement of elastic moduli, study of press fits, determination of nodularity in cast iron, and metallurgical research on phenomena such as structure, hardening, and inclusion count in various metals.

For the successful application of ultrasonic inspection, the inspection system must be suitable for the type of inspection being done, and the operator must be sufficiently trained and experienced. If either of these prerequisites is not met, there is a high potential for gross error in inspection results. For example, with inappropriate equipment or with a poorly trained operator, discontinuities having little or no bearing on product performance may be deemed serious, or damaging discontinuities may go undetected or be deemed unimportant.

The term flaw as used in this article means a detectable lack of continuity or an imperfection in a physical or dimensional attribute of a part. The fact that a part contains one or more flaws does not necessarily imply that the part neither is nonconforming to specification nor unfit for use. It is important that standards be established so that decisions to accept or reject parts are based on the probable effect that a given flaw will have on service life or product safety. Once such standards are established, ultrasonic inspection can be used to characterize flaws in terms of a real effect rather than some arbitrary basis that may impose useless or redundant quality requirements.

I.4.2 General characteristics of ultrasonic waves

Ultrasonic (UT) waves are mechanical waves (in contrast to, for example, light or x-rays, which are electromagnetic waves) that consist of oscillations or vibrations of the atomic or molecular particles of a substance about the equilibrium positions of these particles.

Ultrasonic waves behave essentially the same as audible sound waves. They can propagate in an elastic medium, which can be solid, liquid, or gaseous, but not in a vacuum.

In many respects, a UT beam is similar to a beam of light; both are waves and obey a general wave equation.

Each travels at a characteristic velocity in a given homogeneous medium - a velocity that depends on the properties of the medium, not on the properties of the wave. Like beams of light, ultrasonic beams are reflected from surfaces, refracted when they cross a boundary between two substances that have different characteristic sound velocities, and diffracted at edges or around obstacles. Scattering by rough surfaces or particles reduces the energy of an ultrasonic beam making it comparable to the manner in which scattering reduces the intensity of a light beam.

The general characteristics of sonic or ultrasonic waves are conveniently illustrated by analogy with the behaviour of waves produced in a body of water when a stone is dropped into it. Casual observation might lead to the erroneous conclusion that the resulting outward radial travel of alternate crests and troughs represents the movement of water away from the point of impact. The fact that water is not thus transported is readily deduced from the observation that a small object floating on the water does not move away from the point of impact, but instead merely bobs up and down. The waves travel outward only in the sense that the crests and troughs (which can be compared to the compressions and rarefactions of sonic waves in an elastic medium) and the energy associated with the waves propagate radially outward. The water particles remain in place and oscillate up and down from their normal positions of rest.

Continuing the analogy, the distance between two successive crests or troughs is the wavelength, λ. The fall from a crest to a trough and subsequent rise to the next crest (which is accomplished within this distance) is a cycle. The number of cycles in a specific unit of time is the frequency, f, of the waves. The height of a crest or the depth of a trough in relation to the surface at equilibrium is the amplitude of the waves.

The velocity of a wave and the rates at which the amplitude and energy of a wave decrease as it propagates are constants that are characteristic of the medium in which the wave is propagating. Stones of equal size and mass striking oil and water with equal force will generate waves that travel at different velocities. Stones impacting a given medium with greater energy will generate waves having greater amplitude and energy but the same wave velocity.

The above attributes apply similarly to sound waves, both audible and ultrasonic, propagating in an elastic medium. The particles of the elastic medium move, but they do not migrate from their initial spatial orbits; only the energy travels through the medium. The amplitude and energy of sound waves in the elastic medium depend on the amount of energy supplied. The velocity and attenuation (loss of amplitude and energy) of the sound waves depend on the properties of the medium in which they are propagating.

Ultrasonic waves (and other sound waves) propagate to some extent in any elastic material. When the atomic or molecular particles of an elastic material is displaced from their equilibrium positions by any applied force, internal stress acts to restore the particles to their original positions. Because of the interatomic forces between adjacent particles of material, a displacement at one point induces displacements at neighbouring points and so on, thus propagating a stress-strain wave. The actual displacement of matter that occurs in ultrasonic waves is extremely small.

The amplitude, vibration mode, and velocity of the waves differ in solids, liquids, and gases because of the large differences in the mean distance between particles in these forms of matter. These differences influence the forces of attraction between particles and the elastic behaviour of the materials.

The relation of velocity to frequency and wavelength is given by:

$$v = f\lambda \qquad \text{(I.1)}$$

where v is velocity (in meters/second), f is frequency (in hertz), and λ is wavelength (in meters/cycle). Other consistent units of measure can be used for the variables in equation I.1, where convenient.

On the basis of the particle displacement mode, ultrasonic waves are classified as:

- longitudinal waves,
- transverse waves,
- surface waves,
- Lamb waves.

Longitudinal waves, sometimes called compression waves, are the type of ultrasonic waves most widely used in the inspection of materials. These waves travel through materials as a series of alternate compressions and rarefactions in which the particles transmitting the wave vibrate back and forth in the direction of travel of the waves.

Longitudinal ultrasonic waves and the corresponding particle oscillation and resultant rarefaction and compression are shown schematically in Figure I.26.a; a plot of amplitude of particle displacement versus distance of wave travel, together with the resultant rarefaction trough and compression crest, is shown in Figure I.26.b. The distance from one crest to the next (which equals the distance for one complete cycle of rarefaction and compression) is the wavelength, λ. The vertical axis in Figure I.26.b could represent pressure instead of particle displacement. The horizontal axis could represent time instead of travel distance because the speed of sound is constant in a given material and because this relation is used in the measurements made in ultrasonic inspection.

Longitudinal ultrasonic waves are readily propagated in liquids and gases as well as in elastic solids. The mean free paths of the molecules of liquids and gases at a pressure of 1 atm are so short that longitudinal waves can be propagated simply by the elastic collision of one molecule with the next. The velocity of longitudinal ultrasonic waves is about 6000 m/s in steel, 1500 m/s in water, and 330 m/s in air.

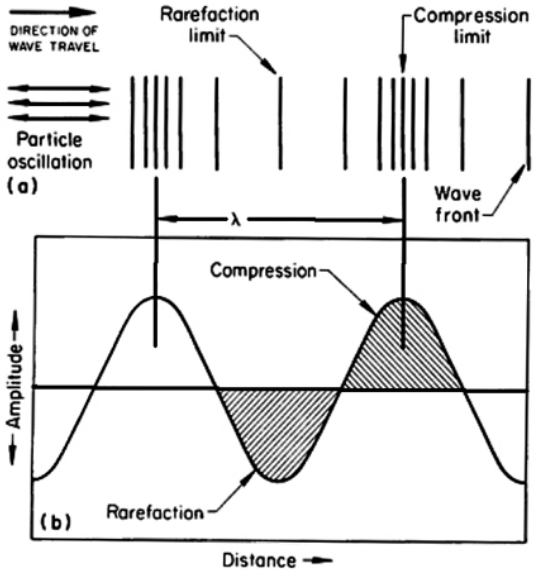

Figure I.26: Schematic of longitudinal ultrasonic waves. (a) Particle oscillation and resultant rarefaction and compression. (b) Amplitude of particle displacement vs. distance of wave travel. The wavelength, λ, is the distance corresponding to one complete cycle.

Transverse waves (shear waves) are also extensively used in the ultrasonic inspection of materials. Transverse waves are visualized readily in terms of vibrations of a

rope that is shaken rhythmically, in which each particle, rather than vibrating parallel to the direction of wave motion as in the longitudinal wave, vibrates up and down in a plane perpendicular to the direction of propagation. A transverse wave is illustrated schematically in Figure I.27, which shows particle oscillation, wave front, direction of wave travel, and the wavelength, , corresponding to one cycle.

Unlike longitudinal waves, transverse waves cannot be supported by the elastic collision of adjacent molecular or atomic particles. For the propagation of transverse waves, it is necessary that each particle exhibit a strong force of attraction to its neighbours so that as a particle moves back and forth it pulls its neighbour with it, thus causing the sound to move through the material with the velocity associated with transverse waves, which is about 50% of the longitudinal wave velocity for the same material.

Air and water will not support transverse waves. In gases, the forces of attraction between molecules are so small that shear waves cannot be transmitted. The same is true of a liquid, unless it is particularly viscous or is present as a very thin layer.

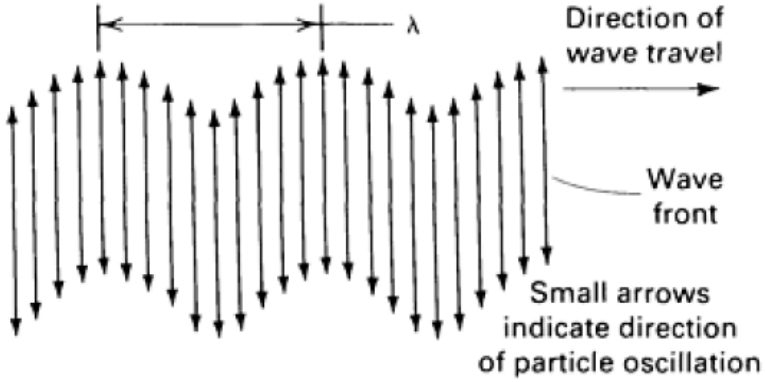

Figure I.27: Schematic of transverse (shear) waves.

Surface waves (Rayleigh waves) are another type of ultrasonic wave used in the inspection of materials. These waves travel along the flat or curved surface of relatively thick solid parts. For the propagation of waves of this type, the waves must be travelling along an interface bounded on one side by the strong elastic forces of a solid and on the other side by the practically negligible elastic forces between gas molecules. Surface waves leak energy into liquid couplant and do not exist for any significant distance along the surface of a solid immersed in a liquid, unless the liquid covers the solid surface only as a very thin film.

Surface waves are subject to attenuation in a given material, as are longitudinal or transverse waves. They have a velocity approximately 90% of the transverse wave velocity in the same material. The region within which these waves propagate with effective energy is not much thicker than about one wavelength beneath the surface of the metal. At this depth, wave energy is about 4% of the wave energy at the surface, and the amplitude of oscillation decreases sharply to a negligible value at greater depths.

Surface waves follow contoured surfaces. For example, surface waves travelling on the top surface of a metal block are reflected from a sharp edge, but if the edge is rounded off, the waves continue down the side face and are reflected at the lower edge, returning to the sending point. Surface waves will travel completely around a cube if all edges of the cube are rounded off. Surface waves can be used to inspect parts that have complex contours.

In surface waves, particle oscillation generally follows an elliptical orbit, as shown schematically in Figure I.28. The major axis of the ellipse is perpendicular to the surface along which the waves are travelling. The minor axis is parallel to the direction of propagation. Surface waves can exist in complex forms that are variations of the simplified waveform illustrated in Figure I.28. The wavelength, λ, is the distance corresponding to one complete cycle.

Lamb waves, also known as plate waves, are another type of ultrasonic wave used in the nondestructive inspection of materials. Lamb waves are propagated in plates (made of composites or metals) only a few wavelengths thick. A Lamb wave consists of a complex vibration that occurs throughout the thickness of the material. The propagation characteristics of Lamb waves depend on the density, elastic properties, and structure of the material as well as the thickness of the testpiece and the frequency. Their behaviour in general resembles that observed in the transmission of electromagnetic waves through waveguides.

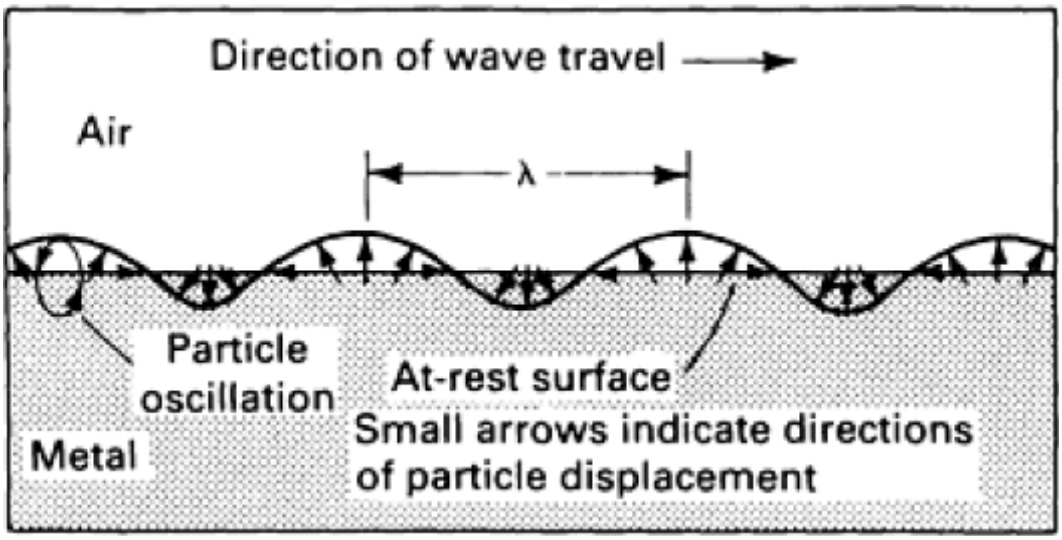

Figure I.28: Diagram of surface (Rayleigh) waves propagating at the surface of a metal along a metal/air interface.

There are two basic forms of Lamb waves:

- Symmetrical, or dilatational
- Asymmetrical, or bending

The form is determined by whether the particle motion is symmetrical or asymmetrical with respect to the neutral axis of the testpiece. Each form is further subdivided into several modes having different velocities, which can be controlled by the angle at which the waves enter the testpiece. Theoretically, there are an infinite number of specific velocities at which Lamb waves can travel in a given material. Within a given plate, the specific velocities for Lamb waves are complex functions of plate thickness and frequency.

In symmetrical (dilatational) Lamb waves, there is a compression (longitudinal) particle displacement along the neutral axis of the plate and an elliptical particle displacement on each surface (Figure I.29.a). In asymmetrical (bending) Lamb waves, there is a shear (transverse) particle displacement along the neutral axis of the plate and an elliptical particle displacement on each surface (Figure I.29.b). The ratio of the major to minor axes of the ellipse is a function of the material in which the wave is being propagated.

The major variables that must be considered in ultrasonic inspection include both the characteristics of the ultrasonic waves used and the characteristics of the parts being inspected. Equipment type and capability interact with these variables; often, different types of equipment must be selected to accomplish different inspection objectives.

The frequency of the ultrasonic waves used affects inspection capability in several ways. Generally, a compromise must be made between favorable and adverse effects to achieve an optimum balance and to overcome the limitations imposed by equipment and test material.

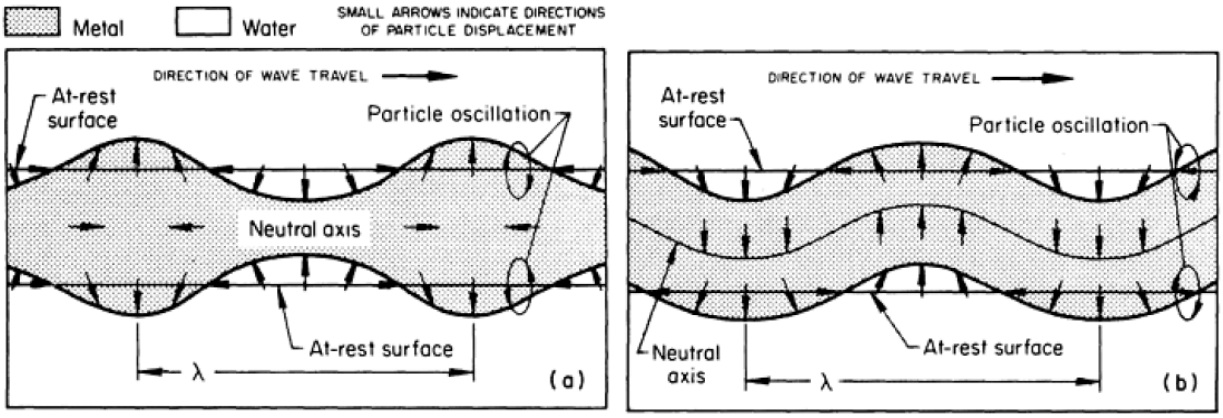

Figure I.29: Diagram of the basic patterns of (a) symmetrical (dilatational) and (b) asymmetrical (bending) Lamb waves.

Sensitivity, or the ability of an ultrasonic inspection system to detect a very small discontinuity, is generally increased by using relatively high frequencies (short wavelengths). Resolution, or the ability of the system to give simultaneous, separate indications from discontinuities that are close together both in depth below the front surface of the testpiece and in lateral position, is directly proportional to frequency bandwidth and inversely related to pulse length. Resolution generally improves with an increase of frequency.

Penetration, or the maximum depth (range) in a material from which useful indications can be detected, is reduced by the use of high frequencies. This effect is most pronounced in the inspection of metal that has coarse grain structure or minute inhomogeneities, because of the resultant scattering of the ultrasonic waves; it is of little consequence in the inspection of fine-grain, homogeneous metal.

Beam spread, or the divergence of an ultrasonic beam from the central axis of the beam, is also affected by frequency. As frequency decreases, the shape of an ultrasonic beam increasingly departs from the ideal of zero beam spread. This characteristic is so pronounced as to be observed at almost all frequencies used in inspection. Other factors, such as the transducer (search unit) diameter and the use of focusing equipment, also affect beam spread. Sensitivity, resolution, penetration, and beam spread are largely determined by the selection of the transducer and are only slightly modified by changes in other test variables.

When ultrasonic waves traveling through one medium impinge on the boundary of a second medium, a portion of the incident acoustic energy is reflected back from the boundary while the remaining energy is transmitted into the second medium. The characteristic that determines the amount of reflection is the acoustic impedance of the two materials on either side of the boundary. If the impedances of the two materials are equal, there will be no reflection; if the impedances differ greatly (as between a metal and

air, for example), there will be virtually complete reflection. This characteristic is used in the ultrasonic inspection of metals to calculate the amounts of energy reflected and transmitted at impedance discontinuities and to aid in the selection of suitable materials for the effective transfer of acoustic energy between components in ultrasonic inspection systems.

The acoustic impedance for a longitudinal wave, Z_1, given in grams per square centimeter-second, is defined as the product of material density, ρ, given in grams per cubic centimeter, and longitudinal wave velocity, v_1, given in centimeters per second:

$$Z_1 = \rho v_1 . \tag{I.2}$$

The percentage of incident energy reflected from the interface between two materials depends on the ratio of acoustic impedances (Z_2/Z_1) and the angle of incidence. When the angle of incidence is 0^o (normal incidence), the reflection coefficient, R, which is the ratio of reflected beam intensity, I_r, to incident beam intensity, I_i, is given by:

$$R = I_r/I_i = [(Z_2 - Z_1)/(Z_2 + Z_1)]^2 = [(r - 1)/(r + 1)]^2 , \tag{I.3}$$

where Z_1 is the acoustic impedance of medium 1, Z_2 is the acoustic impedance of medium 2, and r equals Z_2/Z_1 and is the impedance ratio, or mismatch factor. With T designating the transmission coefficient, $R + T = 100\%$, because all the energy is either reflected or transmitted, and T is simply obtained from this relation.

The transmission coefficient, T, can also be calculated as the ratio of the intensity of the transmitted beam, I_t, to that of the incident beam, I_i, from:

$$T = I_t/I_i = 4Z_2Z_1/(Z_2 + Z_1)^2 = 4r/(r + 1)^2 . \tag{I.4}$$

When a longitudinal ultrasonic wave in water (medium 1) is incident at right angles to the surface of an aluminium alloy 1100 testpiece (medium 2), the percentages of acoustic energy reflected and transmitted are calculated as shown below:

Impedance ratio :

$$(r) = Z_2/Z_1 = 1.72/0.149 = 11.54$$

Reflection coefficient:

$$(R) = [(r-1)/(r+1)]^2 = (10.54/12.54)^2 = 0.71 = 71\%$$

Transmission coefficient

$$(T) = 1 - R = 0.29 = 29\%$$

The same values are obtained for R and T when medium 1 is the aluminium alloy and medium 2 is water. For any pair of materials, reversing the order of the materials does not change the values of R and T.

Only when an ultrasonic wave is incident at right angles on an interface between two materials (normal incidence; that is, angle of incidence = 0°) do transmission and reflection occur at the interface without any change in beam direction. At any other angle of incidence, the phenomena of mode conversion (a change in the nature of the wave motion) and refraction (a change in direction of wave propagation) must be considered. These phenomena may affect the entire beam or only a portion of the beam, and the sum total of the changes that occur at the interface depends on the angle of incidence and the velocity of the ultrasonic waves leaving the point of impingement on the interface. All possible ultrasonic waves leaving this point are shown for an incident longitudinal ultrasonic wave in Figure I.30. Not all the waves shown in Figure I.30 will be produced in any specific instance of oblique impingement of an ultrasonic wave on the interface between two materials. The waves that propagate in a given instance depend on the

ability of a waveform to exist in a given material, the angle of incidence of the initial beam, and the velocities of the waveforms in both materials.

The general law that describes wave behaviour at an interface is known as Snell's law. Although originally derived for light waves, Snell's law applies to acoustic waves (including ultrasound) and too many other types of waves. According to Snell's law, the ratio of the sine of the angle of incidence to the sine of the angle of reflection or refraction equals the ratio of the corresponding wave velocities. Snell's law applies even if mode conversion takes place.

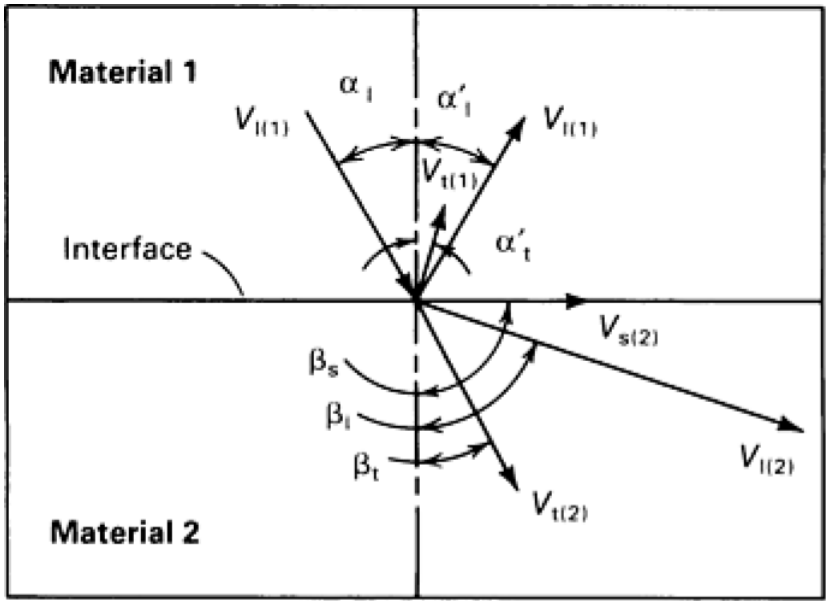

Figure I.30: Relationship (by vectors) of all possible reflected and refracted waves to an incident longitudinal wave .

Mathematically, Snell's law can be expressed as:

$$\sin\alpha/\sin\beta = V_1/V_2 \tag{I.5}$$

where α is the angle of incidence, β is the angle of reflection or refraction, and V_1, and V_2 are the respective velocities of the incident and reflected or refracted waves. Both α and β are measured from a line normal to the interface.

Equation I.6 is the general relationship applying to reflection and refraction, taking into account all possible effects of mode conversion for an incident longitudinal ultrasonic wave, as shown in Figure I.30:

$$\begin{aligned} &\sin\alpha_l/V_{l(1)} = \sin\alpha'_l/V_{l(1)} = \sin\alpha'_t/V_{t(1)} \\ &\sin\beta_l/V_{l(2)} = \sin\beta_t/V_{t(2)} \end{aligned} \tag{I.6}$$

where α_l is the angle of incidence for incident longitudinal wave in material 1, α'_l is the angle of reflection for reflected longitudinal wave in material 1 = α_l, α'_t is the angle of reflection for reflected transverse wave in material 1, β_l is the angle of refraction for refracted longitudinal wave in material 2, β_t is the angle of refraction for refracted transverse wave in material 2, $V_{l(1)}$ is the velocity of incident longitudinal wave in material 1 = velocity of reflected longitudinal wave in material 1, $V_{t(1)}$ is the velocity of reflected transverse wave in material 1, $V_{l(2)}$ is the velocity of refracted longitudinal wave in material 2, and $V_{t(2)}$ is the velocity of refracted transverse wave in material 2.

For quantities that are shown in Figure I.30 but do not appear in I.6, β_s is the angle of refraction for refracted surface (Rayleigh) wave in material 2 = 90°, and $V_{s(2)}$ is the velocity of refracted surface (Rayleigh) wave in material 2. Equation I.6 can apply to similar relationships for an incident transverse (instead of longitudinal) wave by substituting the term $\sin \alpha_t / V_{t(1)}$ for the first term, $\sin \alpha_l / V_{l(1)}$. Correspondingly, in Figure I.30, the incident longitudinal wave at angle α_l, (with velocity $V_{l(1)}$ in material 1) would be replaced by an incident transverse angle α_t equal to α_t' (with velocity $V_{t(1)}$).

I.4.3 Basic inspection methods

The two major methods of ultrasonic inspection are the transmission method and the pulse-echo method. The primary difference between these two methods is that the transmission method involves only the measurement of signal attenuation, while the pulse-echo method can be used to measure both transit time and signal attenuation.

The pulse-echo method, which is the most widely used ultrasonic method, involves the detection of echoes produced when an ultrasonic pulse is reflected from a discontinuity or an interface of a testpiece. This method is used in flaw location and thickness measurements. Flaw depth is determined from the time-of-flight between the initial pulse and the echo produced by a flaw. Flaw depth might also be determined by the relative transit time between the echo produced by a flaw and the echo from the back surface. Flaw sizes are estimated by comparing the signal amplitudes of reflected sound from an interface (either within the testpiece or at the back surface) with the amplitude of sound reflected from a reference reflector of known size or from the back surface of a testpiece having no flaws.

The transmission method, which may include either reflection either through transmission, involves only the measurement of signal attenuation. This method is also used in flaw detection. In the pulse-echo method, it is necessary that an internal flaw reflect at least part of the sound energy onto a receiving transducer. However, echoes from flaws are not essential to their detection. Merely the fact that the amplitude of the back reflection from a testpiece is lower than that from an identical workpiece known to be free of flaws implies that the testpiece contains one or more flaws. The technique of detecting the presence of flaws by sound attenuation is used in transmission methods as well as in the pulse-echo method.

The main disadvantage of attenuation methods is that flaw depth cannot be measured.

The application of ultrasonic techniques also involves other methods, such as:

- acoustical holography,
- acoustical microscopy,
- the frequency modulation technique,
- spectral analysis,
- sound conduction.

The first two of these methods will be presented in other paragraphs of this chapter. The other three methods are briefly summarized below.

The frequency modulation (FM) method, which was the precursor of the pulse-echo method, is another flaw detection technique. In the FM method, the ultrasonic pulses are transmitted in wave packets whose frequency varies linearly with time. The frequency variation is repeated in successive wave packets so that a plot of frequency versus time

has a saw-tooth pattern. There is a time delay between successive packets. Returning echoes are displayed on the readout device only if they have certain characteristics as determined by the electronic circuitry in the instrument. Although not as widely used as the pulse-echo method, the FM method has a lower signal-to-noise ratio and therefore somewhat greater resolving power.

Spectral analysis, which can be used in the through transmission or pulse-echo methods, involves determination of the frequency spectrum of an ultrasonic wave after it has propagated through a testpiece. The frequency spectrum can be determined either by transmitting a pulse and using a fast Fourier transform to obtain the frequency spectrum of the received signal or by sweeping the transmission frequency in real time and acquiring the response at each frequency. The increasing use of the pulse method is attributed to improvements in the speed of digital fast Fourier transform devices.

Spectral analysis is used in transducer evaluations and may be useful in defect characterization. However, because the spectral signatures of defects are influenced by several other factors (such as the spectrum of the input pulse, coupling details, and signal attenuation), defect characterization primarily involves the qualitative interpretation of echoes in the time domain.

Spectral analysis can also be used to measure the thickness of thin-wall specimens. A short pulse of ultrasound is a form of coherent radiation; in a thin-wall specimen that produces front and back wall echoes, the two reflected pulses show phase differences and can interfere coherently. If the pulse contains a wide band of frequencies, interference maxima and minima can occur at particular frequencies, and these can be related to the specimen thickness.

Sound conduction is utilized in flaw detection by monitoring the intensity of arbitrary waveforms at a given point on the testpiece. These waveforms transmit ultrasonic energy, which is fed into the testpiece at some other point without the existence of a well-defined beam path between the two points.

I.4.4 Pulse-echo methods

In pulse-echo inspection, short bursts of ultrasonic energy (pulses) are introduced into a testpiece at regular intervals of time. If the pulses encounter a reflecting surface, some or all of the energy is reflected. The proportion of energy that is reflected is highly dependent on the size of the reflecting surface in relation to the size of the incident ultrasonic beam.

The direction of the reflected beam (echo) depends on the orientation of the reflecting surface with respect to the incident beam. Reflected energy is monitored; both the amount of energy reflected in a specific direction and the time delay between transmission of the initial pulse and receipt of the echo are measured.

Most pulse-echo systems consist of:

- An electronic clock
- An electronic signal generator, or pulser
- A sending transducer
- A receiving transducer
- An echo-signal amplifier
- A display device

In the most widely used version of pulse-echo systems, a single transducer acts alternately as a sending and receiving transducer. The clock and signal generator are

usually combined in a single electronic unit. Frequently, circuits that amplify and demodulate echo signals from the transducer are housed in the same unit.

A pulse-echo system with a single transducer operates as follows. At regular intervals, the electronic clock triggers the signal generator, which imposes a short interval of high-frequency alternating voltage or a unipolar (negative) spike on the transducer. Simultaneously, the clock activates a time-measuring circuit connected to the display device. The operator can pre-select a constant interval between pulses by means of a pulse-repetition rate control on the instrument; pulses are usually repeated 60 to 2000 times per second. In most commercially available flaw detectors, the pulse-repetition rate is controlled automatically except for some larger systems. Also, most systems are broadband when they transmit, but may be tuned or filtered for reception. The operator can also pre-select the output frequency of the signal generator. For best results, the frequency (and sometimes the pulse-repetition rate) should be tuned to achieve the maximum response of the transducer (resonance in the vibrating element) and maximum signal-to-noise ratio (lowest amount of electronic noise) in the electronic equipment.

The transducer then converts the pulse of voltage into a pulse of mechanical vibration having essentially the same frequency as the imposed alternating voltage. The mechanical vibration (ultrasound) is introduced into a testpiece through a couplant and travels by wave motion through the testpiece at the velocity of sound, which depends on the material.

When the pulse of ultrasound encounters a reflecting surface that is perpendicular to the direction of travel, ultrasonic energy is reflected and returns to the transducer. The returning pulse travels along the same path and at the same speed as the transmitted pulse, but in the opposite direction. Upon reaching the transducer through the couplant, the returning pulse causes the transducer element to vibrate, which induces an alternating electrical voltage across the transducer. The induced voltage is instantaneously amplified (and sometimes demodulated), then fed into the display device. This process of alternately sending and receiving pulses of ultrasonic energy is repeated for each successive pulse, with the display device recording any echoes each time.

Theoretically, the maximum depth of inspection is controlled by the pulse-repetition rate. For example, if a 10 MHz pulse is transmitted at a pulse-repetition rate of 500 pulses per second, a longitudinal wave pulse can travel almost 12 m in steel or aluminium before the next pulse is triggered. This means one pulse can travel to a depth of 6 m and return before the next pulse is initiated.

Practically, however, inspection can be performed only to a depth that is considerably less than the theoretical maximum.

Sound attenuation in a testpiece can limit the path length. The practical limit varies with the type and condition of the test material, test frequency, and system sensitivity. Furthermore, it is highly desirable for all ultrasonic vibrations (including successively re-reflected echoes of the first reflected pulse) to die out in the testpiece before the next initial pulse is introduced. As a rule, the pulse-repetition rate should be set so that one pulse can traverse the testpiece enough times to dissipate the sonic energy to a non-displayable level before the next pulse is triggered. Both sound attenuation and pulse reverberation are of little consequence except when inspecting large parts (for example, in the axial inspection of long shafts).

Pulse-echo inspection can be accomplished with longitudinal, shear, surface, or Lamb waves. Straight-beam or angle-beam techniques can be used, depending on testpiece shape and inspection objectives. Data can be analyzed in terms of type, size, location, and orientation of flaws, or any combination of these factors. It should be noted,

however, that some forms of data presentation are inherently unable to pin-point the location of flaws unless the flaws are favourably oriented with respect to the transmitted sonic beam. Similarly, type, location, and orientation of flaws often influence the procedures and techniques used to estimate flaw size.

Sometimes it is advantageous to use separate sending and receiving transducers for pulse-echo inspection. (Separate transducers are always used for through transmission inspection.) Depending mainly on geometric considerations these separate transducers can be housed in a single search unit or in two separate search units. The term pitch-catch is often used in connection with separate sending and receiving transducers, regardless of whether reflection methods or transmission methods are involved.

Information from pulse-echo inspection can be displayed in different forms. The basic data formats include:

- A-Scans: This format provides a quantitative display of signal amplitudes and time-of-flight data obtained at a single point on the surface of the testpiece. The A-scan display, which is the most widely used format, can be used to analyze the type, size, and location (chiefly depth) of flaws
- B-Scans: This format provides a quantitative display of time-of-flight data obtained along a line of the testpiece. The B-scan display shows the relative depth of reflectors and is used mainly to determine size (length in one direction), location (both position and depth), and to a certain degree the shape and orientation of large flaws
- C-Scans: This format provides a semi-quantitative or quantitative display of signal amplitudes obtained over an area of the testpiece surface. This information can be used to map out the position of flaws on a plan view of the testpiece. A C-scan format also records time-of-flight data, which can be converted and displayed by image-processing equipment to provide an indication of flaw depth
- D-Scan: This format provides the same information as a C-Scan, with the exception that the D-Scan reports the time of flight (TOF), obtained over an area or test piece, instead the signal amplitudes
- FV-Scan: Can be defined as a D-scan where are available also information about the width, Z axis (2½ D – the UT probe is always orthogonal to the inspected surface) and discontinuities inside the material. In the case of a robot arm displacement system the UT probe will try always to remain orthogonal to the piece surface.

A-Scan and B-Scan data are usually presented on an oscilloscope screen; C-Scan, D-Scan and FV-Scan data are recorded by an x-y plotter and/or displayed/saved on a computer monitor/file. With computerized data acquisition and image processing, the display formats can be combined or processed into more complex displays.

I.4.5 A-scan

A-scan display is basically a plot of amplitude versus time, in which a horizontal baseline on an oscilloscope screen indicates elapsed time while the vertical deflections (called indications or signals) represent echoes (Figure I.31). Flaw size can be estimated by comparing the amplitude of a discontinuity signal with that of a signal from a discontinuity of known size and shape; the discontinuity signal also must be corrected for distance losses.

Flaw location (depth) is determined from the position of the flaw echo on the oscilloscope screen. With a calibrated time base (the horizontal sweep of the oscilloscope), flaw location can be measured from the position of its echo on the horizontal scale calibrated to represent sound travel within the test object. The zero point on this scale represents the entry surface of the testpiece.

A-scan data can be displayed in either of two modes:

- radio frequency (RF) mode, in which the individual cycles comprising each pulse are visible in the trace;
- video mode, in which only a rectified voltage corresponding to the envelope of the RF wave packet is displayed. The video mode is usually suitable for ordinary ultrasonic inspection, but certain applications demand use of the RF mode for optimum characterization of flaws.

A typical A-scan setup that illustrates the essential elements in a basic system for pulse-echo inspection is shown in Figure I.31. These elements include:

- Power supply, which may run on alternating current or batteries
- Electronic clock, or timing circuit, to trigger pulser and display circuits
- Pulser circuit, or rate generator, to control frequency, amplitude, and pulse-repetition rate of the voltage pulses that excite the search unit
- Receiver-amplifier circuit to convert output signals from the search unit into a form suitable for oscilloscope display
- Sweep circuit to control
  (a) time delay between search-unit excitation and start of oscilloscope trace
  (b) rate at which oscilloscope trace travels horizontally across the screen
- Oscilloscope screen, including separate controls for trace brightness, trace focus, and illuminated measuring grid

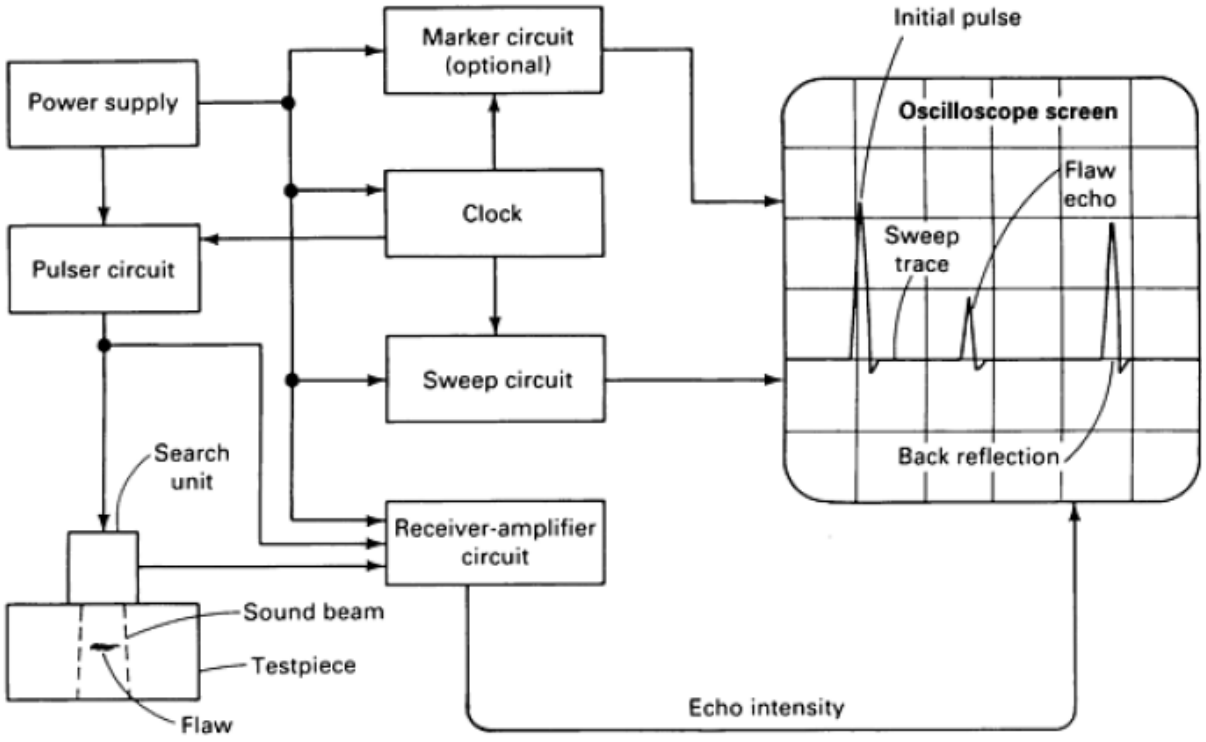

Figure I.31: Typical block diagram of an analog A-scan setup, including video-mode display, for basic pulse-echo ultrasonic inspection.

The search unit and the coaxial cable, although not strictly part of the electronic circuitry, must be matched to the electronics. Otherwise, the response of the transducer element to excitation voltages and the output voltage corresponding to echo vibrations can exhibit excessive ringing or an apparently low sensitivity.

The oscilloscope screen illustrates a typical video-mode A-scan display for a straight-beam test. The trace exhibits a large signal corresponding to the initial pulse, shown at left on the screen, and a somewhat smaller signal corresponding to the back reflection, at right on the screen. Between these two signals are indications of echoes from any interfaces within the testpiece; one small signal corresponding to the flaw shown in the testpiece, appears between the initial pulse and the back reflection on the screen.

The depth of the flaw can be quickly estimated by visual comparison of its position on the main trace relative to the positions of the initial pulse and back reflection. Its depth can be more accurately measured by counting the number of vertical reference lines from either the initial pulse or the back reflection of the flaw signal location on the screen in Figure I.31.

The A-scan display is not limited to the detection and characterization of flaws; it can also be used for measuring thickness, sound velocities in materials of known thickness, attenuation characteristics of specific materials, and beam spread of ultrasonic beams. Commercial instruments are usually adequate for these purposes, as well as for detecting the small cracks, porosity, and inclusions that are within the limits of resolution for the particular instrument and inspection technique. In addition to conventional single-transducer pulse-echo inspection, A-scan display can be used with transmission or reflection techniques that involve separate sending and receiving transducers.

I.4.6 B-scan

B-scan display is a plot of time versus distance, in which one orthogonal axis on the display corresponds to elapsed time, while the other axis represents the position of the transducer along a line on the surface of the testpiece relative to the position of the transducer at the start of the inspection. Echo intensity is not measured directly as it is in A-scan inspection, but is often indicated semiquantitatively by the relative brightness of echo indications on an oscilloscope screen. A B-scan display can be likened to an imaginary cross section through the testpiece where both front and back surfaces are shown in profile. Indications from reflecting interfaces within the testpiece are also shown in profile, and the position, orientation, and depth of such interfaces along the imaginary cutting plane are revealed.

A typical B-scan system is shown in Figure I.32. The system functions are identical to the A-scan system except for the following differences.

First, the display is generated on an oscilloscope screen that is composed of a long-persistence phosphor, that is, a phosphor that continues to fluoresce long after the means of excitation ceases to fall on the fluorescing area of the screen. This characteristic of the oscilloscope in a B-scan system allows the imaginary cross section to be viewed as a whole without having to resort to permanent imaging methods, such as photographs. (Photographic equipment, facsimile recorders, or x-y plotters can be used to record B-scan data, especially when a permanent record is desired for later reference.)

Second, the oscilloscope input for one axis of the display is provided by an electromechanical device that generates an electrical voltage or digital signals proportional to the position of the transducer relative to a reference point on the surface of the testpiece. Most B-scans are generated by scanning the search unit in a straight line across

the surface of the testpiece at a uniform rate. One axis of the display, usually the horizontal axis, represents the distance travelled along this line.

Third, echoes are indicated by bright spots on the screen rather than by deflections of the time trace. The position of a bright spot along the axis orthogonal to the search-unit position axis, usually measured top to bottom on the screen, indicates the depth of the echo within the testpiece.

Finally, to ensure that echoes are recorded as bright spots, the echo-intensity signal from the receiver-amplifier is connected to the trace-brightness control on the oscilloscope. In some systems, the brightness corresponding to different values of echo intensity may exhibit enough contrast to enable semiquantitative appraisal of echo intensity, which is related to flaw size and shape.

The oscilloscope screen in Figure I.32, illustrates the type of video-mode display that is generated by B-scan equipment. On this screen, the internal flaw in the testpiece shown at left in Figure I.32 is shown only as a profile view of its top reflecting surface. Portions of the testpiece that are behind this large reflecting surface are in shadow. The flaw length in the direction of search-unit travel is recorded, but the width (in a direction mutually perpendicular to the sound beam and the direction of search-unit travel) is not recorded except as it affects echo intensity and therefore echo-image brightness. Because the sound beam is slightly conical rather than truly cylindrical, flaws near the back surface of the testpiece appear longer than those near the front surface.

The chief value of B-scan presentations is their ability to reveal the distribution of flaws in a part on a cross section of that part. Although B-scan techniques have been more widely used in medical applications than in industrial applications, B-scans can be used for the rapid screening of parts and for the selection of certain parts, or portions of certain parts, for more thorough inspection with A-scan techniques. Optimum results from B-scan techniques are generally obtained with small transducers and high frequencies.

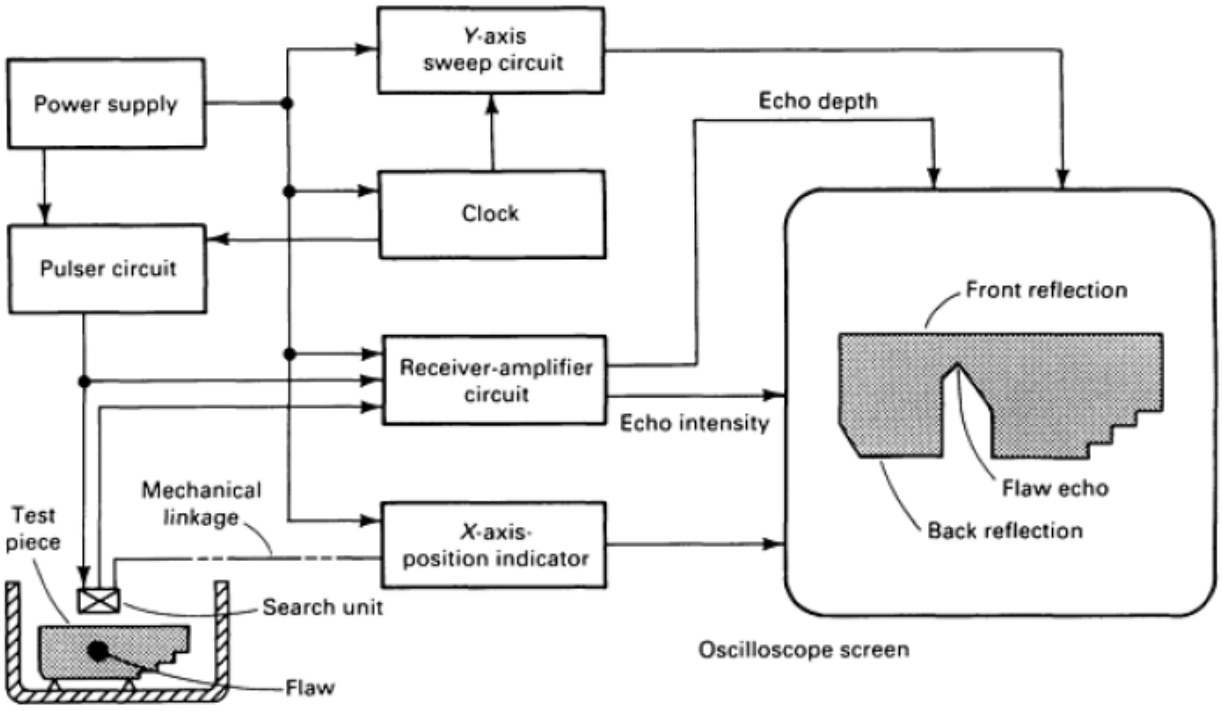

Figure I.32: B-scan setup, including video-mode display, for pulse-echo UT inspection.

I.4.7 C-scan

C-scan display records echoes from the internal portions of testpieces as a function of the position of each reflecting interface within an area. Flaws are shown on a readout, superimposed on a plan view of the testpiece, and both flaw size (flaw area) and position within the plan view are recorded. Flaw depth normally is not recorded, although it can be measured semiquantitatively by restricting the range of depths within the testpiece that is covered in a given scan. With an increasing number of C-scan systems designed with on-board computers, other options in image processing and enhancement have become widely used in the presentation of flaw depth and the characterization of flaws. An example of a computer-processed C-scan image is shown in Figure I.33, in which a Cu 99.99% brazed assembly was examined using time-of-flight data. The damage level is displayed with a colour scale in the upper side of the image.

In a basic C-scan system, shown schematically in Figure I.34, the search unit is moved over the surface of the testpiece in a search pattern. The search pattern may take many forms; for example, a series of closely spaced parallel lines, a fine raster pattern, or a spiral pattern (polar scan). Mechanical linkage connects the search unit to x-axis and y-axis position indicators, which in turn feed position data to the x-y plotter or facsimile device. Echo-recording systems vary; some produce a shaded-line scan with echo intensity recorded as a variation in line shading, while others indicate flaws by an absence of shading so that each flaw shows up as a blank space on the display (see Figure I.34).

An electronic depth gate is another essential element in C-scan systems. A depth gate is an electronic circuit that allows only those echo signals that are received within a limited range of delay times following the initial pulse or interface echo to be admitted to the receiver-amplifier circuit. Usually, the depth gate is se t so that front reflections and back reflections are just barely excluded from the display. Thus, only echoes from within the testpiece are recorded, except for echoes from thin layers adjacent to both surfaces of the testpiece. Depth gates are adjustable. By setting a depth gate for a narrow range of delay times, echo signals from a thin slice of the testpiece parallel to the scanned surface can be recorded, with signals from other portions being excluded from the display.

Some C-scan systems, particularly automatic units, incorporate additional electronic gating circuits for marking, alarming, or charting. These gates can record or indicate information such as flaw depth or loss of back reflection, while the main display records an overall picture of flaw distribution.

The interpretation of pulse-echo data is relatively straightforward for B-scan and C-scan presentations. The B-scan always records the front reflection, while internal echoes or loss of back reflection, or both, are interpreted as flaw indications.

Flaw depth is measured as the distance from the front reflection to a flaw echo, with the latter representing the front surface of the flaw. The length of a flaw can be measured as a proportion of the scan length or can be estimated visually in relation to total scan length or to the size of a known feature of the testpiece. The position of a flaw can be determined by measuring its position along the scan with respect to either a predetermined reference point or a known feature of the testpiece.

C-scan presentations are interpreted mainly by comparing the x and y coordinates of any flaw indication with the x and y coordinates of either a predetermined reference point or a known feature of the testpiece. The size of a flaw is estimated as a percentage of the scanned area. If a known feature is the size or position reference for the interpretation of either B-scan or C-scan data, it is presumed that this feature produces an appropriate echo image on the display.

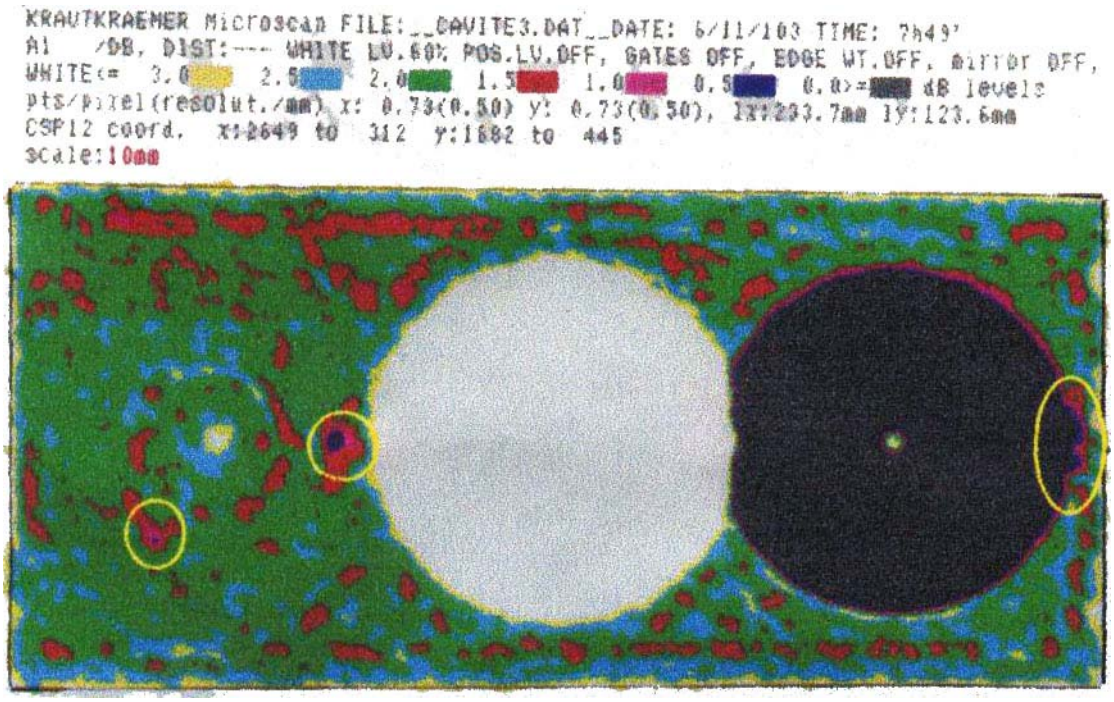

Figure I.33: Time-of-flight C-scan image of two Cu 99.99% brazed plates (yellow circles are presenting areas of brazing discontinuity).

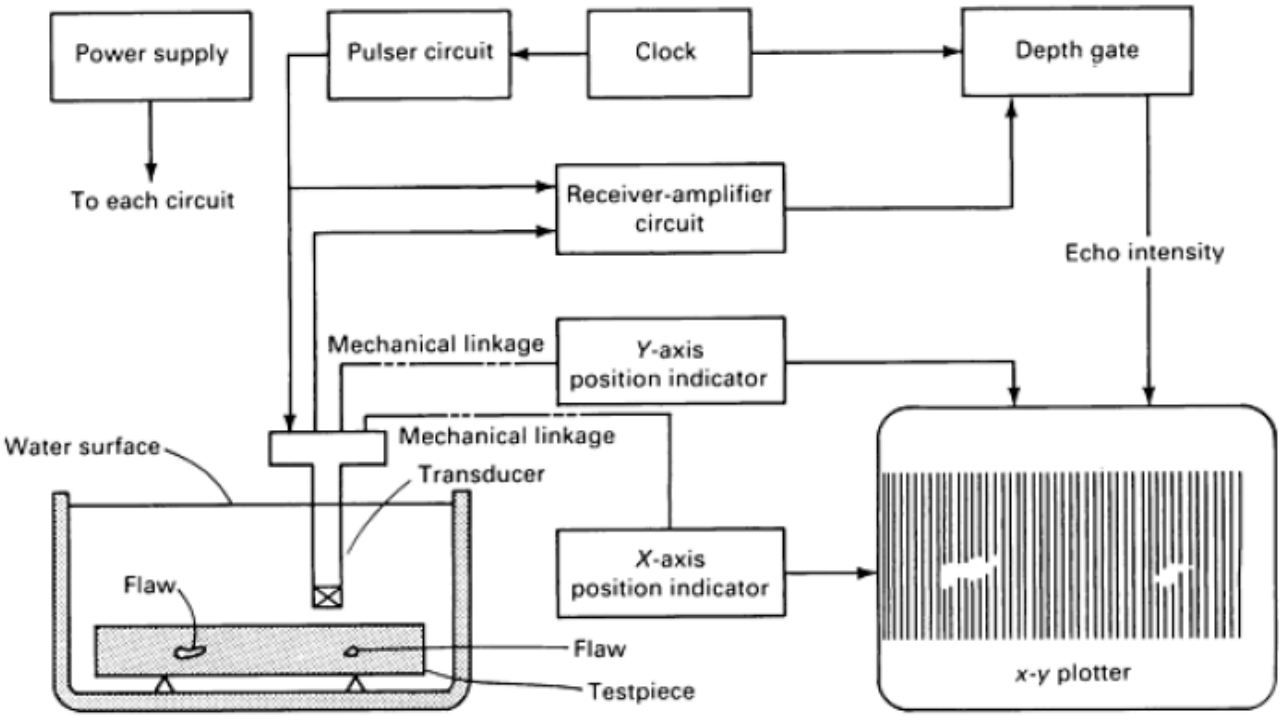

Figure I.34: Typical C-scan setup, including display, for basic pulse-echo ultrasonic immersion inspection.

In contrast to normal B-scan and C-scan displays, A-scan displays are sometimes quite complex. They may contain electronic noise, spurious echoes, or extra echoes resulting from scattering or mode conversion of the transmitted or interrogating pulse, all of which must be disregarded in order to focus attention on any flaw echoes that may be present.

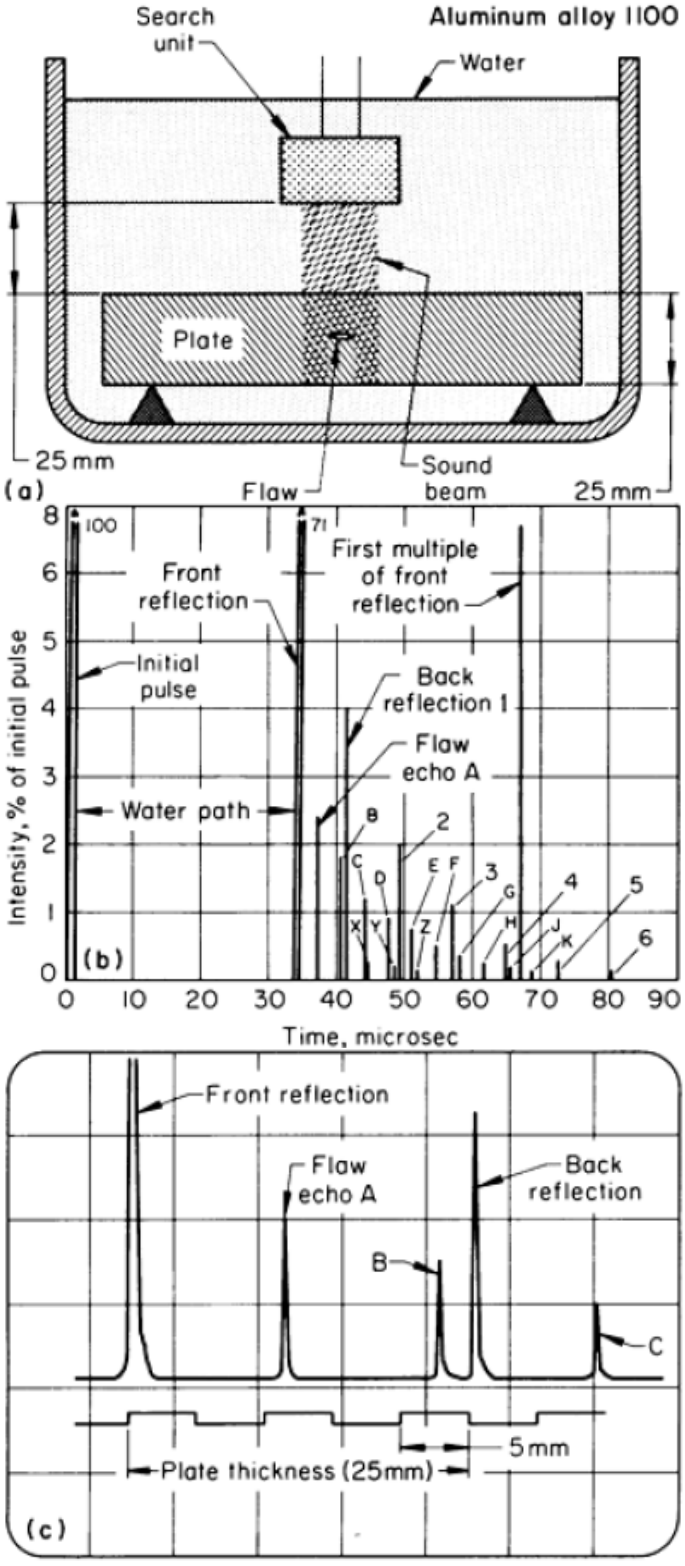

(a)

(b)

(c)

Figure I.35: Schematic of straight-beam immersion inspection of a 25 mm (1 in.) thick aluminium alloy 1100 plate containing a planar discontinuity showing (a) inspection setup, (b) complete video-mode A-scan display, and (c) normal oscilloscope display.

Furthermore, flaw echoes may exhibit widely varying shapes and amplitudes. Accurate interpretation of an A-scan display depends on the ability of the operator to:

- Recognize the type of flaw based on echo shape or echo-intensity effects

- Determine flaw location by accurately measuring echo position on the time trace
- Estimate flaw size, mainly from echo amplitudes with or without simultaneously manipulating the search unit
- Assess the quality of the testpiece by evaluating the A-scan data in terms of appropriate specifications or reference standards

Basic A-scan displays are of the type shown in Figure I.35 for the immersion inspection of a plate containing a flaw. The test material used was 25 mm thick aluminium alloy 1100 plate containing a purely reflecting planar flaw. The flaw depth was 45% of plate thickness (11.25 mm), exactly parallel to the plate surfaces, and had an area equal to one-third the cross section of the sound beam. Straight-beam immersion testing was done in a water-filled tank. There were negligible attenuation losses within the test plate, only transmission losses across front and back surfaces.

Figures I.35.a, I.35.b, and I.35.c, respectively, illustrate the inspection setup, the complete video-mode A-scan display, and the normal video-mode display as seen on the oscilloscope screen.

The normal display (Figure I.35.c) represents only a portion of the complete display (Figure I.35.b). The normal display is obtained by adjusting two of the oscilloscope controls (horizontal position and horizontal sweep) to display only the portion of the trace corresponding to the transit time (time of flight - TOF) required for a single pulse of ultrasound to traverse the testpiece from front surface to back surface and return.

Also, the gain in the receiver-amplifier is adjusted so that the height of the first back reflection equals some arbitrary vertical distance on the screen, usually a convenient number of grid lines.

As illustrated in Figure I.35.b, there is a tendency for echoes to reverberate, that is, to bounce back and forth between reflecting surfaces. Each time an echo is reflected from the front surface, a portion of the sound wave energy escapes through the boundary to impinge on the transducer and produce an indication on the display. In Figure I.35 (b), the indications labelled 1 through 6 are reverberations of the back reflection; those labelled A through K are reverberations of the primary flaw echo, and those labelled X through Z are reverberations of a subordinate flaw echo induced by re-reflection of the first back reflection.

Only a few types of flaws will produce the types of indications described above. Most flaws are not exactly parallel to the surface of the testpiece, not truly planar but have rough or curved interfaces, not ideal reflectors, and of unknown size.

These factors, together with the specific sound-attenuating characteristics of the bulk material, affect the size and shape of the echo signals. The following sections describe how specific material conditions produce and modify A-scan indications.

Echo shape is primarily affected by the shape, orientation, and sound-reflecting characteristics of an interface. Metal/air interfaces produce sharp indications if the interfaces are relatively smooth and essentially parallel to the front surface. If an interface is curved (such as the surface of a large pore) or rough (such as a crack, seam, or lamination) or if it is not ideally reflecting (such as the surface of a metallic inclusion or a slag inclusion), the interface will produce a broadened echo indication, as shown in Figure I.36.

If the interface is smaller in area than the cross section of the ultrasonic beam or if ultrasonic waves are transmitted through the interface, a back-surface echo (back reflection) will appear to the right of the flaw echo on the oscilloscope screen, as shown in Figure I.36.a. However, if the flaw is larger than the ultrasonic beam or if the back surface

is not normal to the direction of wave travel, no back reflection will appear on the screen, as shown in Figure I.36.b. Often, the amplitude of a broad indication will decrease with increasing depth, as in Figure I.36.b, especially when the echo is from a crack, seam, or lamination rather than an inclusion. Sometimes, especially if the echo is from a spherical flaw or from an interface that is not at right angles to the sound beam, the echo amplitude will increase with depth.

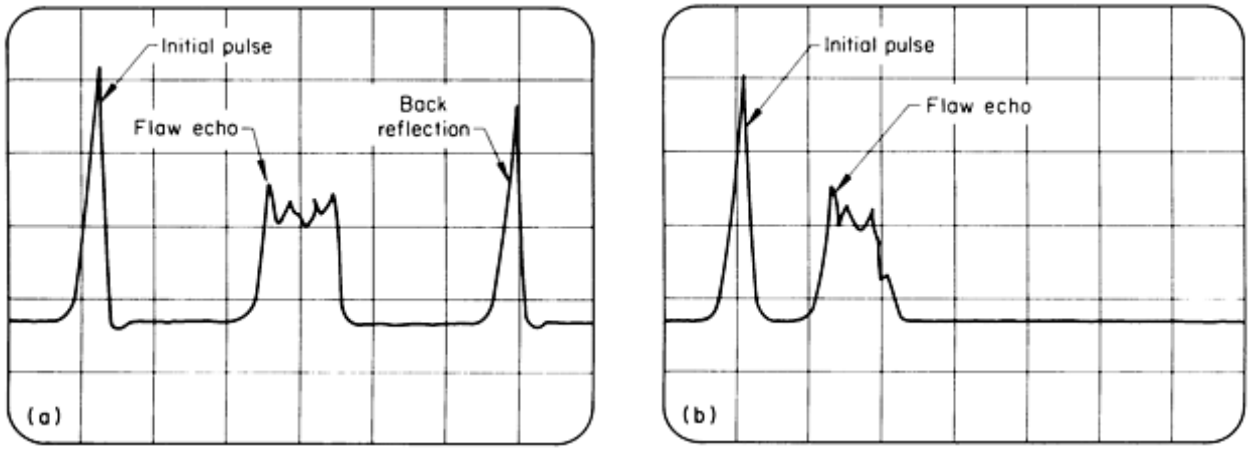

Figure I.36: A-scan displays of broadened-echo indications from curved rough or scattering interfaces showing:
(a) indications with back reflection and (b) indications without back reflection.

Echo amplitude, which is a measure of the intensity of a reflected sound beam, is a direct function of the area of the reflecting interface for flat parallel reflectors. If the interface is round or curved or is not perpendicular to the sound beam, echo amplitude will be reduced. The effects of roughness, shape, and orientation of the interface on echo amplitude must be understood because these factors introduce errors in estimates of flaw size.

Flaw size is most often estimated by comparing the amplitude of an echo from an interface of unknown size with the amplitude of echoes from flat-bottom holes of different diameter in two or more reference blocks. To compensate for any sound attenuation within the testpiece, these guidelines should be followed:

- Reference holes should be about the same depth from the front (entry) surface of the reference block as the flaw is from the front surface of the testpiece
- Reference blocks should be made of material with acoustic properties similar to those of the testpiece
- The sound beam should be larger than the flaw. (This can best be determined by moving the search unit back and forth on the surface of the part being inspected relative to a position centered over the flaw and observing the effect on both flaw echo and back reflection. If the search unit can be moved slightly without affecting the height of either the flaw echo or back reflection, it can be assumed that the sound beam is sufficiently larger than the flaw)
- Control settings on the instrument and physical arrangement of search unit, couplant, and specimen are the same regardless of whether the specimen is a testpiece or a reference block.

In practice, a calibration curve is constructed using reference block (See Figure 1.37). Flaw size is then determined by reading the hole size corresponding to the

amplitude of the flaw echo directly from the calibration curve. Flaw size determined in this manner is only an estimate of minimum size and should not be assumed equal to the actual flaw size. The amount of sound energy reflected back to the search unit will be less than that from a flat-bottom hole of equal size if an interface has a surface rougher than the bottom surfaces of the reference holes, is oriented at an angle other than 90° to the sound beam, is curved, or transmits some of the sound energy rather than acting as an ideal reflector. Therefore, to produce equal echo heights, actual flaws having any of these characteristics must be larger than the minimum size determined from the calibration curve. This is why flaw sizes are frequently reported as being no smaller than x, where x is the flaw size that has been estimated from the calibration curve.

It may seem logical to estimate flaw size by comparing the amplitude of a flaw echo to the amplitude of the back reflection. Although an assumption that the ratio of flaw-echo height to back reflection amplitude is equal to the ratio of flaw area to sound beam cross section has been used in the past, this assumption should be considered to be completely unreliable, even when distance-amplitude corrections are applied.

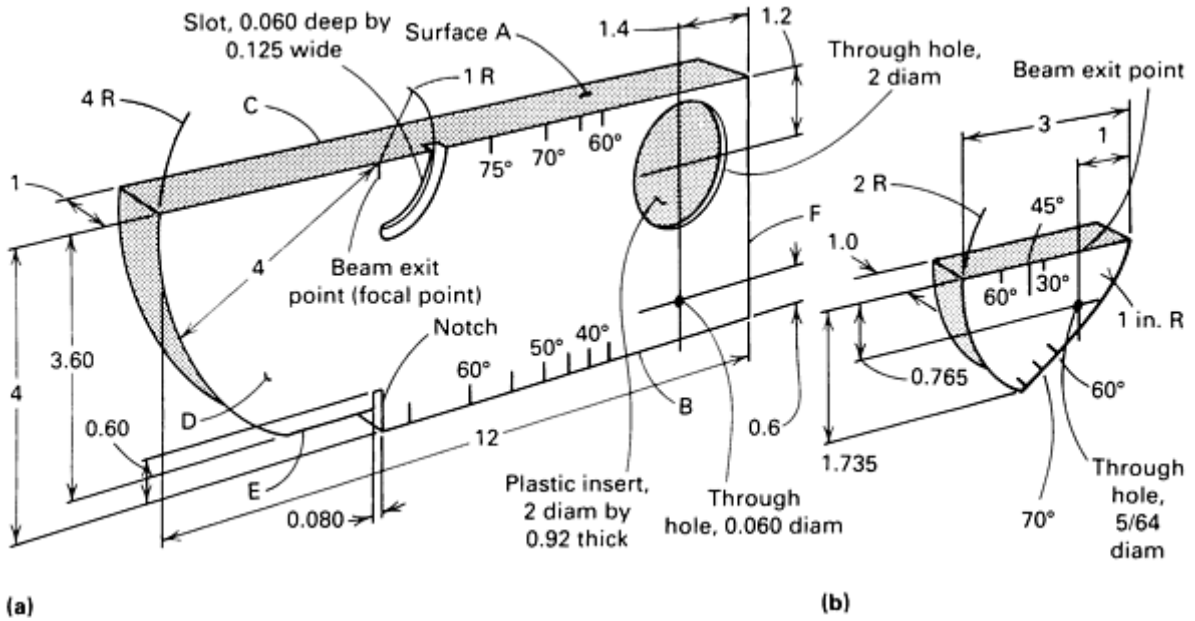

Figure I.37: Two standard reference blocks used in ultrasonic inspection: (a) IIW, type 1, block. (b) Miniature anglebeam block..

If a flaw is larger than a few percent of the cross section of a sound beam, the amplitude of the back reflection is less than that of a similar region of the testpiece (or of another testpiece) that is free of flaws.

Because sound travels essentially in straight lines, the reflecting interfaces within the testpiece (flaws) cast sound shadows on the back surface, in a manner similar to that in which opaque objects introduced into a beam of light cast shadows on a screen. Sound shadows reduce the amount of energy reflected from the back surface by reducing the effective area of the sound beam. The back reflection is not reduced in direct proportion to the percentage of the original sound beam intercepted by the flaw; the exact proportion varies widely. This effect is termed loss of back reflection, regardless of whether the back-surface signal echo is lost completely or merely reduced in amplitude.

A flaw indication is produced when an internal interface reflects sound onto the receiving transducer. A loss of back reflection can occur even if no flaw indication appears on the A-scan display. If the sound is reflected to the side, where the reflection cannot be

picked up by the transducer, there is still a loss of back reflection because of the shadow effect.

This provides an additional means of detecting the presence of flaws. Although no direct indication shows on the oscilloscope screen, the size of a flaw can be estimated from the percentage lost from the height of the back reflection indication. This estimate is generally less accurate than an estimate made from an actual flaw indication. There is no assurance that only one flaw produces a given loss of back reflection; other factors, such as excessive roughness of the back surface or internal microporosity, can also reduce the amplitude of the back reflection.

One means of distinguishing whether a certain loss of back reflection is due to the presence of identifiable flaws is to move the search unit back and forth about a mean position over the suspected flaw. If the back reflection rises and falls as the search unit is moved, the presence of specific identifiable flaws can be presumed. Angle-beam techniques or other nondestructive inspection methods can then be used for positive identification of the flaw. However, if the back reflection remains relatively steady as the search unit is moved but the amplitude of the indication is measurably lower than the expected or standard value, the material presumably contains many small flaws distributed over a relatively broad region.

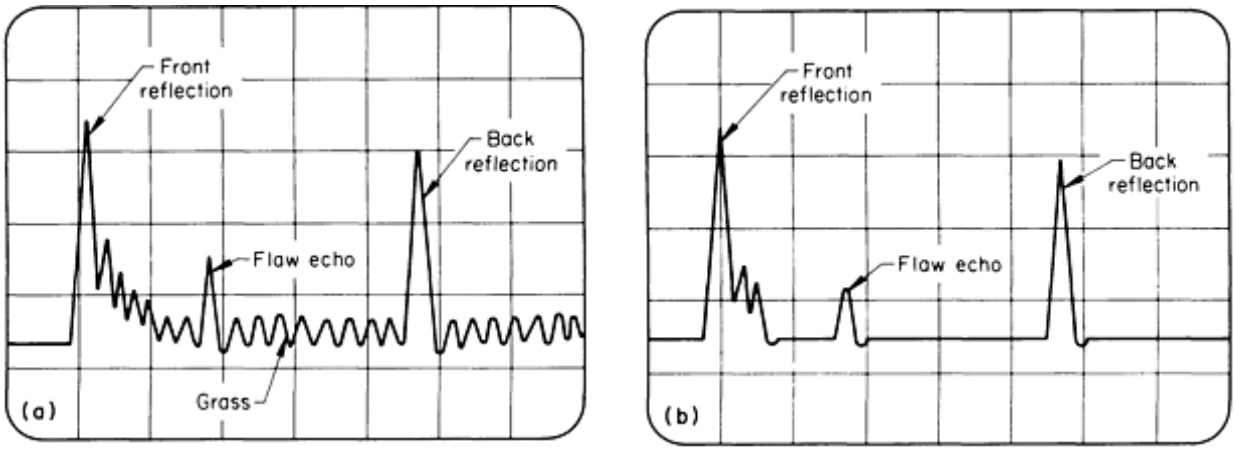

Figure I.38: A-scan displays showing:
(a) appearance of electronic noise as waviness (grass) and (b) grass filtered out by use of a reject circuit with some attendant loss of echo-signal amplitude

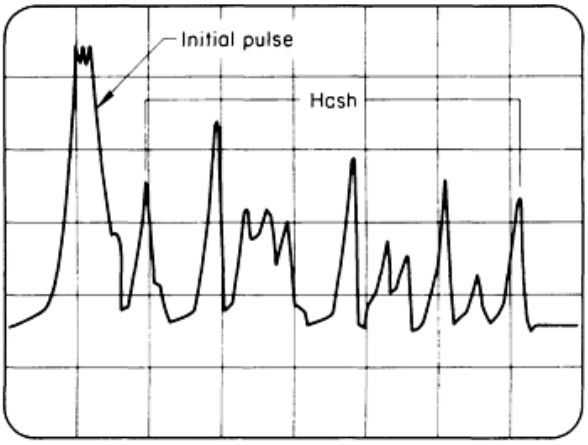

Figure I.39: A-scan display showing coarse-grain indications (hash) that interfere with detection of discontinuities

This material condition may or may not be amenable to further study using other ultrasonic techniques or other nondestructive methods.

Spurious indications from reflections or indications of sources other than discontinuities are always a possibility.

Reflections from edges and corners, extra reflections due to mode conversion, and multiple reflections from a single interface often look like flaw indications. Sometimes, these false, or nonrelevant, indications can be detected by correlation of the apparent flaw location with some physical feature of the testpiece. On other occasions, only the experience of the operator and thorough preliminary analysis of probable flaw types and locations can separate nonrelevant indications due to echoes from actual flaws.

As a rule, any indication that remains consistent in amplitude and appearance as the search unit is moved back and forth on the surface of the testpiece should be suspected of being a nonrelevant indication if it can be correlated with a known reflective or geometric boundary. Nonrelevant indications are more likely to occur in certain types of inspection--for example, in longitudinal wave inspection from one end of a long shaft, inspection of complex-shape testpieces, inspection of parts where mixed longitudinal and shear waves may be present, and various applications of shear wave or surface wave techniques.

There are certain other types of indications that may interfere with the interpretation of A-scan data. All electronic circuits generate a certain amount of noise consisting of high-frequency harmonics of the main-signal frequency. Electronic noise is generally of low amplitude and is troublesome only when the main signal is also of low amplitude. In ultrasonic inspection, electronic noise can appear on an A-scan display as a general background, or waviness (called grass), in the main trace at all depths (Figure I.38.a). This waviness, or grass, is more pronounced at the higher gain settings. Many instruments are equipped with reject circuits that filter out grass, although usually with some attendant loss of echo-signal amplitude, as shown in Figure I.38.b. When reject circuits are used, they should be adjusted so that grass is reduced only enough not to be a hindrance. If too much rejection is used, small-amplitude echoes will be suppressed along with the grass, and there will be a loss in sensitivity of the inspection technique and the linearity of the instrument will be affected.

A second type of interference occurs when coarse-grain materials are inspected. Reflections from the grain boundaries of coarse-grain materials can produce spurious indications throughout the test depth (see Figure I.39). This type of interference, called hash, is most often encountered in coarse-grain steels; it is less troublesome with fine-grain steels or nonferrous metals. Sometimes, hash can be suppressed by adjusting the frequency and pulse length of the ultrasonic waves so that the sound beam is less sensitive to grain-boundary interfaces.

I.4.8 Piezoelectric transducers

Piezoelectricity is pressure-induced electricity; this property is characteristic of certain naturally occurring crystalline compounds and some man-made materials. As the name piezoelectric implies, an electrical charge is developed by the crystal when pressure is applied to it. Conversely, when an electrical field is applied, the crystal mechanically deforms (changes shape). Piezoelectric crystals exhibit various deformation modes; thickness expansion is the principal mode used in transducers for ultrasonic inspection.

The most common types of piezoelectric materials used for UT search units are:

- quartz,

- lithium sulfate,
- polarized ceramics such as barium titanate, lead zirconate titanate, and lead metaniobate.

Quartz crystals were initially the only piezoelectric elements used in commercial ultrasonic transducers. Properties of the transducers depended largely on the direction along which the crystals were cut to make the active transducer elements. Principal advantages of quartz-crystal transducer elements are electrical and thermal stability, insolubility in most liquids, high mechanical strength, wear resistance, excellent uniformity, and resistance to aging. A limitation of quartz is its comparatively low electromechanical conversion efficiency, which results in low loop gain for the system.

Lithium Sulfate. The principal advantages of lithium sulfate transducer elements are ease of obtaining optimum acoustic damping for best resolution, optimum receiving characteristics, intermediate conversion efficiency, and negligible mode interaction. The main disadvantages of lithium sulfate elements are fragility and a maximum service temperature of about 75 °C (165 °F).

Polarized ceramics generally have high electromechanical conversion efficiency, which results in high loop gain and good search-unit sensitivity. Lead zirconate titanate is mechanically rugged, has a good tolerance to moderately elevated temperature, and does not lose polarization with age. It does have a high piezoelectric response in the radial mode, which sometimes limits its usefulness.

Barium titanate is also mechanically rugged and has a high radial-mode response. However, its efficiency changes with temperature, and it tends to depolarize with age, which makes barium titanate less suitable for some applications than lead zirconate titanate.

Lead metaniobate exhibits low mechanical damping and good tolerance to temperature. Its principal limitation is a high dielectric constant, which results in a transducer element with a high electrical capacitance.

Selection of a piezoelectric transducer for a given application is done on the basis of size (active area) of the piezoelectric element, characteristic frequency, frequency bandwidth, and type (construction) of search unit.

Different piezoelectric materials exhibit different electrical-impedance characteristics. In many cases, tuning coils or impedance-matching transformers are installed in the search-unit housing to render a better impedance match to certain types of electronic instrumentation. It is important to match impedances when selecting a search unit for a particular instrument.

Both the amount of sound energy transmitted into the material being inspected (radiated power) and beam divergence are directly related to the size (active area) of the transducer element. Thus, it is sometimes advisable to use a larger search unit to obtain greater depth of penetration or greater sound beam area.

Each transducer has a characteristic resonant frequency at which ultrasonic waves are most effectively generated and received. This resonant frequency is determined mainly by the material and thickness of the active element. Any transducer responds efficiently at frequencies in a band centered on the resonant frequency. The extent of this band, known as bandwidth, is determined chiefly by the damping characteristics of the backing material that is in contact with the rear face of the piezoelectric element.

Narrow-bandwidth transducers exhibit good penetrating capability and sensitivity, but presents relatively poor resolution. Sensitivity is the ability to detect small flaws; resolution is the ability to separate echoes from two or more reflectors that are close together in depth.) Broad-bandwidth transducers exhibit greater resolution, but lower sensitivity and penetrating capability, than narrow-bandwidth transducers.

Operating frequency, bandwidth, and active-element size must all be selected on the basis of inspection objectives. For example, high penetrating power may be most important in the axial examination of long shafts. It may be best to select a large-diameter, narrow-bandwidth, low-frequency transducer for this application, even though such a transducer will have both low sensitivity (because of low frequency and large size) and low resolution (because of narrow bandwidth).

When resolution is important, such as in the inspection for near-surface discontinuities, use of a broad-bandwidth transducer is essential. Penetrating capability probably would not be very important, so the relatively low penetrating power accompanying the broad bandwidth would not be a disadvantage. If necessary, high sensitivity could be achieved by using a small, high-frequency, broad-bandwidth transducer; an increase in both sensitivity and penetrating power would require the use of a large, high-frequency transducer, which would emit a more directive ultrasonic beam.

Resolution can also be improved by using a very short pulse length, an immersion technique, or delay-tip or dual-element contact-type search units.

Array Transducers. In recent years, there has been a growing need to increase the speed of ultrasonic inspections. The fastest means of scanning is the use of an array of transducers that are scanned electronically by triggering each of the transducers sequentially. Such transducers consist of several crystals placed in a certain pattern and triggered one at a time, either manually or by a multiplexer. Array transducers can either transmit normal to their axis or can have an angle beam. To perform beam steering, sound is generated from the various crystals with a predetermined phase difference. The degree of difference determines the beam angle.

EMA Transducers. Electromagnetic-acoustic (EMA) phenomena can be used to generate ultrasonic waves directly into the surface of an electrically conductive specimen without the need for an external vibrating transducer and coupling. Similar probes can also be used for detection, so that a complete non-contact transducer can be constructed. The method is therefore particularly suitable for use on high-temperature specimens, rough surfaces, and moving specimens. The received ultrasonic signal strength in EMA systems is 40 to 50 dB lower than a conventional barium titanate probe, but input powers can be increased.

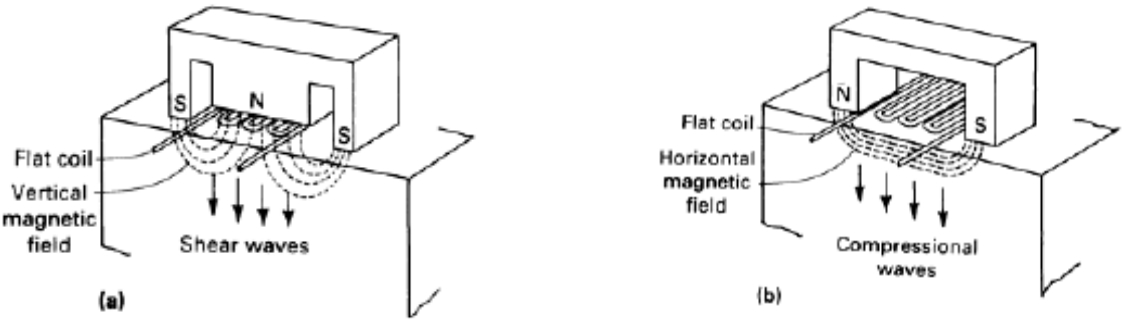

Figure I.40: Schematic of EMA transducer. (a) Arrangement for the production of shear waves. (b) Arrangement for the production of compressional waves.

The principle of EMA transducers is illustrated in Figure I.40. A permanent magnet or an electromagnet produces a steady magnetic field, while a coil of wire carries an RF current. The radio frequency induces eddy currents in the surface of the specimen, which interact with the magnetic field to produce Lorentz forces that cause the specimen surface to vibrate in sympathy with the applied radio frequency. When receiving ultrasonic energy, the vibrating specimen can be regarded as a moving conductor or a magnetic field, which generates currents in the coil. The clearance between the transducer and the metal surface affects the magnetic field strength and the strength of the eddy currents generated, and the ultrasonic intensity falls off rapidly with increasing gap.

Magnetostriction Transducers. Although magnetostriction transducers are seldom used in the ultrasonic inspection of metals, magnetostriction has advantages in the Lamb wave testing of wire specimens.

Magnetostrictive materials change their form under the influence of a magnetic field, and the most useful magnetostrictive material in practice is nickel. A nickel rod placed in a coil carrying a current experience a change in length as a function of the current through the coil. A stack of plates of magnetostrictive material with a coil through them can produce an ultrasonic beam at right angles to the plate stack, and the frequency depends on the thickness. Transducers of this type are useful for very low ultrasonic frequencies (<200 kHz).

I.4.9 Couplants

Air is a poor transmitter of sound waves at megahertz frequencies, and the impedance mismatch between air and most solids is great enough that even a very thin layer of air will severely retard the transmission of sound waves from the transducer to the testpiece. To perform satisfactory contact inspection with piezoelectric transducers, it is necessary to eliminate air between the transducer and the testpiece by the use of a couplant.

Couplants normally used for contact inspection include water, oils, glycerine, petroleum greases, silicone grease, wallpaper paste, and various commercial pastelike substances. Certain soft rubbers that transmit sound waves may be used where adequate coupling can be achieved by applying hand pressure to the search unit.

The following should be considered in selecting a couplant:

- Surface finish of testpiece
- Temperature of test surface
- Possibility of chemical reactions between test surface and couplant
- Cleaning requirements (some couplants are difficult to remove)

Water is a suitable couplant for use on a relatively smooth surface; however, a wetting agent should be added. It is sometimes appropriate to add glycerine to increase viscosity; however, glycerine tends to induce corrosion in aluminium and therefore is not recommended in aerospace applications.

Heavy oil or grease should be used on hot or vertical surfaces or on rough surfaces where irregularities need to be filled.

Wallpaper paste is especially useful on rough surfaces when good coupling is needed to minimize background noise and yield an adequate signal-to-noise ratio.

Water is not a good couplant to use with carbon steel testpieces, because it can promote surface corrosion. Oils, greases, and proprietary pastes of a noncorrosive nature can be used.

Heavy oil, grease, or wallpaper paste may not be good choices when water will suffice, because these substances are more difficult to remove. Wallpaper paste, like some proprietary couplants, will harden and may flake off if allowed to stand exposed to air. When dry and hard, wallpaper paste can be easily removed by blasting or wire brushing. Oil or grease often must be removed with solvents.

Couplants used in contact inspection should be applied as a uniform, thin coating to obtain uniform and consistent inspection results. The necessity for a couplant is one of the drawbacks of ultrasonic inspection and may be a limitation, such as with high-temperature surfaces. When the size and shape of the part being inspected permit, immersion inspection is often done. This practice satisfies the requirement for uniform coupling.

I.4.10 Search units

Search units with piezoelectric transducers are available in many types and shapes. Variations in search-unit construction include transducer-element material; transducer-element thickness, surface area, and shape; and type of backing material and degree of loading. A reference that is frequently used in determining search-unit characteristics is American Society for Testing and Materials (ASTM) specification E 1065.

The four basic types of search units are the straight-beam contact type, the angle-beam contact type, the dual-element contact type, and the immersion type (focused, not focused).

Primary applications of four basic types of ultrasonic search units with piezoelectric transducers are:

- ✓ Straight-beam contact-type units
  - o Manufacturing-induced flaws
    - ➢ Billets: inclusions, stringers, pipe
    - ➢ Forgings: inclusions, cracks, segregations, seams, flakes, pipe
    - ➢ Rolled products: laminations, inclusions, tears, seams, cracks
    - ➢ Castings: slag, porosity, cold shuts, tears, shrinkage cracks, inclusions
  - o Service-induced flaws
    - ➢ Fatigue cracks, corrosion, erosion, stress-corrosion cracks
- ✓ Angle-beam contact-type units
  - o Manufacturing-induced flaws
    - ➢ Forgings: cracks, seams, laps
    - ➢ Rolled products: tears, seams, cracks, cupping
    - ➢ Welds: slag inclusions, porosity, incomplete fusion, incomplete penetration, drop-through, suck-back, cracks in filler metal and base metal
    - ➢ Tubing and pipe: circumferential and longitudinal cracks
  - o Service-induced flaws
    - ➢ Fatigue cracks, stress-corrosion cracks
- ✓ Dual-element contact-type units
  - o Manufacturing-induced flaws

- Plate and sheet: thickness measurements, lamination detection
- Tubing and pipe: measurement of wall thickness

- Service-induced flaws
  - Wall thinning, corrosion, erosion, stress-corrosion cracks

✓ Immersion-type units

- Manufacturing-induced flaws
  - Billets: inclusions, stringers, pipe
  - Forgings: inclusions, cracks, segregations, seams, flakes, pipe
  - Rolled products: laminations, inclusions, tears, seams, cracks
  - Welds: inclusions, porosity, incomplete fusion, incomplete penetration, drop through, cracks, base-metal laminations
  - Adhesive-bonded, soldered or brazed products: lack of bond
  - Composites: voids, resin rich, resin poor, lack of filaments
  - Tubing and pipe: circumferential and longitudinal cracks
- Service-induced flaws
  - Corrosion, fatigue cracks

I.4.11 Focused units

Sound can be focused by acoustic lenses in a manner similar to that in which light is focused by optic lenses. Most acoustic lenses are designed to concentrate sound energy, which increases beam intensity in the zone between the lens and the focal point. When an acoustic lens is placed in front of the search unit, the effect resembles that of a magnifying glass; that is, a smaller area is viewed but details in that area appear larger. The combination of a search unit and an acoustic lens is known as a focused search unit or focused transducer; for optimum sound transmission, the lens of a focused search unit is usually bonded to the transducer face. Focused search units can be immersion or contact types.

Acoustic lenses are designed similarly to optic lenses. Acoustic lenses can be made of various materials; several of the more common lens materials are methyl methacrylate, polystyrene, epoxy resin, aluminium, and magnesium. The important properties of materials for acoustic lenses are:

- Large index of refraction in water
- Acoustic impedance close to that of water or the piezoelectric element
- Low internal sound attenuation
- Ease of fabrication

Acoustic lenses for contour correction are usually designed on the premise that the entire sound beam must enter the testpiece normal to the surface of the testpiece. For example, in the straight-beam inspection of tubing, a narrow diverging beam is preferred for internal inspection and a narrow converging beam for external inspection. In either case, with a flat-face search unit there is a wide front-surface echo caused by the inherent change in the length of the water path across the width of the sound beam, which results in a distorted pattern of multiple back reflections (see Figure I.41.a). A cylindrically focused search unit completely eliminates this effect (see Figure I.41.b).

The shapes of acoustic lenses vary over a broad range; two types are shown in Fig. 42 – a cylindrical (line-focus) search unit in Figure I.42.a and a spherical (spot-focus)

search unit in Figure I.42.b. The sound beam from a cylindrical search unit illuminates a rectangular area that can be described in terms of beam length and width. Cylindrically focused search units are mainly used for the inspection of thin-wall tubing and round bars. Such search units are especially sensitive to fine surface or subsurface cracks within the walls of tubing. The sound beam from a spherical search unit illuminates a small circular spot. Spherical transducers exhibit the greatest sensitivity and resolution of all the transducer types; but the area covered is small, and the useful depth range is correspondingly small.

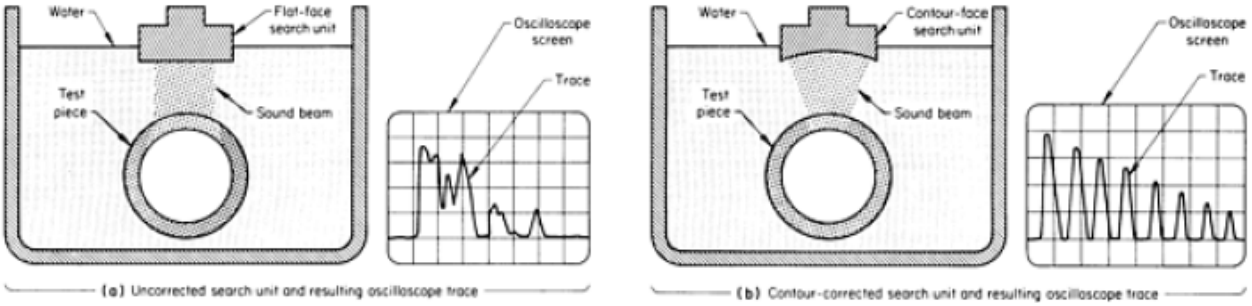

Figure I.41: Comparison of oscilloscope traces resulting from straight-beam immersion inspection by (a) an uncorrected (flat-face) search unit and (b) a contour-corrected (contour-face or cylindrically focused) search unit.

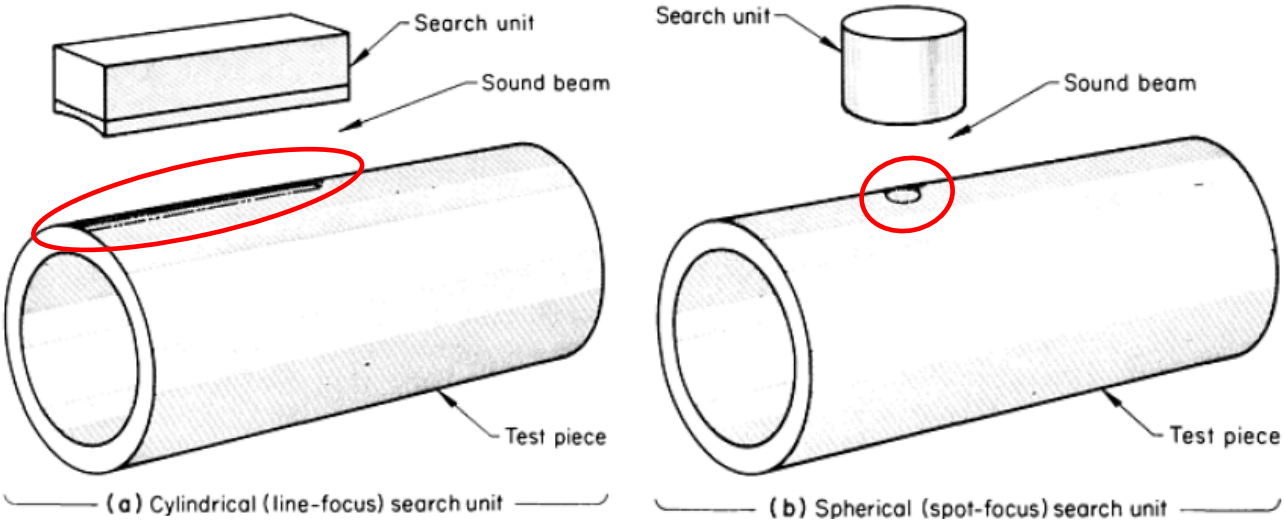

Figure I.42: Two types of focused search units, and the sound beam shapes produced.

Focusing can also be achieved by shaping the transducer element. The front surface of a quartz crystal can be ground to a cylindrical or spherical radius. Barium titanate can be formed into a curved shape before it is polarized. A small piezoelectric element can be mounted on a curved backing member to achieve the same result.

I.4.12 Focal length

Focused transducers are described by their focal length, that is, short, medium, long, or extralong. Short focal lengths are best for the inspection of regions of the testpiece that are close to the front surface. The medium, long, and extralong focal lengths are for increasingly deeper regions. Frequently, focused transducers are specially designed for a specific application. The longer the focal length of the transducer, the deeper into the testpiece the point of high sensitivity will be.

The focal length of a lens in water has little relation to its focal depth in metal, and changing the length of the water path in immersion inspection produces little change in focal depth in a testpiece. The large differences in sonic velocity between water and metals cause sound to bend at a sharp angle when entering a metal surface at any oblique angle.

Therefore, the metal surface acts as a second lens that is much more powerful than the acoustic lens at the transducer, as shown in Figure I.43. This effect moves the focal spot very close to the front surface, as compared to the focal point of the same sound beam in water. This effect also causes the transducer to act as a notably directional and distance-sensitive receiver, sharpens the beam, and increases sensitivity to small reflectors in the focal zone. Thus, flaws that produce very low amplitude echoes can be examined in greater detail than is possible with standard search units.

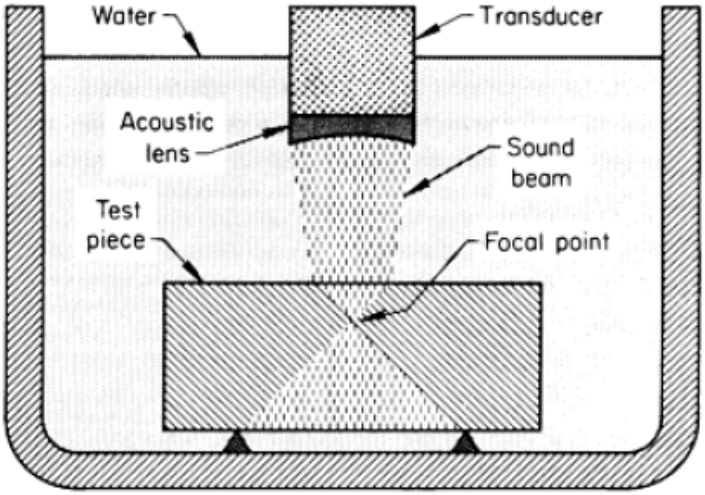

Figure I.43: Effect of a metal surface on the convergence of a focused sound beam.

The most useful portion of a sound beam starts at the point of maximum sound intensity (end of the near field) and extends for a considerable distance beyond this point. Focusing the sound beam moves the maximum-intensity point toward the transducer and shortens the usable range beyond.

The useful range of focused transducers extends from about 0.25 to approximately 250 mm below the front surface. In materials 0.25 or less in thickness, resonance or antiresonance techniques can be used. These techniques are based on changes in the duration of ringing of the echo, or the number of multiples of the back-surface echo.

The advantages of focused search units are listed below; these advantages apply mainly to the useful thickness range of 0.25 to 250 mm below the front surface:

- High sensitivity to small flaws
- High resolving power
- Low effects of surface roughness
- Low effects of front-surface contour
- Low metal noise (background)

The echo-masking effects of surface roughness and metal noise can be reduced by concentrating the energy into a smaller beam. The side lobe energy produced by a flat transducer is reflected away by a smooth surface. When the surface is rough, some of the side lobe energy returns to the transducer and widens the front reflection, causing loss of resolving power and increasing the length of the dead zone. The use of a focusing lens on a transducer will reduce the side lobe energy, thus reducing the effects of rough surfaces. The limitation of focused search units is the small region in the test part in the area of

sound focusing that can be effectively interrogated.

Material noise (background) consists of low-amplitude, random signals from numerous small reflectors irregularly distributed throughout the testpiece. Some of the causes of metal noise are grain boundaries, microporosity, and segregations. The larger the sound beam area, the greater the number of small reflectors encountered by the beam. If echoes from several of these small reflectors have the same transit time, they may produce indication on the amplitude that exceeds the acceptance level. Focused beams reduce background by reducing the volume of metal inspected, which reduces the probability that the sound beam will encounter several small reflectors at the same depth. Echoes from discontinuities of unacceptable size are not affected and will rise well above the remaining background.

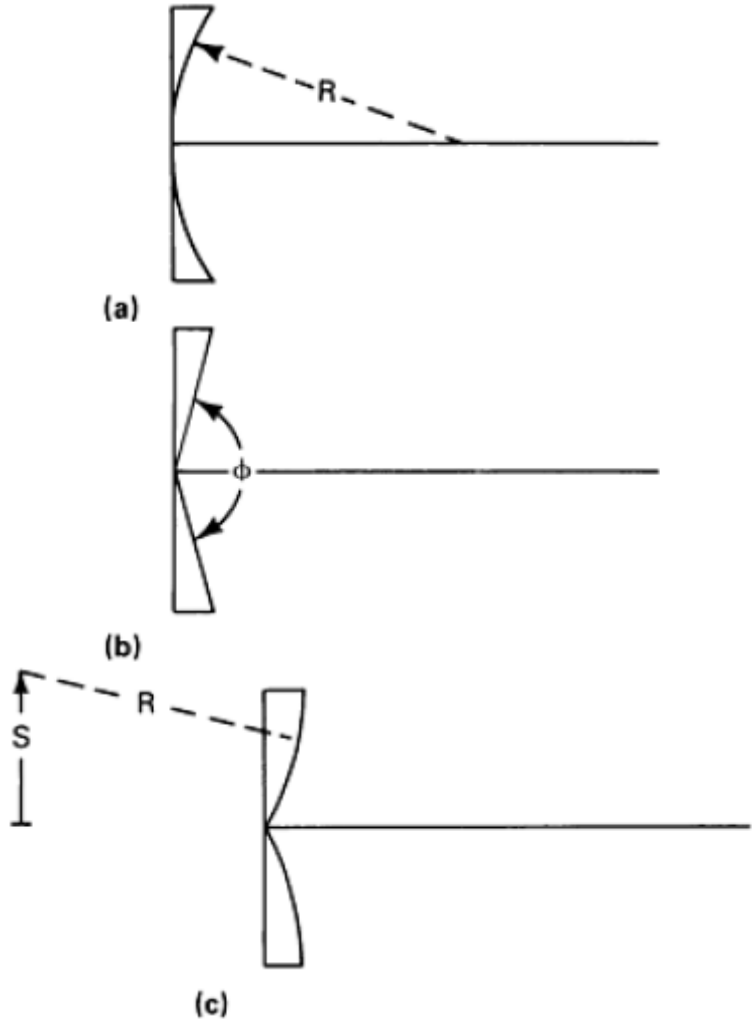

Figure I.44: Aperture geometries for transducer focusing:
(a) Spherical. (b) Conical. (c) Toroidal.

Focused search units allow the highest possible resolving power to be achieved with standard ultrasonic equipment. When a focused search unit is used, the front surface of the testpiece is not in the focal zone, and concentration of sound beam energy makes the echo amplitude from any flaw very large. The resolving power of any system can be greatly improved by using a focused transducer designed specifically for the application and a defined region within the testpiece. Special configurations consist of spherical, conical, and toroidal apertures (Figure I.44) with improvements in beam width and depth of field.

I.5 Visual and optical testing

I.5.1 Holography nondestructive testing (HNDT)

Optical Holographic techniques can be used for nondestructive testing of materials (HNDT). Non-optical Holography techniques include Acoustical, Microwave, X-Ray and Electron beam Holography.

Holography is a process for creating a whole image - that is, a 3D image - of a diffusely reflecting object having some arbitrary shape. More precisely, it is a means of recording and subsequently reconstructing wave fronts that have been reflected from or transmitted through an object of interest. Because the entire wave front and not just a 2D image is reconstructed, an image of the original object can be viewed with full depth of field, location, and parallax.

The process involves two steps. In the first step, both the amplitude and phase of any type of coherent wave motion emanating from the object are recorded by encoding this information in a suitable medium. This recording is called a hologram.

At a later time, the wave motion is reconstructed from the hologram by a coherent beam in a process that results in the regeneration (reconstruction) of an image having the true shape of the object. The utility of holography for the nondestructive inspection of materials, components, and structures lies in the fact that this reconstructed image can then be used as a kind of three-dimensional template against which any deviations in the shape or dimensions of the object can be observed and measured.

In principle, holography can be performed with any wavelike radiation encompassed in the entire electromagnetic spectrum, any particulate radiation (such as neutrons and electrons) that possesses wave-equivalent properties, and non-electromagnetic wave radiation (such as sound waves). The two methods currently available for practical nondestructive inspection are:

- Optical holography, using visible light waves
- Acoustical holography, using ultrasonic waves

An optical holographic system can be designed to do only one task or various tasks. A system can be purchased as a unit or assembled in-house from components, or holography can be purchased as an outside service. The selection of a system requires weighing the advantages and disadvantages of each type.

Optical holographic interferometry has been successfully used both in research and testing applications as a non-contacting tool for displacement, strain and vibration studies, depth-contour mappings, and transient/dynamic phenomena analyses.

HNDT is widely applied in aerospace to find impact damage, corrosion, delamination, debonds, and cracks in high performance composite aircraft parts as well as turbine blades, solid propellant rocket motor casings, unbonded regions within pneumatic tires and other laminates, hydraulic fittings and air foils, but HNDT is also finding new applications in commercial and defense related industries to investigate and test object ranging from microscopic computer chips and circuits to cultural articles, paintings and restoration.

The advantages and disadvantages of using optical holographic interferometry for nondestructive inspection are described below.

The advantages of using optical holographic interferometry for nondestructive inspection include the following:

- It can be applied to any type of solid material - ferromagnetic or non-ferromagnetic; metallic, non-metallic, or composite; electrically or thermally conductive or nonconductive; and optically transparent or opaque
- It can be applied to test objects of almost any size and shape, provided a suitable mechanism exists for stressing or otherwise exciting the object
- Pulsed-laser techniques allow the inspection of test objects in unstable or hostile environments
- It has an inherent sensitivity to the displacement or deformation of at least one-half an optical wavelength, or about 125 nm (1250 Å). This permits the use of low levels of stress during inspection. Further, special analysis techniques can provide improved sensitivity of almost 1000-fold
- It does not rely on data acquisition by either point-by-point determinations or scanning processes; instead, three-dimensional images of interference fringe fields are obtained of the entire surface (front, back, and internal, if desired) or a large fraction thereof
- It allows flexibility of readout. For example, in flaw detection applications, the images can be examined purely qualitatively for localized fringe anomalies within the overall fringe field. If, on the other hand, the application involves the strain analysis of an object subjected to a specific type of stress, the image can be analyzed to yield a highly quantitative point-by-point map of the resulting surface displacements
- It permits comparison of the responses of an object to two different levels of stress or other excitation.
- The frame of reference for this differential measurement is usually, but not always, the unstressed or natural state of the test object. This differential type of measurement contrasts with absolute types, which are made without a frame of reference, and with comparative measurements, in which a similar, but different, object is used as a frame of reference
- The interferograms can be reconstructed at any later time to produce three-dimensional replicas of the previously recorded test results

The disadvantages of using optical holographic interferometry for nondestructive inspection include the following:

- Although no physical contact with the test object is required to effect the interaction of the coherent light with either the test object or the photographic plate, it is often necessary to provide fixturing not only for the test object but also for the stressing source. The success of a holographic inspection procedure depends largely on the adequacy of design and the practical performance of both the fixturing and the stress-imparting mechanisms
- It is limited to test objects with wall or component thicknesses that will offer sufficiently large displacements without requiring stressing forces that will cause rigid-body movement or damage to the object. For sandwich structures, the thickness of the skin is the limiting factor; the maximum skin thickness that can be tested is a function of the stressing method
- Holographic methods are best suited to diffusely reflecting surfaces with high reflectivity. Removable coatings are often sprayed onto strongly absorbing materials and specularly reflecting surfaces
- Although holographic interferometry is capable of accurately locating a flaw within the surface area of the test object being inspected, the cross-sectional

size of the flaw can often be only approximately determined, and information concerning the depth of the flaw, when obtainable at all, is qualitative in nature. Furthermore, a direct correspondence does not always exist between the shape of a flaw indicative fringe anomaly and the actual shape of the flaw and between the size of the fringe anomaly and that of the flaw. For a given set of test conditions in which only the type of the applied stress is varied, the fringe anomalies indicating the presence of a flaw will vary. In many cases, flaw detection by means of holographic inspection is impeded by the appearance of spurious fringes associated with rigid body motion and/or rigid-body displacements

- Where visual interpretation of interferograms is to be performed, holographic interferometry may be limited in its dynamic range for some applications. However, electronic methods for fringe interpretation have been used to provide increased sensitivity and dynamic range
- Test results sometimes cannot be analyzed because of the localization of the interference fringes in space rather than on the surface of the test object (in real-time holographic interferometry) or on the reconstructed image of the object (in double-exposure holographic interferometry)
- With the exception of holographic-contouring applications, holographic interferometry is currently limited to differential tests, in which the object is compared to itself after it has been subjected to changes in applied stress. Comparative tests, in which a given object can be compared to a standard object, are not feasible with holographic interferometry because of inherent random variations in test object surfaces
- Personnel performing holographic inspection must be properly trained. The greater the sophistication of the equipment, the greater the required operating skill. Because lasers are a necessary part of holographic equipment, operating personnel must adhere strictly to existing safety codes, particularly with respect to eye safety

When visible light waves are employed in holography, the hologram is recorded with an optical system often referred to as a holocamera (Figure I.45.a). A monochromatic laser beam of phase-coherent light is divided into two beams by a variable beam splitter. One beam - the object beam - is expanded and filtered by a lens/pinhole spatial filter that reduces the effects of dirt and dust in the beam path. The expanded divergent beam is then directed to illuminate the object uniformly. A portion of the laser light reflected from the object is intercepted by a high-resolution photographic plate, as shown in Figure I.45.a.

The second beam - the reference beam - originating from the beam splitter diverges from a second spatial filter and is steered onto the photographic plate directly without reflecting from the object. With either the object beam or reference beam absent, a uniformly exposed photographic plate will result. However, with both coherent beams falling on the plate simultaneously, an interference pattern is generated as a result of the coherent interaction of the two beams, and this pattern is recorded by the photographic emulsion. In fact, this complex interference pattern recorded on the photographic plate contains all the information necessary to reconstruct an extremely high fidelity, three-dimensional image of the object.

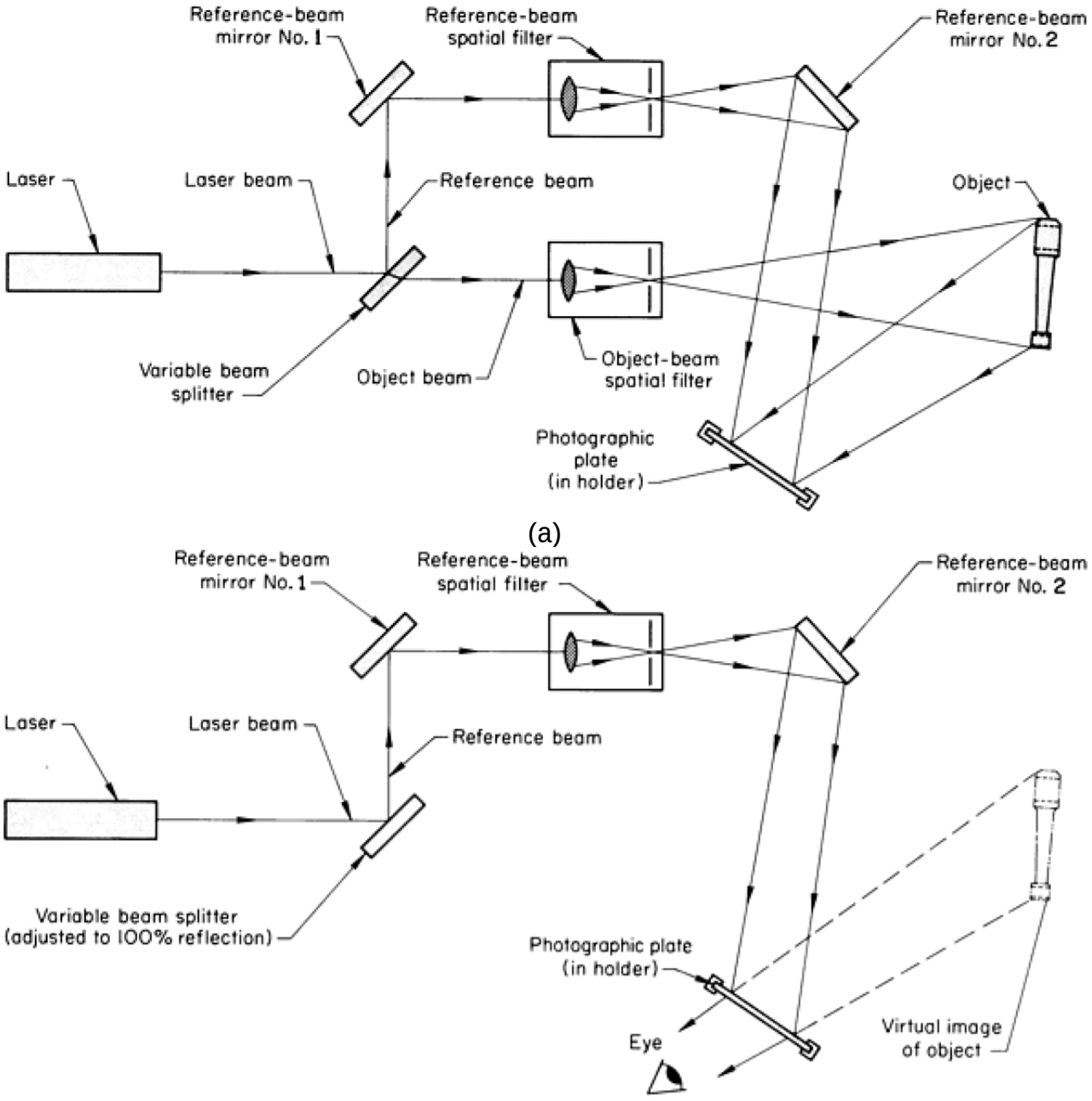

Figure I.45: Schematics of the basic optical systems used in continuous-wave holography. (a) Holocamera used to record hologram of an object on a photographic plate. (b) Optical system for reconstructing a virtual image of the object from the hologram on the photographic plate

The basic components of a holocamera are the:

- Light source (laser)
- Exposure controls
- Beam splitter
- Beam expanders (spatial filters)
- Mirrors
- Photographic plate or film holder
- Lenses
- Mounts for the equipment

- Tables to support the holographic system

In the reconstruction process (Figure I.45.b), the complex interference pattern recorded on the hologram is used as a diffraction grating. When the grating is illuminated with the reference beam only, three angularly separated beams emerge: a zeroorder, or undeflected, beam and two first-order diffracted beams. The diffracted beams reconstruct real and virtual images of the object to complete the holographic process. The real image is pseudoscopic, or depth inverted, in appearance.

Therefore, the virtual image (also referred to as the true, primary, or nonpseudoscopic image) is the one that is of primary interest in most practical applications of holography. In Figure I.45.b, only the first-order diffracted beam that yields the virtual image has been shown; the other two beams were omitted for reasons of clarity. If the original object is three dimensional, the virtual image is a genuine three-dimensional replica of the object, possessing both parallax and depth of focus.

However, if the configuration of the optical system or the wavelength of light used during reconstruction differs from that used during recording, then distortion, aberration, and changes in magnification can occur.

The holographic recording and reconstruction systems can be designed to minimize these effects.

The light intensity in the reconstructed image depends on the diffraction efficiency of the hologram. This efficiency is a function of several recording parameters, the most significant of which is the type of recording medium (film) used.

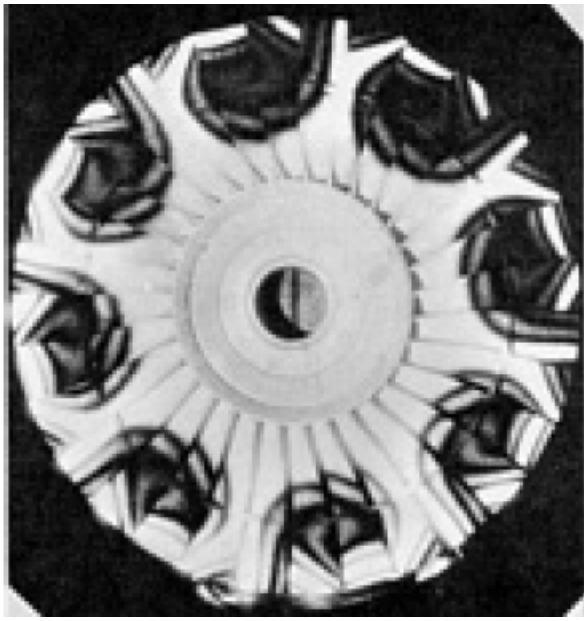

Figure I.46: Continuous-exposure interferogram of one side of an 813 mm diameter jet engine fan assembly.

Under ideal conditions, gelatin or polymeric films, which modify only the phase of the reconstructing light without absorbing it, can provide nearly 100% holographic diffraction efficiency. Commercially available holocameras using thermoplastic phase holograms, which can be developed by a thermal process without removing the film from its holder, provide diffraction efficiencies up to about 20%. High-resolution black-and-white film plates, which are used to form absorption holograms, have theoretical efficiencies up to 6.25%. For a typical hologram of this type, however, the intensity is usually less than 3% of the incident reconstructing light intensity.

Once reconstructed, the light in the image beam can be used just as one would use the light from an illuminated object viewed through a window. Pictures of the reconstructed image can be recorded photographically or electronically.

HNDT has a great ability to observe one entire surface of a large test object at one time, rather than in a series of limited views. One entire surface of an 810 mm diameter jet engine fan assembly can be recorded in a single hologram, as shown in Figure I.46., considerably facilitating the performance of a vibrational-mode analysis that alternatively would require transducers placed over the entire assembly.

I.5.2 Acoustical holography

Acoustical holography is the extension of holography into the ultrasonic domain. The principles of acoustical holography are the same as those of optical holography because the laws of interference and diffraction apply to all forms of radiation obeying the wave equation. Differences arise only because the methods for recording and reconstructing the hologram must accommodate the form of radiation used. This need to accommodate the form of radiation restricts the practical range of sound wave frequency that can be used in acoustical holography, as discussed later in this article.

At present, only two types of basic systems for acoustical holography are available:

- The liquid-surface type
- The scanning type

These utilize two different detection methods, and these methods in turn dictate the application of the systems to nondestructive inspection. Neither of these two types of systems relies on the interferometric techniques of optical holographic inspection, in which information on flaws at or near the surface of a test object is obtained from the pattern formed by interference between two nearly identical holographic images that are created while the object is differentially stressed. Instead, systems for acoustical holography obtain information on internal flaws directly from the image of the interior of the object.

The basic system for liquid-surface acoustical holography is similar to the basic system for optical holography except for the method of readout.

In liquid-surface systems (Figure I.47), two separate ultrasonic transducers supply the object beam and reference beam, which are both usually pulsed. The two transducers and the test object are immersed in a water-filled tank. The test object is positioned in the object plane of an acoustic (ultrasonic) lens, which is also immersed in the tank.

The practical limits for the object beam transducer in a commercial system are a wave frequency of 1 to 10 MHz, a pulse length of 50 to 300 s, and a pulse-repetition rate of 60 to 100 per second. This transducer is placed so that its beam passes through the test object. (Occasionally, the object beam transducer is glued to the bottom of the test object, but more often there is a liquid path between them.) As the object beam passes through the test object, it is modified by the object.

The modification is generally in both amplitude and phase. The object beam then passes through an acoustic lens, which focuses the image of the test object at the liquid surface. This image contains a wave front nearly identical to that emanating from the test object. (A small disk of a material having very high acoustic impedance can be placed at the focal point of the acoustic lens to prevent any unmodified portion of the object beam from reaching the surface of the liquid.)

The reference beam transducer is connected to the same oscillator as the object beam transducer so that it emits a second wave front coherent with the wave front from the object beam transducer. The reference beam transducer is aimed at the same region

of the liquid surface as the object beam, where the wave fronts interfere. The pressure of the beams distorts the liquid surface in this region, levitating portions of it to form a static ripple pattern that acts as a relief hologram.

Pulsed ultrasonic beams are used more often than continuous beams. With pulsed beams, the time of arrival of the reference beam at the liquid surface can be varied to compensate for any variations in transit time of the object beam as it traverses the test object and for any significant differences in the path lengths of the beams; this ensures that both beams will arrive at the liquid surface at precisely the same instant to form the ripple pattern.

A water-filled isolation tank is situated inside the immersion tank and serves to prevent ambient vibrations from interfering with the formation of the hologram. A second reason that pulsed ultrasonic beams are used more often than continuous beams is to avoid the creation of standing waves in the immersion tank that would make isolation more difficult.

Although liquid-surface acoustical holography is ideally suited to the use of the ultrasonic object beam in the transmission mode, theoretically there is no reason that the beam cannot be used in the reflection mode to form the image. Practically, however, the high level of object beam intensity and the high quality of object beam transducer required for reflection mode operation prevent the liquid-surface system from being effective in this mode.

The practical limits for the object beam transducer in a commercial system are a wave frequency of 1 to 10 MHz, a pulse length of 50 to 300 μs, and a pulse-repetition rate of 60 to 100/second. This transducer is placed so that its beam passes through the test object. (Occasionally, the object beam transducer is glued to the bottom of the test object, but more often there is a liquid path between them.) As the object beam passes through the test object, it is modified by the object.

The modification is generally in both amplitude and phase. The object beam then passes through an acoustic lens, which focuses the image of the test object at the liquid surface. This image contains a wave front nearly identical to that emanating from the test object. A small disk of a material having very high acoustic impedance can be placed at the focal point of the acoustic lens to prevent any unmodified portion of the object beam from reaching the surface of the liquid.

The reference beam transducer is connected to the same oscillator as the object beam transducer so that it emits a second wave front coherent with the wave front from the object beam transducer. The reference beam transducer is aimed at the same region of the liquid surface as the object beam, where the wave fronts interfere. The pressure of the beams distorts the liquid surface in this region, levitating portions of it to form a static ripple pattern that acts as a relief hologram.

Pulsed ultrasonic beams are used more often than continuous beams. With pulsed beams, the time of arrival of the reference beam at the liquid surface can be varied to compensate for any variations in transit time of the object beam as it traverses the test object and for any significant differences in the path lengths of the beams; this ensures that both beams will arrive at the liquid surface at precisely the same instant to form the ripple pattern.

A water-filled isolation tank is situated inside the immersion tank and serves to prevent ambient vibrations from interfering with the formation of the hologram. A second reason that pulsed ultrasonic beams are used more often than continuous beams is to avoid the creation of standing waves in the immersion tank that would make isolation more difficult.

Although liquid-surface acoustical holography is ideally suited to the use of the ultrasonic object beam in the transmission mode, theoretically there is no reason that the beam cannot be used in the reflection mode to form the image. Practically, however, the high level of object beam intensity and the high quality of object beam transducer required for reflection mode operation prevent the liquid-surface system from being effective in this mode.

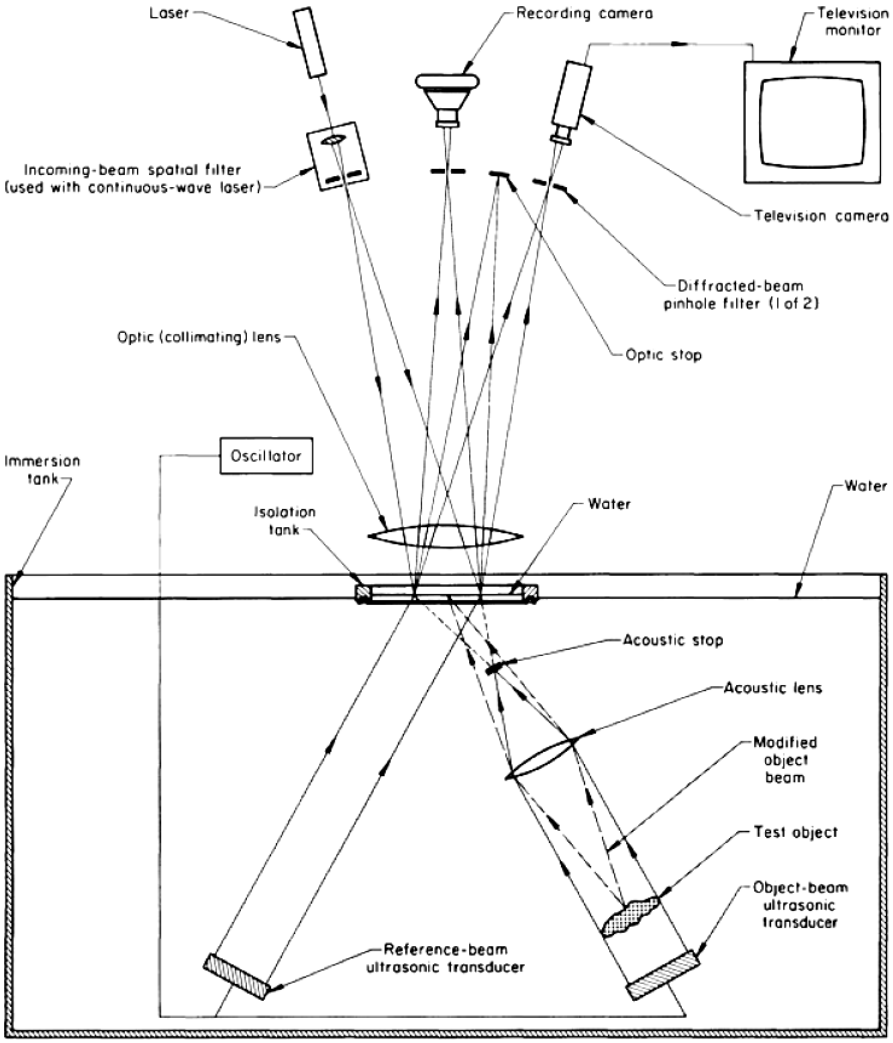

Figure I.47: Schematic of the basic acoustical and optical systems used in nondestructive inspection by liquid-surface acoustical holography.

The basic system for scanning acoustical holography is shown in Figure I.48. No reference beam transducer is required in this system, because electronic phase detection is used to produce the hologram; that is, the required interaction (mixing) between the piezoelectrically detected object beam signal and the simulated reference beam signal occurs in the electronic domain. A pulser circuit (consisting of a continuous-wave oscillator and a pulse gate that is triggered by an electronic clock) and a power amplifier feed a single focused ultrasonic transducer that is scanned over an area above the test object while alternately transmitting and receiving the ultrasonic signals. The transducer and the test object are immersed in a water-filled tank or coupled by a water column.

The signal is pulsed so that time gating can be used to reject undesired surface echoes. The pulse length can be set to any desired value from a few periods of the wave frequency to an upper limit of 50% of the time between successive pulses.

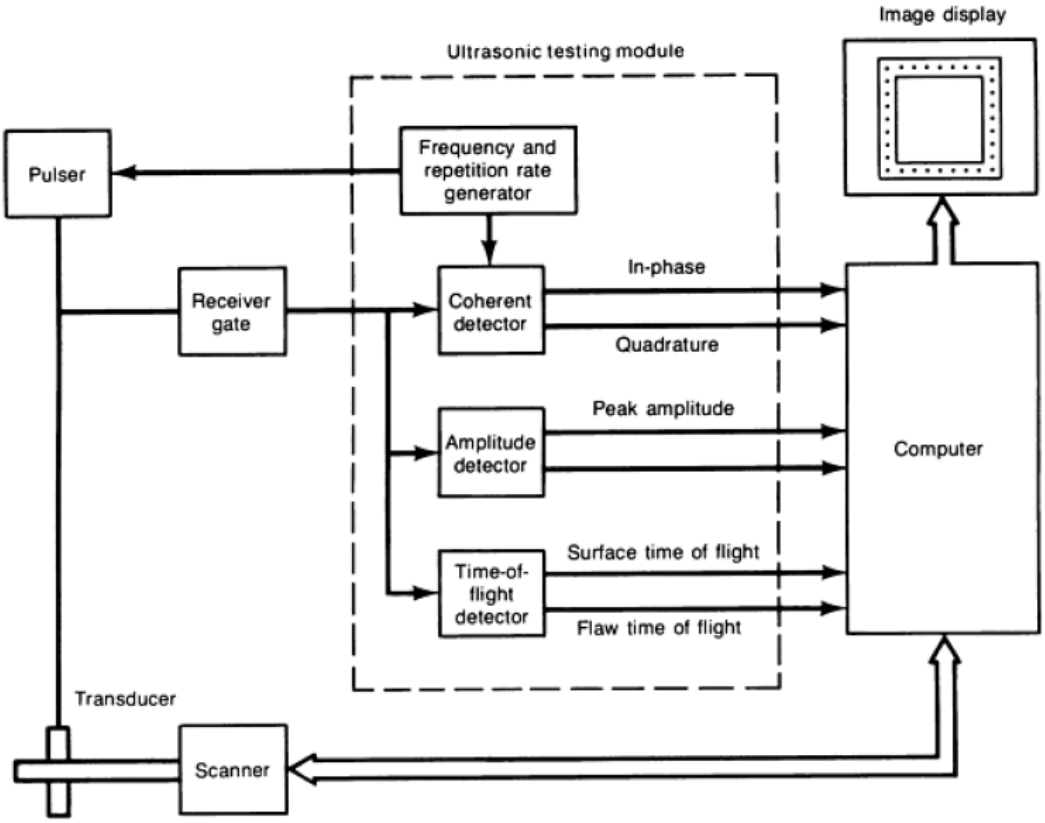

Figure I.48: Block diagram of a commercial ultrasonic and light detection system with capability for A-scan, B-scan, and C-scan imaging and holography

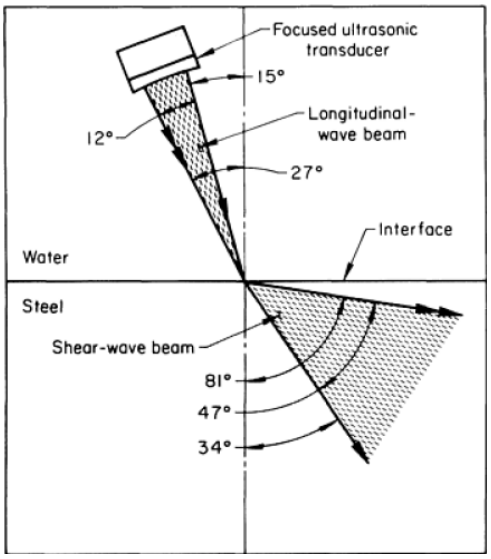

Figure I.49: Diagram of refraction of a longitudinal wave ultrasonic beam focused on a water/steel interface at incident angles that produced a shear wave beam in the steel.

Long pulse lengths are used to examine regions lying deep within the metal, while short pulse lengths are required for the regions near the surface so that transmitted energy is not mixed with reflected energy. The practical limits of the transducer in a commercial system are a wave frequency of 1 to 10 MHz, a pulse length of 5 to 20 μs, and a pulse repetition rate of 500 to 1000/second. The frequency band of a given transducer is relatively narrow (±5% of the mean frequency).

The transducer is positioned so that its focal point is at the surface of the test object. In this way, the pulse enters the object and travels through it as a spherical wave front diverging from a point on the surface. Because of refraction at the water/metal interface, the solid angle formed by the conical beam of energy in the metal will be greater than that formed by the focused conical beam from the transducer. This is illustrated in Figure I.49 by a longitudinal wave ultrasonic beam focused at the surface of a steel test object and angled to produce shear waves in the steel. In this situation, the range of angles of incidence must lie between 15 and 27° to produce only shear waves in the steel, and this range of angles will produce a 47° cone of shear-wave energy in the steel.

Either longitudinal or shear waves can be used in the scanning system illustrated in Figure I.50. For the longitudinal wave mode, the transducer is oriented parallel to the object surface; for the shear wave mode, the transducer is oriented at the appropriate angle of incidence. With either mode, the wave travels through the object to a flaw, where some of the energy is reflected back to the transducer. This reflected signal is passed through a transmitter - receiver switch to a gate that is triggered by the electronic clock through a time-delay circuit adjusted to compensate for the water-path transit time. This gate is adjusted in delay and width so that it will pass the reflections from the particular thin segment of the object under examination during the scan and will reject all others.

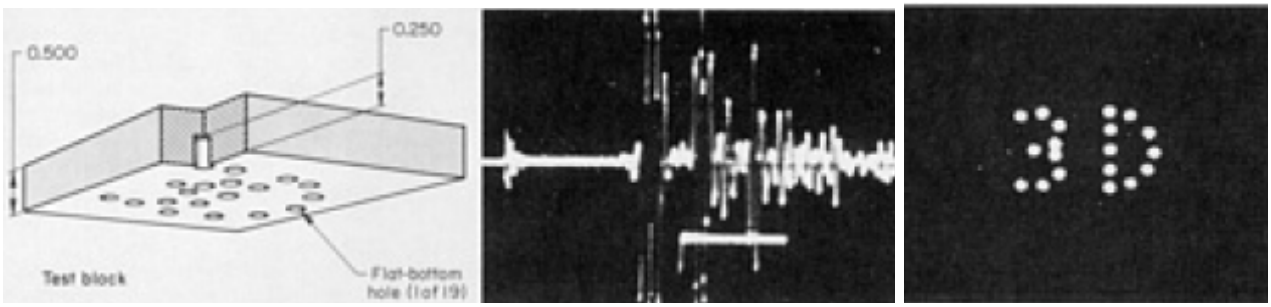

(a) (b) (c)

Figure I.50: Test block with flaws simulated by pattern of flat-bottom holes (a), oscilloscope display (b) and displays obtained by scanning the block with the equipment for scanning acoustical holography (c).

The reflected signal is split and sent to two balanced mixers, which are also fed by signals derived from the oscillator.

These signals are phase shifted by 90° from each other. The outputs of the two mixers are therefore equivalent to the sine and cosine Fourier coefficients of the reflected signal. These coefficients are complete descriptors of the phase and amplitude of the signal reflected by the flaw and thus is constitute a hologram.

The outputs of the balanced mixers are sampled, converted to digital numbers by an analog-to-digital converter, and stored in the memory of a personal computer. Thus, the result of a two-dimensional scan of a planar surface is a matrix of complex numbers recorded on the computer disk (see Figure I.50).

I.6 Electromagnetic testing

I.6.1 Eddy-current testing (ECT/ECI)

Eddy current inspection is based on the principles of electromagnetic induction and is used to identify or differentiate among a wide variety of physical, structural, and metallurgical conditions in electrically conductive ferromagnetic and nonferromagnetic metals and metal parts. Eddy current inspection can be used to:

- Measure or identify such conditions and properties as electrical conductivity, magnetic permeability, grain size, heat treatment condition, hardness, and physical dimensions
- Detect seams, laps, cracks, voids, and inclusions
- Sort dissimilar metals and detect differences in their composition, microstructure, and other properties
- Measure the thickness of a nonconductive coating on a conductive metal, or the thickness of a nonmagnetic metal coating on a magnetic metal.

Because eddy currents are created using an electromagnetic induction technique, the inspection method does not require direct electrical contact with the part being inspected. The eddy current method is adaptable to high-speed inspection and, because it is nondestructive, can be used to inspect an entire production output if desired. The method is based on indirect measurement, and the correlation between the instrument readings and the structural characteristics and serviceability of the parts being inspected must be carefully and repeatedly established.

Eddy current inspection is extremely versatile, which is both an advantage and a disadvantage. The advantage is that the method can be applied to many inspection problems provided the physical requirements of the material are compatible with the inspection method. In many applications, however, the sensitivity of the method to the many properties and characteristics inherent within a material can be a disadvantage; some variables in a material that are not important in terms of material or part serviceability may cause instrument signals that mask critical variables or are mistakenly interpreted to be caused by critical variables.

In eddy current inspection, the eddy currents create their own electromagnetic field, which can be sensed either through the effects of the field on the primary exciting coil or by means of an independent sensor. In nonferromagnetic materials, the secondary electromagnetic field is derived exclusively from eddy currents. However, with ferromagnetic materials, additional magnetic effects occur that are usually of sufficient magnitude to overshadow the field effects caused by the induced eddy currents. Although undesirable, these additional magnetic effects result from the magnetic permeability of the material being inspected and can normally be eliminated by magnetizing the material to saturation in a static (direct current) magnetic field. When the permeability effect is not eliminated, the inspection method is more correctly categorized as electromagnetic or magnetoinductive inspection.

The development of the eddy current method of inspection has involved the use of several scientific and technological advances, including:

- Electromagnetic induction
- Theory and application of induction coils
- The solution of boundary-value problems describing the dynamics of the electromagnetic fields within the vicinity of induction coils, and especially the

dynamics of the electromagnetic fields, electric current flow, and skin effect in conductors in the vicinity of such coils

- Theoretical prediction of the change in impedance of eddy current inspection coils caused by small flaws
- Improved instrumentation resulting from the development of vacuum tubes, semiconductors, integrated circuits, and microprocessors which led to better measurement techniques and response to subtle changes in the flow of eddy currents in metals
- Metallurgy and metals fabrication
- Improved instrumentation, signal display, and recording

Electromagnetic induction was discovered by Faraday in 1831. He found that when the current in a loop of wire was caused to vary (as by connecting or disconnecting a battery furnishing the current), an electric current was induced in a second, adjacent loop. This is the effect used in eddy current inspection to cause the eddy currents to flow in the material being inspected and it is the effect used to monitor these currents.

In 1864, Maxwell presented his classical dissertation on a dynamic theory of the electromagnetic field, which includes a set of equations bearing his name that describe all large-scale electromagnetic phenomena. These phenomena include the generation and flow of eddy currents in conductors and the associated electromagnetic fields. Thus, all the electromagnetic induction effects that are basic to the eddy current inspection method are described in principle by the equations devised by Maxwell for particular boundary values for practical applications.

In 1879, Hughes, using an eddy current method, detected differences in electrical conductivity, magnetic permeability, and temperature in metal. However, use of the eddy current method developed slowly, probably because such an inspection method was not needed and because further development of the electrical theory was necessary before it could be used for practical applications.

Calculating the flow of induced current in metals was later developed by the solution of Maxwell's equations for specific boundary conditions for symmetrical configurations. These mathematical techniques were important in the electric power generation and transmission industry, in induction heating, and in the eddy current method of inspection.

An eddy current instrument for measuring wall thickness was developed by Kranz in the mid-1920s. An example of early well-documented work that also serves as an introduction to several facets of the eddy current inspection method is that of Farrow, who pioneered in the development of eddy current systems for the inspection of welded steel tubing. He began his work in 1930 and by 1935 had progressed to an inspection system that included a separate primary energizing coil, differential secondary detector coil, and a dc magnetic-saturating solenoid coil. Inspection frequencies used were 500, 1000, and 4000 Hz. Tubing diameters ranged from 6.4 to 85 mm. The inspection system also included a balancing network, a high-frequency amplifier, a frequency discriminator-demodulator, a low-frequency pulse amplifier, and a filter. These are the same basic elements that are used in modern systems for eddy current inspection.

Several artificial imperfections in metals were tried for calibrating tests, but by 1935 the small drilled hole had become the reference standard for all production testing.

The drilled hole was selected for the standard because:

- It was relatively easy to produce
- It was reproducible
- It could be produced in precisely graduated sizes

- It produced a signal on the eddy current tester that was similar to that produced by a natural imperfection
- It was a short imperfection and resembled hard-to-detect, short natural weld imperfections. Thus, if the tester could detect the small drilled hole, it would also detect most of the natural weld imperfections.

Vigners, Dinger, and Gunn described eddy current type flaw detectors for nonmagnetic metals in 1942, and in the early 1940s, Förster and Zuschlag developed eddy current inspection instruments. Numerous versions of eddy current inspection equipment are currently available commercially. Some of this equipment is useful only for exploratory inspection or for inspecting parts of simple shape. However, specially designed equipment is extensively used in the inspection of production quantities of metal sheet, rod, pipe, and tubing.

The eddy current method of inspection and the induction heating technique that is used for metal heating, induction hardening, and tempering have several similarities. For example, both are dependent on the principles of electromagnetic induction for inducing eddy currents within a part placed within or adjacent to one or more induction coils. The heating is a result of I^2R losses caused by the flow of eddy currents in the part. Changes in coupling between the induction coils and the part being inspected and changes in the electrical characteristics of the part cause variations in the loading and tuning of the generator.

The induction heating system is operated at high power levels to produce the desired heating rate. In contrast, the system used in eddy current inspection is usually operated at very low power levels to minimize the heating losses and temperature changes. Also, in the eddy current system, electrical-loading changes caused by variations in the part being inspected, such as those caused by the presence of flaws or dimensional changes, are monitored by electronic circuits. In both eddy current inspection and induction heating, the selection of operating frequency is largely governed by skin effect. This effect causes the eddy currents to be concentrated toward the surfaces adjacent to the coils carrying currents that induce them. Skin effect becomes more pronounced with increase in frequency.

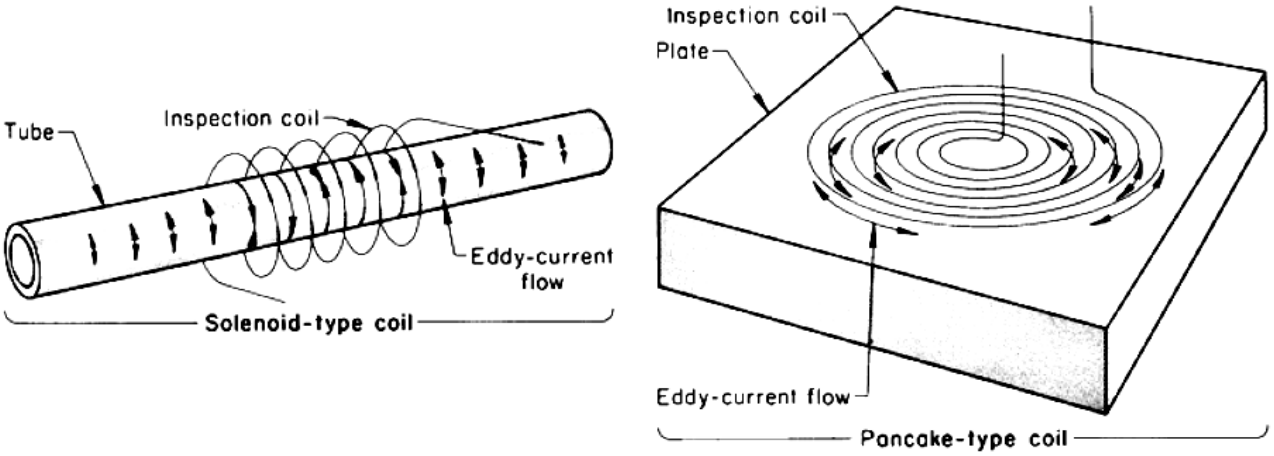

Figure I.51: Two common types of inspection coils and the patterns of eddy current flow generated by the exciting current in the coils. Solenoid-type coil is applied to cylindrical or tubular parts; pancake-type coil, to a flat surface.

The coils used in eddy current inspection differ from those used in induction heating because of the differences in power level and resolution requirements, which necessitate

special inspection coil arrangements to facilitate the monitoring of the electromagnetic field in the vicinity of the part being inspected.

The part to be inspected is placed within or adjacent to an electric coil in which an alternating current is flowing. As shown in Figure I.51, this alternating current, called the exciting current, causes eddy currents to flow in the part as a result of electromagnetic induction. These currents flow within closed loops in the part, and their magnitude and timing (or phase) depend on:

- The original or primary field established by the exciting currents
- The electrical properties of the part
- The electromagnetic fields established by currents flowing within the part

The electromagnetic field in the region in the part and surrounding the part depends on both the exciting current from the coil and the eddy currents flowing in the part. The flow of eddy currents in the part depends on:

- The electrical characteristics of the part
- The presence or absence of flaws or other discontinuities in the part
- The total electromagnetic field within the part

The change in flow of eddy currents caused by the presence of a crack in a pipe is shown in Figure I.52. The pipe travels along the length of the inspection coil as shown in Figure I.52. In section A-A in Figure I.52, no crack is present and the eddy current flow is symmetrical. In section B-B in Figure I.52, where a crack is present, the eddy current flow is impeded and changed in direction, causing significant changes in the associated electromagnetic field. From Figure I.52 it is seen that the electromagnetic field surrounding a part depends partly on the properties and characteristics of the part. Finally, the condition of the part can be monitored by observing the effect of the resulting field on the electrical characteristics of the exciting coil, such as its electrical impedance, induced voltage, or induced currents. Alternatively, the effect of the electromagnetic field can be monitored by observing the induced voltage in one or more other coils placed within the field near the part being monitored.

Each and all of these changes can have an effect on the exciting coil or other coil or coils used for sensing the electromagnetic field adjacent to a part. The effects most often used to monitor the condition of the part being inspected are the electrical impedance of the coil or the induced voltage of either the exciting coil or other adjacent coil or coils.

Eddy current systems vary in complexity depending on individual inspection requirements. However, most systems provide for the following functions:

- Excitation of the inspection coil
- Modulation of the inspection coil output signal by the part being inspected
- Processing of the inspection coil signal prior to amplification
- Amplification of the inspection coil signals
- Detection or demodulation of the inspection coil signal, usually accompanied by some analysis or discrimination of signals
- Display of signals on a meter, an oscilloscope, an oscillograph, or a strip chart recorder; or recording of signal data on magnetic tape or other recording media
- Handling of the part being inspected and support of the inspection coil assembly or the manipulation of the coil adjacent to the part being inspected

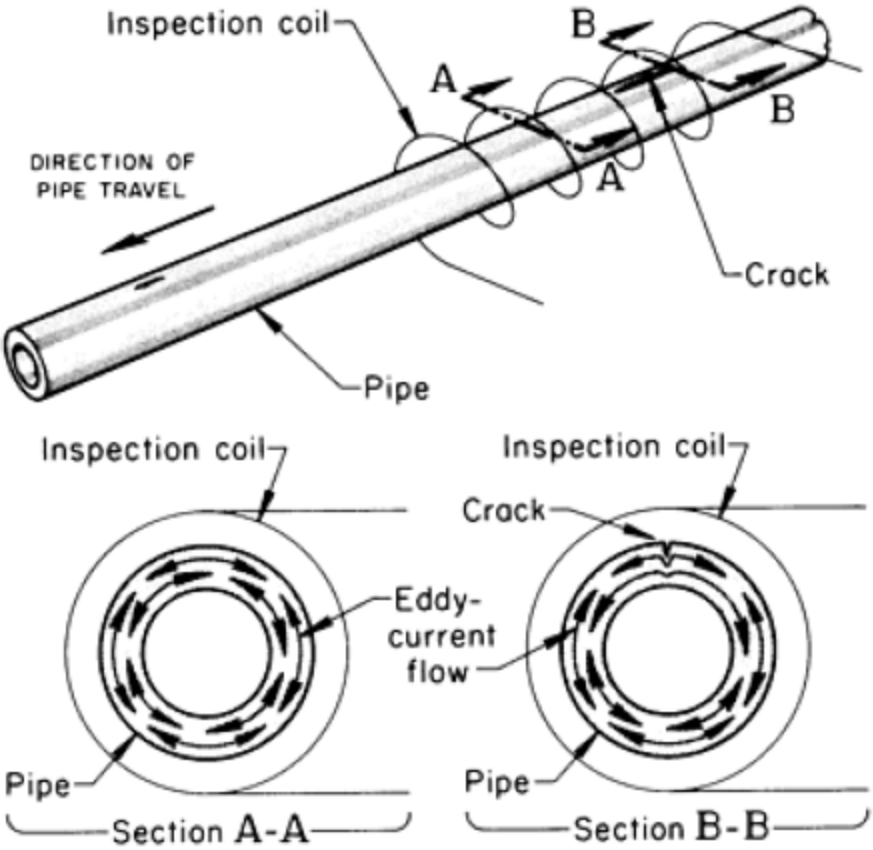

Figure I.52: Effect of a crack on the pattern of eddy current flow in a pipe.

Elements of a typical inspection system are shown schematically in Figure I.53. The particular elements in Figure I.53 are for a system developed to inspect bar or tubing. The generator supplies excitation current to the inspection coil and a synchronizing signal to the phase shifter, which provides switching signals for the detector. The loading of the inspection coil by the part being inspected modulates the electromagnetic field of the coil. This causes changes in the amplitude and phase of the inspection coil voltage output.

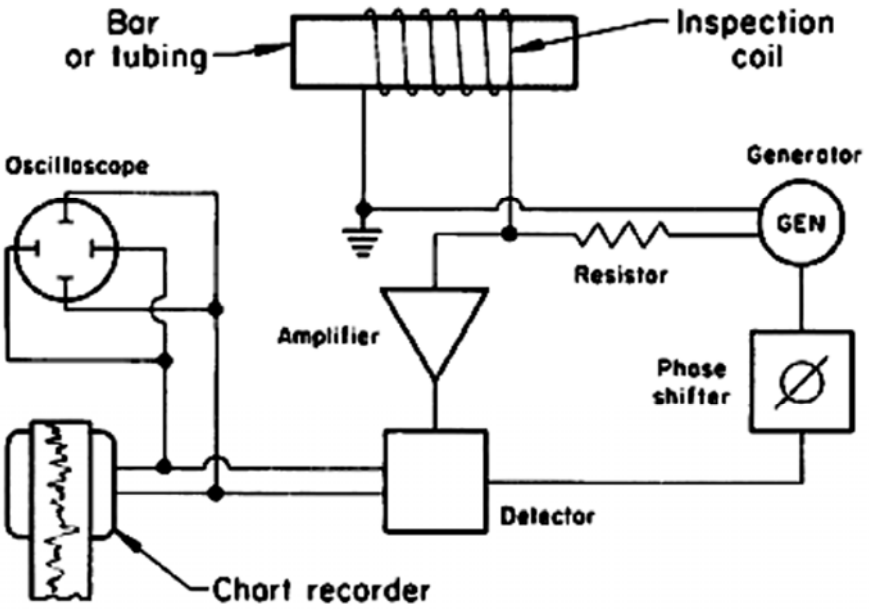

Figure I.53: Principal elements of a typical system for eddy current inspection of bar or tubing..

The output of the inspection coil is fed to the amplifier and detected or demodulated by the detector. The demodulated output signal, after some further filtering and analyzing, is then displayed on an oscilloscope or a chart recorder. The displayed signals, having been detected or demodulated, vary at a much slower rate, depending on:

- The speed at which the part is fed through an inspection coil
- The speed with which the inspection coil is caused to scan past the part being inspected.

The inspection frequencies used in ECI range from about 200 Hz to 6 MHz or more. Inspections of nonmagnetic materials are usually performed at a few KHz. In general, the lower frequencies, which start at about 1 kHz, are used for inspecting magnetic materials. However, the actual frequency used in any specific eddy current inspection will depend on the thickness of the material being inspected, the desired depth of penetration, the degree of sensitivity or resolution required, and the purpose of the inspection.

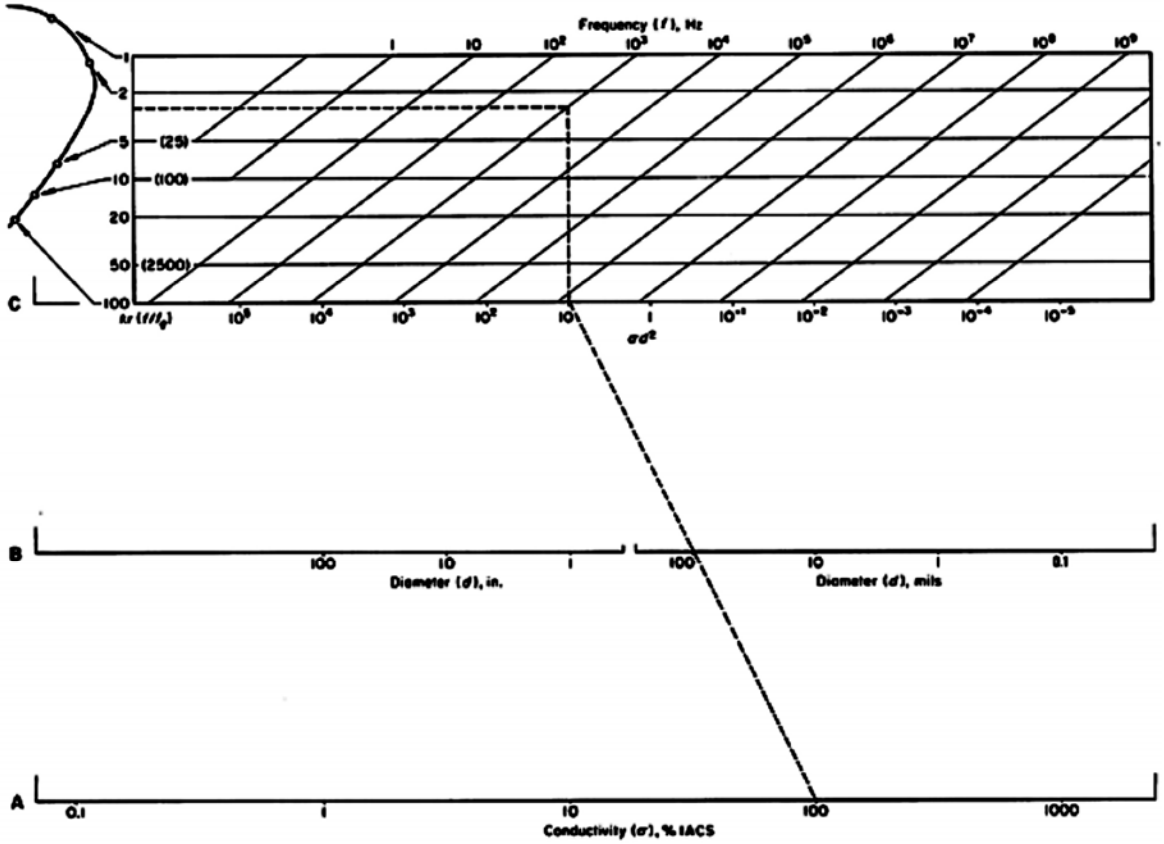

Figure I.54: Chart for selection of frequency for the inspection of nonferromagnetic cylindrical bars.

Step 1 Select the value of electrical conductivity (σ) of the bar in per cent IACS on line A.

Step 2 Select the value of the bar diameter (d) in mils or in inches on either of the scales in line B.

Step 3 Lay a straightedge between these two points, extending the line connecting them to intersect line C.

Step 4 Extend a line vertically from the point on line C found in step 3 until it intersects with a horizontal line corresponding to the desired value of kr.

Step 5 The desired operating frequency is read from the frequency chart (slanted lines), selecting the frequency line that intersects the intersection determined in step 4.

Selection of inspection frequency is normally a compromise. For example, penetration should be sufficient to reach any subsurface flaws that must be detected. Although penetration is greater at lower frequencies, it does not follow that as low a

frequency as possible should be used. Unfortunately, as the frequency is lowered, the sensitivity to flaws decreases somewhat, and the speed of inspection can be curtailed. Normally, therefore, an inspection frequency as high as possible that is still compatible with the penetration depth required is selected. The choice is relatively simple when detecting surface flaws only, in which case frequencies up to several megahertz can be used. When detecting flaws at some considerable depth below the surface, very low frequencies must be used and sensitivity is sacrificed. Under these conditions, it is not possible to detect small flaws.

In inspecting ferromagnetic materials, relatively low frequencies are normally used because of the low penetration in these materials. Higher frequencies can be used when it is necessary to inspect for surface conditions only. However, even the higher frequencies used in these applications are still considerably lower than those used to inspect nonmagnetic materials for similar conditions.

Selection of operating frequency for the inspection of nonferromagnetic cylindrical bars can be estimated using the chart in Figure I.54. The three main variables on the chart are conductivity, diameter of the part, and operating frequency. A fourth variable, the operating point on the simple impedance curve is also taken into account. Usually, the desired operating point for cylindrical bars corresponds to $k_r = r\sqrt{\omega\mu\sigma}$ which is approximately 4, but which can be in the range 2 to 7. In a typical problem, the two variables of the part, conductivity and radius (or diameter), are known, and it is necessary to find the frequency of operation to determine a particular operating point on the single impedance diagram.

The inspection coil is an essential part of every eddy current inspection system. The shape of the inspection coil depends to a considerable extent on the purpose of the inspection and on the shape of the part being inspected. When inspecting for flaws, such as cracks or seams, it is essential that the flow of the eddy currents be as nearly perpendicular to the flaws as possible to obtain a maximum response from the flaws. If the eddy current flow is parallel to flaws, there will be little or no distortion of the currents and therefore very little reaction on the inspection coil.

Of the almost infinite variety of coils employed in eddy current inspection, probe coils and encircling coils are the most commonly used. Normally, in the inspection of a flat surface for cracks at an angle to the surface, a probe-type coil would be used because this type of coil induces currents that flow parallel to the surface and therefore across a crack, as shown in Figure I.55.a. On the other hand, a probe-type coil would not be suitable for detecting a laminar type of flaw. For such a discontinuity, a U-shaped or horseshoe-shaped coil, such as the one shown in Figure I.55.b, would be satisfactory.

To inspect tubing or bar, an encircling coil (Figure I.55.c) is generally used because of complementary configuration and because of the testing speeds that can be obtained with this type of coil. However, an encircling coil is sensitive only to discontinuities that are parallel to the axis of the tube or bar. The coil is satisfactory for this particular application because, as a result of the manufacturing process, most discontinuities in tubing and bar are parallel to the major axis. If it is necessary to locate discontinuities that are not parallel to the axis, a probe coil must be used, and either the coil or the part must be rotated during scanning. To detect discontinuities on the inside surface of a tube or when testing installed tubing an internal or bobbin-type coil (see Figure I.55.d) can be used. The bobbin-type coil, like the encircling coil, is sensitive to discontinuities that are parallel to the axis of the tube or bar.

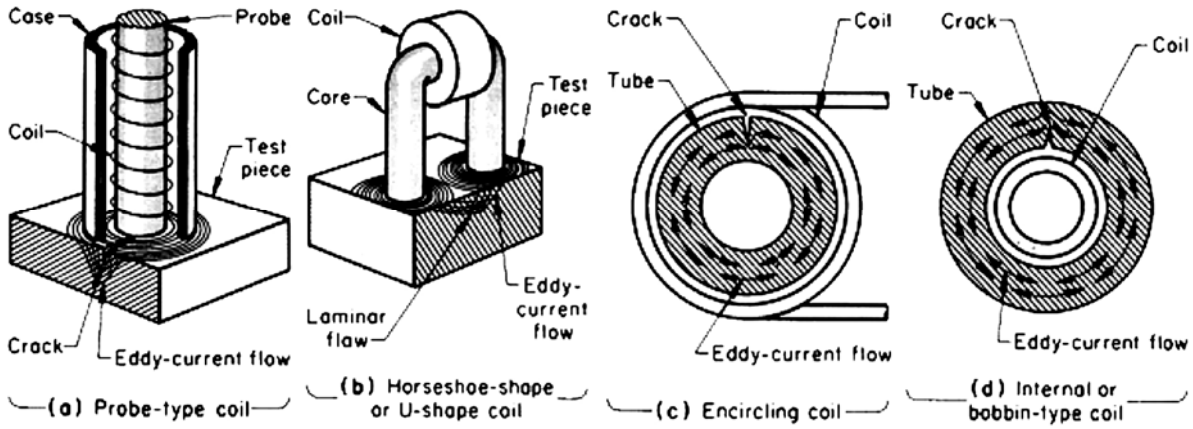

Figure I.55: Types and applications of coils used in eddy current inspection: (a) Probe-type coil applied to a flat plate for detection of a crack. (b) Horseshoe-shaped or U-shaped coil applied to a flat plate for detection of a laminar flaw. (c) Encircling coil applied to a tube. (d) Internal or bobbin-type coil applied to a tube.

In many setups for eddy current inspection, two or more coils are used. The two coils are normally connected to separate legs of an alternating current bridge in a series-opposing arrangement so that when their impedances are the same, there is no output from the pair. Pairs of coils can be used in either an absolute or a differential arrangement (Figure I.56).

In the absolute arrangement (see Figure I.56.a), a sample of acceptable material is placed in one coil, and the other coil is used for inspection. Thus, the coils are comparing an unknown against a standard, with the differences between the two (if any) being indicated by a suitable instrument. Arrangements of this type are commonly employed in sorting applications.

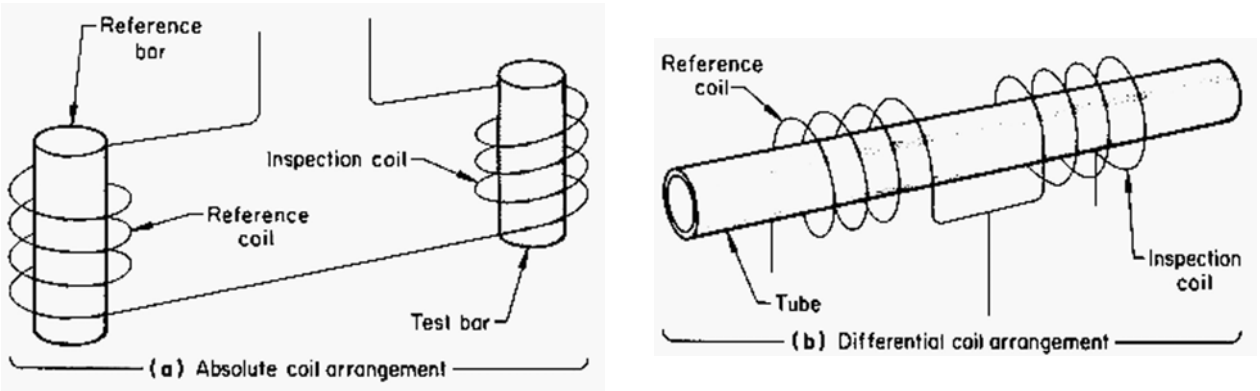

Figure I.56: Absolute and differential arrangements of multiple coils used in eddy current inspection.

In a large number of applications, an absolute coil arrangement is undesirable. For example, in tubing inspection, an absolute arrangement will indicate dimensional variations in both outside diameter and wall thickness even though such variations may be well within allowable limits. To avoid this problem, a differential coil arrangement such as that shown in Figure I.56.b can be used. Here, the two coils compare one section of the tube with an adjacent section. When the two sections are the same, there is no output from the pair of coils and therefore no indication on the eddy current instrument. Gradual dimensional variations within the tube or gross variations between individual tubes are not indicated, while discontinuities, which normally occur abruptly, are very apparent. In this

way, it is possible to have an inspection system that is sensitive to flaws and relatively insensitive to changes that normally are not of interest.

Inspection coils are available in a variety of sizes and shapes. Selection of a coil for a particular application depends on the type of discontinuity. For example, when an encircling coil is used to inspect tubing or bar for short discontinuities, optimum resolution is obtained with a short coil. Alternatively, a short coil has the disadvantage of being sensitive to the position of the part in the coil. Longer coils are not as sensitive to the position of the part, but are not as effective in detecting very small discontinuities. Small-diameter probe coils have greater resolution than larger ones, but are more difficult to manipulate and are more sensitive to lift-off variations.

Eddy current instruments can be classified as belonging to one of the following categories:

- Resistor and single-coil system
- Bridge unbalance system
- Induction bridge system
- Through transmission system

A simple eddy current instrument, in which the voltage across an inspection coil is monitored, is shown in Figure I.57.a. This circuit is adequate for measuring large lift-off variations if accuracy is not extremely important.

A circuit designed for greater accuracy is shown in Figure I.57.b. This instrument consists of a signal source, an impedance bridge with dropping resistors, an inspection coil in one leg, and a balancing impedance in the other leg. The differences in voltage between the two legs of the bridge are measured by an ac voltmeter.

Alternatively, the balancing impedance in the leg opposite the inspection coil may be a coil identical to the inspection coil, as shown in Figure I.57.c, or it may have a reference sample in the coil, as shown in Figure I.57.d. In the latter, if all the other components in the bridge were identical, a signal would occur only when the inspection coil impedance deviated from that of the reference sample.

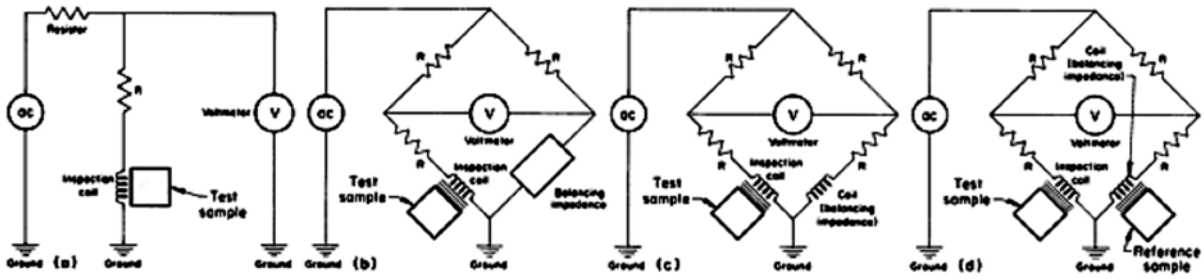

Figure I.57: Four types of eddy current instruments:
(a) A simple arrangement, in which voltage across the coil is monitored. (b) Typical impedance bridge. (c) Impedance bridge with dual coils. (d) Impedance bridge with dual coils and a reference sample in the second coil.

I.6.2 Remote field testing (RFT)

Remote-field eddy current (RFEC) INSPECTION is a nondestructive examination technique suitable for the examination of conducting tubular goods using a probe from the inner surface. Because of the RFEC effect, the technique provides what is, in effect, a through-wall examination using only the interior probe. Although the technique is applicable to any conducting tubular material, it has been primarily applied to

ferromagnetics because conventional eddy current testing techniques are not suitable for detecting opposite-wall defects in such material unless the material can be magnetically saturated. In this case, corrosion/erosion wall thinning and pitting as well as cracking are the flaws of interest. One advantage of RFEC inspection for either ferromagnetic or nonferromagnetic material inspection is that the probe can be made more flexible than saturation eddy current or magnetic probes, thus facilitating the examination of tubes with bends or diameter changes.

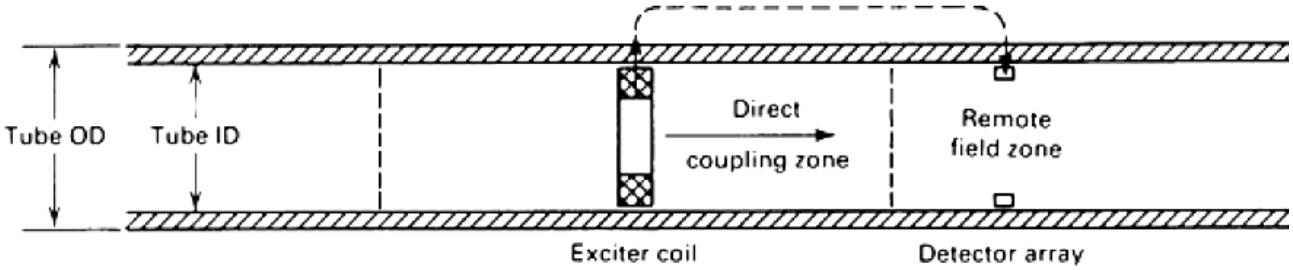

Figure I.58: Schematic showing location of remote-field zone in relation to exciter coil and direct coupling zone.

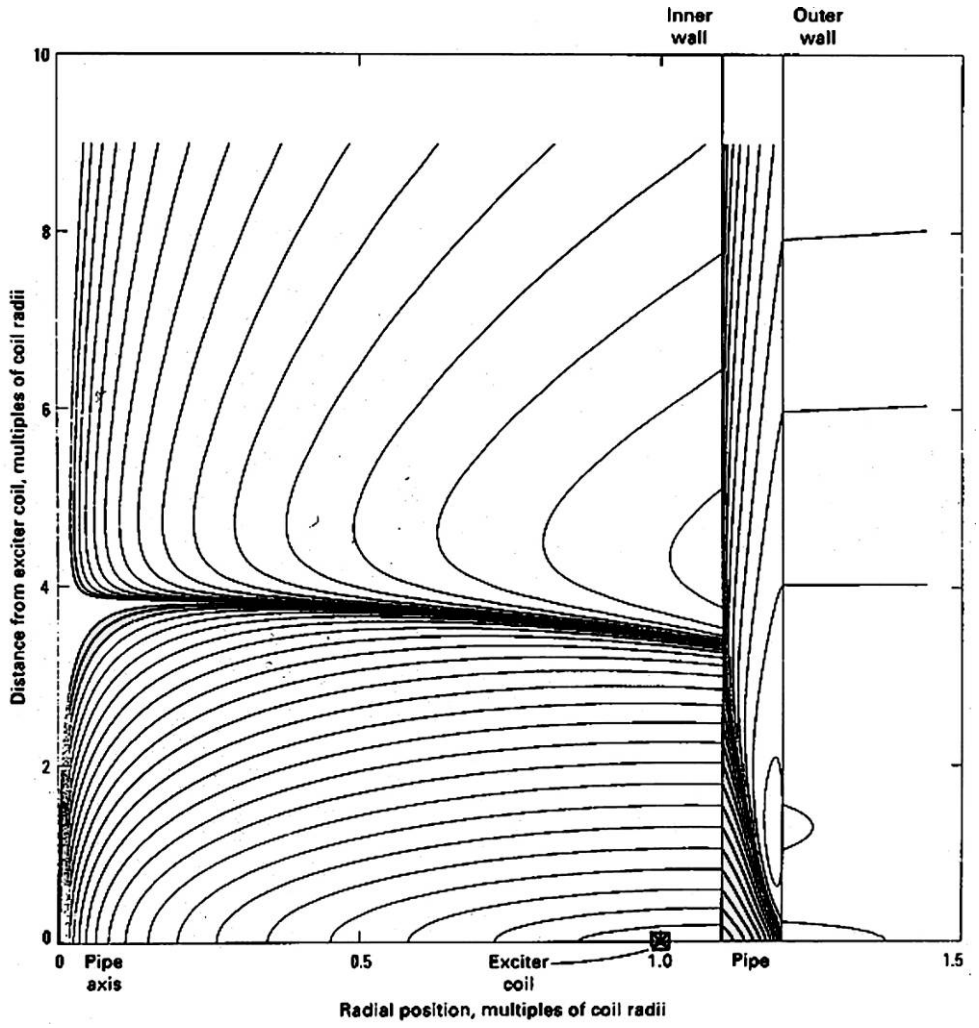

Figure I.59: Instantaneous field lines shown with a log spacing that allows field lines to be seen in all regions. This spacing also emphasizes the difference between the near-field region and the remote-field region in the pipe. The near-field region consists of the more closely spaced lines near the exciter coil in the pipe interior, and the remote-field region is the less dense region further away from the exciter.

Another advantage of RFEC inspection is that it is approximately equal (within a factor of 2) in sensitivity to axially and circumferentially oriented flaws in ferromagnetic material. The major disadvantage of RFEC inspection is that, when applied to nonferromagnetic material, it is not generally as sensitive or accurate as traditional eddy current testing techniques.

In a tubular geometry, an axis-encircling exciter coil generates eddy currents in the circumferential direction. The electromagnetic skin effect causes the density of eddy currents to decrease with distance into the wall of the conducting tube. However, at typical nondestructive examination frequencies (in which the skin depth is approximately equal to the wall thickness), substantial current density exists at the outer wall.

The tubular geometry allows the induced eddy currents to rapidly cancel the magnetic field from the exciter coil inside the tube, but does not shield as efficiently the magnetic field from the eddy currents that are generated on the outer surface of the tube. Therefore, two sources of magnetic flux are created in the tube interior; the primary source is from the coil itself, and the secondary source is from eddy currents generated in the pipe wall (Figure I.58). At locations in the interior near the exciter coil, the first source is dominant, but at larger distances, the wall current source dominates. A sensor placed in this second, or remote field, region is thus picking up flux from currents through the pipe wall. The magnitude and phase of the sensed voltage depend on the wall thickness, the magnetic permeability and electrical conductivity of tube material, and the possible presence of discontinuities in the pipe wall. Typical magnetic field lines are shown in Figure I.59.

The RFEC probe consists of an exciter coil and one or more sensing elements. In most reported implementations, the exciter coil encircles the pipe axis. The sensing elements can be coils with axes parallel to the pipe axis, although sensing coils with axes normal to the pipe axis can also be used for the examination of localized defects. In its simplest configuration, a single axis-encircling sensing coil is used. Interest in this technique is increasing. The technique could be made much more sensitive to localized flaws by the use of multiple sector coils spaced around the inner circumference with axes parallel to the tube axis. This modern RFEC configuration is shown in Figure I.60.

The use of separate exciter and sensor elements means that the RFEC probe operates naturally in a driver-pickup mode instead of the impedance-measuring mode of traditional eddy current testing probes. Three conditions must be met to make the probe work:

- The exciter and sensor must be spaced relatively far apart (approximately two or more tube diameters) along the tube axis
- An extremely weak signal at the sensor must be amplified with minimum noise generation or coupling to other signals. Exciter and sensing coils may consist of several hundred turns of wire in order to maximize signal strength
- The correct frequency must be used. The inspection frequency is generally such that the standard depth of penetration (skin depth) is the same order of magnitude as the wall thickness (typically 1 to 3 wall thicknesses)

When these conditions are met, changes in the phase of the sensor signal with respect to the exciter are directly proportional to the sum of the wall thicknesses at the exciter and sensor. Different wall thickness can cause a phase and amplitude change that can be used to detect defects such as cracks, corrosion thinning, and pitting.

Instrumentation includes a recording device, a signal generator, an amplifier (because the exciter signal is of much greater power than that typically used in eddy

current testing), and a detector. The detector can be used to determine exciter/sensor phase lag or can generate an impedance-plane type of output such as that obtained with conventional driver-pickup eddy current testing instruments. Instrumentation developed specifically for use with RFEC probes is commercially available. Conventional eddy current instruments capable of operating in the driver-pickup mode and at low frequencies can also be used. In this latter case, an external amplifier is usually provided at the output of the eddy current instrument to increase the drive voltage. The amplifier can be an audio amplifier designed to drive loudspeakers if the exciter impedance is not too high. Most audio amplifiers are designed to drive a 4 - to 8 - Ω load.

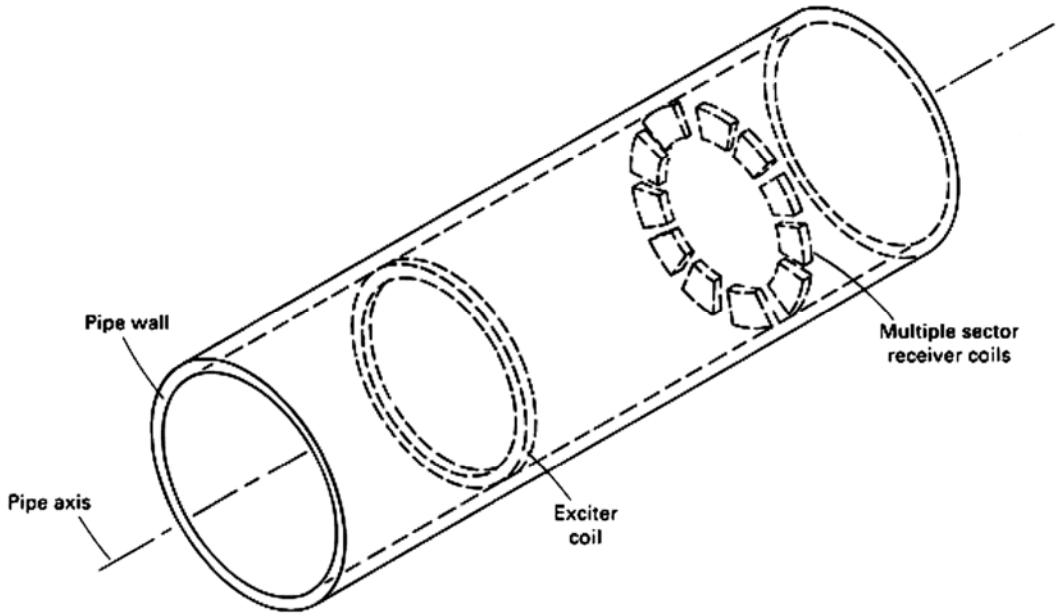

FigureI.60: RFEC configuration with exciter coil and multiple sector receiver coils.

I.6.3 Magnetic-particle inspection (MT or MPI)

Magnetic field testing includes some of the older and more widely used methods for the nondestructive evaluation of materials. Historically, such methods have been in use for more than 50 years in the examination of magnetic materials for defects such as cracks, voids, or inclusions of foreign material. More recently, magnetic methods for assessing other material properties, such as grain size, texture, or hardness, have received increasing attention.

Because of this diversion of applications, it is natural to divide the field of magnetic materials testing into two parts, one directed toward defect detection and characterization and the other aimed at material properties measurements.

All magnetic methods of flaw detection rely in some way on the detection and measurement of the magnetic flux leakage field near the surface of the material, which is caused by the presence of the flaw. For this reason, magnetic testing techniques are often described as flux leakage field or magnetic perturbation methods. The magnetic particle inspection method is one such flux leakage method that derives its name from the particular method used to detect the leakage field.

It is conceivable that leakage field fluctuations associated with metallurgical microstructure might be used in the analysis of material properties, the characterization methods now in use rely on bulk measurements of the hysteretic properties of material

magnetization or of some related phenomenon, such as Barkhausen noise. The principles and applications of magnetic characterization presented in this article are not intended to be exhaustive, but rather to serve as illustrations of this type of magnetic testing.

The origin of the flaw leakage field is illustrated in Figure I.61. In Figure I.61.a is presented a uniformly magnetized rod, which consists of a large number of elementary magnets aligned with the direction of magnetization. Inside the material, each magnetic pole is exactly compensated by the presence of an adjacent pole of opposite polarity, and the net result is that interior poles do not contribute to the magnetic field outside the material. At the surfaces, however, magnetic poles are uncompensated and therefore produce a magnetic field in the region surrounding the specimen. This is illustrated in Figure I.61.a by flux lines connecting uncompensated elementary poles.

If a slot is cut in the rod, as illustrated in Figure I.61.b, the poles on the surface of this slot are now also uncompensated and therefore produce a localized magnetic field near the slot. This additional magnetic field, which is represented by the extra flux lines in Figure I.61.b, is the leakage field associated with the slot.

Figure I.61, although adequate for a qualitative understanding of the origin of leakage fields, does not provide an exact quantitative description. The difficulty is the assumption that the magnetization remains uniform when the flaw is introduced. In general, this does not happen, because the presence of the flaw changes the magnetic field in the vicinity of the flaw, and this in turn leads to a change in magnetization near the flaw. With regard to Figure I.61, this means that the strengths and orientations of the elementary dipoles (magnets) actually vary from point to point in the vicinity of the flaw, and this variation also contributes to the flaw leakage field. The end result is that the accurate description of a flaw leakage field poses a difficult mathematical problem that usually requires a special-purpose computer code for its solution.

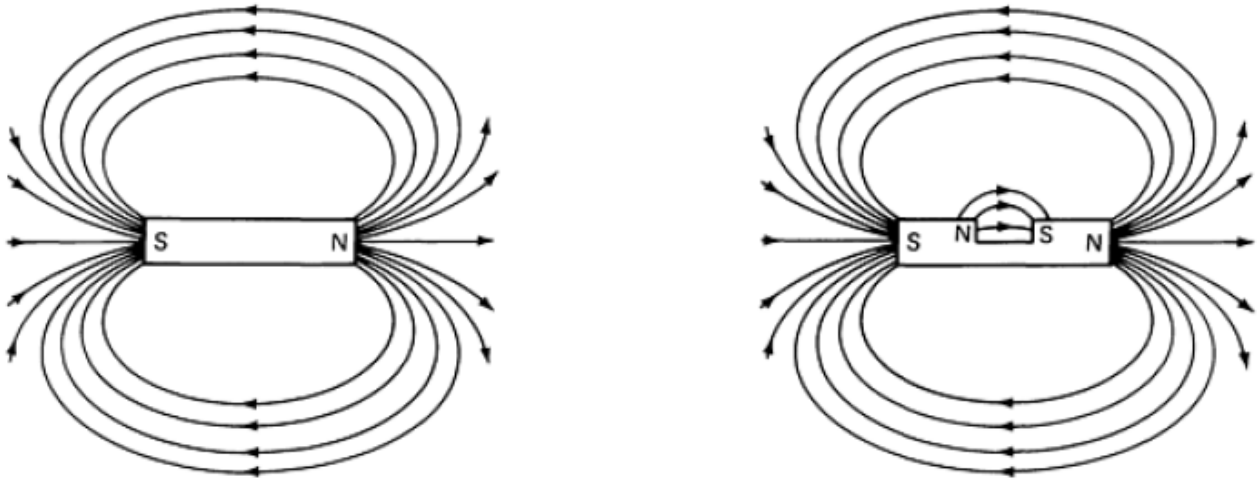

(a) (b)

Figure I.61: Origin of defect leakage fields. (a) Magnetic flux lines of a magnet without a defect. (b) Magnetic flux lines of a magnet with a surface defect.

One of the first considerations in the experimental application of magnetic leakage field methods is the generation of a suitable magnetic field within the material. In some ferromagnetic materials, the residual field (the field that remains after removal of an external magnetizing field) is often adequate for surface flaw detection. In practice, however, residual magnetization is rarely used because use of an applied magnetizing field ensures that the material is in a desired magnetic state (which should be known and well

characterized) and because applied fields provide more flexibility (that is, one can produce a high or low flux density in the specimen as desired.

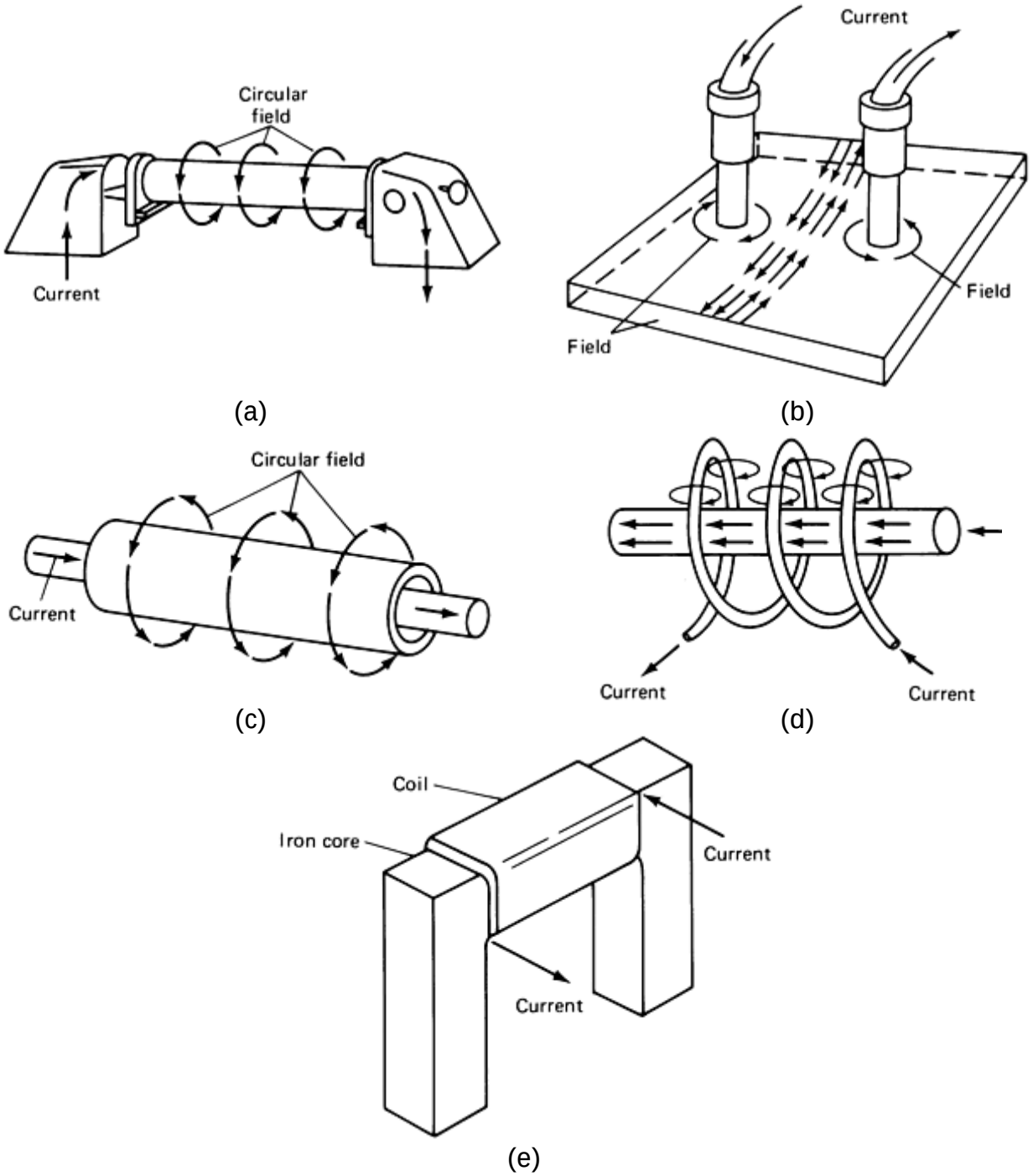

Figure I.62: Methods of magnetization:
(a) Head-shot method; (b) Magnetization with prods; (c) Magnetization with a central conductor; (d) Longitudinal magnetization; (e) Yoke magnetization.

Experience has shown that control of the strength and direction of the magnetization can be useful in improving flaw detectability and in discriminating among different types of flaws. In general, the magnitude of the magnetization should be chosen to maximize the flaw leakage field with respect to other field sources that might interfere with flaw detection; the optimum magnetization is usually difficult to determine in advance

of a test and is often approached by trial-and-error experimentation. The direction of the field should be perpendicular to the largest flaw dimension to maximize the effect of the flaw on the leakage field.

It is possible to generate a magnetic field in a specimen either directly or indirectly. In direct magnetization, current is passed directly through the part. With the indirect approach, magnetization is induced by placing the part in a magnetic field that is generated by an adjacent current conductor or permanent magnet. This can be done, for example, by threading a conductor through a hollow part such as a tube or by passing an electric current through a cable wound around the part. Methods of magnetizing a part both directly and indirectly are illustrated schematically in Figure I.62.

I.7 Acoustic emission testing

Acoustic emissions are stress waves produced by sudden movement in stressed materials. The classic sources of acoustic emissions are defect-related deformation processes such as crack growth and plastic deformation. The process of generation and detection is illustrated in Figure I.63. Sudden movement at the source produces a stress wave, which radiates out into the structure and excites a sensitive piezoelectric transducer. As the stress in the material is raised, many of these emissions are generated. The signals from one or more sensors are amplified and measured to produce data for display and interpretation.

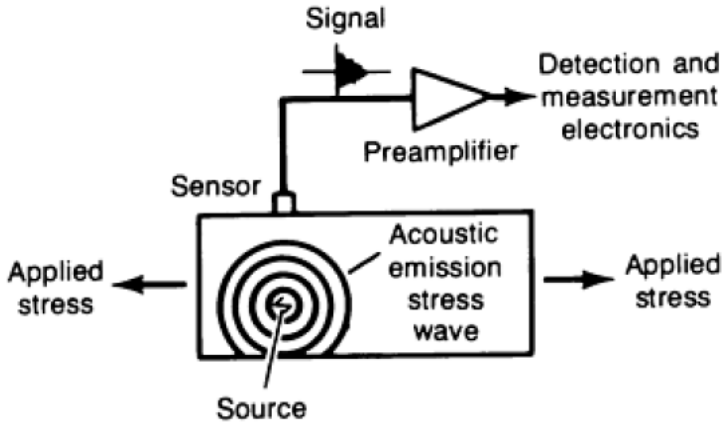

Figure I.63: Basic principle of the acoustic emission method.

The source of the acoustic emission energy is the elastic stress field in the material. Without stress, there is no emission.

Therefore, an acoustic emission (AE) inspection is usually carried out during a controlled loading of the structure. This can be a proof load before service, a controlled variation of load while the structure is in service, a fatigue test, a creep test, or a complex loading program. Often, a structure is going to be loaded anyway, and AE inspection is used because it gives valuable additional information about the performance of the structure under load. Other times, AE inspection is selected for reasons of economy or safety, and a special loading procedure is arranged to meet the needs of the AE test.

Acoustic emission differs from most other nondestructive testing (NDT) methods in two key respects. First, the signal has its origin in the material itself, not in an external source. Second, acoustic emission detects movement, while most other methods detect

existing geometrical discontinuities. The consequences of these fundamental differences are summarized in Table I.3.

Acoustic emission	Other methods
Detects movement of defects	Detect geometric form of defects
Requires stress	Do not require stress
Each loading is unique	Inspection is directly repeatable
More material-sensitive	Less material-sensitive
Less geometry-sensitive	More geometry-sensitive
Less intrusive on plant/process	More intrusive on plant/process
Requires access only at sensors	Require access to whole area of inspection
Tests whole structure at once	Scan local regions in sequence
Main problems: noise related	Main problems: geometry related

Table I.3: Characteristics of AE inspection compared with other inspection methods.

Often in NDT there is no one method that can provide the whole solution; for cost effectiveness, technical adequacy, or both, it is best to use a combination of methods. Because acoustic emission has features that distinguish it so sharply from other methods, it is particularly useful when used in combination with them.

A major benefit of AE inspection is that it allows the whole volume of the structure to be inspected nonintrusively in a single loading operation. It is not necessary to scan the structure looking for local defects; it is only necessary to connect a suitable number of fixed sensors; which are typically placed 1 to 6 meters apart. This leads to major savings in testing large structures, for which other methods require removal of insulation, decontamination for entry to vessel interiors, or scanning of very large areas.

Typically, the global AE inspection is used to identify areas with structural problems, and other NDT methods are then used to identify more precisely the nature of the emitting defects. Depending on the case, acceptance or rejection can be based on AE inspection alone, other methods alone, or both together.

Acoustic emission is a natural phenomenon occurring in the widest range of materials, structures, and processes. The largest-scale acoustic emissions are seismic events, while the smallest-scale processes that have been observed with AE inspection are the movements of small numbers of dislocations in stressed metals. In between, there is a wide range of laboratory studies and industrial testing.

In the laboratory, AE inspection is a powerful aid to materials testing and the study of deformation and fracture. It gives an immediate indication of the response and behavior of a material under stress, intimately connected with strength, damage, and failure. Because the AE response of a material depends on its microstructure and deformation mode, materials differ widely in their AE response. Brittleness and heterogeneity are two major factors conducive to high emissivity. Ductile deformation mechanisms, such as micro void coalescence in soft steels, are associated with low emissivity.

In production testing, AE inspection is used for checking and controlling welds, brazed joints, thermo-compression bonding, and forming operations such as shaft straightening and punch press operations. In general, AE inspection can be considered whenever the process stresses the material and produces permanent deformation.

In structural testing, AE inspection is used on pressure vessels, storage tanks, pipelines and piping, aircraft and space vehicles, electric utility plants, bridges, railroad

tank cars, bucket trucks, and a range of other equipment items. Acoustic emission tests are performed on both new and in-service equipment. Typical uses include the detection of cracks, corrosion, weld defects, and material embitterment.

Procedures for AE structural testing have been published by The American Society of Mechanical Engineers (ASME), the American Society for Testing and Materials (ASTM), and other organizations. Successful structural testing comes about when the capabilities and benefits of AE inspection are correctly identified in the context of overall inspection needs and when the correct techniques and instruments are used in developing and performing the test procedure.

Acoustic emission equipment is highly sensitive to any kind of movement in its operating frequency range (typically 20 to 1200 kHz). The equipment can detect not only crack growth and material deformation but also such processes as solidification, friction, impact, flow, and phase transformations. Therefore, AE techniques are also valuable for:

- In-process weld monitoring
- Detecting tool touch and tool wear during automatic machining
- Detecting wear and loss of lubrication in rotating equipment, and tribological studies
- Detecting loose parts and loose particles
- Detecting and monitoring leaks, cavitation, and flow
- Monitoring chemical reactions, including corrosion processes, liquid-solid transformations, and phase transformations.

When these same processes of impact, friction, flow, and so on, occur during a typical AE inspection for cracks or corrosion, they constitute a source of unwanted noise. Many techniques have been developed for eliminating or discriminating against these and other noise sources. Noise has always been a potential barrier to AE applicability. This barrier is constantly being explored and pushed outward, bringing previously impractical projects into the realm of feasibility.

Acoustic emission is a remarkable tool for studying material deformation because the information it provides is both detailed and immediate. With its sensitivity to microstructure and its intimate connection with failure processes, AE inspection can give unique insights into the response of material to applied stress. Acoustic emission analysis is most useful when used in conjunction with other diagnostic techniques, such as stress-strain measurements, microscopy, crack opening - displacement measurements and potential drop (for crack growth), or ultrasonic damping measurements (for dislocation studies). Acoustic emission complements these techniques and offers additional information on the dynamics of the underlying deformation processes, their interplay, and the transitions from one type of deformation to another.

Many materials studies involve the development of a test approach for eventual field application. Such work can be valuable, but it is subject to the difficulty of simulating defect emissivities and other field conditions in the laboratory.

Laboratory tests are often done with simple uniaxial stresses applied parallel to the rolling direction, while materials in industrial service are often subjected to complex biaxial or triaxial stress fields. In such cases, the acoustic emissions from the laboratory tests will not be a good model of the acoustic emissions from materials in industrial service.

Acoustic emissions are not generated by the reversible, homogeneous alteration of inter-atomic spacing that constitutes elastic deformation. Acoustic emissions are only generated when some abrupt and permanent change takes place somewhere in the material. Mechanisms that produce acoustic emissions in metals include the movement and multiplication of dislocations; slip; twinning; fracture and debonding of precipitates,

inclusions, and surface layers; some corrosion processes; micro-crack formation and growth; small and large crack jumps; and frictional processes during crack closure and opening.

The amount of AE energy released depends primarily on the size and speed of the local deformation process. The formation and movement of a single dislocation does produce an AE stress wave, but it is not a large enough process to be detected in isolation. However, when millions of dislocations are forming and moving at the same time during yielding of a tensile specimen, the individual stress waves overlap and superimpose to give a detectable result. The result is a continuous excitation of the specimen and sensor that is detectable as soon as the voltage it produces becomes comparable with the background noise. The higher the strain rate and the larger the specimen, the larger this signal becomes. This so called continuous emission is different from burst-type emission in that the individual source events are not discernible.

Continuous emission is best measured with RMS or energy rate measuring circuitry.

Continuous emission from the plastic deformation of steels, aluminium alloys, and many other metals has been extensively studied, and there have been many detailed findings relating acoustic emissions to dislocation activity and precipitates, microstructure, and materials properties. Such studies can yield valuable insights for alloy and material development. Most studies have focused primarily on continuous emission during and after yield; burst-type emissions sometimes observed in the nominally elastic region are less well explained.

In a small but important class of applications, AE inspection is applied during a manufacturing process to check the quality of the product or one of its components before final assembly and/or delivery. A common application of AE inspection in production quality control is the monitoring of welding and shaft straightening processes. Other efforts have been directed toward the inspection of integrated circuits. In the early 1970s, for example, an entire satellite launch mission failed because of a loose particle inside the cavity of a single integrated circuit. As a result, integrated circuits for critical applications are now routinely tested by particle impact noise detection technology, an inexpensive derivative of AE testing. During the manufacturing process, other types of flaws in integrated circuits can also be effectively controlled with AE inspection. Acoustic emissions from bonding processes and from ceramic substrate cracking were investigated by Western Electric researchers during the 1970s and were used as accept/reject criteria for parts on automated assembly lines.

The AE monitoring of welding processes has been part of the technology since its early days. Slag-free, more-automated weld techniques such as resistance welding, laser and electron beam welding, and gas tungsten arc and gas metal arc welding are the easiest to monitor. In the case of resistance welding, AE monitoring is carefully synchronized to the weld-cycle, and the various phases of the weld process are treated separately. Emission during solidification and cooling is correlated with nugget size and therefore with weld strength, while high-amplitude signals from expulsions can be used to switch off the weld current at the optimum time to avoid over-welding and to save power and electrode life. In the case of gas tungsten arc and gas metal arc welding, real-time computer algorithms have been developed to recognize the characteristic AE signatures of particular types of defects and to report these defects while the weld is being made. These procedures are effective even in the presence of substantial background noise. Gas tungsten arc welded injector tubes for the space shuttle are among the welded components routinely monitored by AE inspection in the production environment.

Shaft straightening is another production process that lends itself to quality control by AE monitoring. Forged shafts are routinely straightened in special machinery that detects any imperfections in alignment and applies suitable bending forces to correct them. The quality of the product is threatened by micro-cracking of the hardened surface of the shaft during the bending process. Acoustic emission inspection detects this very effectively and is incorporated into the machinery to warn personnel and to halt the process when potentially damaging micro-cracking occurs.

In welding and shaft straightening, the stresses that activate acoustic emissions are already present in the normal production processes (in welding, they are thermal stresses). In other cases, the stress is applied for the express purpose of AE testing.

I.8 Infrared and thermal testing

Thermal inspection comprises all methods in which heat-sensing devices are used to measure temperature variations in components, structures, systems, or physical processes. Thermal methods can be useful in the detection of subsurface flaws or voids, provided the depth of the flaw is not large compared to its diameter. Thermal inspection becomes less effective in the detection of subsurface flaws as the thickness of an object increases, because the possible depth of the defects increases.

Thermal inspection is applicable to complex shapes or assemblies of similar or dissimilar materials and can be used in the one-sided inspection of objects. Moreover, because of the availability of infrared sensing systems, thermal inspection can also provide rapid, non-contact scanning of surfaces, components, or assemblies.

Thermal inspection does not include those methods that use thermal excitation of a test object and a non-thermal sensing device for inspection. For example, thermally induced strain in holography or the technique of thermal excitation with ultrasonic or acoustic methods does not constitute thermal inspection.

The basic principle of thermal inspection involves the measurement or mapping of surface temperatures when heat flows from, to, or through a test object. Temperature differentials on a surface, or changes in surface temperature with time, are related to heat flow patterns and can be used to detect flaws or to determine the heat transfer characteristics of a test body.

For example, during the operation of a heating system, a hot spot detected at a joint in a heating duct may be caused by a hot air leak. Another example would be a hot spot generated when an adhesive-bonded panel is uniformly heated on one side. A localized debonding between the surface being heated and the substructure would hinder heat flow to the substructure and thus cause a region of higher temperature when compared to the rest of the surface. Generally, the larger the imperfection and the closer it is to the surface, the greater the temperature differential.

The surface condition of the test object is important for thermal inspection. Inspection results can be influenced by variations in surface roughness, cleanliness, foreign material (such as decals), and the uniformity and condition of paint or other surface coatings. A good practice is to clean the surface, remove or strip poorly adhering coatings (if present), and then apply a uniform coating of readily removable flat-black paint. This will allow uniform heat transfer into (or from) the subject and will also produce a reasonably uniform emissivity.

In thermal inspection, the test object can be classified as either thermally active or thermally passive. Thermally active test objects generate the necessary heat flow during

their operation, while thermally passive test objects require an external heat source or heat sink.

Some test objects can be inspected without the application or removal of heat because they are involved in a process that either generates or removes heat. When a defect results in an abnormal temperature distribution on the surface, no external heating or cooling is required. When the heat transfer process is transient, the timing of the inspection is important. An example of this would be a fluid-contaminated honeycomb panel on an aircraft that has just landed after a long flight at high altitudes. Although the entire aircraft would be warming up from the cooler temperatures experienced at high altitude, the contaminated regions would not warm as rapidly as the uncontaminated areas and therefore could be detected as cool spots in the structure if the inspection were performed immediately after landing. However, if the inspection were delayed, the entire structure would reach an equilibrium temperature, and the contaminated regions would no longer be detectable.

When the heat transfer process is in a steady-state condition, timing no longer becomes critical. An example is an electronic circuit board. Defective electronic components, in which the defect changes the electrical resistance of the component, will be either hotter or cooler than the same component properly operating on another circuit board. Another example would be a blocked tube in a heat exchanger. Temperatures along the tube would be different from temperatures along adjacent, unblocked tubes.

Thermally passive test objects require an external heat source or heat sink to establish the flow of heat to or from the test object. Generally, infrared or thermal measurement techniques become more sensitive as the average temperature of the subject increases. Consequently, the most common form of excitation is heating. However, in cases where additional heating could cause damage, cooling is used to create the required heat flow.

The main applications can be divided into the following categories:

- Hot and cold equipment
- Process control
- Liquid intrusion
- Disbonds, delaminations, and voids
- Electronic devices
- Research

Many types of hot and cold equipment that conduct or generate heat during operation are likely candidates for thermographic methods. Heating ducts, steam lines, radiators, heat exchangers, exhaust systems/chimney stacks, and refrigeration systems are heat transfer devices for which thermal inspection techniques can be used during periodic inspections for leaks, clogged passages, and missing or defective insulation.

Furnaces, ovens, salt baths, autoclaves, reaction stacks, and hot manufacturing equipment (such as presses and rolling mills) may also require periodic inspection for unnecessary heat losses. Thermographic techniques are also used to inspect cryogenic tanks.

Other equipment, such as engines (see Figure I.64), bearings, slides, brakes, transmitting antennas, and electrical equipment, generates heat during operation. Localized hot areas are usually a symptom of a mechanical or electrical malfunction, and early detection provides the opportunity to replace the defective components during regularly scheduled maintenance or before more serious damage occurs.

Thermal inspection methods are appropriate for certain processes in which the products are above room temperature as they exit a process. Examples are heat-set and

heat-shaped plastics, hot-worked metal components; hot coating processes, and welds components. Components can be monitored as they exit the process. Abnormal temperatures would indicate an out-of-control process, and corrections can be made to prevent the production of large numbers of defective parts. An example of an actively heated process control method is the technique for monitoring phosphate coating thickness using infrared absorption characteristics.

Water or fuel intrusion in honeycomb structures is a significant problem for aircraft maintenance. Inspections can be performed immediately after flight to detect such liquids as the structure warms to ambient temperature. Water intrusion in roofs can also be detected in the evening as ambient temperature drops. This method has been reported to be successful in detecting leaks and retained moisture in insulation. The level of fluids in a sealed tank can also be determined thermo-graphically. This is accomplished by either heating or cooling the tank and then noting the location of a sharp differential in resulting tank temperature.

Modern fabrication techniques rely heavily on the use of bonding for structures and protective coatings. Thermal techniques are good candidates for the detection of disbonds, delaminations, and voids in thin laminates, honeycomb to thin face sheets, and protective coatings. As the specimen thickness increases, thermal inspection becomes less effective because the possible depth of the defect may be greater.

Thermal inspection may also be difficult with bonded metal structures, such as adhesive-bonded aluminium. The radiative heating of aluminium is relatively inefficient because of the low surface absorptivity, and the thermal-emission signal is low because of the low emissivity. For such reasons, as well as to avoid reflective noise, the aluminium parts must normally be black-painted prior to thermal inspection. Moreover, the high thermal diffusivity of aluminium requires a high thermal-power injection to produce a visible thermal pattern before thermal uniformization is reached within the structure.

Nevertheless, the possibility of evaluating adhesive-bonded aluminium structures at the rapid pace afforded by thermal inspection is attractive, particularly for online applications. The following two examples describe the thermal inspection of adhesive-bonded aluminium after black-painting.

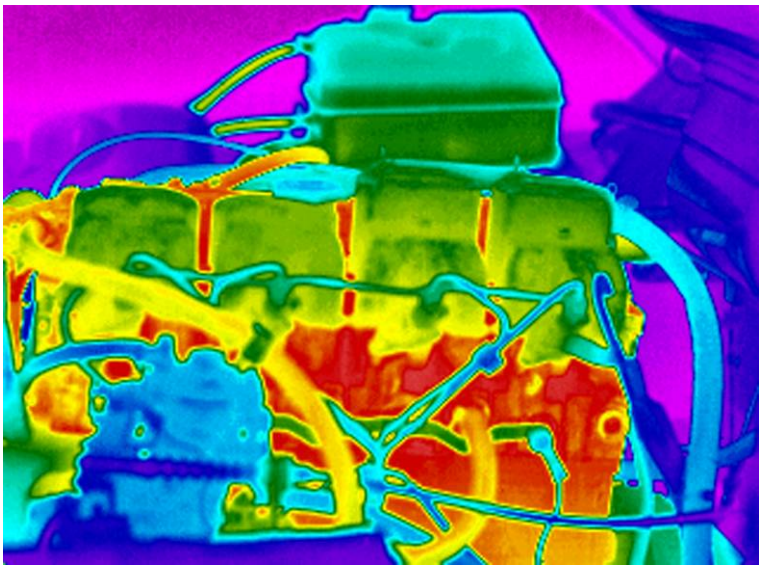

Figure I.64: Engine thermography

Chapter II

Ultrasonic Nondestructive Evaluation Systems

II.1. System hardware

II.1.1 Introduction

The ultrasonic (UT) hardware system was projected by taking in consideration different research needs that could be presented during this research work. The actual system is capable to be configured for each nondestructive test in order to adjust to each part inspection procedures.

The system also is in continuous update each time that a new UT instrument is procured or an old one is substituted. This update process permits to have a numerous ultrasonic system available at the same time, things that have as a final result the increment of ultrasonic inspected parts and like this work volume increased.

For this reasons in this research work we will present two ultrasonic NDE systems and two software suites. Also independent plug-ins will be presented at the end of this chapter.

The various common characteristics will be presented only for one system. For installing/mounting procedures of different instruments (boards) same rule is applied.

Moreover, for different instruments/components we will present only the necessary details. More details and full description of those instruments are available in the manual of use supplied by each manufacturer.

II.1.2 Ultrasonic 2D & 3D NDE scanning system (1st UT NDE system)

The first ultrasonic nondestructive evaluation system is the more complex one being capable to follow all UT scan types. This system is made out of the following components:

- ✓ Ultrasonic generator/receiver: Krautkrämer USIP 12
- ✓ Digital oscilloscope: LeCroy 9400
- ✓ Displacement system: Stäubli RX 60 L + controller CS7B
- ✓ Personal computer with:
  - ➢ National Instruments PCI-GPIB IEEE-488.2
  - ➢ Ethernet board 10/100 Mbit/s

From figure II.1 is possible to observe the general scheme of the first UT NDE system. During an UT scan the software will send through the Ethernet interface, by using a typical FTP protocol, the needed information to the controller that will move the 6 axis robot arm in the position where the UT probe has to acquire the UT signal. In this

moment the USIP 12 will retrieve the signal from the UT scan probe as an analog signal. This signal will be then send to the oscilloscope that through GPIB board is retransmitted to the Pc by way of 488 communication protocol.

Once the signal was received the software will save the file in "*.dat" extension. In the same file information related to the movement coordinates are reported, and this values will be used in an ulterior data processing phase.

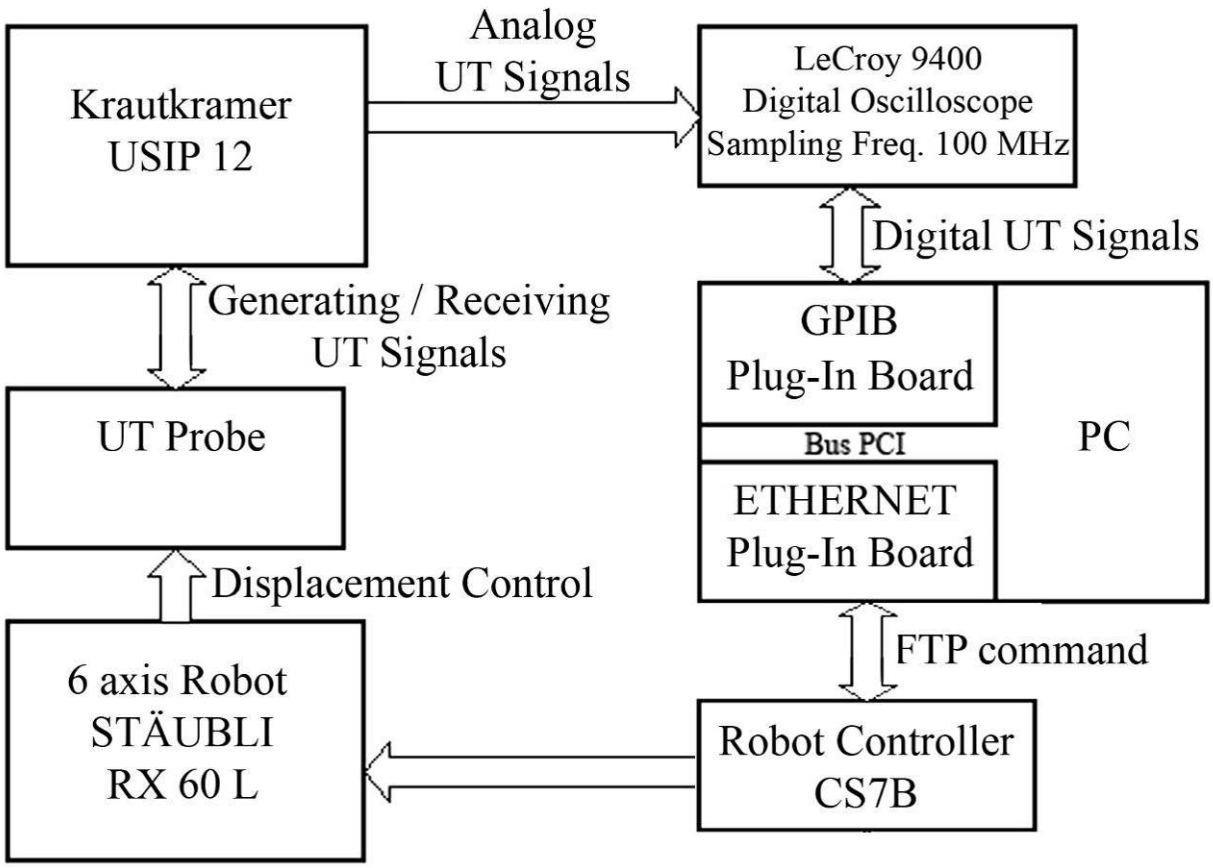

Figure II.1: First UT NDE 2D & 3D scaning system.

In the following paragraphs each system component (see Figure II.1) will be presented.

Krautkrämer USIP 12

Krautkrämer USIP 12 (see Figure II.2) is one of the main components of all the UT systems because he generates the signals and is sending them to the UT probe. The UT probe will transform these signals in UT signals. Also the Krautkrämer USIP 12 generates and receives signals in the same moment, and the return signals are amplified. This instrument is capable to run some preliminary analysis on the returning UT wave in order to eliminate various signal back noise and/or electric disruption. This analysis is made from the panel GATES, which permits to send to the oscilloscope only the needed signal parts, such as FA (Frequency Analysis) that through an internal hardware trigger will fix the UT signal on the front echo corresponding to the entrance in the material. Other option is that of sending the full UT wave and this signal acquisition mode is called RF (radio Frequency).

Figure II.2: Krautkrämer USIP 12.

Between the most important characteristics of this instrument we find:

- Possibility of working with a single transducer – reflection – or with two – transmission.
- Great choose of frequencies of the ultrasonic beam, which is, obviously, the first parameter to set. It is possible generate pulses of 0.5, 1, 2.25, 5, 10, 15 and 25 MHz.
- Possibility on amplifying the pulse received with a gain that can reach 100 dB and can be varied on a scale of 20 dB (from 0 to 60), or on a scale of only 2 dB (from 0 to 40 dB), which allows the most adequate choice of gain to any single operation.

The ultrasonic instrument contains three exits, one digital on a parallel port, not used because it is very slow, and the other two analogical. The first one is an exit in high frequency (RF) connected to the oscilloscope; the second one is an exit in direct current connected to the channel 0 of the acquisition board A/D-D/A inside the computer.

Lecroy 9400

LeCroy 9400 (Figure II.3) is an digital oscilloscope capable to sample the received signals, and after to present them on a cathodic tube in order to be able to change some signals settings, such as: time axis setup (x axis), signal amplitude (y axis). LeCroy 9400 presents 2 signal acquisition channels, each one of them having a analog/digital converter at 8 bit and a memory of 32kByte with a maximum sampling frequency of 100 MSamples/s, 100MHz. By using both cursors positioning it is possible to read the time of flight between two peaks of the UT wave that are of our interest.

A particularity of LeCroy 9400 is that presents a serial 9 pin port and a GPIB board in order to connect to a personal computer with the same connection ports.

This last characteristic is rendering LeCroy 9400 a good instrument for UT control, because through remote option all the settings can be done directly from the software oscilloscope panel, without being need to move from the computer, set up the waves and after proceed with the scan process.

The remote option is controlled through the GPIB board present in both devices (oscilloscope and PC) and the data speed is superior to 400 KB/s, by using the IEEE 488 protocols, or 7MB/s by using the HS 488 protocol.

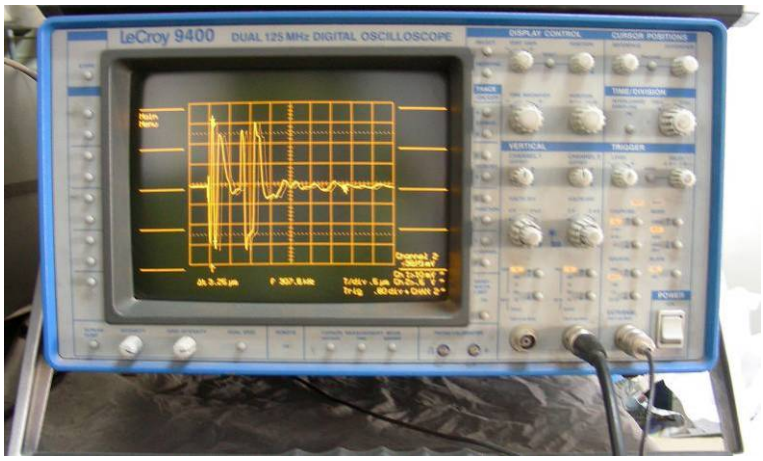

Figure II.3: LeCroy 9400.

Stäubli RX 60 L and CS7B controller

Stäubli RX 60 L is an anthropomorphic robot arm that presents a spherical pulse. This is permitting a fast and precise positioning and orientation in Cartesian 3D space of the ultrasonic probe. The anthropomorphic geometry is made of 3 round joints. The first one is called “Foot” (Joint 1 on Stäubli RX60 L joystick). Just immediately after this first joint we can observe the second joint called “Shoulder” (Joint 2 on Stäubli RX60 L joystick).

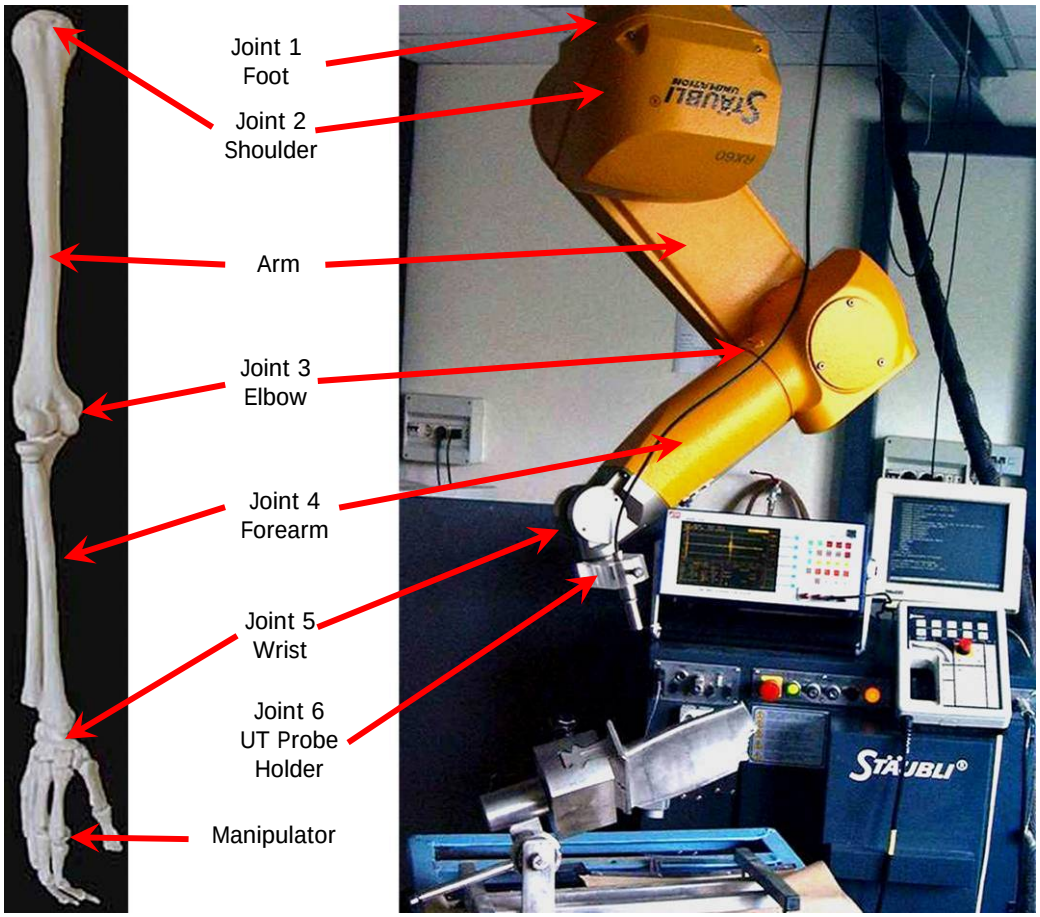

(a) (b)

Figure II.4: Comparison between human arm (a) and the anthropomorphic robot arm (b).

How is possible to observe from the Figure II.4 the anthropomorphic robot arm (Figure II.4.b) is similar to the human arm (Figure II.4.a). In this case the third joint that connects the arm and the forearm is called “Elbow” (Joint 3 on Stäubli RX60 L joystick).

The manipulation is carried by the spherical pulse that has 3 Degree of Freedom (DOF) realised by the round joints. This spherical pulse guarantees different orientation angles in a 3D work space. The round joints present in the spherical pulse are: forearm joint (Joint 4 on Stäubli RX60 L joystick), wrist joint (Joint 5 on Stäubli RX60 L joystick) and the UT probe holder joint (Joint 6 on Stäubli RX60 L joystick). The joint 6 present a flange that is used to mount the UT probe holder.

RX60 L has a total arm length equal to 865 mm (Figure II.5) and the repeatability is 33 micron. The accuracy for small volume is 50 micron. The maximum Cartesian speed is 1.8 mm/sec, and the maximum piece weight is equal to 1.5 Kg.

The RX60 L can be mounted on the floor level, on reinforced walls and ceiling.

The manipulator is completed by a command controller, a terminal with keyboard control and by the joystick (MCP). The controller is the intelligent side of the system, controlling the arm movement through different numerical gain amplifier for each joint or axis (X, Y, Z). The conversion of electrical power is assured by a power controller that the necessary tension needed to execute joint displacements. The controller is supplied by a three phase current.

The controller is composed by:

- Central unit that is controlling all peripherals
- Flash disk
- Serial ports
- Ethernet port
- User interface peripherals: alphanumeric terminal, joystick
- Interface AWC board
- Interface board between the axis engine controls and command amplifiers
- Other optional boards

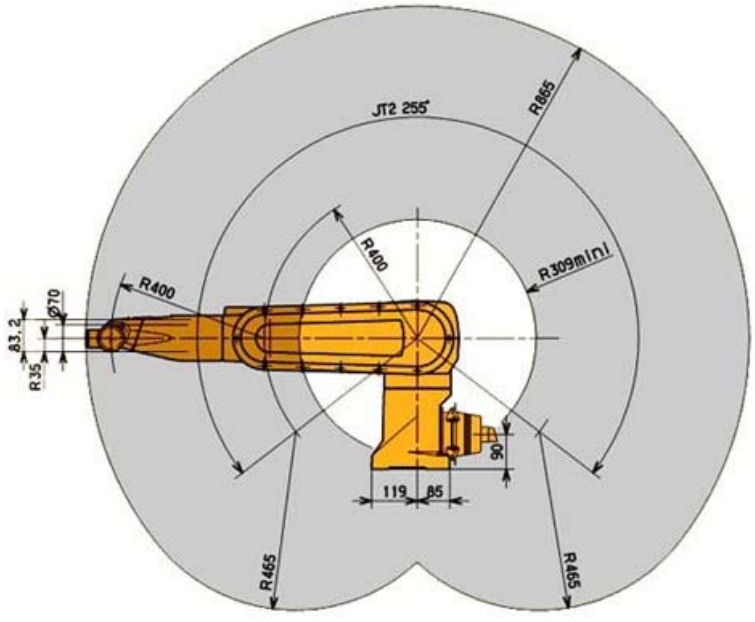

Figure II.5: RX60 L work area (sphere with 865 mm radius).

The INTERFACE AWC board is controlling all the signals in order to keep all the system in safety and also is taking care of some of the in/out signals. The interface board is sending to numerical amplifiers the reference signals for the power supply control and speed for each joint. By following the indications given by the user from the joystick, the numerical amplifiers will send the necessary information (signal form) for the displacement of each arm. This information is incremental position type, the real position is determined starting from a determined absolute start position. The joystick is the peripheral, which permits the manual control of the Robot. The alphanumeric terminal made of a 14" cathode tube and an alphanumeric keyboard, which permits to insert programs in the internal memory of the controller. Also the terminal is used to setup and recalibrate the anthropomorphic arm.

Personal Computer

The Personal Computer (PC) (Table II.1) is essentially used for dedicated application software execution, for the automation of displacement control through Ethernet board and for full ultrasonic wave acquisition from the LeCroy 9400 through GPIB board. The personal computer serves as mass storage for all the acquisition data for each UT inspected component.

Also on the PC data post scanning processing will be carried out, by using already existing packages, or by using external plug-ins that can present the results in a variety of colour range and also being possible to observe them in 3D wireframe or solid.

Table II.1.
The computer main characteristics

Mother board	IBM compatibile with SiS 645 chipset
Processore	Intel Pentium 4 2500 MHz
RAM	512 MB, DDR 400 MHz, PC-3200
Hard disk drive	EIDE, ATA-133, 200 GB, 7200 rpm, 8 MB cache
Video board	ATI Radeon 256 MB, 128 bit
Optic unit	DVD-RW unit
Floppy disk	3,5 inch disk reader
Ethernetboard	Realtek 10/100 MB/s
GPIB board	NI PCI-GPIB 488.2
Display	LCD Acer 19", 8 ms
Operating system	Microsoft Windows Xp Professional SP2

We can observe that the characteristics of the PC implemented in the system are analog to a standard office computer. This is justified by the facts that at the moment when the PC was purchased their components were at the top, but given the fast update of the informatics product market we are now using a normal office desk to operate the UT system.

In this case is opportune to verify the validity and the dimensioning of this PC thinking at the level of information that he has to respond. For this case we have build a simple M/G/1 model, where a unique user, the PC, presents a infinite data cue using a FIFO rules and a exponential arrival distribution of the data with a frequency λ equal to 3 points/sec. The acquired waves from the digital oscilloscope through the GPIB board and

data saving are “blocked” by the EIDE HDD that has intermediate time for the positioning of the mechanical parts on the disks.

From this analysis and using the HS 488 GPIB high data exchange speed protocol (up to 7 Mbit/sec), and given the high capacity of cache memory of the HDD (access data time p to 12ms) we can obtain cue waiting time inferior to the minimum limit of the system in 99 % of the cases. This is the needed confirmation that the PC is well dimensioned for the real-time acquisition and data saving of the UT scan files. In the case of 3D signal elaboration the needs of higher capacity mathematical processor and components is required.

II.1.3 Interface PC/Robot

The physical connection between PC and robot controller is made by an Ethernet link. The Ethernet link is a broad band communication between various components of a Local Area Network (LAN). Thi was first developed by the Digital Equipment Corporation and Xerox Corporation and afterwards was standardised by the Institute of Electrical and Electronic Engineering as IEEE 802.3 protocol. Ethernet term includes both physical and transmission data protocol for each channel.

In our case the physical connection is supported by two 10BASE-T twisted pair 5E category cables. This type of channel requires a star type network, where for each unit connected a cable is required. In order to complete the network connection a network hub is required. However, seen the high quantity of information and high level of data exchange in the LAN we have build a private network connection between the PC and robot controller. In this case the network cable used was a host-to-host type (sending receiving cables are inversed between the two ends).

The communication between the robot controller and the PC is based on a client/server interaction. The server is the application that offers various services to the users from a network area. The user is one that requires at least one of the services offered by the server.

In this particular case the robot controller is the server, and the service offered is the arm displacement application. The controller is remote accessed by the client that in this case is our PC.

The communication protocol between is a low level TCP/IP type (Transmission Control Protocol/Internet Protocol).The TCP/IP communication protocol serves to assure on the Ethernet channel a safe and continuous data exchange. These options are simplifying very much the communication control over the Ethernet link.

II.1.4 Inspection system assembly

Board install

Inside the personal computer all the necessary boards were correctly installed, and for those we recommend to leave them as they are set-up from the initial install. Any other operation can damage the system viability.

In the case when setup parameters were lost or the boards must be installed to another computer the following procedure has to be followed:

First of all we have to install the GPIB board drivers. In this case is sufficiently to follow the guided procedure on the driver installation disk (installer) because the GPIB is

being setup by the producer to self adjust to ad-hoc software packages. However, we need to verify that the IRQ address assigned to the GPIB board by the PC is ZERO (controller). This is made by following the link “NI-488.2” in Control Panel window. All the other parameters MUST remain UNCHANGED.

Also the GPIB oscilloscope board has to be setup with the address 4, which must remain UNGHANGED. If this value is different than 4, from the back of the oscilloscope LeCroy 9400 we will turn the respective button in order to obtain the value 4.

Once the GPIB board was installed we will insert the secondary network board in the PCI slot. In order to be recognised we will have to restart the computer and than on yhe network properties menu we will have to insert (in TCP/IP connection protocol) the following IP: 176.16.108.1 and as a Subnet Mask 255.255.255.0.

Electrical cables connections

The electrical cabling has to follow the procedure and order presented below.

- Connect the UT probe at the frontal panel of the USIP 12 at the connector “EXT 1” through an axial cable and a LEMO connector.
- Connect the high frequency exit “RF” on the back panel of USIP 12 to the Channel 2 of the LeCroy 9400 oscilloscope through an axial cable that presents two BNC cable connections.
- Connect the synchronizing signal exit from the USIP 12 to the trigger connector on the LeCroy 9400 oscilloscope through a coaxial cable with a 0.50” connector at one side and to the other side with a normal BNC connector.
- Connect the GPIB cable to the GPIB interface on the back panel of the LeCroy 9400 and with the GPIB board connector on the PC (second slot starting from downside).
- Connect the Ethernet host to host cable (ends with two standard RJ45 connectors) once to the Ethernet connection board of the robot controller and the second end to the Ethernet board connector of the PC.
- Connect all the power supply cables of all the components to the electrical network. It is recommended to connect each component to a diverse plug connection due to the increasing of various interferences in the 50 Hz frequency network. and due to a possible bad ground connection.

System start-up

After that the power connections to all peripherals were connected we will start the robot controller fallowing the next procedure:

- Turn on the alphanumeric terminal from the switch on the lower right side of the 14” display;
- Turn on the Robot controller from the round switch on the top left side of the controller;
- Than we will have to wait until all phases (start-up, calibration, etc.) are finished. At the end “push button in 15 seconds” will appear on the display. The green colour button on the central panel of the controller will flash (for 15 seconds)

- We can push the button and the 6 axis arm will be able to work. However, if the 15 seconds passed, in order to enable the robot arm we will write on the alphanumeric keyboard “enable power” and then return. Another way of starting the robot is through the COMP/PWR” button present on the joystick (manual control);
- If we want to cut-off the power supply to the arm we will write on the terminal keyboard “disable power” and the return or by selecting again the button “COMP/PWR” on the manual control.
- At the end of the start-up procedure the display will show the next information:
  - "Local Address : 172.16.108.102
  - "Listening for connection to port : 1234"

  which indicates that the robot controller and the arm were correctly turned on and that a Ethernet connection is pending.

The program that realise the communication control between PC and controller (called Server TCP/IP) is started automatically during the start-up procedure of the robot. N the case that by any reason the program was not started we can write the following line on the alphanumeric keyboard “EX/C TCP.SRVR”.

In this moment all the system is ready to be used, and after the calibration of the signal on both USIP 12 and LeCroy 9400 we can start the UT scan.

II.1.5 Ultrasonic 2D NDE scanning system (2nd UT NDE system)

The second ultrasonic nondestructive evaluation system has most of the components presented in the 1st UT NDE system. The major difference is the displacement control that is a scanning tank capable to execute only 2D UT scan by following a boustrophedon pattern. The scanning tank is made by IsoTest and the remote control is made through a parallel communication port. The computer has mounted a MIO 16 board that is sending controlled electronic impulses in order to control the displacement of the tank in both directions: X- axis and Y axis.

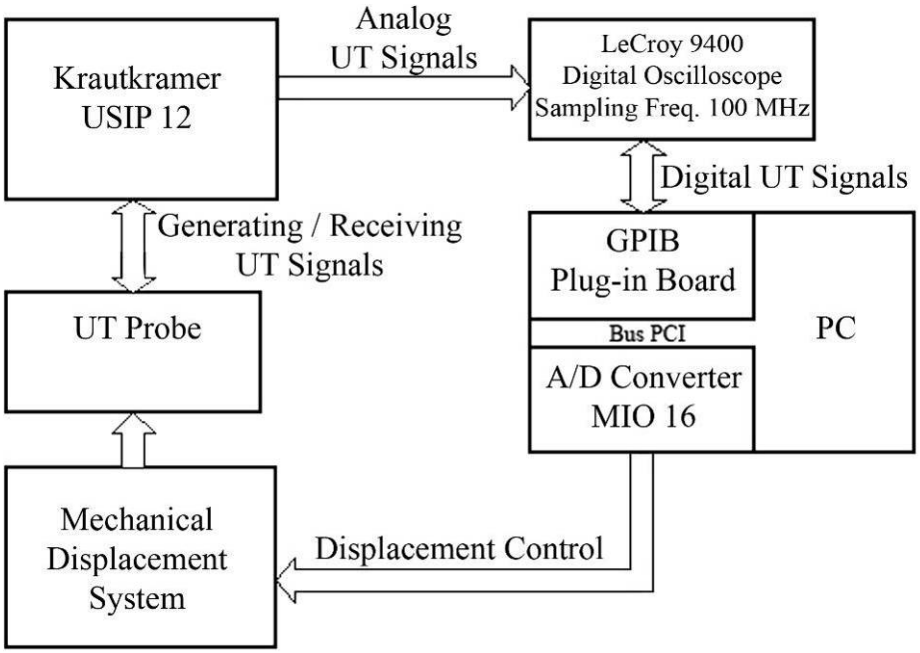

Figure II.6: UT system hardware configuration.

The system hardware configuration (Figure II.6) is made of:

- ✓ Ultrasonic generator/receiver: Krautkrämer USIP 12
- ✓ Digital oscilloscope: LeCroy 9400
- ✓ Displacement system: IsoTest tank containing the UT coupling medium (water) and a bi-dimensional actuator providing for UT probe displacement in the x-y plane
- ✓ Personal computer for UT waveform acquisition and processing as well as UT probe displacement control with acquisition boards:
  - ➢ National Instruments PCI-GPIB IEEE-488.2
  - ➢ National Instruments MIO-16

It is possible to observe in Figure II.6 that during the scanning the software developed in LabView is sending through MIO16 board and parallel communication port the displacement commands to the bi-dimensional actuator that provides for the UT probe displacement in the needed direction.

At this point the ultrasonic generator/receiver USIP 12 is transmitting the signal received from the UT probe to the digital oscilloscope and after was sampled at a 100 MHz frequency will be transferred through GPIB interface using the 488 communication protocol to ECUS Inspection software suite and after a UT scan file will be generated.

The UT scan file saved in "*.dat" extension is then used for post scan signal elaboration.

IsoTest tank for UT probe displacement

The IsoTest tank (see Figure II.7) is containing the UT coupling medium (water) and a bi-dimensional actuator providing for UT probe displacement in the x-y plane. In the steel frame of the IsoTest tank we have used a small PVC water tank containing as well the piece to be measured. On the external side is present a window that allow us the visualisation of the UT probe displacement and also to visualise the piece under inspection.

Figure II.7: IsoTest UT tank with a 2D actuator for a bi-axial displacement

The tank presents two gliding bars in anodized aluminium for a better displacement movement on X axis. Another threaded anodised aluminium bar is used under the control panel in order to execute the displacement along Y axis (see Figure II.8)

Figure II.8: Gliding bars made in anodized aluminium. Manual control is present on the external side of the control panel.

The tank can work under different conditions:

- It can be manually guided by the two round controls present on the external side of the control panel. This is used for a preliminary setting of the UT scan, and for positioning at the start point of the same UT scan.
- Semiautomatic control mode it is activated from the switch present on the control panel and by switching it off/on the manual controls is turned on/off.
- Automatic displacement control it is made by the software and the interface MIO16 parallel port. Mio 16 board is sending quad waves to the displacement step-by-step engine controllers.

The displacement system presents as well a manual emergency button that will block immediately the power supply to the internal electrical components (including step-by-step engines).

Electrical cables connections

The electrical cabling has to follow the procedure and order presented below.

- Connect the UT probe at the frontal panel of the USIP 12 at the connector “EXT 1” through an axial cable and a LEMO connector.
- Connect the high frequency exit “RF” on the back panel of USIP 12 to the Channel 2 of the LeCroy 9400 oscilloscope through an axial cable that presents two BNC cable connections.
- Connect the synchronizing signal exit from the USIP 12 to the trigger connector on the LeCroy 9400 oscilloscope through a coaxial cable with a

0.50” connector at one side and to the other side with a normal BNC connector.

- Connect the GPIB cable to the GPIB interface on the back panel of the LeCroy 9400 and with the GPIB board connector on the PC (second slot starting from downside).
- Connect to the MIO16 the parallel cable to one side and to the parallel port to the other side.
- Connect all the power supply cables of all the components to the electrical network. It is recommended to connect each component to a diverse plug connection due to the increasing of various interferences in the 50 Hz frequency network. and due to a possible bad ground connection.

System start-up

After all peripherals were connected to the electrical system we will start the IsoTest tank. In this moment all the system is ready to be used after the calibration of the signal on both USIP 12 and LeCroy 9400 and after that the automatic displacement control is switch of we can start the UT scan.

II.2 System software

In the following paragraphs all the software packages used for ultrasonic nondestructive inspection will be presented. The software presented is at the second edition V 2.0. Also ad-hoc software packages (called plug-ins applications) necessary for data post processing will be presented.

The applications presented are:

ECUS Inspection v2.0 – is implemented on the 2nd UT NDE scanning system

RoboTEST v2.0 – is implemented on the 1st UT NDE scanning system

Ad-hoc software – plug-ins – can be used in data post processing incoming from both UT scan systems.

II.2.1 ECUS Inspection v.2.0

ECUS Inspection was the first UT software made by our laboratory (Laboratory of Advanced Production and Technology - LAPT). Also it was the software that was able to control in remote the displacement of the IsoTest bi-actuator UT tank. The ultrasonic waves were saved and after post analysed. An ultrasonic scan consists in an inspection step-by-step of the piece under control, and also in the identification of the transducer position for each scanning point, for one or more tension values proportional with the measure carried out

The only disadvantage is that the system is available only for 2D scan (in plane scan). For 3D UT scan we will use the RoboTEST v2.0 software package that will be presented further in this chapter.

The main advantage is the possibility to create a grey scale image representing the in-plane damage in order to understand better and faster the different defect areas in the inspected piece .

The first version of this software was realised on Mac OS8.x platform and was created in LabView 5.0 for Mac.

The new version of this software (Figure is made in IDE LabView7.1 and operative system Microsoft Windows XP Professional SP2. This was possible by reprogramming all the error management, connectivity management protocols and was inserted an images elaboration section (not available in the v.1.0).

This change was necessary because the platform update for Mac OS 8.x and LabView 5.0 Mac stopped a couple of years ago. Even National Instruments is creating more functions in order to simply update the system with new modules, without being forced to reprogram all the software.

Figure II.9: ECUS Inspection v 2.0 Software package.

In following paragraphs the ECUS Inspection options and capabilities will be presented.

Scan Setup

The first window is the main control widow where is possible to setup the scan parameters such as: scanning area (lengths and width), scanning step, define the UT probe used. This window is reported in the Figure II.10.

Following strictly the theory on ultrasonic nondestructive inspection the software presents different test capabilities such as: "**A-Scan**", "**C-Scan**", and "**FV-Scan**". These capabilities are used in 2D or 2½ D ultrasonic inspection tests.

The reading of the previously saved files is made from the option "**Image Analysis**".

The two main functions used during the UT test are:

"**C-Scan**": that permits the saving for each scanning point one tension value for each wave, which is proportional to the maximum amplitude counted in a time of flight widow previously chosen. This time window is accurate setup on the USIP 12 (corresponding to front echo, internal piece echo or back echo). This will transmit to the software the tension signal corresponding to the maximum amplitude value in that specific time window.

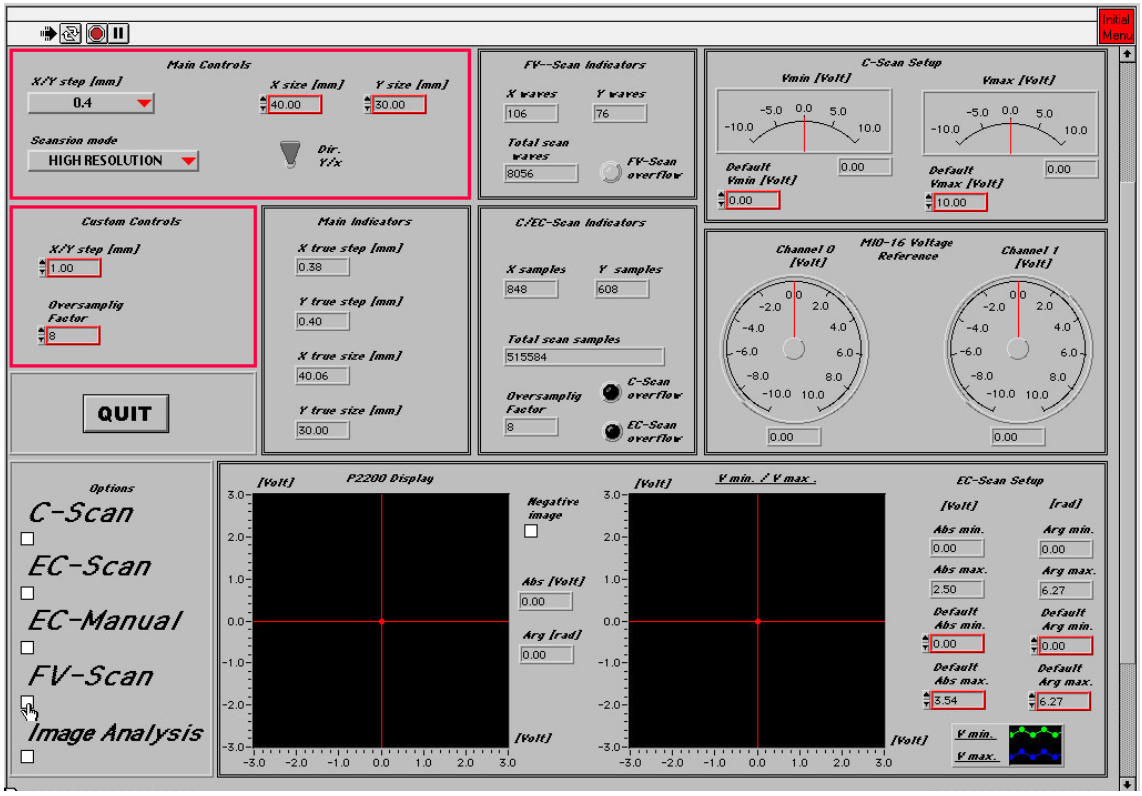

Figura3.4: Main Menu of ECUS Inspection v 2.0 software package.

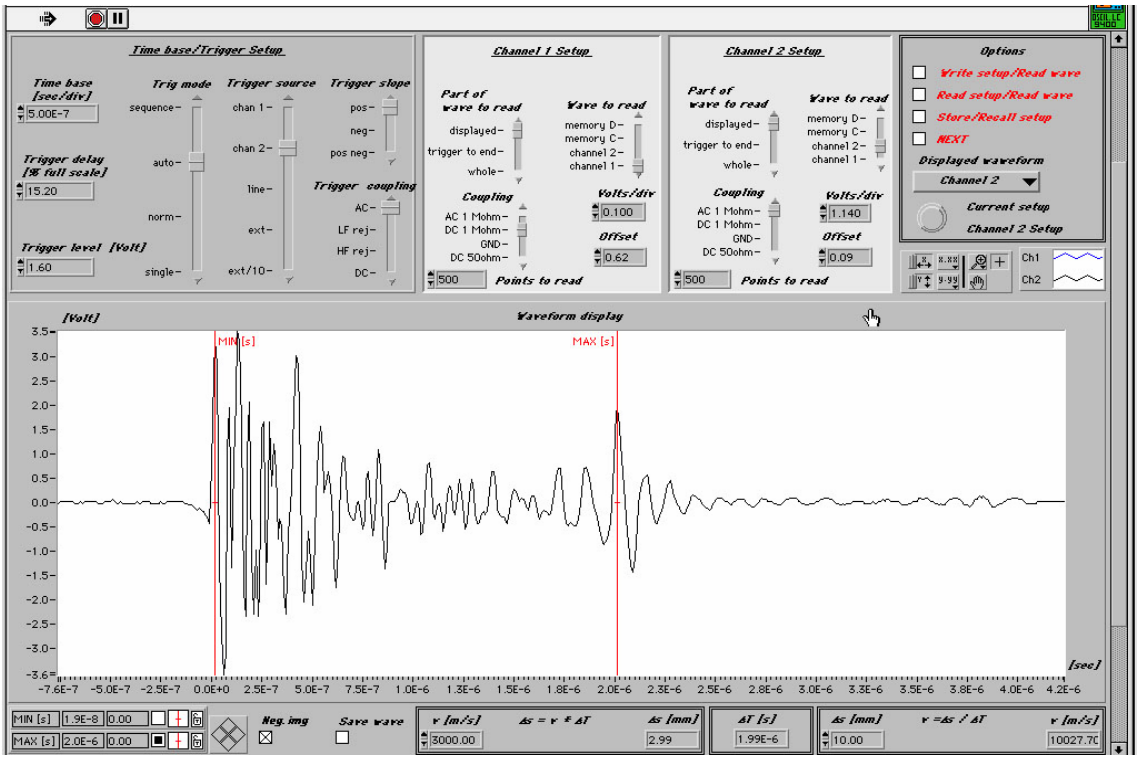

Figure II.11: Thickness measurement obtained from the correspondence between the Time-of-Flight and the measured thickness of the piece during UT tests.

"**FV-Scan**": This scan type is the most utilised because we can retrieve for each scanning point the full scan UT wave, and this permits us to realise a complete characterisation of the piece under inspection.

The UT wave is digitised by the oscilloscope that is connected to the RF exit of USIP12.

The FV-Scan permits us to measure the thickness of the piece under testing by knowing the difference between the time of flight (TOF) since the entrance and exit from the material of the analog wave. Contrary we can characterise the material capabilities such as the ultrasonic speed in the material (if it is not a standard material) by knowing the TOF inside the material and the measured piece thickness (Figure II.11).

Full Volume Ultrasonic Scan

After setting the scan parameters it is possible to start the actual scan.

The UT probe displacement can be followed during the entire test by looking at the moving cursor on the “Pick up position” tab (Figure II.12). The cursor can be moved on the grid that follows the indication of number of scan steps on each axis and the relative distance between each step.

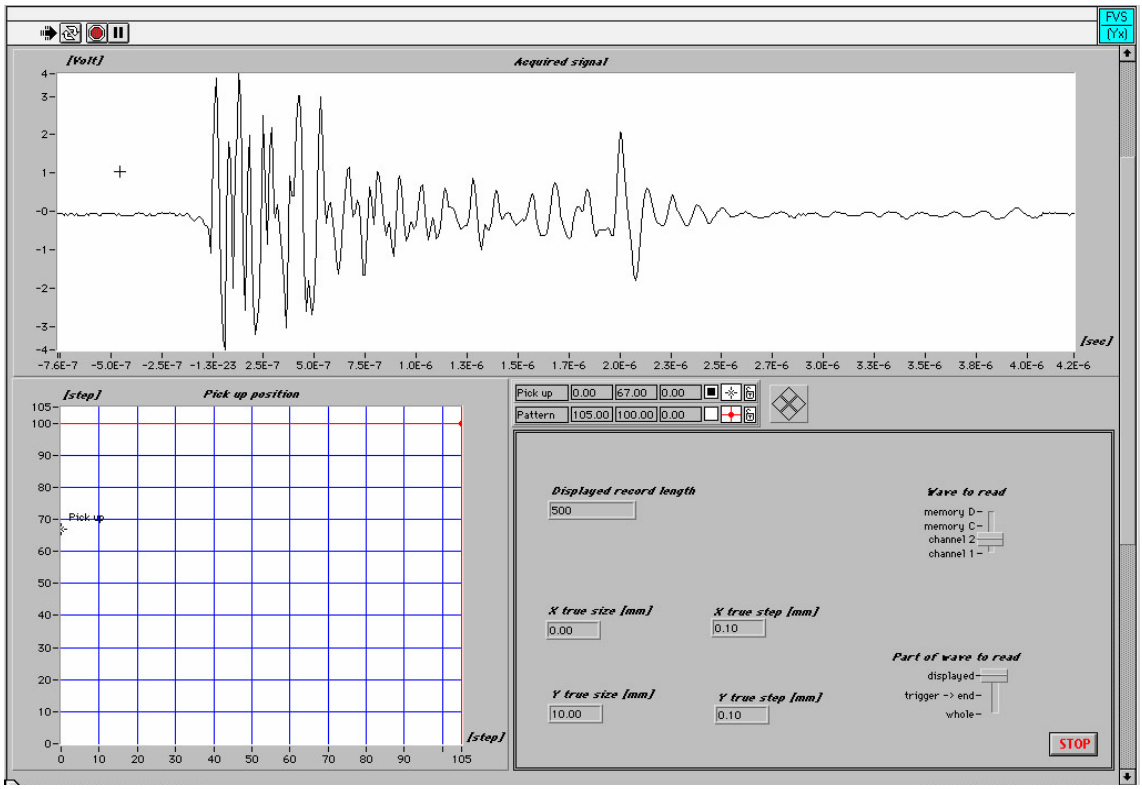

Figure II.12: Ultrasonic signal corresponding to the selected point on the scan matrix.

Ultrasonic Images

At the end of the UT scan it is possible to retrieve images that are corresponding to each section of the ultrasonic wave. Also, it is possible to obtain from the volumetric file each single UT wave for each point in the scan area.

It is possible as well to retrieve information about the scan setup values (file size, piece sizes, the scanning step and the number of UT waves acquired. Moreover, is possible to change the characteristic parameters in order to improve image visualisation (colours and dimensions of the images) (Figure II.13).

From the menu “**Change Limits**” we can pass to a submenu where the UT wave

presented is the one that we have precedent chose. In this case we can position the two cursors accordingly to our necessities (Figure III.14)

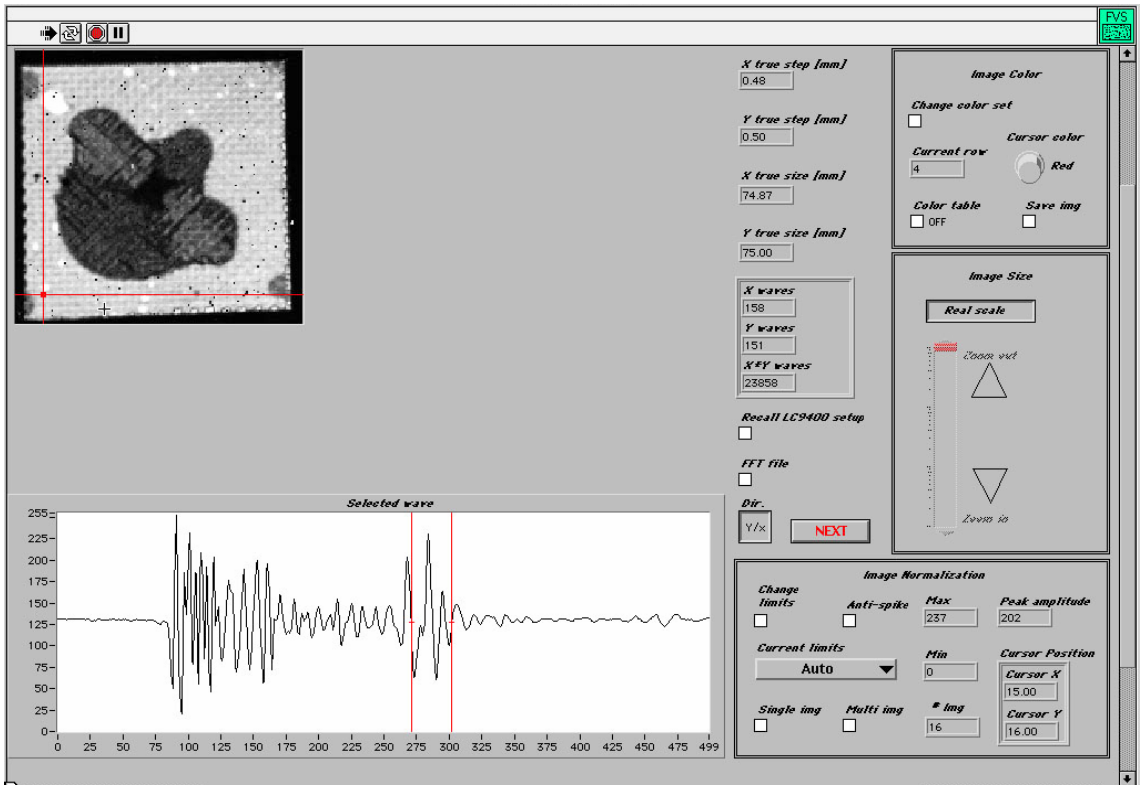

Figure II.13: Back echo time gate and the corresponding image for a carbon fiber reinforced plastic impacted laminate.

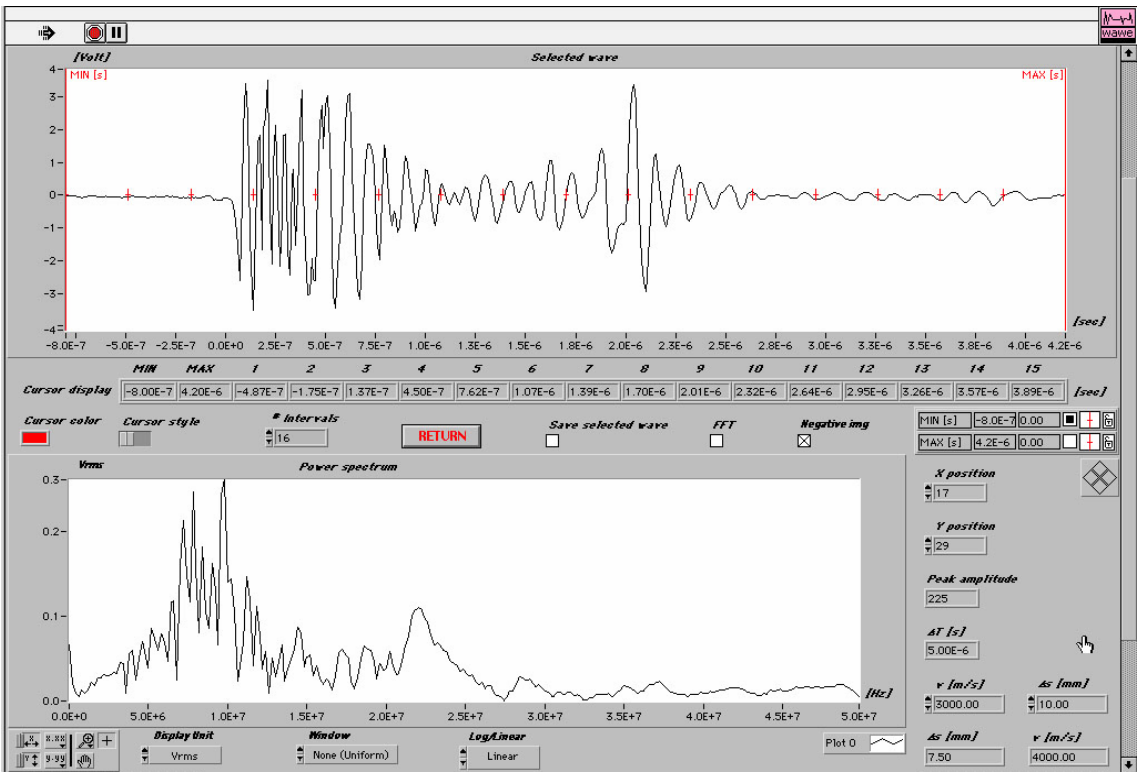

Figure II.14: FFT graphic (lower graphic) corresponding to previously chosen UT wave (upper graphic). It is also possible to observe the scan settings on the lower right corner.

In this menu is possible to position the time gates on the UT wave and dived it in equal parts (max 30μm thick for interval, and maximum 16 levels at one time as showed in figure II.14). In our case we have divided the UT signal in 16 sub-gates. In this case we will obtain 16 ultrasonic images corresponding to each sub-gate (see Figure II.15).

Each image is corresponding to 1/16 part of total piece thickness (impacted FRP laminate).

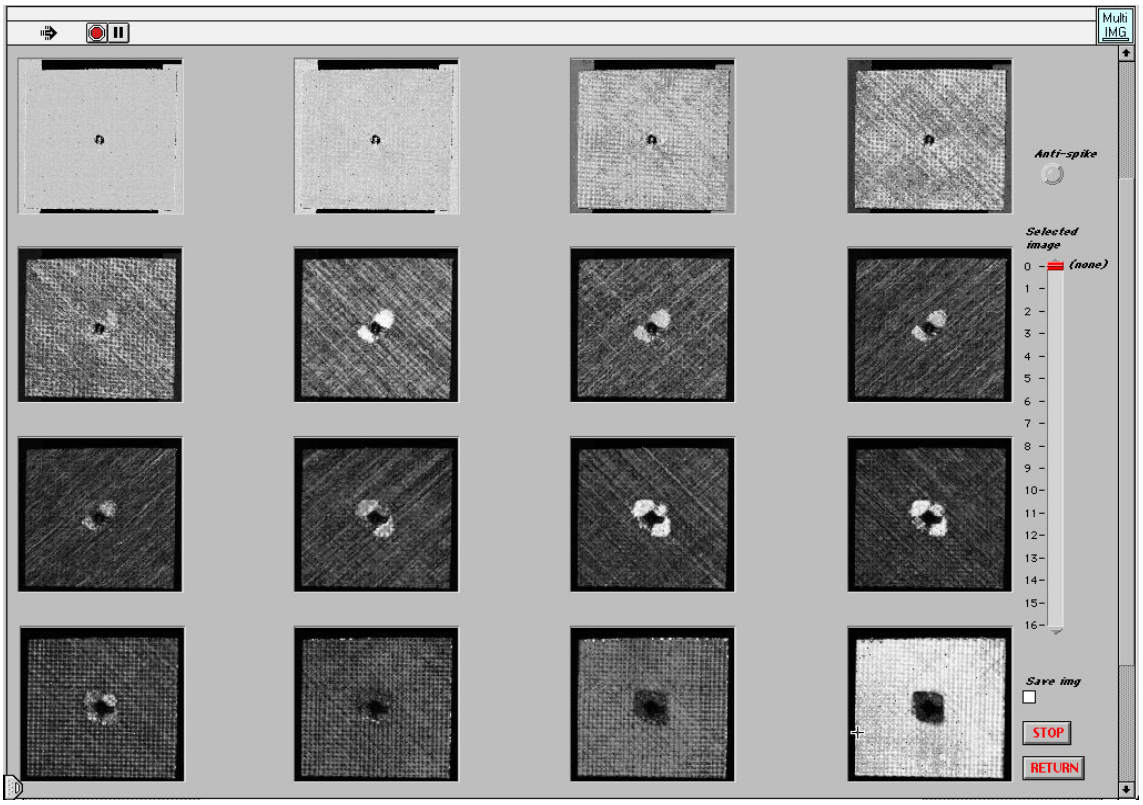

Figure II.15: 16 images corresponding to each time sub-gate and to a 1/16 of total piece thickness.

Ultrasonic images processing

From menu "**Single Image**" (Figure II.10), is possible go to menu "**Image Analysis**" (Figure II.16) where we can find different image processing subprograms:

- "**Noise reduction**": eliminates peak with high values and visualizing the internal damage as result of impact tests (Figure II.17);
- "**Histogram clipping**": permits the set-up of diverse grey tone scale. The effect of this option is to obtain better grey tones differences between sound and damaged areas (Figure II.18 and II.19);
- "**2D-FFT**": calculates a 2D Fast Fourier Transform (FFT) and presents the results in the Nyquist domain of frequencies for each single image chosen in the previous "**Single image**" menu. Also is being reported the phase diagram that presents, for the same image, the fibre orientation directions (Figure II.20);
- "**3D-Graph**": this option creates a 3D diagram by setting up relationships between the different values of grey tones at different thick levels. It is possible to observe the 3D shape of the internal damage in the corresponding section (Figure II.21);

- "**Negative Image**": visualise the UT image with inverted colours (see Figure II.22).

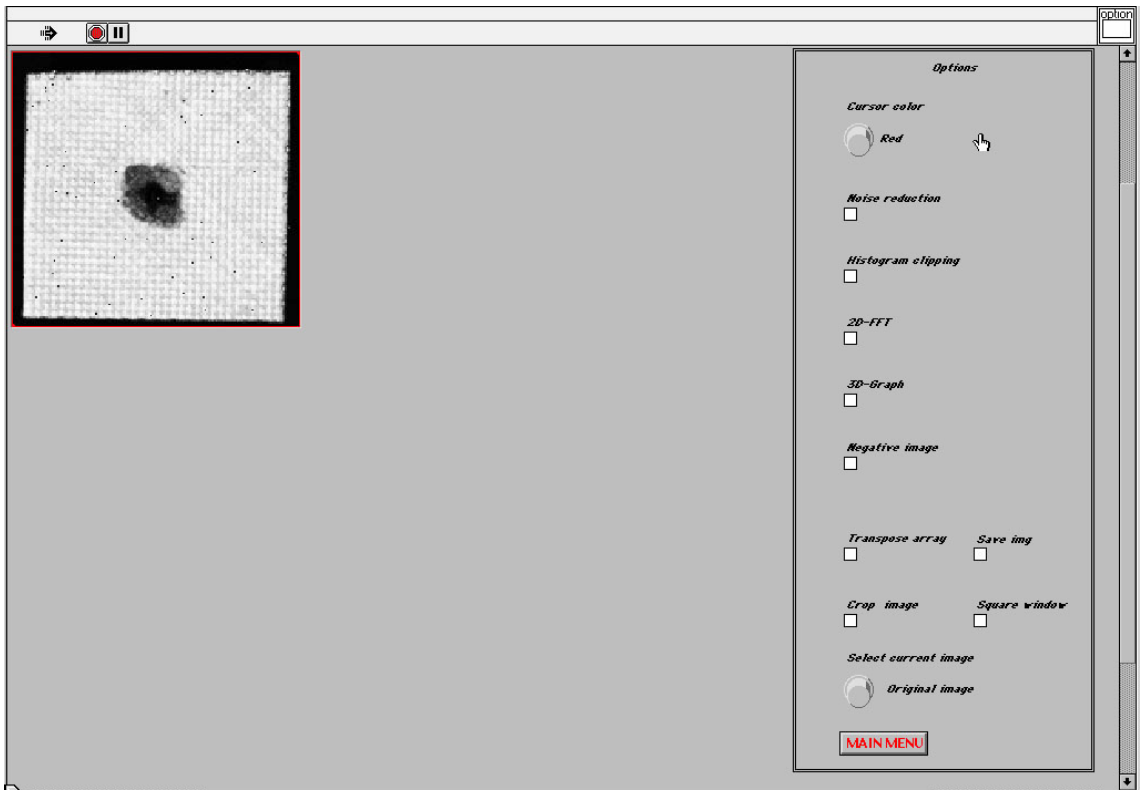

Figure II.16: Menu "Image Analysis".

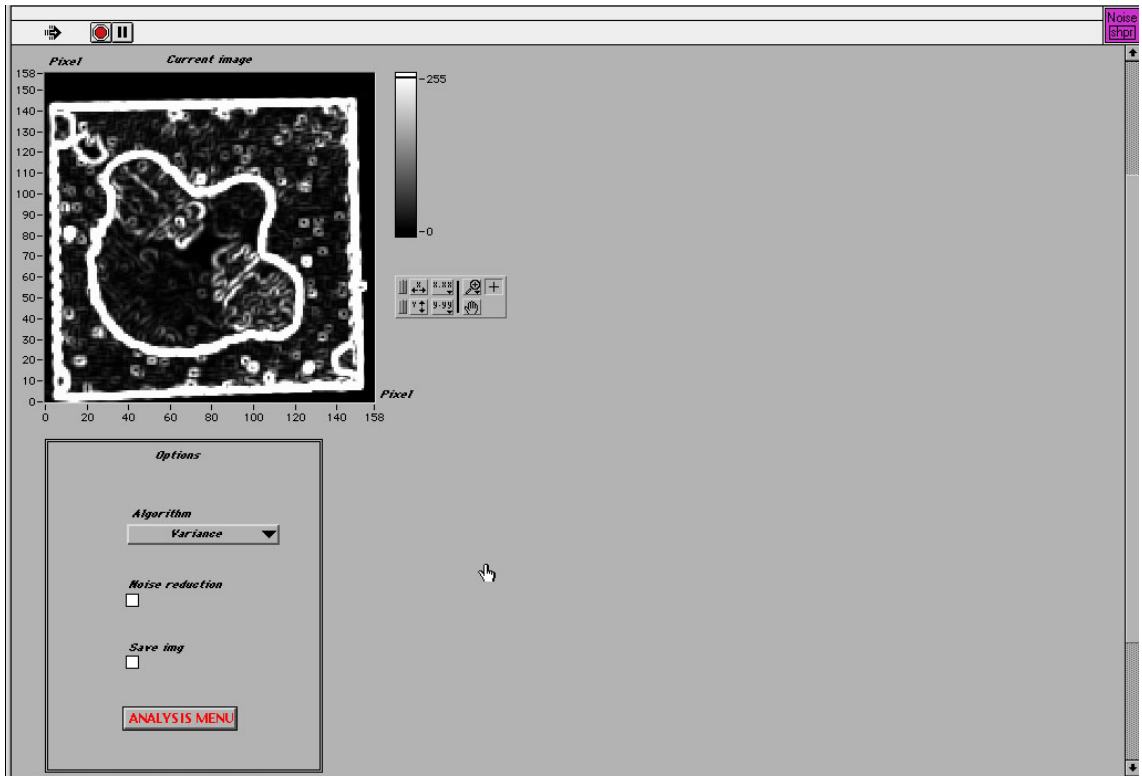

Figure II.17: Submenu "Noise Reduction".

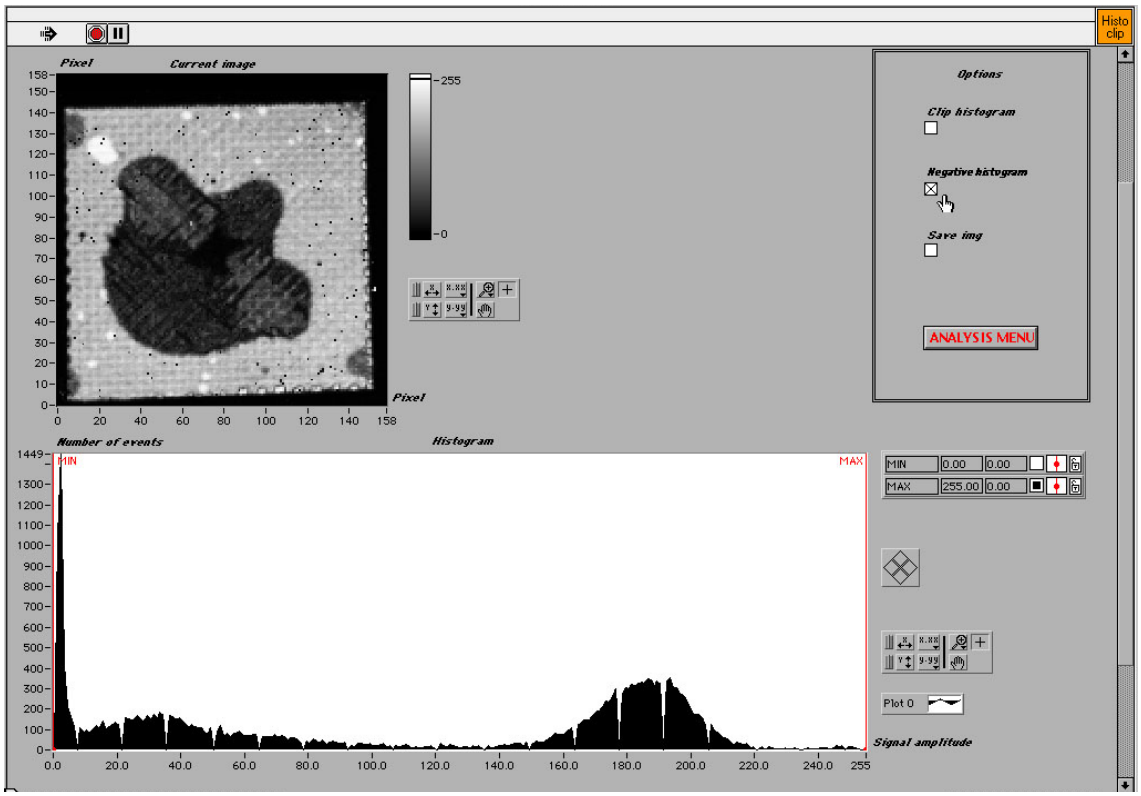

Figure II.18: Submenu “Histogram clipping” before image processing.

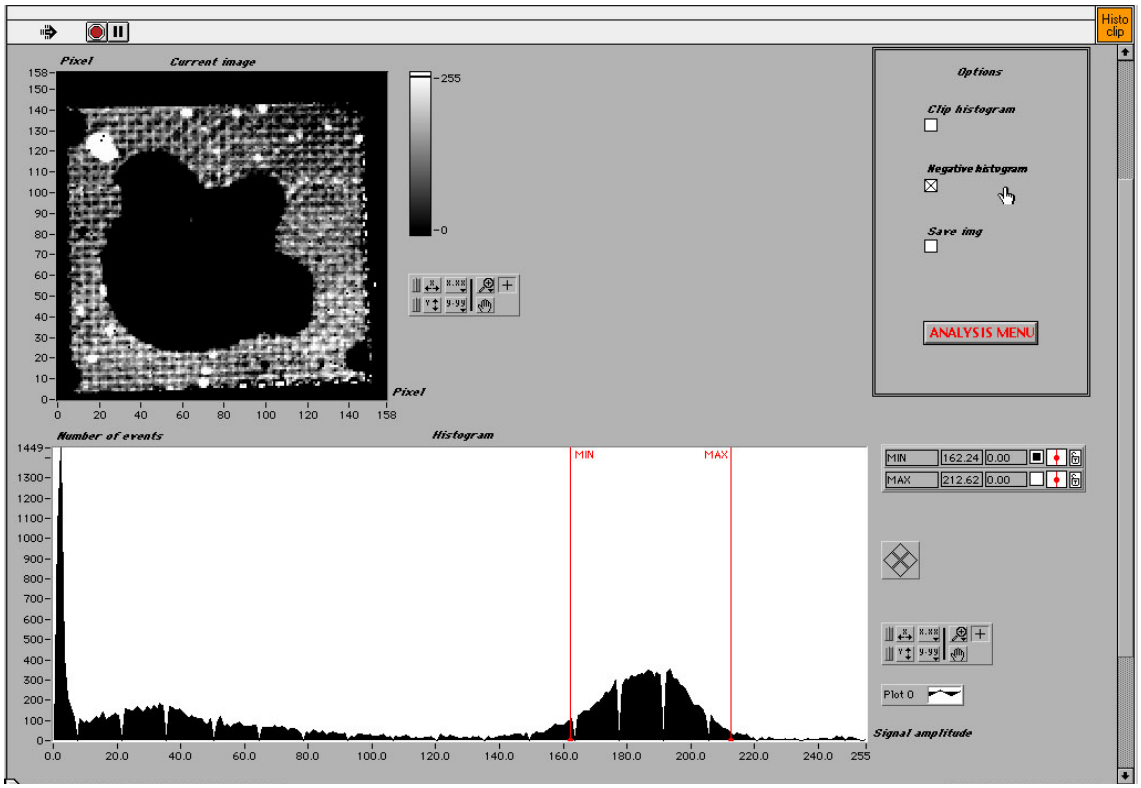

Figure II.19: Submenu “Histogram Clipping” after image processing.

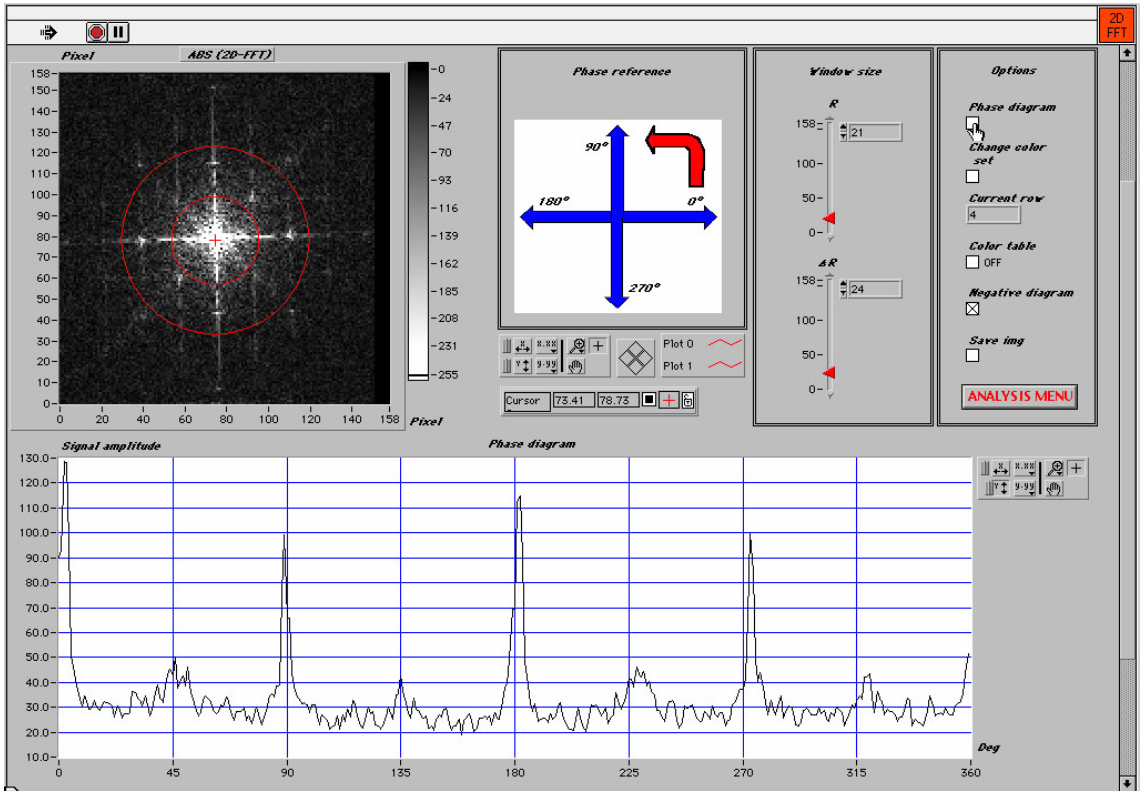

Figure II.20: Submenu “2D-FFT”.

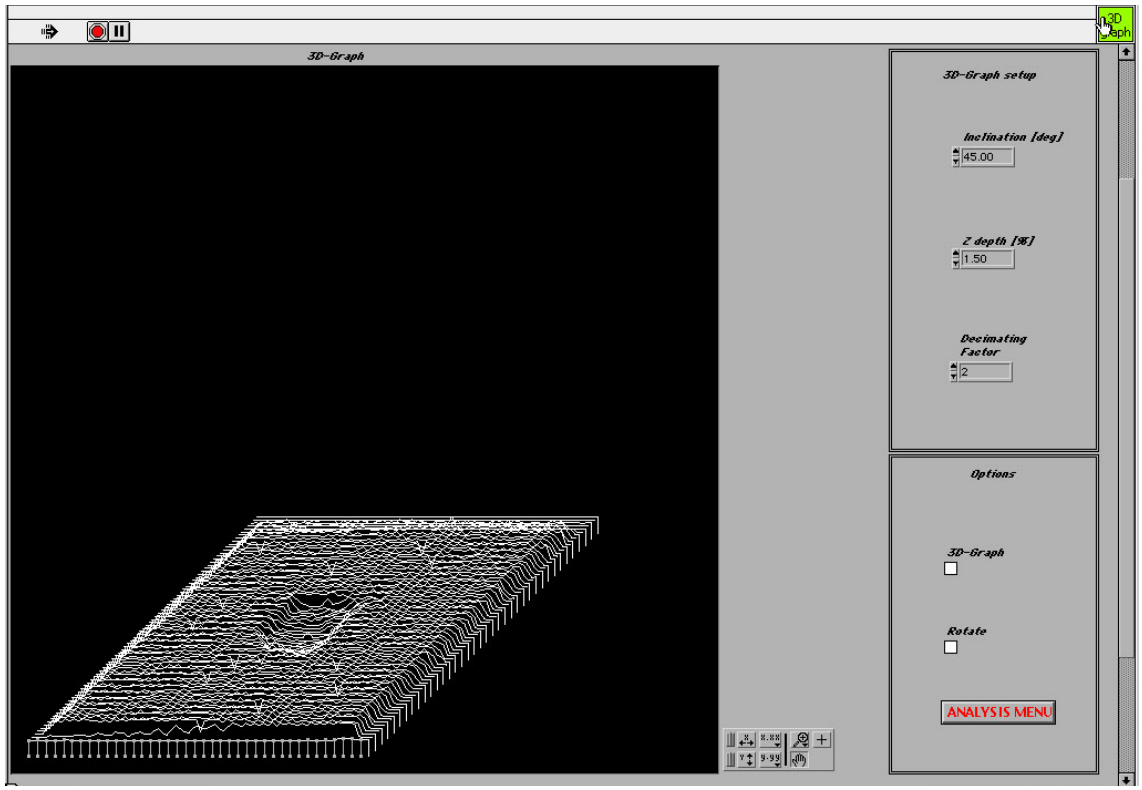

Figure II.21: Submenu “3D”.

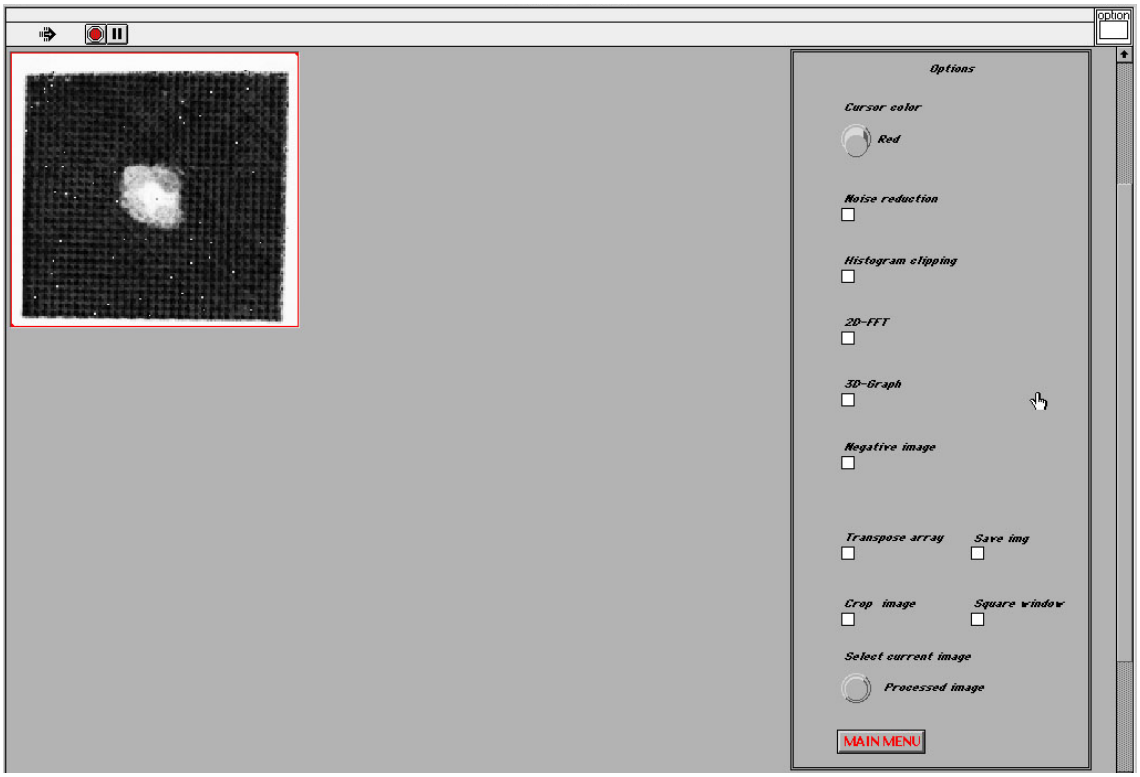

Figure II.22: Submenu “Negative Image”.

II.2.2 RoboTEST v.2.0

RoboTEST is the software package corresponding to the first UT NDE system. This is capable to command the displacement of the robotic arm Stäubli RX60 L. From the functional point of view this system is capable to acquire, save and afterwards post process the UT data. The results can appear as images in grey tones or pseudo colour representation.

One of the new UT scan capabilities introduced in v 2.0 is the adaptive scanning, which will be explained further in this chapter. This type of scanning is a 3D complex geometry scan method completely automatic without having any type of information about the geometry.

RoboTEST v1.0 was build on IDE LabView 5.0 but some of the programming packages were rewritten in LabView 7.1, in order to have a more stable system It was as well introduced a control management system of the UT signal quality, which by means of mathematical instruments such as correlation and autocorrelation offers a higher quality of the UT images generated.

The main panel of RoboTEST v 2.0 (Figure II.23) presents all the different buttons necessary to start one of the applications such as various scan types, manual control for the robotic arm displacement and oscilloscope control, and various post processing options (2D or 3D post processing graphical modules).

This is the main window for all the applications that the system is capable to perform.

The functions presented on the main window are:

- **Adaptive Scan**: Starts the program part needed to acquire the 3D piece geometry. This is a preliminary scan and no wave is acquired;
- **Full Volume Scan**: Starts a full volume scan on the piece that has to be inspected. All wave length is acquired for each scanning point

- **Simple Scan**: Stats a FV-Scan in plane without being necessary t execute a preliminary adaptive scan
- **Manual Distance and Thickness Measurements**: Starts the application that will help us individuate in manual mode the distance and thickness
- **Robot Manual Control**: Is visualised the control panel used to move the robotic arm Stäubli RX60 L
- **Oscilloscope**: LeCroy 9400 oscilloscope panel is viewed
- **2D Image**: 2D UT signal and image post processing is launched
- **3D image e Surface Profiling**: The 3D image post processing module present also in ECUS Inspection is started up
- **Quit**: Exit from RoboTEST v2.0 program.

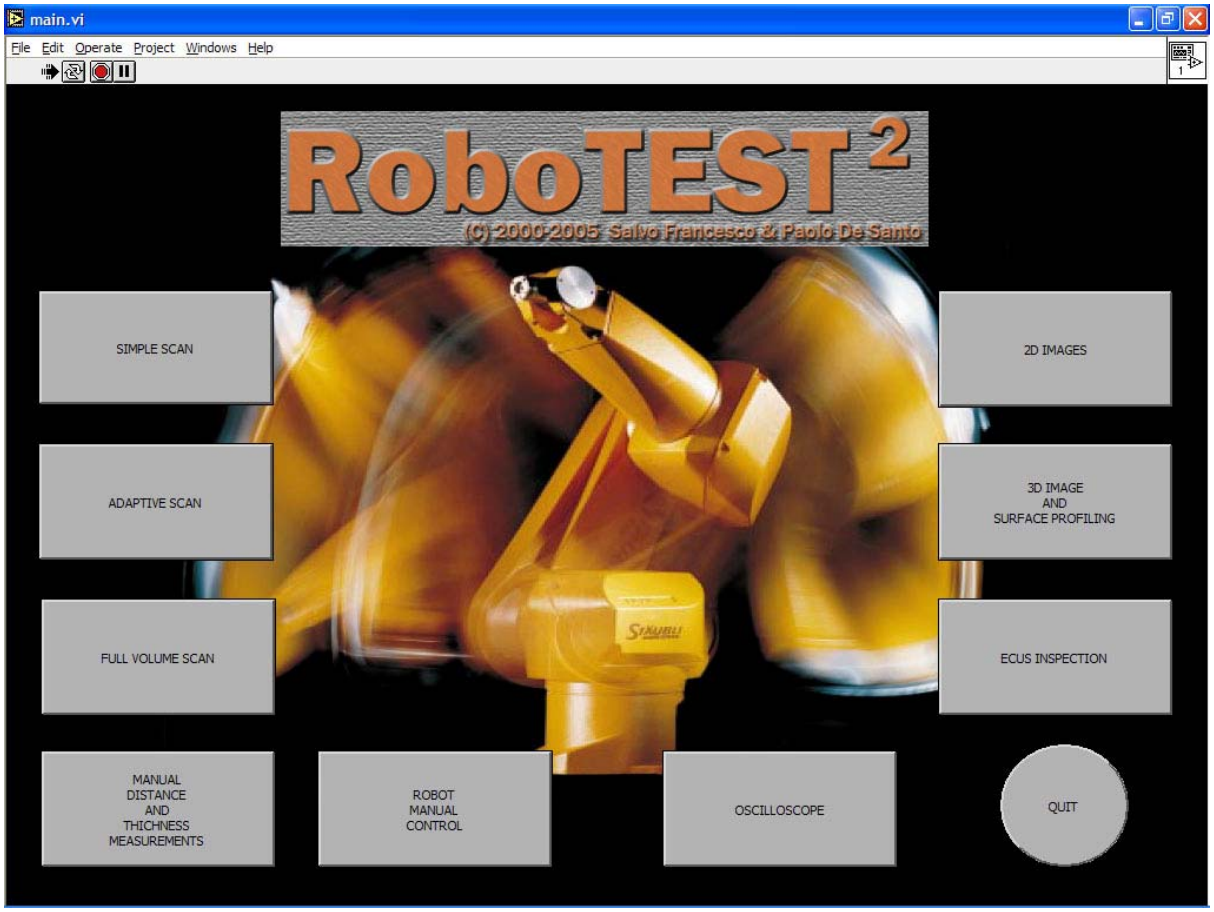

Figure II.23: Main control panel for RoboTEST v 2.0.

Setup robot RX60 L (Robot manual control)

The "SETUP ROBOT STAUBLI RX60 L" (see Figure II.24) provides to the user a series of information needed for the complete robotic arm control, and a connection to the robot controller is made each time that a parameter is changed and/or the robotic arm is moved in different positions.

All possible robotic arm settings are divided in 5 sections and will be presented in the following subparagraphs.

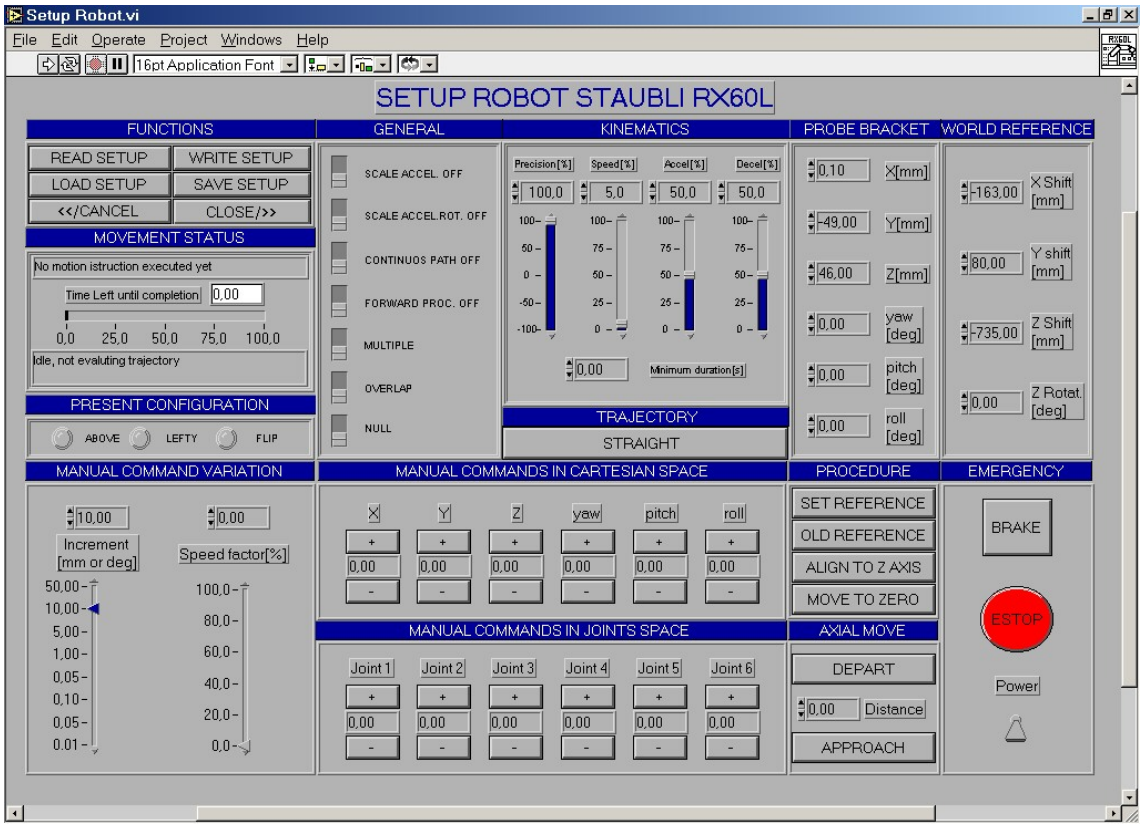

Figure II.24: Setup Robot control panel.

General settings

- **Scale Accel**.: Enable or disable the reduction of the acceleration/deceleration during the displacements and this is proportional to the imposed speed
- **Scale Accel. Rot**.: Specifies if the acceleration has to take in account the Cartesian rotations speed during the straight line scan. If is ON the minimum value between the linear and rotational speed in the Cartesian space is used in the deceleration. If OFF only the minimum linear speed is taken into account if **Scale Accel.** option is activated
- **Continuous Path**: Enable/disable Continuous Path function
- **Forward Proc**.: Enable/disable Forward Processing function
- **Multiple/Single**: enable/disable the complete pulse joint rotation. If the option is YES than the pulse joints are limited to values between [-180,180] degrees. If OFF the maximum rotation of the pulse joint is permitted
- **Overlap/No Overlap**: enable/disable pulse joint limit control. If the option is enabled each time that a multiple joint rotation is needed an error is generated. If is the disabled then no influence on the robot displacement will be noted.
- **Null/No Null**: Enable/disable the cancelling error positioning at the end of each displacement in continuous movement. When this option is enabled the system attends that all joints are positioned after a continuous displacement. This option is in direct control by the "**Precision**" option in the kinematics control settings

Kinematics setup

- **Precision**: is setting up the positioning precision of the robotic arm joints. Takes values in the interval [-100,100].Higher value of the parameter smaller the positioning error value will have
- **Speed**: is setting up the speed for the following robot arm displacements, and takes values between [0,100]. Is a Percentage representation of the maximum allowed inspection speed
- **Accel.**: is setting up the acceleration for the following displacement and takes values between [0,100]. Also is a percentage representation of the maximum allowed acceleration
- **Decell.**: is setting up the deceleration for the following displacement and takes values between [0,100]. Also is a percentage representation of the maximum allowed deceleration
- **Maximum Duration**: is setting up the minimum time for the robotic arm until the next scan point position. If is = 0 no time consideration between movements will be taken in consideration

Probe Bracket Parameters

The parameters X, Y, Z, yaw, pitch and roll are defining a robot internal transformation that specifies the positioning and the internal orientations of the UT probe regarding the tool reference system (TRS).
In our case we have translated the TRS from the center axis of the joint 6 to the center axis of Joint 1 (now the UT probe axis is identical with the robot arm Z axis) (see Figure II.25)

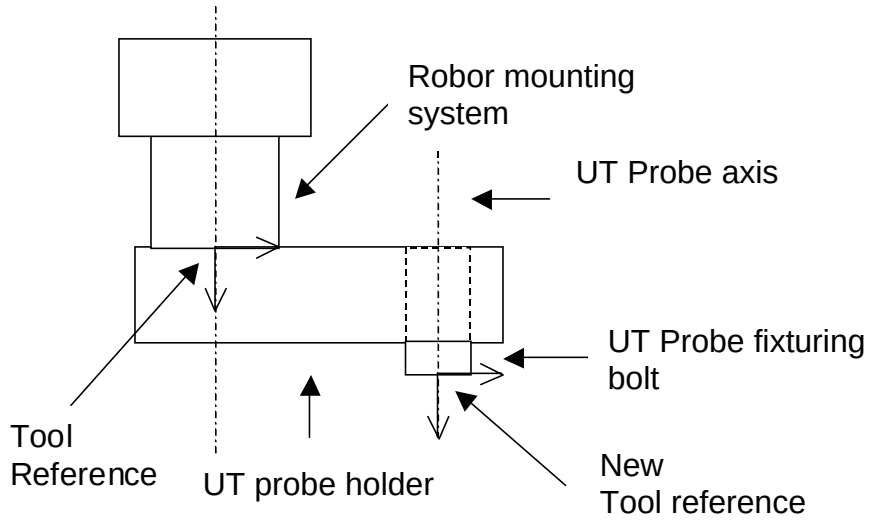

Figure II.25: UT probe bracket.

The offset parameters are given by the different UT probe geometry when the focal distance and the UT probe diameter are the main requested parameters as inputs.

World Reference System (WRS)

The robot arm world reference system id fixed in the working space in order that X-Y plane is parallel to the mounting robot surface, and the X axis is given by an angle made by Joint 1 equal to zero and that the Z axis coincides with the joint 1 rotational axis.

The robot origin is at the intersection between the intersection point of the joint 1 and joint 2.

This parameters block consents the robotic WRS translation and rotation in different points of the working space (except for the 15° angle of joint 1 representing the no movement area due to the different cable connector to the controller and UT instruments).

- **X_shift**: describes the X component real value that describes the x axis position in a certain point in the working area. This is the new x axis value for the world coordinate system
- **Y_shift**: same description as X_shift but for Y axis
- **Z_shift**: same description as X_shift but for Z axis
- **Z_Rotation**: same description as X_shift but for rotation around Z axis

This system transformation has no influence on the system default reference system and on the space defined joint positioning.

Trajectory

If the trajectory switch is straight permits only straight displacements. If switch position is Interpolate than interpolate displacement in the joint working area will b obtained.

In the first case the straight displacements are assured and the final displacement of the UT probe is straight. The UT probe will be rotated at the end of the movement in order to keep the imaginary straight line.

In the opposite case the final movement is calculated using the initial joint and final joint positioning and in this case no trajectory control will be available due to the arc type movement that the robotic arm will try to follow.

Manual Controls

The manual controls are described in this subparagraph and are necessary to configure the robot before the scan start.

Manual command variation:

- **Increment**: Is setting the displacement increment in manual mode in the Cartesian space. With the cursor we can chose between 0.01 and 50 mm or 0.01 and 50 degrees displacement values depending on the operation needed (translation or rotation)
- **Speed factor**: Is setting the joints speed reduction factor previously setup in kinematics tab.

Manual Controls in Cartesian space

In this control tab it is possible to observe a numerous buttons that are permitting us to follow different displacements (increasing/decreasing value) for each single parameter such as X direction, Y direction, Z direction translations and Yaw, Pitch and Roll

rotations. The coordinates presented in the window are the ones referring to the last tool reference system. By pushing "+" or "-" buttons we will obtain and increase or a decrease of the values, and the increasing step is given by the Increment manual control setting (0.01 and 50 mm / 0.01 and 50 degrees)

Manual commands in joint working space

The buttons in this tab are permitting the single joint rotation. By pushing "+" or "-" buttons we will obtain and increase or a decrease of the values, and the increasing step is given by the Increment manual control setting (0.01 and 50 mm / 0.01 and 50 degrees). The speed factor is determining the maximum joint displacement speed. No change occurs if we go and change the manual control values in the Cartesian working space.

The axial movements are **Approach** and **Depart**. When one of this buttons is pushed then the UT probe will follow and approach/depart on the individuated trajectory at a distance that was already setup in the increment manual control setting (0.01 and 50 mm / 0.01 and 50 degrees).

Procedure

- **Set reference**: By activating this control the global reference system is translated in the actual UT probe position, and the WRS vlues are automatically brought to zero
- **Old Reference**: will move the robotic arm (with the speed value setup previously) to the last global reference system. **ATTENTION** should be made in this case (if the last global reference system was lower than the upper inspected part then the UT probe will hit the piece and both could present damages)
- **Align to Z axis**: Will align the probe bracket axis to Z = 0 axis and will bring the Yaw, roll and Pith parameters to zero
- **Move to zero**: Will bring the UT probe extremity to zero by maintaining the last reference system, but with the actual orientation.

Emergency

These sets of command are to be used only in case of emergency only, or if the command sets send to the robotic arm are wrong. In order to have this command sets available "FORWARD PROC." Option in general tab has to be enabled.

- **Brake**: Causes the immediately stop of the current displacement.
- **E-stop**: This command causes the immediately stop of the system and also will cut-off the power supply to the robotic arm
- **Power**: Visualise the state of the power supply button of the robot controller. For safety measures this button is not available to be used directly from the RoboTEST. The switching ON/OFF of the power supply to the controller has to be.

Robot status

On this window the status and the robot configuration is visualized and updated in real-time.

Movement Status presents the next options on the displacement movement:

- **Error**: indicates the status of the displacement execution.

- **Time left until completion**: is an ETF – estimate time to finish that indicates in real-time the number of seconds until the finish of the scanning process. Null value is equal to no displacement is available
- **Motion complete**: indicates the percentage of the completed UT scan process. 100% indicates that the Motion is complete (UT scan completed).
- **Motion segment**: present information about the status of the actual motion path.

Present configuration is a collection of indicators which are permitting to verify the actual geometrical configuration of the robotic arm.

However, in order to obtain better work conditions for the assign UT scan is better to follow a better configuration of the robotic arm. The robotic arm can change the configuration only through manual commands or through the Joystick control.. The next options are available:

- **Above/Below**: is the information about the position of the Elbow (Joint 3) above or below the shoulder arm. This configuration can be changed by moving the Joints 2 and 3
- **Lefty/Rightly**: is the information about the way that the robot arm is configured as a left hand or right hand use. This configuration can be change from the joint 1 and 2
- **Flip/NoFlip**: is the information about the Joint 5 position positive angle (NoFlip) negative angle (FLIP)

Functions

- **Read setup**: updates setup parameters viewed in the current robot arm settings
- **Write setup**: transfer the setup parameters from PC to robot controller
- **Save setup**: is saving the setup parameters to a file on the local PC HDD. The file created is *.RCF type
- **Load setup**: is loading a previously saved setup parameters file from the local HDD
- **<< /Cancel**: returns to the previous tab (window) or cancels the different changes made
- **Close/ >>**: passes to the next tab (window) and confirms the changes made in the current tab

Oscilloscope setup

This window presents the LeCroy 9400 virtual oscilloscope (Figure II.26), which is capable to remote control the real LeCroy 9400 oscilloscope.

In our case all the available function on the real instrument were perfectly reconstructed in LabView and in this case we will explain briefly the use of the oscilloscope. For more information please refer to the user LeCroy 9400 Manual.

With this virtual oscilloscope we are able to read the existing setup on the LeCroy 9400 "**Acquire**". In this case all the settings in the window will be changed in automatic. In the case that we have made different changes to the Time/Division, Trigger, Vertical 1 and 2 tabs we can either save the configuration file "**Save setup**" to the local HDD in *.OSS file type, either load the configuration "**Load setup**". In the case that for our

interest is the single wave (A-Scan) we can "**Save wave**" in ASCII file type. This file can be afterwards open with a normal text editor or by a spreadsheet based programm.

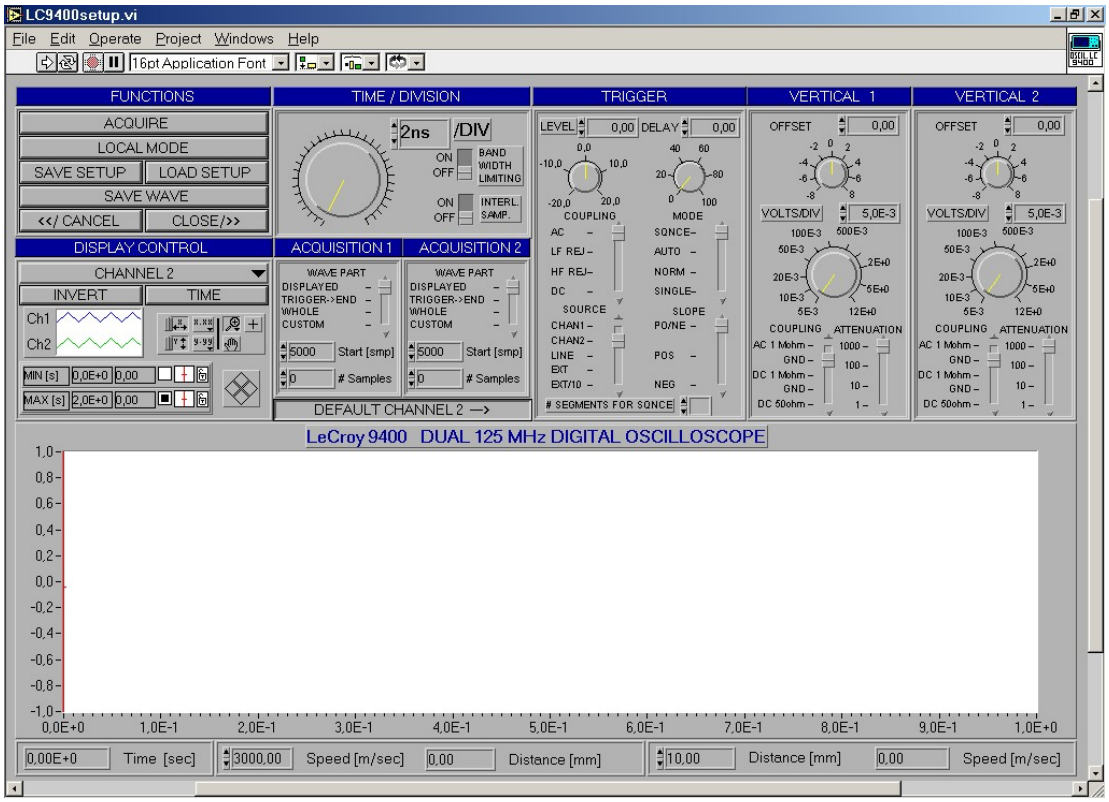

Figure II.26: Oscilloscope setup tab.

The channel used for the wave and oscilloscope setup is Channel 2. The software has the capability to acquire waves and different setup for each channel at the same moment.

On the visualised wave we are able to carry ultrasonic speed test and thickness measurement test. The obtained results will are presented on the bottom level of the window.

Adaptive scan

The adaptive scan procedure is completely automatic and consents to sample the surface of the piece to be inspected in order to create a geometrical base needed for the final and complete FV-Scan procedure. In Figure III.28 the Adaptive scan setup window is reported.

The main request data refers to the Probe characteristics "**Probe data**". In this tab we will insert the **focal distance** of the UT probe the **effective length** in order to define the exact position of the focused UT signal. The adaptive scan can be done following three surface types of scans: **Cartesian coordinates, Cylindrical coordinates, Spherical coordinates**.

It is very important to indicate the main scanning direction, the number of steps and the distance between two steps. To start the adaptive scan it is necessary to push "**Start scan**". Will be then reported the robot arm setup tab. When all the robot arm parameters were verified and the new coordinate system was setup we will pass to the

oscilloscope window. Once all the parameters were setup and the reference wave was visualised we can pass to the last tab, where we will be required to save the file.

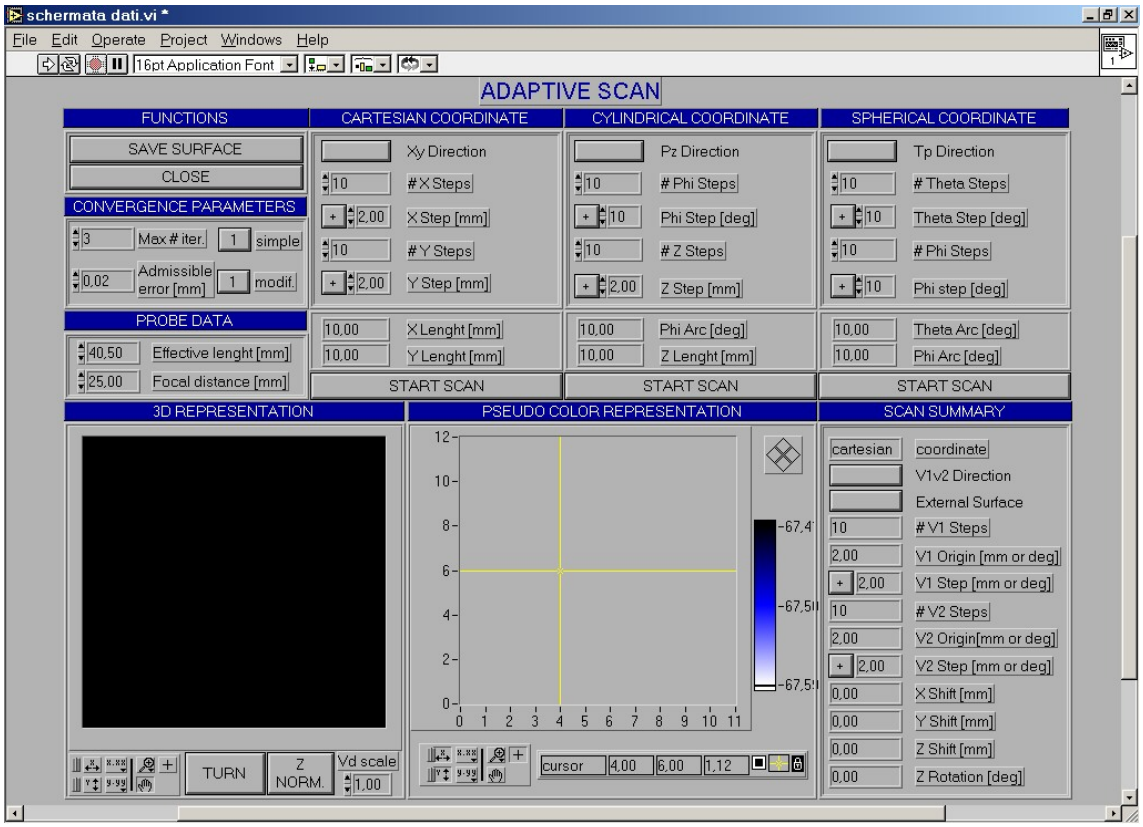

Figure II.28: Adaptive scan parameter setup.

During the adaptive scan the tab reported in Figure II.29 is viewed. The following sets of information are reported:

- **Base domain**: previews the robot arm movements in surface base domain
- **Scan monitor**: is a graphical representation of the iteration number realised and the measurement errors corresponding for each acquired point
- **Scan Status**: presents in real time the actual position of the robot, the total number of points and the number of the acquired points in percentage
- **Maximum correlation**: reports in a 2D graphic the distance between each acquired point and the base domain. Also the reference signal is presented
- **Scan summary**: is resuming all principal scan parameters.

From the reported graphics and by direct view on the robot movements can be evaluated the validity of the adaptive scan in progress. If errors are encountered from the joystick control we will have to push "**DIS PWR**" and the robotic arm power supply will be cut-off.

The results of the adaptive scan are reported as graphics:

- pseudo colour representation
- 3D representation

- Data format containing the summary of all scan parameters

In order to use this adaptive scan in a second moment "**Save surface**" button must be pushed. The surface file is an ASCII file type that can be opened by a normal text editor.

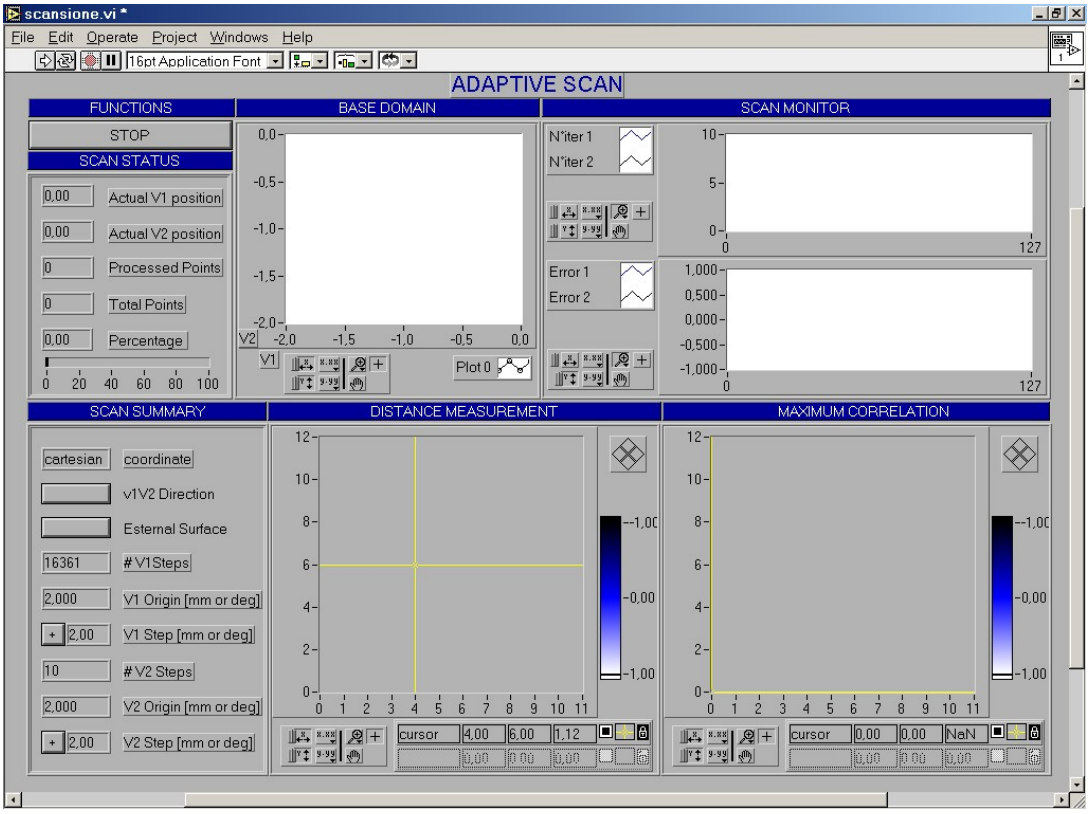

Figure II.29: Adaptive scan window during the scan.

Full Volume scan

The Full Volume scan procedure is made from two parts one is the retrieve of the surface geometry from the adaptive scan, previously saved, and on this base but with smaller scan steps then the second part, consisting in a complete UT scan, will be carried. In Figure III.28 the Full Volume scan setup window is reported.

As for the case of the adaptive scan the main request data refers to the Probe characteristics "**Probe data**". In this tab we will insert the **focal distance** of the UT probe the **effective length** in order to define the exact position of the focused UT signal. The adaptive scan can be done following three surface types of scans: **Cartesian coordinates, Cylindrical coordinates, Spherical coordinates**.

It is very important to indicate the main scanning direction, the number of steps and the distance between two steps. To start the adaptive scan it is necessary to push "**Start scan**". Will be then reported the robot arm setup tab.

It is recommended that in this scan phase the speed values must be in the interval (**50-70%)**. When all the robot arm parameters were verified and the new coordinate system was setup we will pass to the oscilloscope window.

The trigger circuit parameters in this case will be:

- Trigger Sbource: EXT
- Trigger Slope: POS
- Trigger Coupling: DC

- Trigger Level: 2 Volt or any other value in order to visualise a stable signal
- Trigger Delay: 0 %
- Trigger Mode: SINGLE

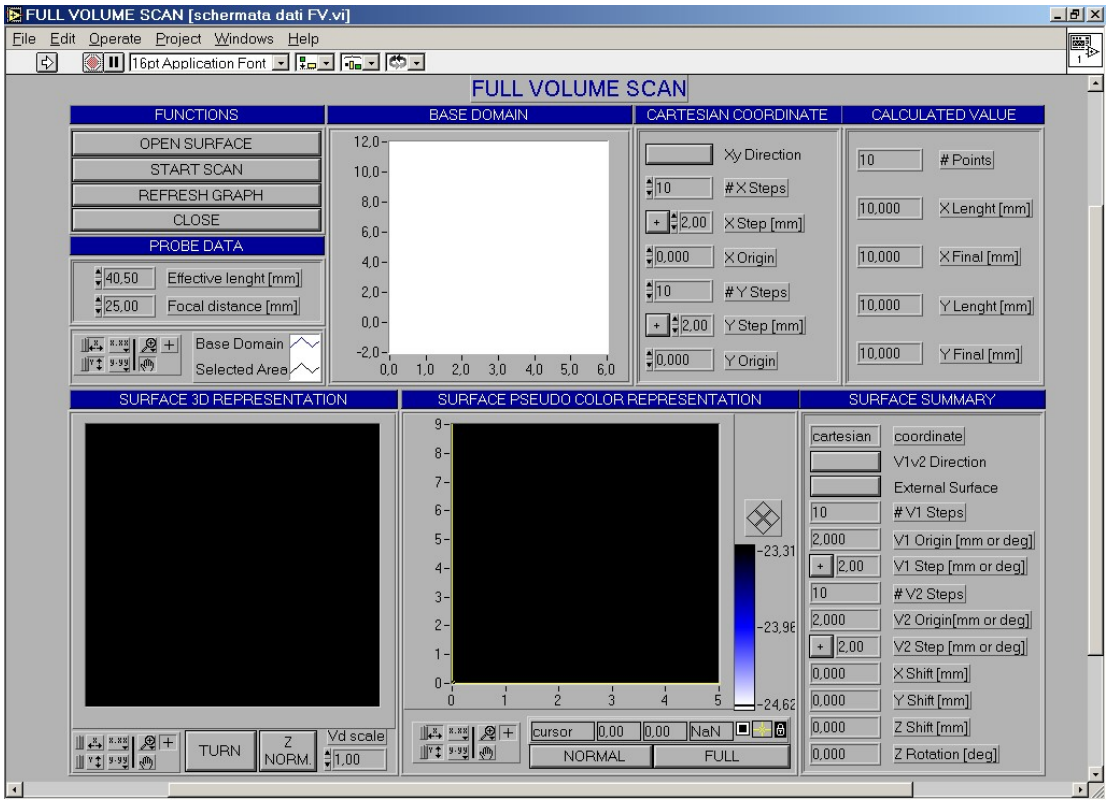

Figure II.30: Adaptive scan parameter setup.

Once all the parameters were setup and the reference wave was visualised we can pass to the last tab, where we will be required to save the file.

During the FV-scan the Figure from Figure II.31 is reported, and the following data can be observed:

- **Base domain**: previews the robot arm movements in surface base domain
- **Scan Status**: presents in real time the actual position of the robot (Actual V1 position and Actual V2position), the total number of points (Total Points and Processed points) and the state of the scan in percentage (Percentage)
- **Scan summary**: is resuming all principal scan parameters
- **Signal Acquired**: represents the Full UT wave acquired in real-time. In the graphic we can observe that on Y axis is reported the amplitude in Volts (when a maximum value is reached the Y axis scales automatically) and on x axis is reported the Time-of-Flight (TOF) where the first cursor is positioned on the main bang time interval.

From the reported graphics and by direct view on the robot movements can be evaluated the validity of the adaptive scan in progress. If errors are encountered from the joystick control we will have to push "**DIS PWR**" and the robotic arm power supply will be cut-off.

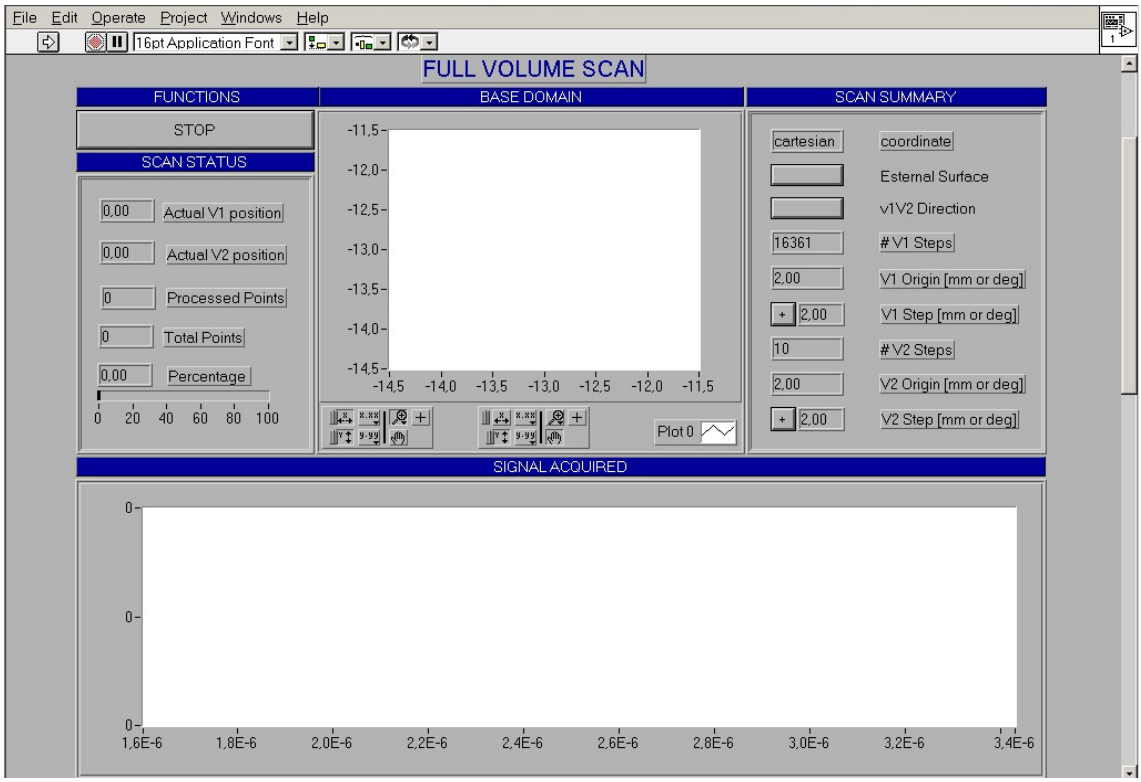

Figure II.31: Full Volume scan window during the scan

3D scan processing

In this paragraph the processing of the 3D scan will be carried out. The bi-dimensional UT waves are integrated with the relative information of the UT probe positioning for each scanning point. In this case cloud points will be obtained, and frontal and back surfaces will describe the piece in a 3D space. It is possible also to obtain 4D representations by introducing one of sensors indirect information (such as time-of-flight, thickness measurement). The images are presented in 3D shape, wireframes, pseudo colour representation, profile and prospect.

The Figure II.32 presents the main window of a 3D signal processing.

In order to obtain the graphical results we have to load either the front or back surface. Then the "**Open data file**" button will be pressed, and the data of the Full Volume scan file will be loaded. The second step is the load of the surface file, and this is made through the "**Open surface**" and we will have to open the *.SFM file.

We will obtain than the scan parameters and the information regarding the adaptive scan cloud of points.

Once finished the load of the two surfaces the image reported in Figure II.33 is viewed.

The results of the 3D signal data processing can be saved as ASCII file, where we will have the information in a 3 column format. Also 4D scan parameters can be obtained by selecting the needed 4^{th} direction to be included (TOF measurement or thickness measurement).

The results can also be saved in AutoCAD script file. The file extension is SCR type and can be viewed in AutoCAD by running the command "**RUNSCRIPT**"

In order to close the file processing is enough to push "**Close**" Button. Then we will be back to the main menu of the RoboTEST v 2.0 menu.

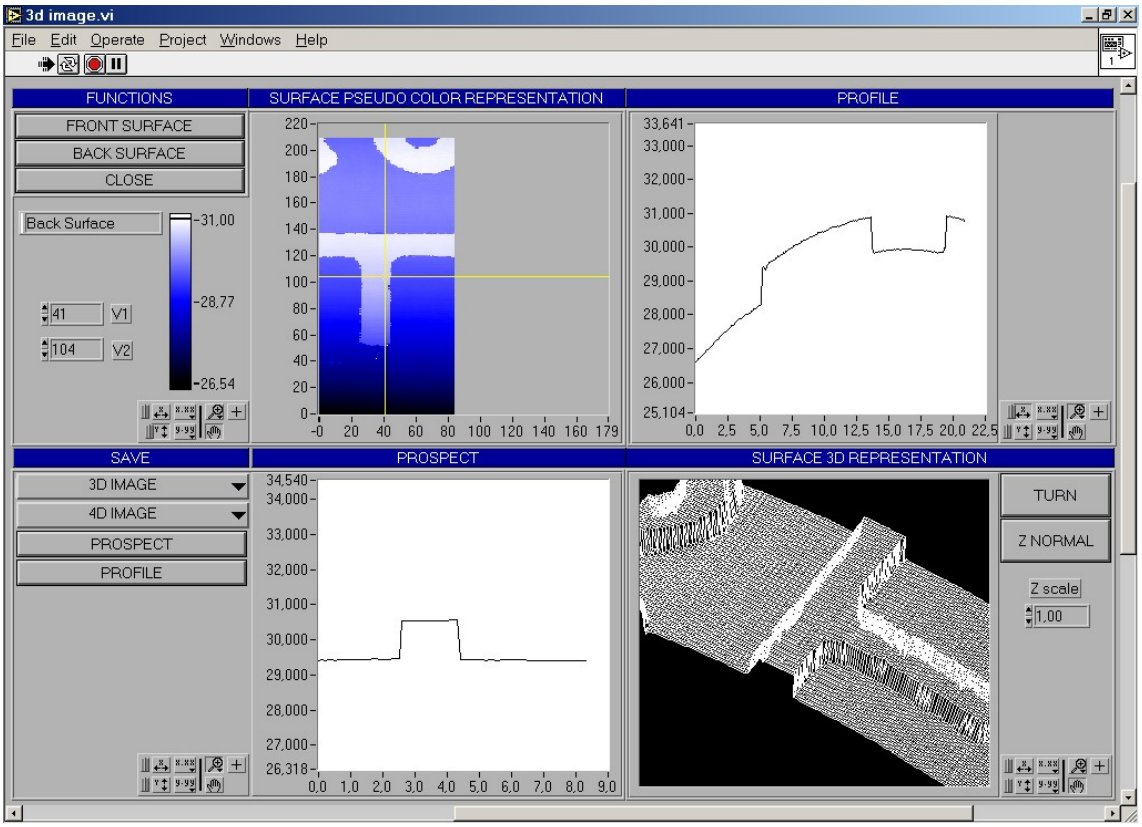

Figure II.32: 3D processing data.

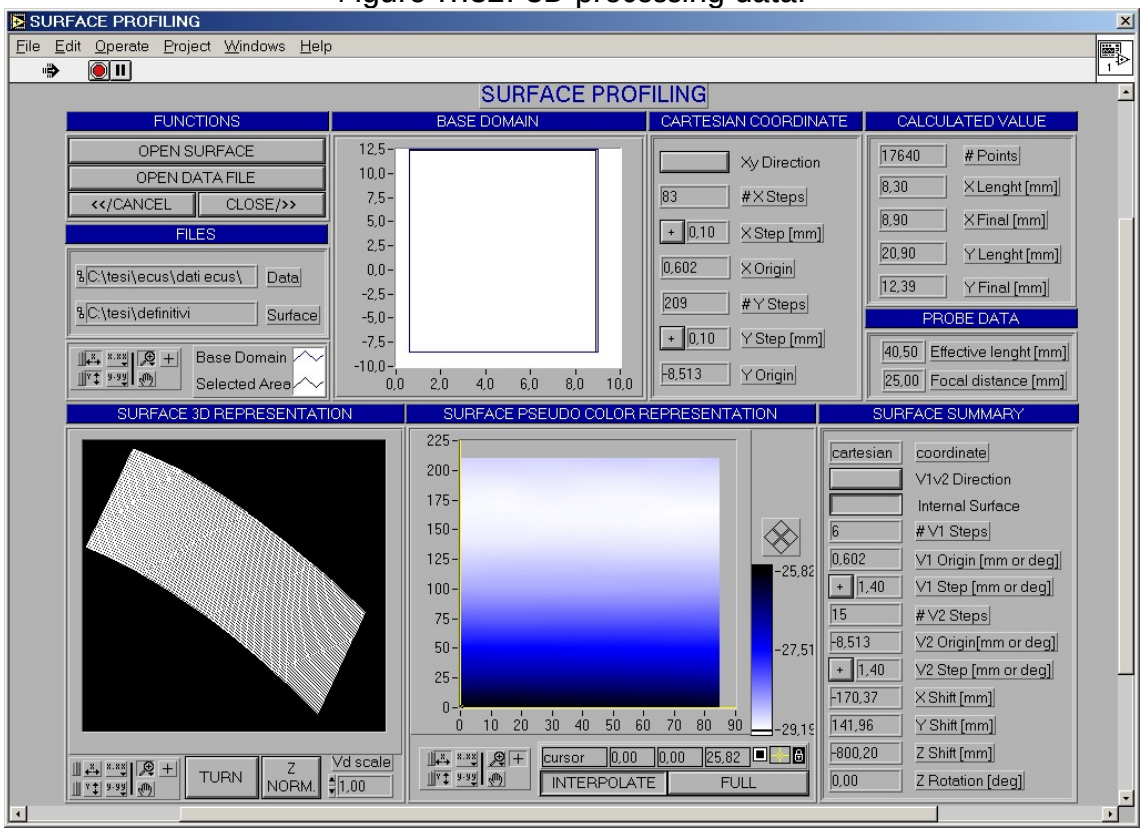

Figure II.33: Data selection files and surface profiling.

II.2.3 Ad-Hoc software – plug-in

The ad-hoc software packages, with difference regarding the two suite previously introduced, are the instruments dedicated to the execution of particular functions; they can be defined like multifunction software plug-in.

The fact that are separated from the two suites is due to their recent realisation, and for that it was considered opportune to run them separated from the main program and at the end of their stability test period will be inserted between the principal functions

The particularity of the first plug-in was to introduce different filters for image enhancement and reverse engineering functions such as complex 3D geometrical profiles.

UT scan viewer

The first plug-in presented, called UT SCAN VIEWER (see Figure II.34) has the capability to read from both UT scan suites (ECUS Inspection and RoboTEST). Moreover, a navigation drag and drop and real-time pseudo colour image representation for the considered time gate setup on the UT signal window was introduced.

This plug-in presents even real-time image and signal enhancement which renders better visible the UT control. This plug-in automatically calculates the reference signal for the correlation between the acquired UT waves.

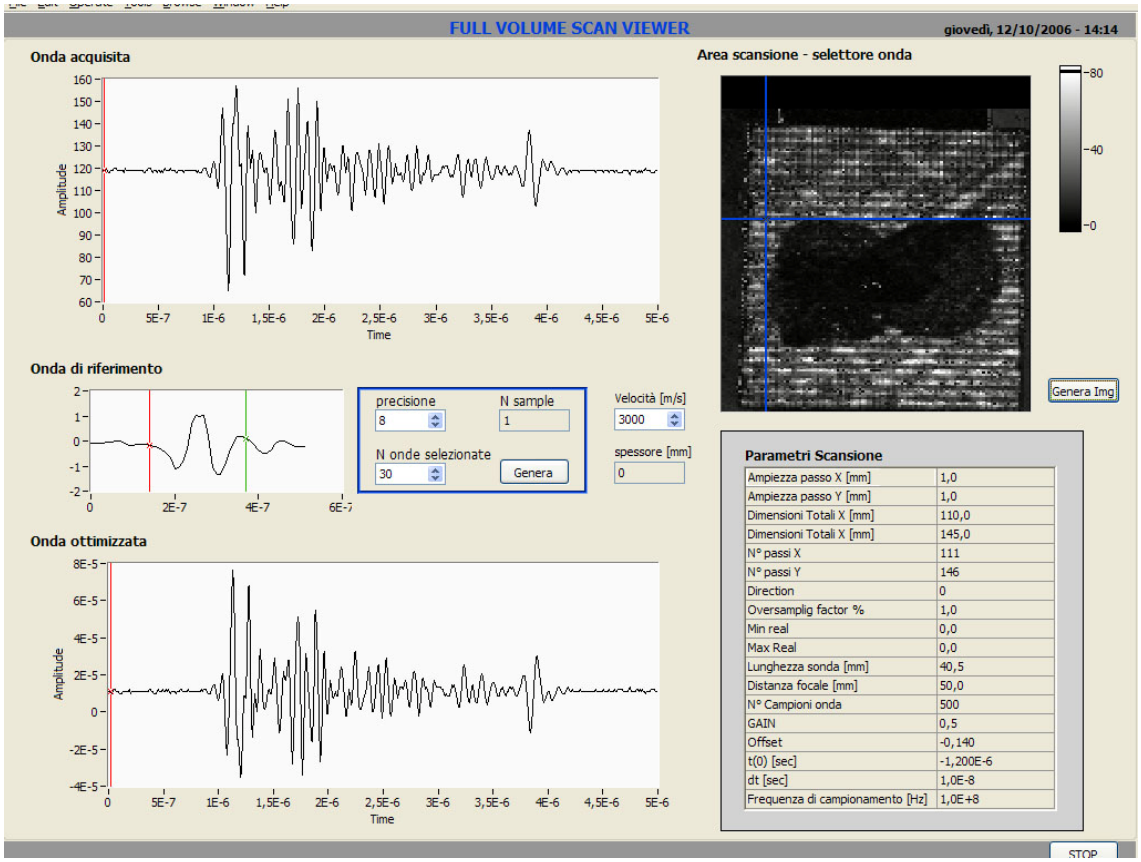

Figure II.34: UT scan viewer plug-in menu.

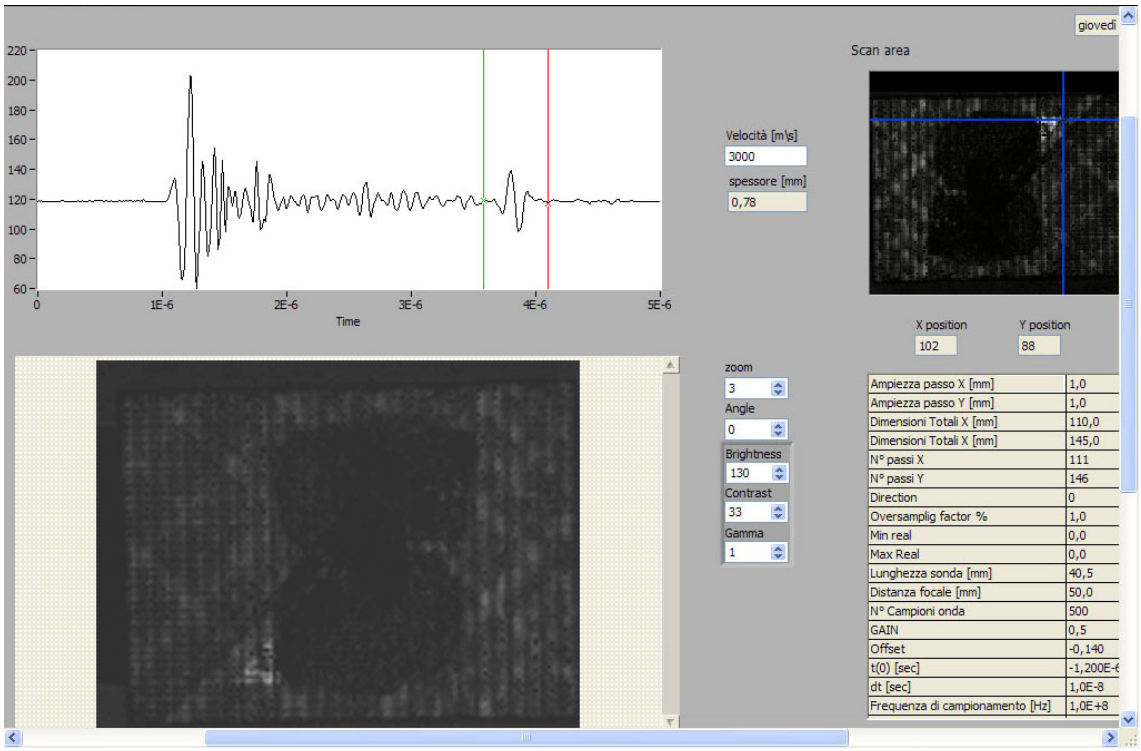

Figure II.35: Image enhacement option.

3D complex geometry profiler

This second plug-in was build in order to obtain different profiles of complex 3D geometries (Figure II.36) on a section plane chose by the user. This is a good example of Reverse Engineering. The software has also the possibility to retrieve wall thickness, just by choosing with the cursor the section of interest. This software presents even a 3D graphical processing engine, which permits the reconstruction in space of the external object complex surface.

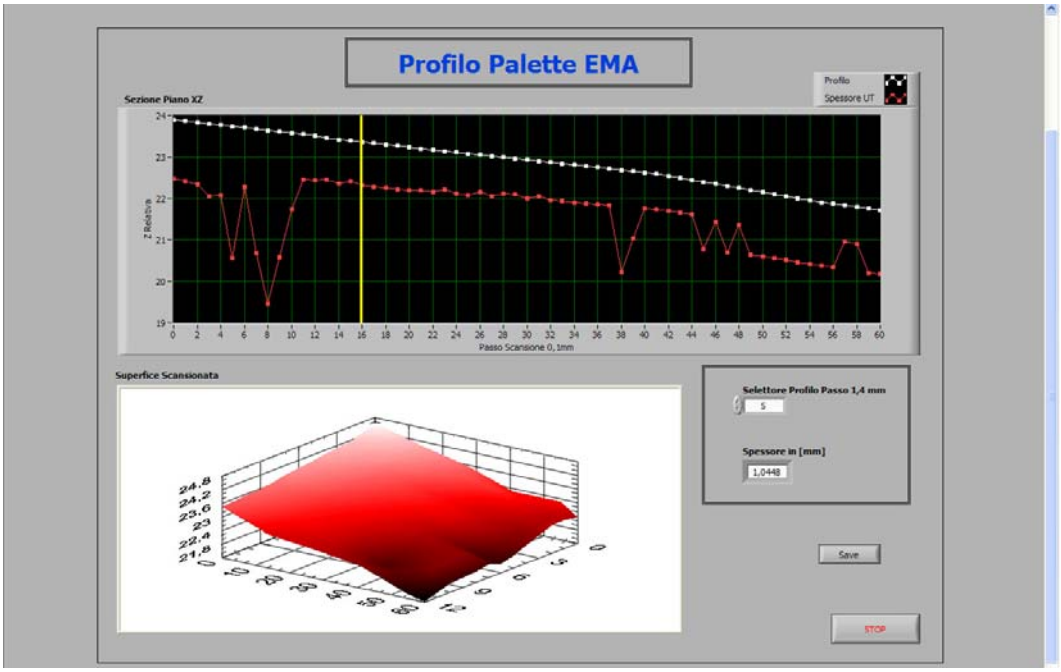

Figure II.36: *3D complex geometry profiler*.

Chapter III

Experimental Ultrasonic Nondestructive Evaluations

III.1. Introduction

In this chapter, the main applications of the Ultrasonic Nondestructive Evaluation Systems, presented in the previous chapters, are reported.

The applications can be divided in different categories, such as:

- ✓ Composite materials testing:
  - ➢ Carbon Fiber Reinforced Plastics (CFRP) Laminates
  - ➢ Non Crimp Fabric (NCF) Laminates
  - ➢ Glass Fiber Reinforced Polymer (GFRP) bonding
- ✓ Brazed assemblies inspection:
  - ➢ Insulated Gate Bipolar Transistor (IGBT) assembly device
  - ➢ Experimental Heat Pipe Prototype for IGBT Applications
  - ➢ Copper 99.99% brazed assembly
- ✓ UT based Reverse Engineering
  - ➢ Turbine blade geometrical characterization

III.2. Carbon fiber reinforced plastics (CFRP) laminates NDE

III.2.1 Introduction

Ultrasonic (UT) non-destructive inspection (NDI) is an effective method for material structure characterization and defect identification, useful to both verify material conditions before destructive testing procedures and evaluate products, either before or during service, in a non-destructive manner. UT control is applicable to different materials such as metals, plastics and composites; in this work, advanced methodologies to obtain, interpret, and display UT NDI metrological results from carbon fibre reinforced plastic (CFRP) composites are presented.

Defects and structural properties of composites that can be characterized through UT NDI include delamination, cracks, porosity, resin rich areas, thickness variations, fibre orientations and elastic properties. To carry out an UT NDI material evaluation procedure, acoustic energy with UT frequency must be generated by an UT sensor and introduced into the material through a coupling medium (water grease, etc.).

The UT waveform enters the material without damaging it and all defects or discontinuities capable to generate reflections of the UT waveform can be detected and analysed.

The minimum detectable defect transverse size is $\lambda/4$, where λ is UT wavelength. Such discontinuities reflect the UT beam according to acoustic laws and can be detected by an appropriate transmitter/receiver UT sensor.

This research work refers a nondestructive evaluation (NDE) of carbon fibre reinforced plastics (CFRP) subjected to low-velocity and high-velocity impact damaging.

The NDE is used to individualize and measure an eventual existence of defects inside the material without damaging the structure and the characteristics of the samples under examination. As we stated in previous chapters, NDE is a procedure capable of individualizing defects, imperfections, and discontinuities or, generally, characteristics non-specified, without damaging the material.

An UT exam measures the energy variation of a mechanical wave, generated by a piezoelectric transducer with frequencies between 500 KHz and 25 MHz, immersed in the material through a coupling medium (water). The energy variations are used to individualize defects inside the material, i.e. find discontinuities on the ultrasonic path.

The scope of this work is the identification of a correlation between impact damage characteristics (damage type, extension, and energy) and the materials mechanical properties. The total damage area of each specimen was calculated after an ultrasonic inspection and, afterwards, a study has been made trying to conclude about the influence of the impact velocity and the support diameter on the amount of delaminated area.

In any case, there are lots of other aspects that must be studied, such as the penetrator diameter, the specimen thickness, etc.

III.2.2 Materials

The laminates used on this work had a $[(0,90)_n/+45_n/-45_n]_s$ stacking sequence, with n = 1 to 4. The round brackets in the lamination sequence indicate plain wave fabric laminate, made of T400 fibres (see Table III.1) and HMF 934 epoxy resin, fabricated by hand lay-up and autoclave cured at 177ºC under 0.7MPa pressure. The remaining layers were made of the same fibre and resin system under form of tape. The nominal thickness of the cured plates was 0.95, 1.90, 2.85 and 3.80 mm for n = 1 to 4, respectively, and the fibre content by volume $V_f \cong 0.60$.

Table III.1
Fibre mechanical properties

Fibre type	σ_R [MPa]	E [GPa]	% Of rupture	Density [Kg/dm^3]
T400	4.5	254	1.8	1.8

From the panels, a diamond saw cut square plates of 70mm in side. The 140x140 mm^2 panels have been fabricated under specials conditions.

III.2.3 Impact tests

Two variables were studied: the impact velocity (static tests and dynamic tests) and the tip diameter ($D_t = 50\ mm$ and $D_t = 100\ mm$). After the impact tests the prove damage was evaluated by an ultrasonic analysis.

Static tests

The mechanical tests were carried out by supporting the composites laminates on a steel plate having a circular opening, and statically loading them at the centre with a hemispherical steel tip. Two support diameters, i.e. $D_t = 50\ mm$ and $D_t = 100\ mm$ (see Figure III.1), and a 12.7mm tip diameter were used (see Figure III.2).

Figure III.1: The two support diameters used (100mm and 50mm).

The tests were performed on an Instron 1251 servo-hydraulic testing machine (Figure III.3) in the stroke control, at a displacement rate v = 5 mm/min. The deflection was evaluated by the stroke position. Some tests were stopped when sudden load drops, clearly indicating significant damage development in the specimen, were observed. Other tests were interrupted at predetermined load levels, suitable to avoid evident damage. On Table III.2, we may see all the impact conditions of the different samples.

Table III.2
Low-velocity impact damage conditions

Name of sample	Test modality	Thickness (mm)	Impactor diameter (mm)	Impact Energy (J)
G3 mm	Posit. Cont. 3 mm	3	12.7	7.7
G5 mm	Posit. Cont. 7.5 mm	3	12.7	25.87
H2,5 mm	Posit. Cont. 2.5 mm	3	12.7	4.93
H5 mm	Posit. Cont. 7.5 mm	3	12.7	26.22
I1 mm	Posit. Cont. 1 mm	3	12.7	1.11
I1,6 mm	Posit. Cont. 1.6 mm	3	12.7	2.15
I2,5 mm	Posit. Cont. 2.5 mm	3	12.7	4.90
I3 mm	Posit. Cont. 3 mm	3	12.7	7.84

Figure III.2: Impactors and respective support

Figure III.3: Instron 1251 servo-hydraulic testing machine

Dynamic tests

Impacts have been performed with a CEAST Fractovis MK4 falling weight machine (see Figure III.4), with a hemispherical steel head tip of 12.7mm and 19.8mm diameter. All the impacts have been performed with two different masses: 1.035kg and 10.455kg.

Figure III.4: CEAST Fractovis MK4 falling weight machine

For this machine, instrumented impactors are available which allow recording the load level acting on the impactor during the contact. Using suitable software, the instant exchange energy can be calculated as well. The energy yielded from the dart to the impacted specimen is absorbed as follow: part as stored elastic, part as plastic deformation, and part as crack propagation energy. The use of an instrumented impactor allows the evaluation of the overall energy, as well as the elastic energy returned back to the dart after the impact. On the Tables III.3 and III.4, are shown the conditions of the impact damages, respectively with support diameter of 50 mm and 100 mm.

Table III.3
High-velocity impact damages with a 50mm support diameter

Name of sample	Thickness (mm)	Dropping mass height (mm)	Impactor mass (Kg)	Impact Energy (J)
Ind3h5	3	50	1.035	0.52
Ind3h10	3	100	1.035	1.03
Ind3h20	3	200	1.035	2.04
Ind3h30	3	300	1.035	3.06
Ind3h40	3	400	1.035	4.08
Ind3h50	3	500	1.035	5.10
Ind3h60	3	600	1.035	6.12
Ind3h70	3	700	1.035	7.13
Ds5H10	3	100	10.455	10.64
Ds5H16	3	160	10.455	16.90
Ds5H24	3	240	10.455	25.26
Ds5H34	3	340	10.455	35.72
Ds5H44	3	440	10.455	46.23

Table III.4
High-velocity impact damages with a 50mm support diameter

Name of sample	Thickness (mm)	Dropping mass height (mm)	Impactor mass (Kg)	Impact Energy (J)
Ds10h10	3	50	1.035	0.52
Ds10h40	3	100	1.035	1.03
Ds10h700	3	200	1.035	2.04
Ds10h1m	3	300	1.035	3.06
Ds10H21	3	400	1.035	4.08
Ds10H23	3	500	1.035	5.10
Ds10H26	3	600	1.035	6.12
Ds10H29	3	700	1.035	7.13
Ds10H10	3	100	10.455	10.64
Ds10H32	3	160	10.455	16.90
Ds10H34	3	240	10.455	25.26
Ds10H47	3	340	10.455	35.72

III.2.4 Ultrasonic NDE tests

2D UT image generation and processing

Impacted CFRP laminates were subjected to an UT NDI procedure based on volumetric scanning using the custom made software code "ECUS Inspection"©. This technique provides for the complete UT waveform detection at each material interrogation point during an X-Y scan. From the volumetric UT file obtained during the scan, images for any CFRP laminate thickness portion can be generated and analysed for impact damage evaluation.

The transducer plays a critical role in UT NDI capabilities. The four main parameters characterising UT sensors are: frequency, sensor diameter, focal length, and focal spot diameter. Accordingly, the following considerations should be taken into account in selecting a UT sensor:

- frequency ↓ with ↑ sensor diameter;
- resolution ↓ with ↓ frequency;
- signal energy ↓ with ↓ sensor diameter;
- focal spot diameter ↑ with ↑ focal length;
- resolution ↓ with ↑ focal spot diameter.

Thus, the highest sensor frequency and shortest focal length should be adopted, material attenuation and thickness permitting.

Pulse-echo immersion volumetric UT scans were carried out on 70 x 70 mm^2 CFRP laminate samples using a focused (25 mm focal length) high frequency (25 MHz) transducer in order to obtain the maximum resolution. The X-Y scan size was 55 mm x 55 mm and the scan step was set at 0.5 mm to increase the UT image resolution.

The result is bi-dimensional matrix of size (number of steps in X direction, number of steps in Y direction), containing the peak amplitude values of the gated signal segment for each material UT interrogation point. These data are mapped to form a 2D image using pseudo colours of grey tones. A 256 grey tone scale was set up by using the minimum or maximum peak amplitude value in the bi-dimensional matrix as the 0 (black) and 255 (white) values in the scale.

Using the above procedure, images for any thickness portion of the material and their examination are generated by simply positioning the gated region along the time axes of the typical UT waveform in the full volume UT database. The time axes also represent the direction of UT signal propagation in the material thickness. The time gate width determines the thickness of the portion of the material to be examined.

UT waveform retrieval

The availability of a full volume UT database makes it possible for an image utilized for non-destructive inspection to become an active interface between user and UT waveform data. Once an image is generated, a pointer device such as a mouse can be used to point and click on any specific location in the image and retrieve from the UT database the original waveform capture at that location. When the UT waveform is displayed, both time domain and frequency domain analysis can be performed.

Experimental procedure

The material under inspection is a carbon fibre reinforced epoxy composite under the form of rectangular plates 3 mm thick (Table III.5).

Pulse-echo immersion UT scans were carried out using a focused (25 mm focal length), high frequency (25 MHz) transducer thus was obtained the maximum resolution. Thirty-one samples of two different sizes (70 mm x 70 mm and 140 mm x 140 mm) were examined with full volume UT scans with two different dimensions – 75 mm x 75 mm area, in the first case, and 55 mm x 55 mm area, in the second one according to the boustrophedon[1] scheme with a 0.5 mm scan step in order to obtain detailed images, although the database size and subsequent processing time had been vast. Also the number of waves acquired was equal to 23858 in the case of the 75 mm x 75 mm laminate, respectively 12876 in the case of 50 mm x 50 mm laminates.

Table III.5
Material used, thickness and samples size

MATERIAL	THICKNESS (mm)	SIZE (mm x mm)
CFRP	3	70 x 70
CFRP	3	140 x 140

As stated before there were three main groups of samples:

- ✓ Low velocity impact damaged ones with a support diameter of 50mm (8 samples) – Table III.6, Figure III.5
- ✓ High velocity impact damaged ones with a support diameter of 50mm (13 samples) – Table III.7, Figure III.6
- ✓ High velocity impact damaged ones with a support diameter of 100mm (11 samples) – Table III.8, Figure III.7

The examination of the UT images allowed for the identification of the material damage and to a posterior delaminated area measurement.

In the following figure only some of the UT tests results will be presented, and for each sample will be selected four images capable of a good damage characterisation.

In the following paragraphs, the UT technique which may help us in a better analysis of the delaminated internal area of a composite material impacted with both, low and high, velocities will be presented.

Table III.6
Low velocity impact damaged samples with a 50 mm support diameter.

SAMPLE	SCAN SIZE	STEP	# WAVEFORMS	FILE NAME
G3mm	75 mm x 75 mm	0,5 mm	23858	G3mm.dat
G5	75 mm x 75 mm	0,5 mm	23858	G5.dat
H2,5	75 mm x 75 mm	0,5 mm	23858	H2,5.dat

[1] Boustrophedon (from the Greek βουστροφῖδον = turning like an ox while plowing): an ancient method of writing in which the lines are inscribed alternatively from right to left and from left to right.

H5	75 mm x 75 mm	0,5 mm	23858	H5.dat
I1mm	75 mm x 75 mm	0,5 mm	23858	I1mm.dat
I1,6mm	75 mm x 75 mm	0,5 mm	23858	I1,6mm.dat
I2,5mm	75 mm x 75 mm	0,5 mm	23858	I2,5mm.dat
I3mm	75 mm x 75 mm	0,5 mm	23858	I3mm.dat

Table III.7
High velocity impact damaged samples with a 50 mm support diameter.

SAMPLE	SCAN SIZE	STEP	# WAVEFORMS	FILE NAME
Ind3h5	75 mm x 75 mm	0,5 mm	23858	Ind3h5.dat
Ind3h10	75 mm x 75 mm	0,5 mm	23858	Ind3h10.dat
Ind3h20	75 mm x 75 mm	0,5 mm	23858	Ind3h20.dat
Ind3h30	75 mm x 75 mm	0,5 mm	23858	Ind3h30.dat
Ind3h40	75 mm x 75 mm	0,5 mm	23858	Ind3h40.dat
Ind3h50	75 mm x 75 mm	0,5 mm	23858	Ind3h50.dat
Ind3h60	75 mm x 75 mm	0,5 mm	23858	Ind3h60.dat
Ind3h70	75 mm x 75 mm	0,5 mm	23858	Ind3h70.dat
ds5H10	75 mm x 75 mm	0,5 mm	23858	Ds5H10.dat
ds5H16	75 mm x 75 mm	0,5 mm	23858	Ds5H16.dat
ds5H24	75 mm x 75 mm	0,5 mm	23858	Ds5H24.dat
ds5H34	75 mm x 75 mm	0,5 mm	23858	Ds5H34.dat
ds5H44	75 mm x 75 mm	0,5 mm	23858	Ds5H44.dat

Table III.8
High velocity impact damaged samples with a 100mm support diameter.

SAMPLE	SCAN SIZE	STEP	# WAVEFORMS	FILE NAME
ds10h10	55 mm x 55 mm	0,5mm	12876	Ds10h10.dat
ds10h40	55 mm x 55 mm	0,5mm	12876	Ds10h40.dat
ds10h70	55 mm x 55 mm	0,5mm	12876	Ds10h70.dat
ds10h1m	55 mm x 55 mm	0,5mm	12876	Ds10h1m.dat
ds10H21	55 mm x 55 mm	0,5mm	12876	Ds10H21.dat
ds10H23	55 mm x 55 mm	0,5mm	12876	Ds10H23.dat
ds10H26	55 mm x 55 mm	0,5mm	12876	Ds10H26.dat
ds10H29	55 mm x 55 mm	0,5mm	12876	Ds10H29.dat
ds10H32	55 mm x 55 mm	0,5mm	12876	Ds10H32.dat
ds10H34	55 mm x 55 mm	0,5mm	12876	Ds10H34.dat
ds10H47	55 mm x 55 mm	0,5mm	12876	Ds10H47.dat

Before the development of the UT NDE systems, the analysis procedure of impacted the samples was carried out through laminate destructive inspection. The method consists in laminate sample cutting in different defect sections. After, evaluation through optical microscope is carried out. Obviously, the UT technique presents us many more vantages, such as the non-obligation of destructing the specimens and giving us immediate access to the images of the internal specimen. These images are chosen by the operator (see Figure III.5, III.6 and III.7) and, with the use of this method, it is possible to choose exactly what part of the specimen we want to analyse just by conveniently setting the

time gates (as presented in Chapter II). In addition, it is possible to make the most suitable image treatment according to the relevant aspects.

A succession of impact tests with the three different conditions: low-velocity impact damaged with a 50 mm support diameter, high velocity impact damaged with a 50 mm support diameter and finally high velocity impact damaged with a 100 mm support diameter, was carried out. The impacted sample were UT inspected.

After all scans were performed, the need to measure the delaminated area was raised. This procedure is very useful because allows optimal studies with the main scope of reaching a relation between an impact energy and the consequent damage.

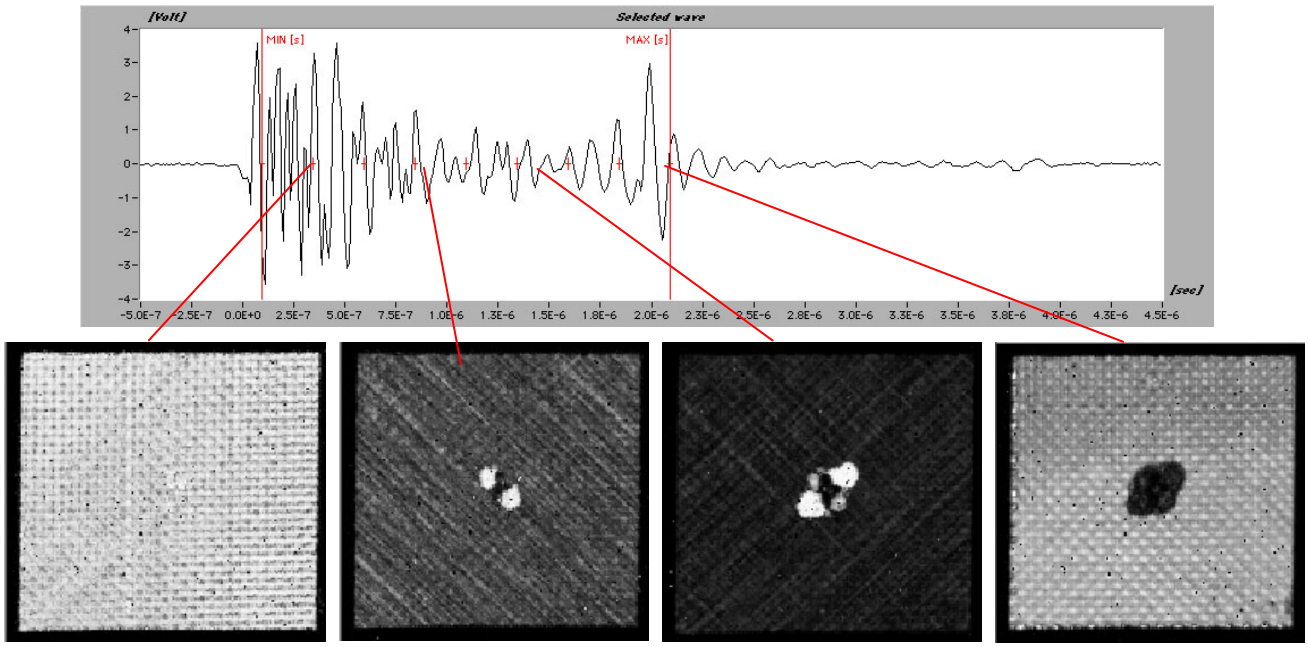

Figure III.5: Low velocity impact damages with a 50 mm support diameter (I1 mm).

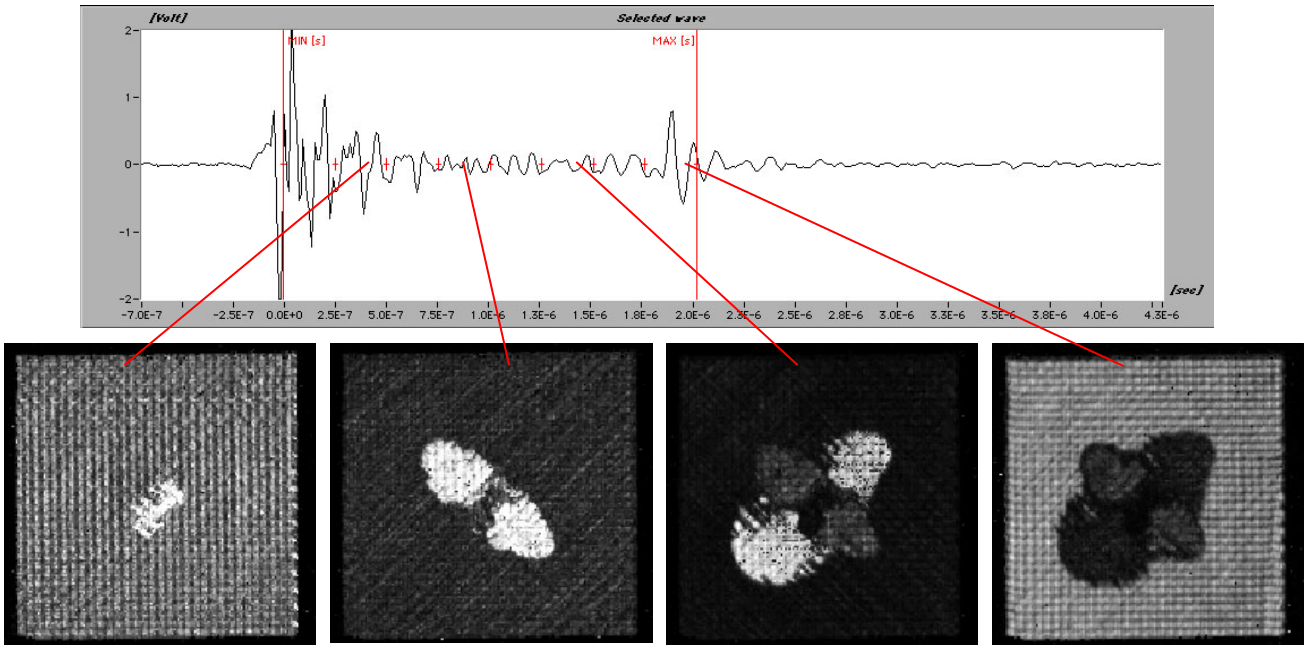

Figure III.6: High velocity impact damages with a 50mm support diameter (Ind3h60I).

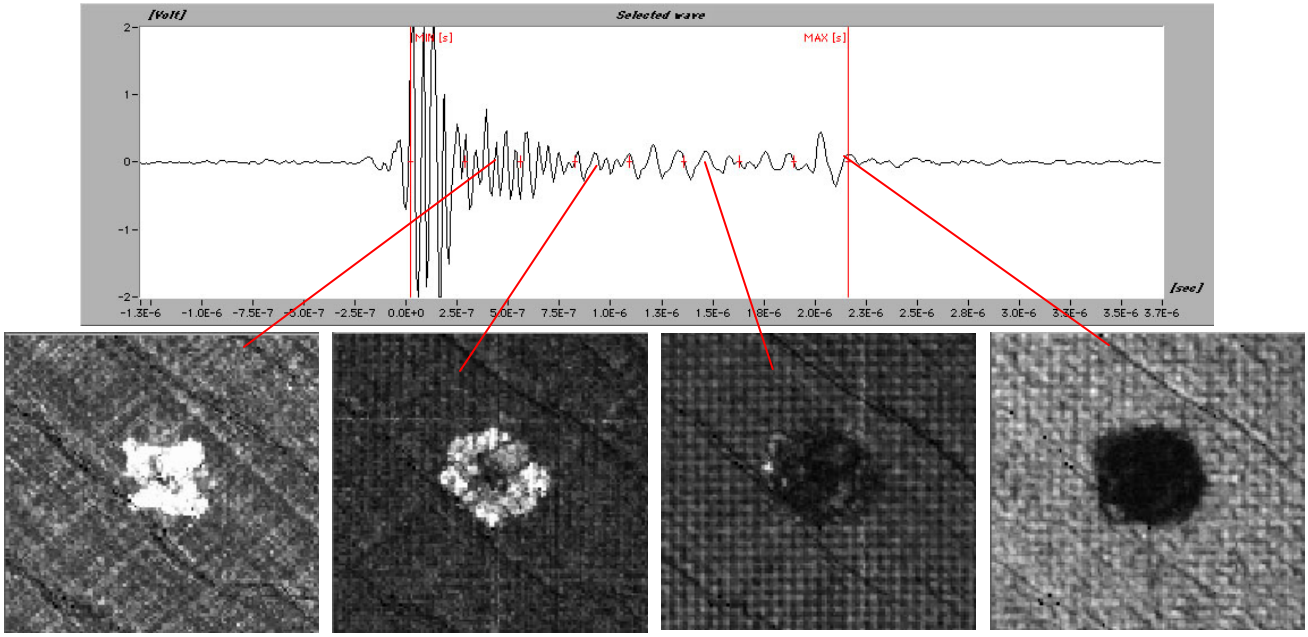

Figure III.7: High velocity impact damages with 100 mm support diameter (ds10h70).

Area measurement procedure

After the scanning process is finished, we have a file with extension "dat" (file_name.dat), which will give us the possibility to set gates and save the necessary images, as described in previous chapter. After, we will create the post scan elaboration images in two different files: one called "Photo8imag.PCT" and the second one "PhotoSinglimg.PCT". This images are corresponding to the photographs of the 8 parts. Then we have divided the specimen in single image, that was considered more suitable to be used in the measurement of the CFRP delaminated area.

This last image file, in-plane damage image, is to be treated in the Adobe PhotoShop, where this will be cropped until we will have only one specimen rectangle (see Figure III.8). This new image is saved as a JPEG file.

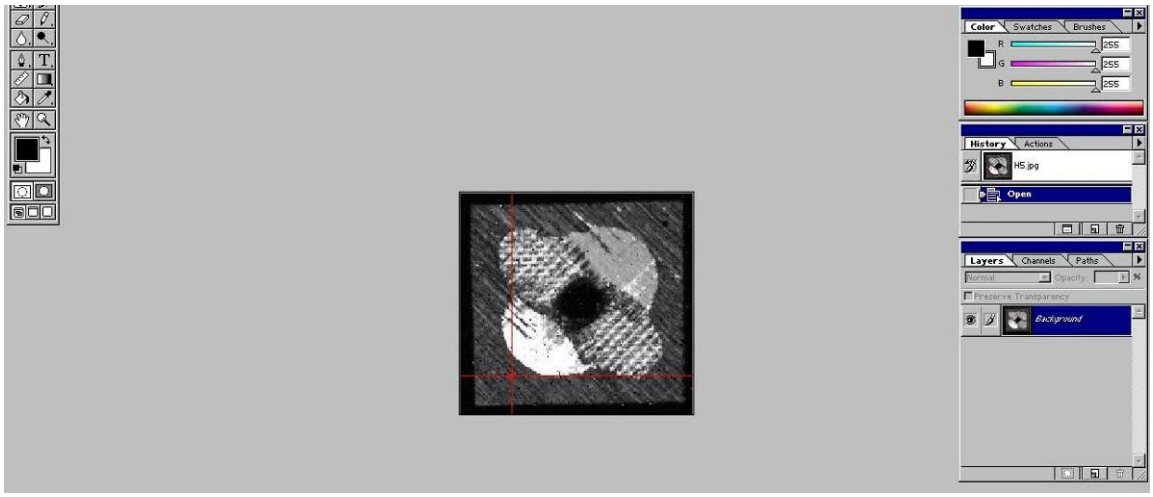

Figure III.8: Cropped image of the specimen as a file JPEG.

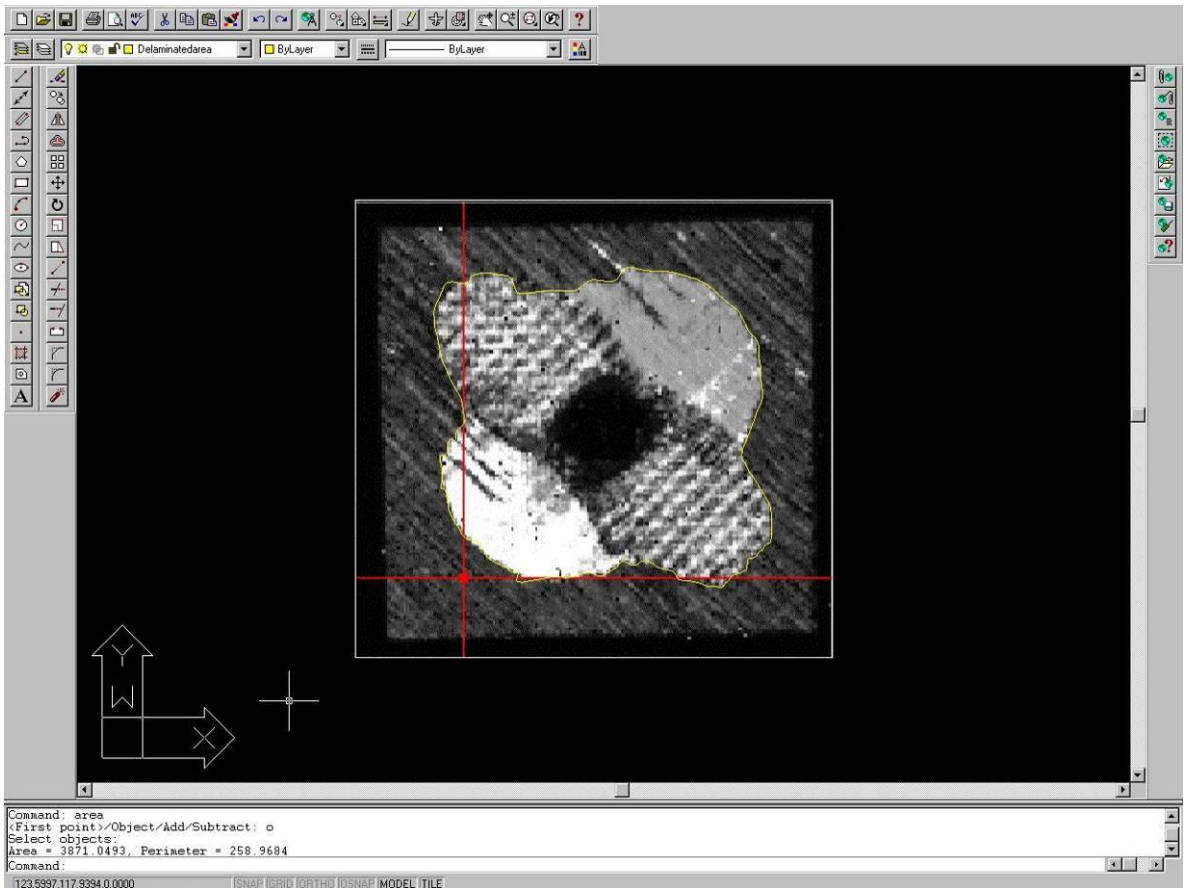

Figure III.9: "Spline" involving the delaminated area (on yellow) with the command "area" and the respective value in CAD units on the scrollbar.

Subsequently in the AutoCAD R14, we import this JPEG file by the option "*Raster Image*" which is into the menu "Insert". Then, already with the image of the specimen on the monitor, we must calculate the delaminated area. It can be done simply creating a region correspondent to the delaminated area and then measuring it.

For this we will choose the command "*Spline*" and with the mouse involve the area we pretend to measure paying attention to close the line, drawing like this a closed figure. Then we must create the region by writing the command "*Region*" the program tells us to select the object. We will click above the line that rounds the delaminated area and the region is automatically created. After that, we write the command "*Area*" and again select the object. Rapidly the value of the delaminated area appears in the command bar (Figure III.9).

However, there is the need to transform this value of area in the unit we want – usually mm^2. For this, we have also measured the area of the entire rectangle in AutoCAD (Figure III.10).

As the dimensions of the rectangle are known, in our case 75 mm x 75 mm or 55 mm x 55 mm, we can convert the delaminated area "CAD" into mm^2, by following the equation III.1:

$$\text{Delaminated Area}\left(mm^2\right) = \frac{\text{Delaminated area CAD x Area of the rectangle}\left(mm^2\right)}{\text{Area of the rectangle CAD}} \quad \text{(III.1)}$$

With the use of Microsoft Excel worksheet we can a sheet with all the information that we obtained (Table III.10).

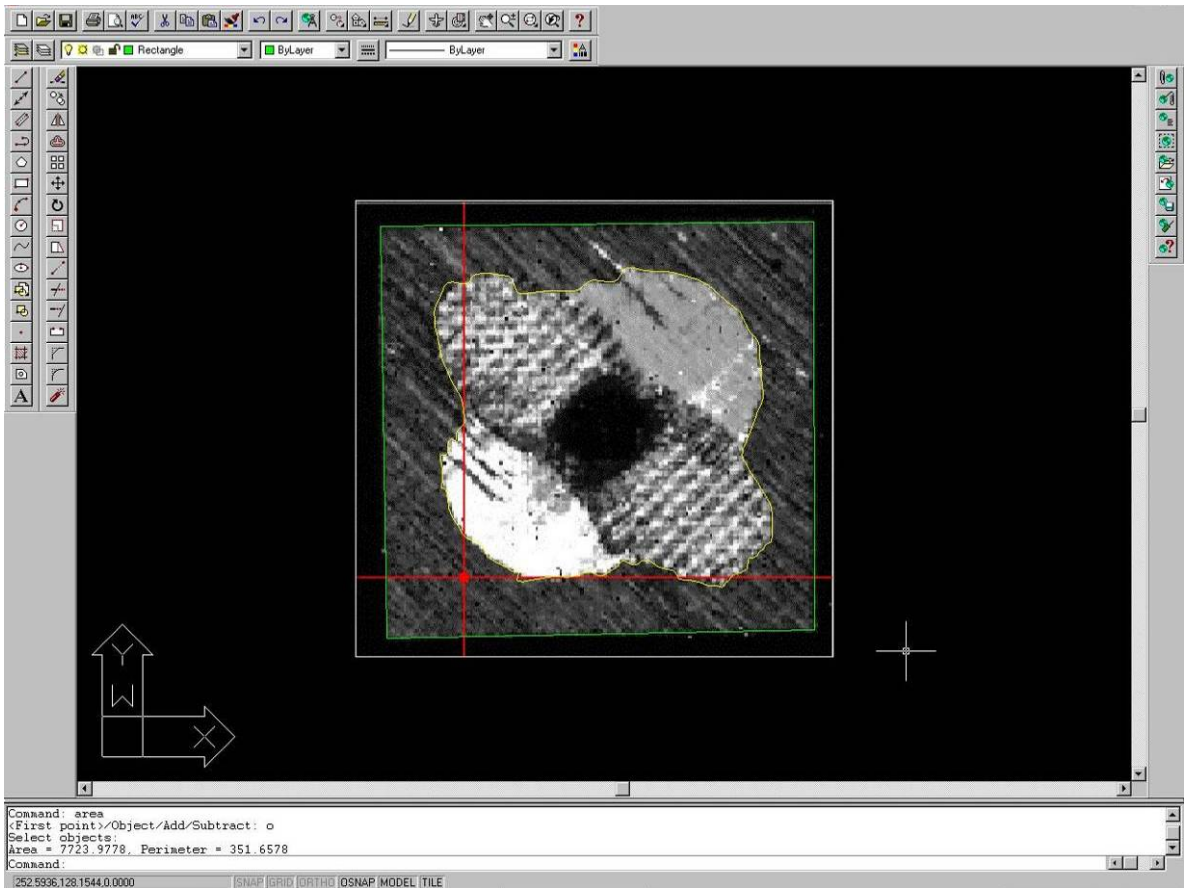

Figure III.10: Area of the entire specimen in CAD units (value showed on the scroll bar).

Physical Interpretation of the delaminated Area

By the UT images, we have noticed that with small increments of impact energy we obtain an increased delamination area (See Figure III.10)

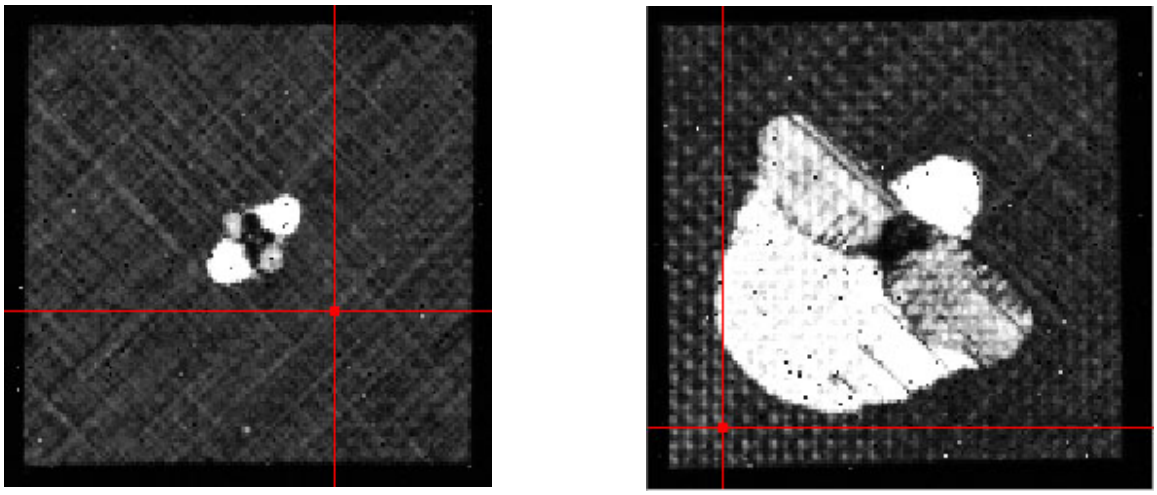

I1 H2.5

Figure III.10: Specimens I1 mm and H2.5 mm, with respective impact energies of 1.106 J and 4.927 J, and measured delamination areas of 138 mm^2 and 1569 mm^2

However, we have seen that from a certain value of impact energy, the delaminated area remained more or less constant (Figure III.11 and Table III.9 for the impact energy values).

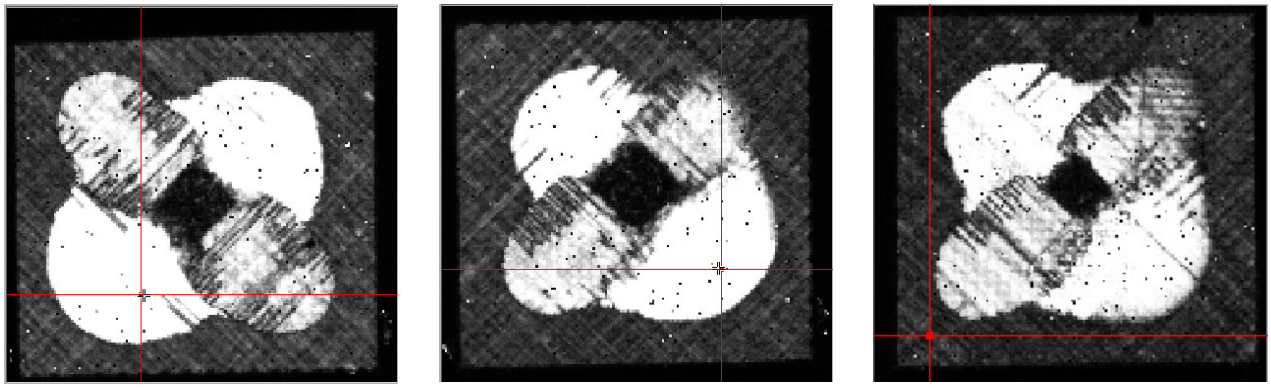

G3 G4 I2

Figure III.11: Delamination images for G3, G4, I2 CFRP laminates.

Table III.9
Characteristic impact energy for G3, G4 and I2 CFRP laminates

	Impact energy	Impact energy
G3	18,56 J	26,47 mm^2
G4	22,22 J	23,62 mm^2
I2	11,94 J	25,40 mm^2

These two phenomena were expected, as explained in consulted references. The zone where exists propagation of the delamination corresponds to the fraction on the load-displacement curve between the points a-b. This fraction of the curve is known by delamination zone and it ends at the point b) which indicates the first fibre failure (see graph in Figure III.12).

After observing all the UT scanning of these specimens, we have continued with the examination of the high-velocity damaged ones, but always using the same support diameter equal to 50 mm.

The trend observed was approximately the same, which means that, again, firstly, the delaminated area increased ample for small increments of impact energy and, then, from a value of impact energy the delaminated area remained constant.

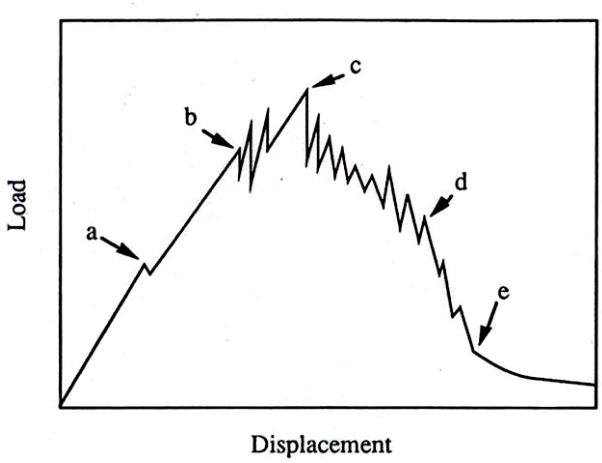

Figure III.12: Schematic of a typical load-displacement curve.

Table III.10
Microsoft Excel worksheet containing the obtained data for all experimental cases

High-velocity impact damages with 50 mm support diameter					
Name of specimen	Damage Area (CAD)	Rectangle Area (CAD)	Delaminated area (mm^2)	Displacement (mm)	Impact energy (J)
Ind3h5	0	77826214	0.0	0.768	0.52
Ind3h10	47336	79556998	2.9	1.053	1.03
Ind3h20	7829202	78860142	486.5	1.304	2.04
Ind3h30	10673307	79086739	661.3	1.655	3.06
Ind3h40	14803798	79332073	914.4	1.954	4.08
Ind3h50	19084064	77921970	1200.1	2.387	5.10
Ind3h60	18812451	77088977	1195.8	2.642	6.12
Ind3h70	23164169	77041332	1473.3	2.765	7.13
ds5H10	27929003	76878489	1780.1	3.757	10.64
ds5H16	48774317	76938593	3106.3	4.846	16.90
ds5H24	40907424	75808365	2644.1	6.337	25.26
ds5H34	44573161	74935696	2914.6	8.353	35.72
ds5H44	54472215	77550117	3441.8	10.855	46.23

High-velocity impact damages with 100 mm support diameter					
Name of specimen	Damage Area (CAD)	Rectangle Area (CAD)	Delaminated area (mm^2)	Displacement (mm)	Impact energy (J)
ds10h10	0	95811518	0.0	1.714	1.032
ds10h40	0	95287958	0.0	2.872	4.089
ds10h70	10147226	95287958	322.1	3.826	7.144
ds10h1m	17061187	95811518	538.7	4.577	11.211
ds10H21	23599334	94659073	754.2	6.842	22.232
ds10H23	31647812	95833333	999.0	7.107	24.310
ds10H26	43293224	95811518	1366.9	7.780	27.455
ds10H29	36086507	95811518	1139.3	8.298	30.584
ds10H32	34323468	95833333	1083.4	9.158	33.748
ds10H34	36750301	96335079	1154.0	9.737	35.858
ds10H47	47136910	95287958	1496.4	13.706	47.405

Low-velocity impact damages with 50 mm support diameter					
Name of specimen	Damage Area (CAD)	Rectangle Area (CAD)	Delaminated area (mm^2)	Displacement (mm)	Impact energy (J)
G3mm	27700282	80679446	1682.4	3.011	
G5	35077964	80068250	2146.7	7.500	25.873
H2,5mm	25225208	78780710	1569.0	2.504	4.927
H5	37741122	77822865	2376.3	7.498	26.223
I1mm	2224679	78767789	138.4	0.997	1.106
I1,6mm	8413034	77341090	533.0	1.597	2.146
I2,5mm	28614872	78146279	1794.2	2.509	4.901
I3mm	28189959	77676526	1778.3	3.000	7.844

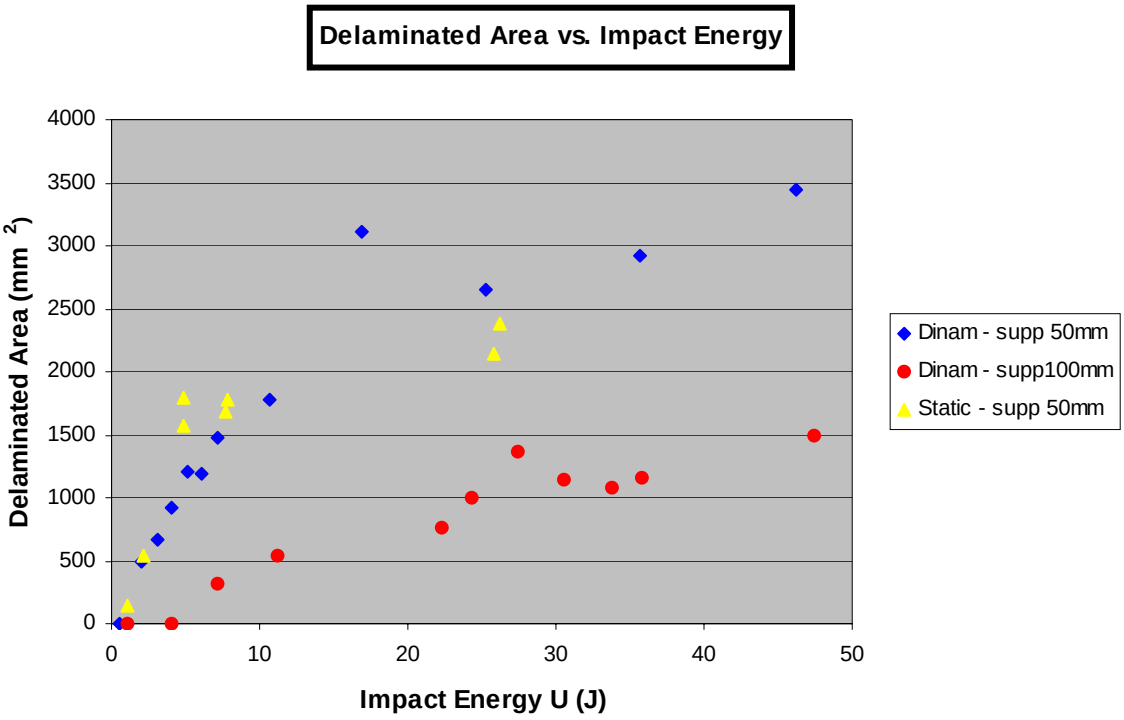

Figure III.13: Obtained curves.

Taking in consideration these conclusions were carried out the same type of research on the samples that were impacted with a support whose diameter was 100mm. A similar behaviour as the one for the same value of impact energy of the impact damages with a 50 mm support diameter was expected. Also was expected a similar quantity of delaminated area. In spite of this, extraordinarily, for the range of impact energies used on the previous specimens, the delaminated area was quite smaller.

At this point, we have initiated a study that allowed us to understand why this phenomenon occurred. The first step taken was to compile all the tests made in a curve Delamination Area vs. Impacted Energy to confirm the law that is supposed should appear.

To realise the graphic all the data were assessed in a Microsoft Excel worksheet (See Table III. 10) and was elaborated the graphic presented in Figure III.13.

By analysing the graphic above, we can confirm that with a 50 mm support diameter the trend of the material is as was expected. Nevertheless, when the support diameter was 100 mm, the trend was much lower.

Also was possible to make an improved confrontation between the diameter differences and also analyse better the possible influence of the impact velocity.

Identification of the CFRP laminates stacking sequence

The main scope of this part of the research was to verify the laminate stacking sequence, provided by the CFRP manufacturer, using the UT NDI procedures. The CFRP laminate chosen, with nominal thickness 3 mm, is stratified as follows $[(0,90)_3 / +45_3 / -45_3]_s$.

Substituting each laminate component for its thickness, the actual laminate total thickness, S, is:

$$S = [(0.21 \times 3) + (0.15 \times 3) + (0.15 \times 3)] \times 2 = 3.06 \text{ mm} \quad \text{(III.2)}$$

By utilizing a UT velocity in the CFRP composite equal to 3000 m/s, the UT time-of-flight for a 3.06 mm thickness is t = 2.04 μs.

The typical UT waveform of the sample under examination was extracted from the volumetric UT file (Figure III.14) and a time gate was set on the whole specimen thickness.

The difference between maximum and minimum time gate limits is (Figure III.16):

$$2.15 \text{ μs} - 0.11 \text{ μs} = 2.04 \text{ μs} \quad \text{(III.3)}$$

corresponding to the 3.06 mm actual thickness.

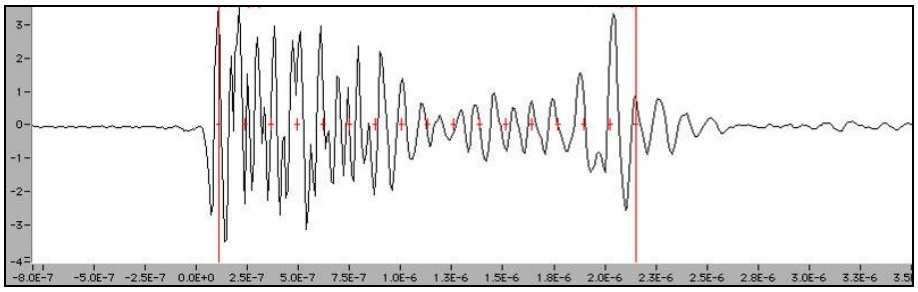

Figure III.14: Typical UT waveform of an impacted CFRP sample with time gate set on the whole specimen thickness.

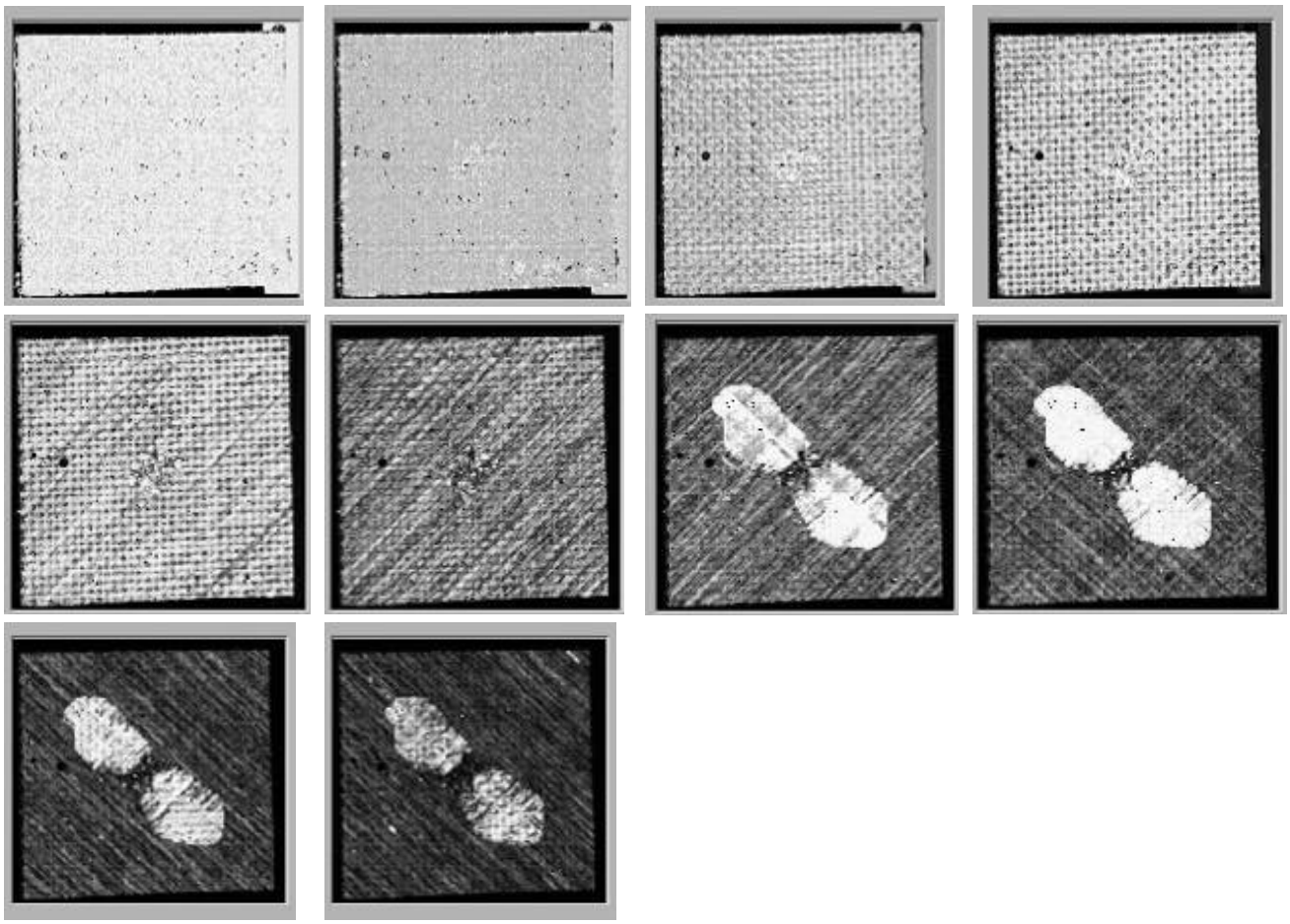

Figure III.15: 10 UT images for the first half of an impacted CFRP specimen thickness. Each image corresponds to a 150 μm thickness portion.

The interface between laminate layer blocks with different fiber orientations was identified by calculating the volumetric percentage for each layer block in the composite stacking sequence: (0°, 90°) fabric layer block = 40%, (+45°) tape layer block = 30%, (-45°) tape layer block = 30%.

Thus, by generating 10 UT images from the first half of the CFRP laminate sample thickness, the first 4 images are expected to represent the (0°, 90°) fabric layer block, the next 3 the (+45°) tape layer block, and the last 3 the (-45°) tape layer block, as shown in Figure III.15. In Figure III.16, the 10 UT images for the second half of CFRP sample thickness are also reported.

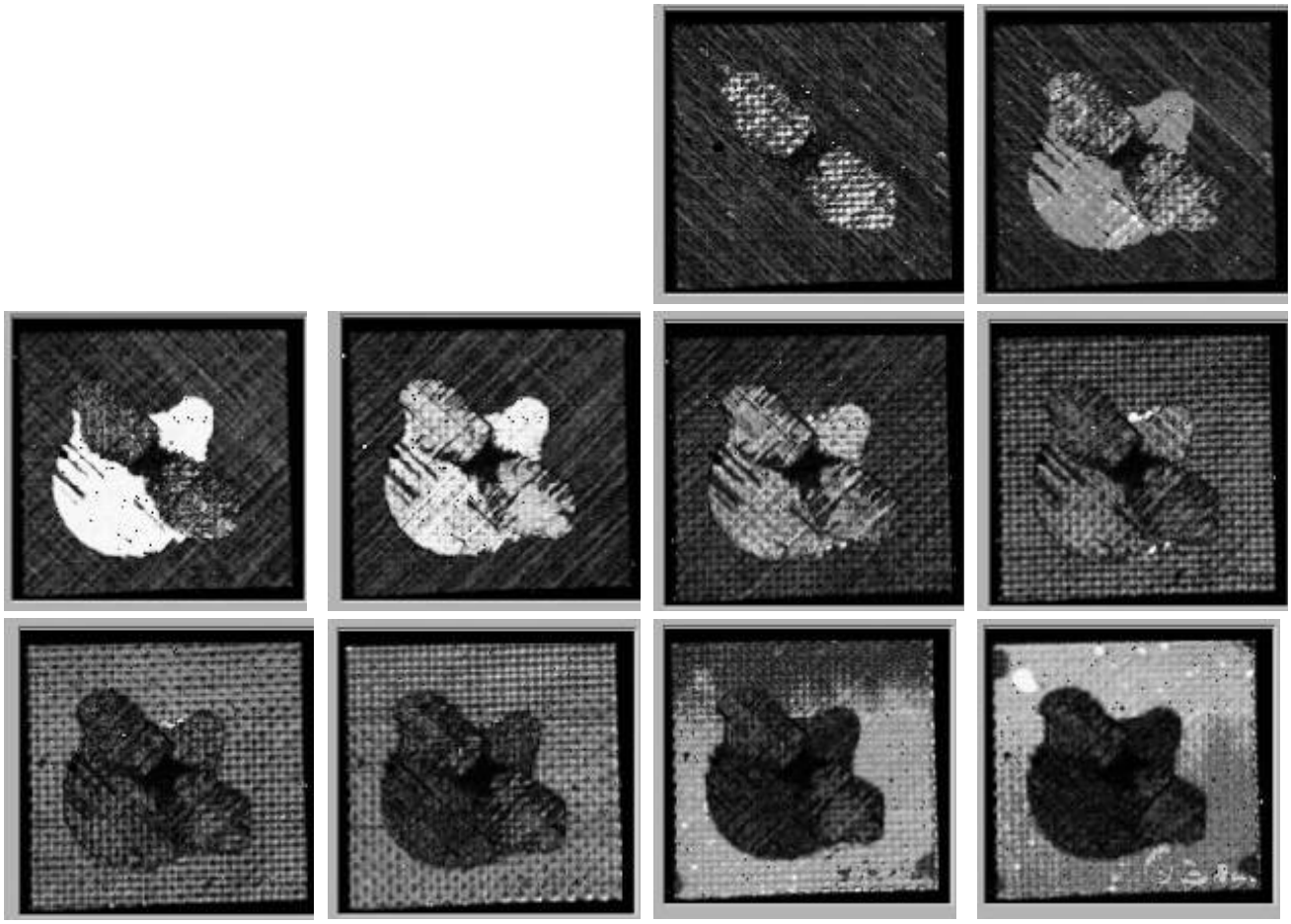

Figure III.16: 10 UT images for the second half of the impacted CFRP specimen thickness of Figure III.15. Each image corresponds to a 150 μm thickness portion.

Damage position in the thickness direction

In this section, the identification of the thickness direction position of the delamination damage caused by impact testing is carried out.

In Figures III.15 and III.16, the image analysis of the entire CFRP sample thickness is shown. From the figures, it can be seen that the first delamination onset takes place in the first $(+45)_3$ layer block. However, as each image in Figures III.15 and III.16 corresponds to a 150 μm thickness portion, the defect position along the laminate thickness can be determined only with an accuracy of 150 μm.

In order to achieve a more precise assessment of the damage position in the laminate thickness direction, the system capability to generate images for the thinnest

possible material thickness portion was verified and the minimum thickness value applicable resulted to be 30 μm.

Figure III.17 reports four 30 μm thickness portion images for the 1st $(+45)_3$ layer block, 2nd $(-45)_3$ layer block, and 2nd $(+45)_3$ layer block, respectively. The fabric layer blocks were not analysed because no delamination damage was evidenced in them.

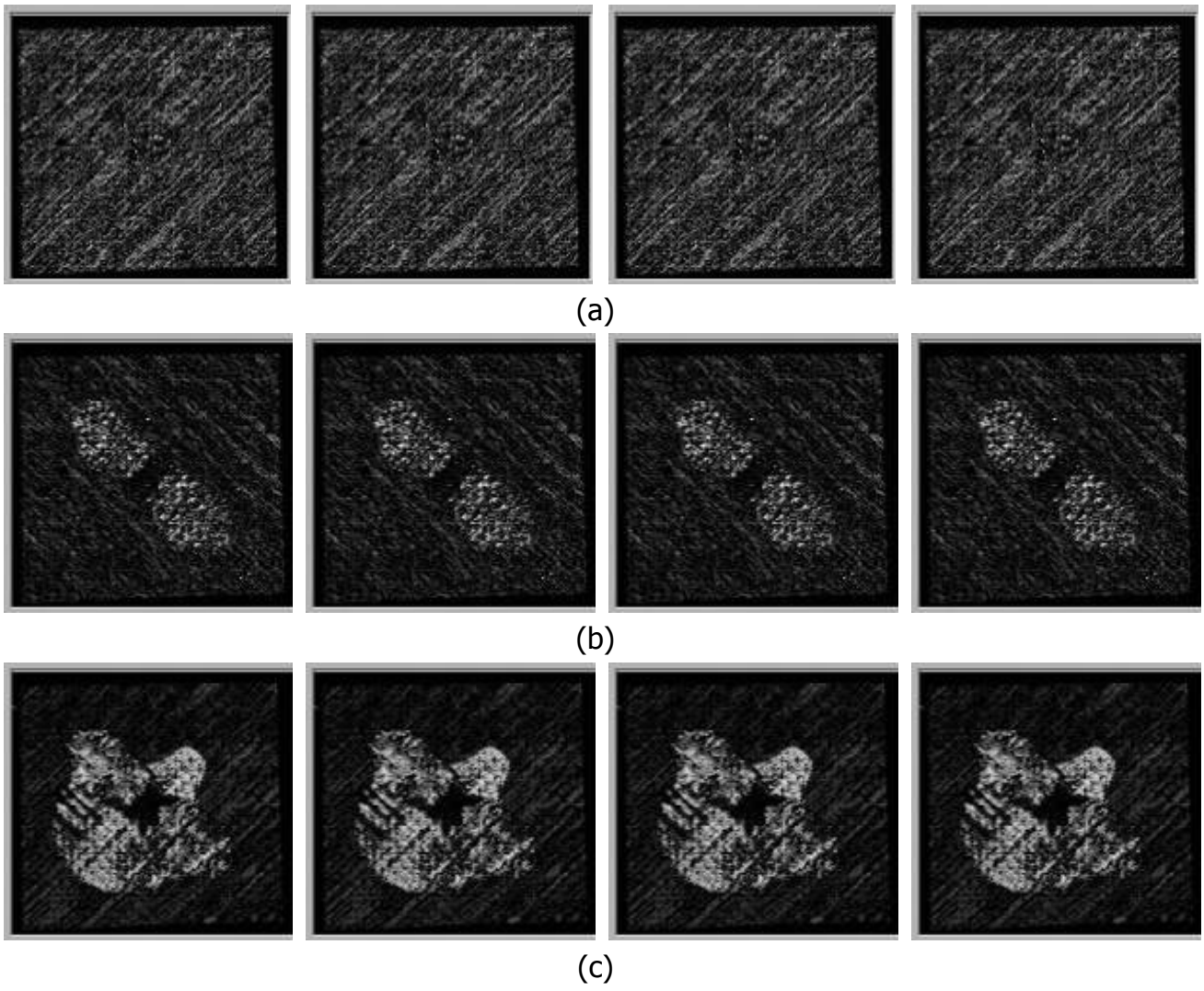

Figure III.17: (a) 1st $(+45°)_3$ tape layer block;.(b) 2nd $(-45°)_3$ tape layer block; (c) 2nd $(+45°)_3$ tape block. Each image refers to a 30 μm thickness portion

From Figure III.17, it can be observed that the first defect appears with sufficient clarity in the 1st $(+45)_3$ tape layer block (Figure III.17.a), i.e. at 930 mm depth from the laminate surface. This defect is a delamination extending in-plane perpendicularly to the fibre direction in the block. The delamination has a typical peanut shell shape with two approximately elliptic lobes, extending symmetrically in the -45º direction from the central dark zone representing the impact indentation.

The second defect becomes visible in the images of 2nd $(-45)_3$ tape layer block, i.e. at 1770 mm depth from the laminate surface. Also this defect is a delamination extending in-plane perpendicularly to the fibre direction in the block (III.17.b). At high impact energy, the delamination typical outline presents a single egg-like shape with a central dark zone at the impact indentation. In the case of Figures III.17.b and III.17.c, because

of the relatively low impact energy, the delamination shape is completely egg-like in the lower left zone and is developing toward the egg-like form in the upper right zone.

III.2.5 Conclusions

Nowadays, composite materials are massively used in a large number of industrial applications. Thus, it is very important to characterize the service behaviour they might have depending on their working conditions.

The study described in this paper is part of a wider investigation whose final objective is to accept or reject components, made of high performance composites, subjected to impact damage during their operational activity.

The focus of the study is on the development of a totally non-destructive method to characterise the impact damage in the CFRP composite without need to section it for microscopic analysis of the internal material structure.

The advanced UT NDI procedure utilised was shown to be an efficient method for the characterization and measurement of the composite delamination damage caused by impact loading.

The delamination damage in-plane extension is very well defined, allowing for a very precise damage area evaluation particularly useful for the establishment of correlations between impact energy and damage extension.

In addition, the UT NDI based on full waveform detection was demonstrated to be a very powerful tool for composite material stacking sequence verification and damage position determination in the thickness direction, realising a full 2½ D non-destructive evaluation of the internal composite material structure.

III.3. High performance composite laminate NDE

III.3.1 Introduction

The evaluation of the damage after impact load can be useful in the determination of the residual properties of advanced composite materials. The interaction between failure modes is also critical to understand damage mode initiation and propagation in these new generation materials.

Since it has been found that relatively low impact energy levels can determine significant strength losses in composite laminates, extensive research efforts have been devoted to the relationships between impact parameters, failure modes, damage extension and residual strength retention after impact.

Due to the increasing interest of the aerospace industry, non-crimp fabric (NCF) composite laminates will be considered in this paragraph.

In comparison with classical laminates introduced in aeronautical structures with the primary goal to reduce weight, NCF composite present lower fabrication costs. Moreover, this composite material type has shown a great potential where high impact resistance is required.

The aim of the present research is to validate what has been found on classical composite laminates in terms of impact damage.

In order to verify the influence of different material design configurations, two different NCF laminate lay-ups were considered.

The ultrasonic (UT) nondestructive evaluation (NDE) system utilized in this work for consists of a purposely designed hardware configuration and a custom made software code, Robotest V2.0©, developed in the Lab View environment.

III.3.2 Materials and experimental work

Low velocity impact tests were carried out on NCF composite laminates 4 mm in thickness, made by the RIFT technology (see Figure III.18).

The matrix was an Hexcel HexPly®M36 resin and the carbon fibres were type Tenax HTS 5632 12k. Polyester stitching yarn (50 dtex) was used for connection with stitch length 2.5 mm. The final fibre volume fraction was 62%.

Biaxial laminates were constructed with stacking sequence [(+45°/-45°), (0°/90°), (+45°/-45°), (0°/90°), (90°/0°), (+45°/-45°), (90°/0°), (+45°/-45°)]s whereas quadriaxial laminates were manufactured with stacking sequence [+45°/0°/-45°/90°, +45°/0°/-45°/90°, 90°/-45°/0°/+45°,90°/-45°/0°/+45°].

In both cases, a final fibre aerial weight of 267 g/m^2 per layer was obtained.

The mechanical tests were carried out on an instrumented falling weight machine type Ceast Fractovis (see Figure III.19) connected to a Das 4000 program for data recording and analysis. Rectangular specimens 100 mm x 150 mm were cut from the laminates and impacted with different impact energies.

A cylindrical indenter with hemispherical nose was used for impact tests. The fixture in Figure III.20 was used for NCF laminate specimen clamping.

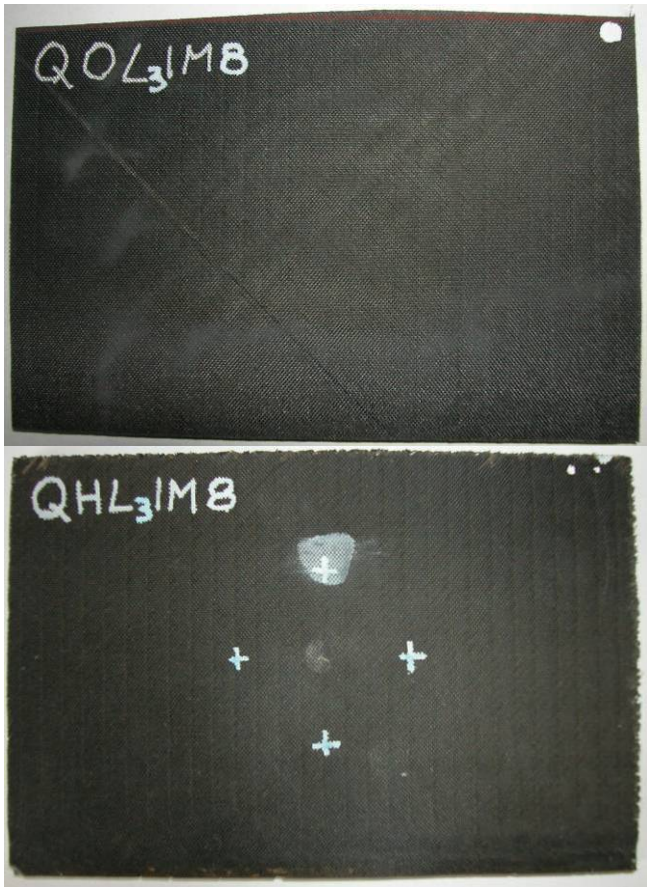

(a)

(b)

Figure III.18: 4 mm thick NCF composite laminates, made by the RIFT technology: (a) composite laminate before impact test, (b) composite laminate after impact test.

Figure III.19: Ceast Fractovis falling weight machine.

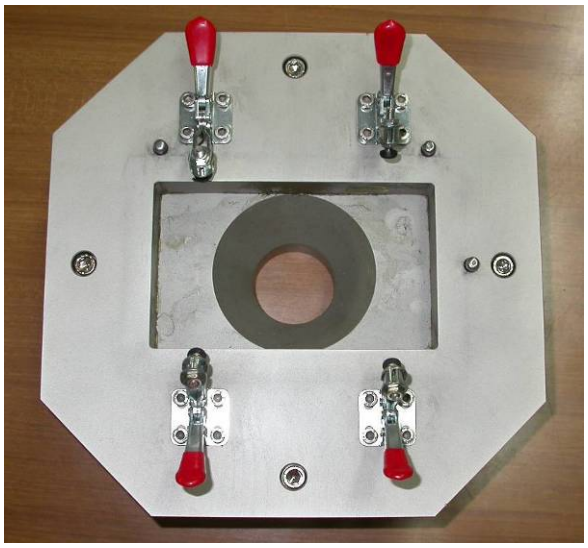

Figure III.20: NCF laminate clamping fixture.

Table III.11
Impact testing program (pen = penetration)

Laminate configuration	**Impact energy (J)**
Quadriaxial	9-12-16-20-25-30-40-pen
Biaxial	9-16-20-30-40-pen

Table III.12
Test conditions for drop weight low-velocity impact tests

Sample id.	Height (m)	Mass (kg)	U (J)	Speed m/s
QHL3IM2	0.255	3.6	9	2.24
QHL3IM3	0.34	3.6	12	2.58
QHL3IM4	0.453	3.6	16	2.98
QHL3IM5	0.567	3.6	20	3.33
QHL3IM2	0.255	3.6	9	2.24
QLL3IM6	0.708	3.6	25	3.73
QLL3IM7	0.546	5.6	30	3.27
QLL3IM8	0.728	5.6	40	3.78
QLL3IM9	0.411	5.6	22.58	2.84
BHLIM2	0.254	3.6	9	2.24
BHLIM3	0.453	3.6	16	2.98
BHLIM4	0.566	3.6	20	3.33
BHLIM5	0.546	5.6	30	3.27

Table III.11 and III.12 summarize the test parameters utilized in the impact testing program. The analysis of the preliminary test data allowed for the selection of suitable energy levels that were adopted in the continuation of the experimental program to obtain controlled damage levels in the specimens (Table III.12).

The force-displacement curves each impact test were recorded and post-analyzed.

III.3.3 Ultrasonic testing

After mechanical testing, the specimens were subjected to UT volumetric scanning using the custom made software code Robotest v2.0© for FV-Scan UT NDE .

Pulse-echo immersion volumetric UT scans were carried out using a focused (49.6 mm focal length), high frequency (15 MHz) transducer for maximum resolution. The oscillator/detector was set up at 90 dB gain and medium damping. The digital oscilloscope was set up at 1 V/div, 0.5 μs/div, and sampling frequency 100 MHz, resulting in 500 samplings detected for each UT waveform.

Each specimen was scanned over an area of 110 x 155 mm with scan step 1 mm. After UT NDE the delaminated area was measured.

III.3.4 Mechanical testing results

In Figure III.21, the delaminated area, measured through UT NDE, is plotted vs. impact energy, U. All experimental points approx. follow a straight line. Interestingly, the biaxial laminates show a smaller damaged area.

In comparison with classical laminates, a larger delaminated area was noted for the NCF material. For the impact energy necessary to obtain the barely visible impact damage (BVID), a delaminated area of 4000 mm^2 was observed, much higher than the correspondent value for classical laminates (2500 mm^2 for the 4 mm thick laminates).

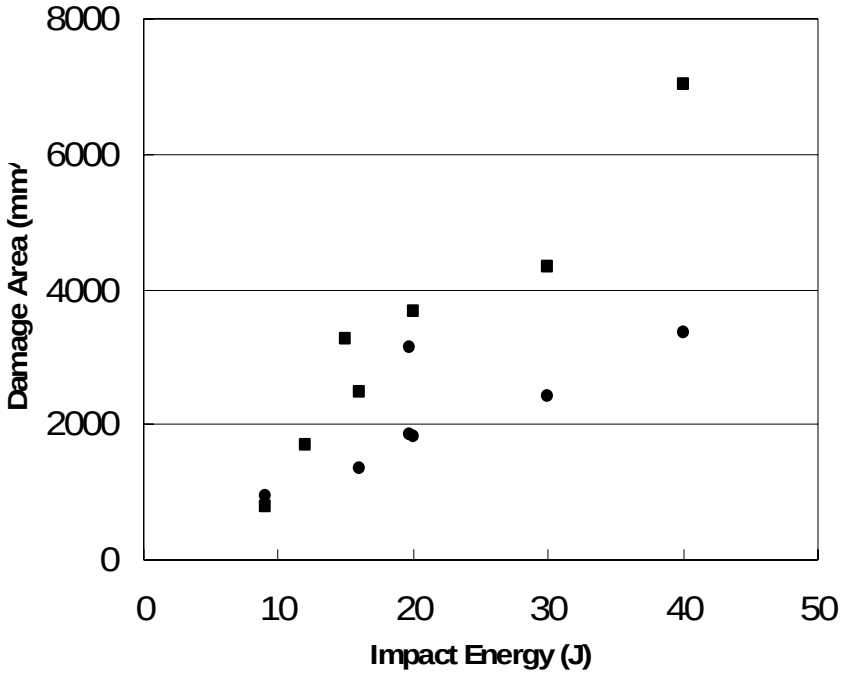

Figure III.21: Delaminated area vs. impact energy.
□ = quadriaxial laminates, ● = biaxial laminates.

The inspection of thick laminates results, therefore, quite critical because very small impact energies may produce large delaminated areas within the material structure whereas the laminate external surface only shows a small damaged zone. The problem is less critical for biaxial laminates that showed smaller delaminated areas under the same test conditions as for the quadriaxial laminates.

III.3.5 Ultrasonic non-destructive evaluation results

UT image generation

As previously illustrated, the Robotest v2.0© software code allows for the generation of single or multiple UT images of any thickness portion of the internal structure of the material under examination by processing the UT volumetric file containing the complete UT waveforms detected during the FV-Scan.

In order to obtain UT images, it is first necessary to retrieve from the volumetric file a typical UT waveform. Then, a time gate is set on this waveform to identify the material portion(s) to be represented. The time gate can be divided into a desired number of equal sub-gates to obtain multiple images. One image is generated for each sub-gate and each image represents the internal structure of the corresponding portion of laminate thickness.

In this work, a multiple image generation procedure was utilized by setting a time gate on the whole UT waveform and dividing it into four parts to generate four UT images, each corresponding to ¼ of the laminate thickness (about 1 mm).

This choice was justified by the laminate stacking sequence and the typical behavior of composite laminates, where delamination develops preferentially at the interfaces between layers having different orientations.

In this work, the peak amplitude value of the segmented signal was calculated. A 2D matrix of size equal to the number of scan steps in the x and y directions, containing the peak amplitude values of the gated signal segment for each material UT interrogation point, was obtained. This matrix was mapped to form 2D images using grey tones or pseudo colors (Figure III.22).

UT image analysis

In Figure III.22, the four UT images obtained from the volumetric UT files of a quadriaxial and biaxial laminate are reported for drop weight low-velocity impact tests with same impact energy (9 J). Each image in the series represents the laminate internal structure of ¼ of the material thickness, starting from the upper surface (first image on the left) down to the opposite lower surface (last image on the right).

By looking at the UT images in Figure III.22, it can be seen that the damage develops along the interfaces between layers having different orientations. Moreover, the delamination extension increases with increasing distance (depth) from the impact surface. This results in the well known hat-shaped configuration of the delamination damage.

The UT analysis also reveals an absence of delamination in a small zone directly below the impactor-material surface contact point.

The presence of a delamination at a given interlayer within the material results in a "shadow" in the subsequent UT images. Consequently, the (d) UT images in Figure III.22 represent the in-plane projection of the damage developed at different depths in the whole laminate thickness, rather than the damage in the fourth portion of the laminate thickness. Their examination allows for the assessment of the global damage induced into the material according to the traditional UT scanning techniques (C-Scan) and was used for global delaminated area measurements.

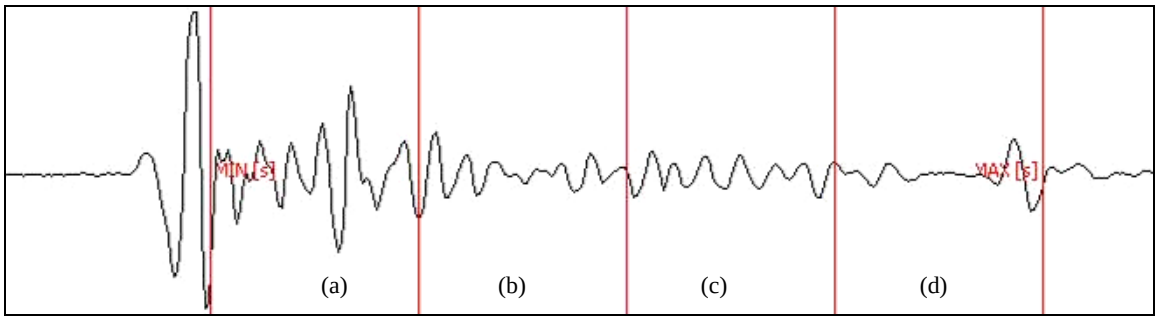

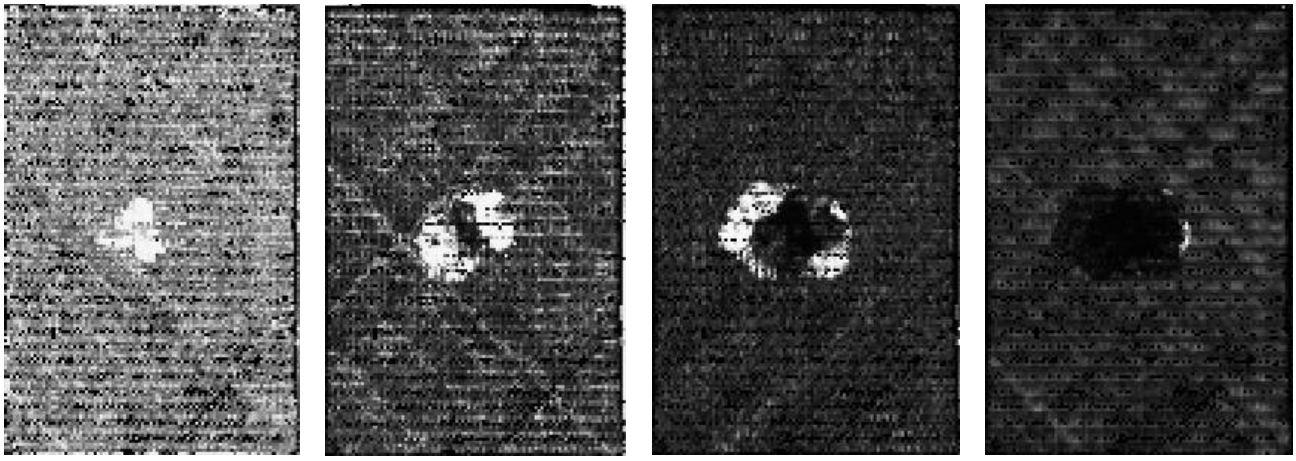

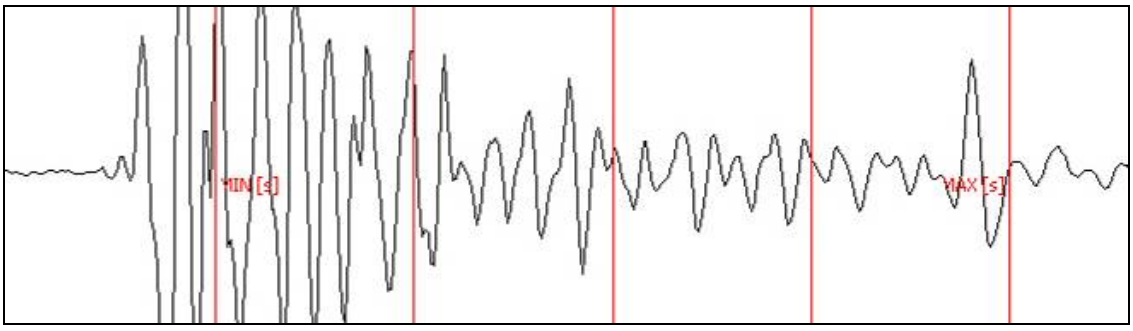

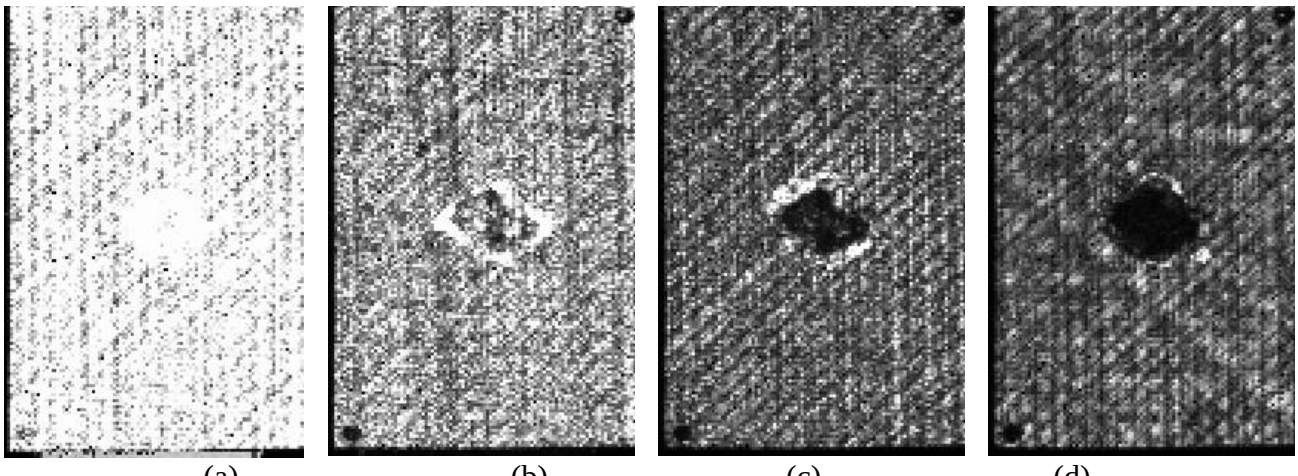

Figure III.22: UT images from drop weight low-velocity impact test specimens QHL3IM2 (upper) and BHLIM2 (lower)
(a) surface damage, (b) and (c) internal damage, (d) in-plane projection of the damage.

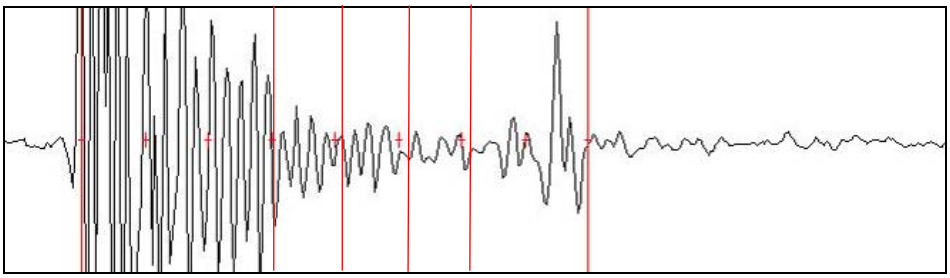

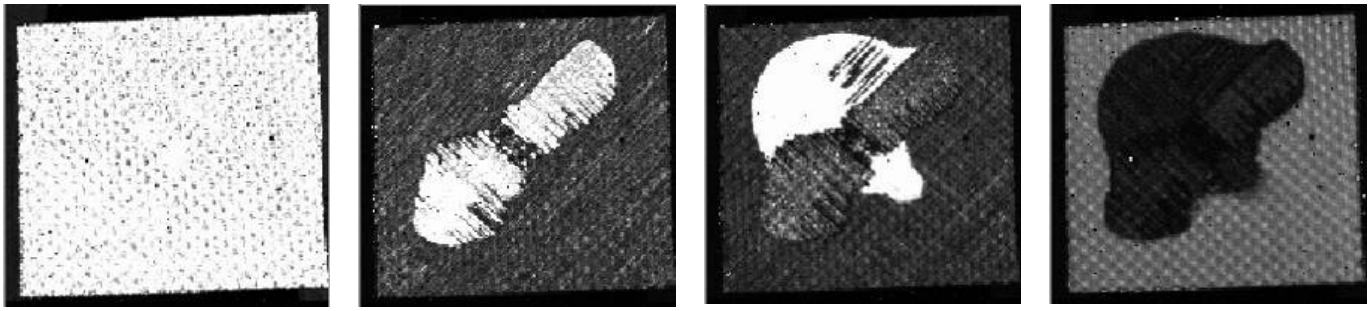

(a) (b) (c) (d)

Figure III.23. UT images from drop weight low-velocity impact test samples for carbon fiber resin reinforced laminate Ind3d1: UT probe 15 MHz, step 0.5 mm, scanning area 75 mm x 75 mm, impact energy 8.43 J: (a) surface damage, (b) and (c) internal damage, (d) in-plane projection of the damage.

By comparing the UT images for the quadriaxial NCF specimen (see Figure III.22 upper image series) and for the biaxial NCF specimens (see Figure III.22 lower image series) impacted under the same testing conditions (see Table III.12), it can be seen that the internal damage is always larger for the quadriaxial laminate, as stated before (see Figure III.21).

In Figure III.23, the four UT images obtained from the volumetric UT file of a classical quasi-isotropic carbon fiber resin reinforced laminate tested under similar conditions as the NCF laminates (UT probe 15 MHz, step 0.5 mm, scanning area 75 mm x 75 mm, impact energy 8.43 J).

By comparing the UT image series of the classical and the NCF laminates, it can be clearly seen that the latte advanced composite material type is characterized by a much more reduced and circumscribed impact induced delamination damage, confirming the great potential of NCF composite laminates when high impact resistance is a critical material property.

Figure III.24 reports the complete series QHL3IMx in order to observe the difference between the same types of NCF laminate at different impact energy level. It is possible to observe that in the case of the surface damage images (a images), no defect is evidenced. In the case of the internal damage defects (b and c images), it is possible to observe the same direction and shape of delamination. In the final in-plane projection of the damage (d images) it is possible to observe and measure the total damage area of the NCF laminates, which increases with the increasing of energy. From the laminate QHL3IM9 further a total back layer delamination can be observed. The difference of in-plane projection between the QHL3IM8 and the QHL3IM9 to QHL3IM11 is due to the fact that the water (UT couplant) is entering the back surface of laminates.

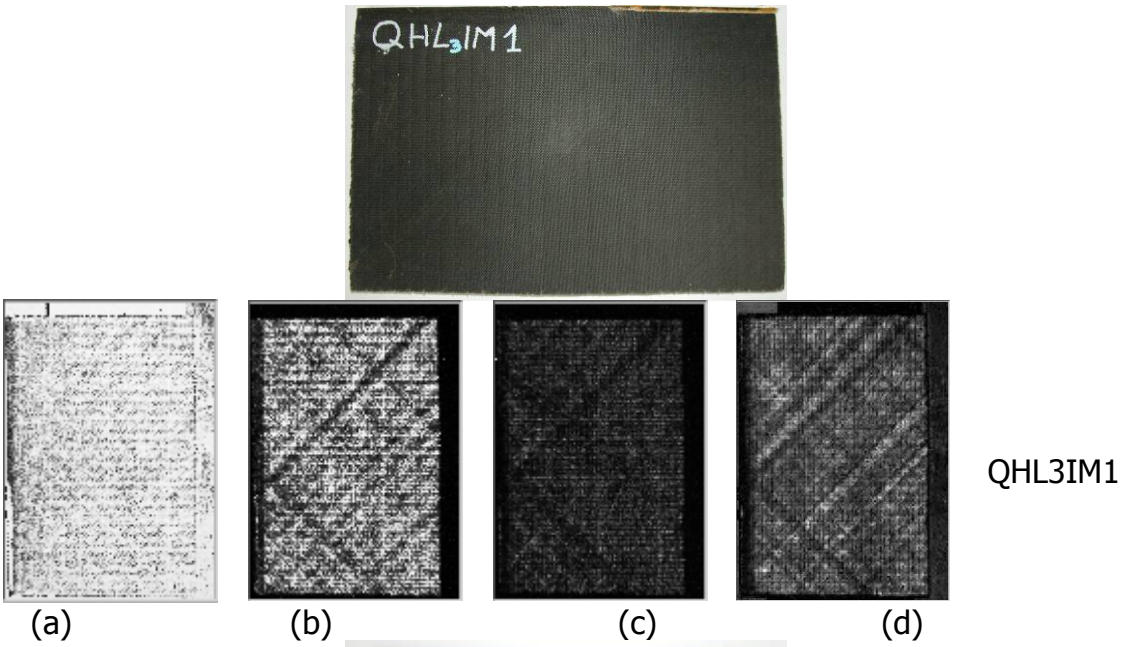

(a) (b) (c) (d)

QHL3IM1

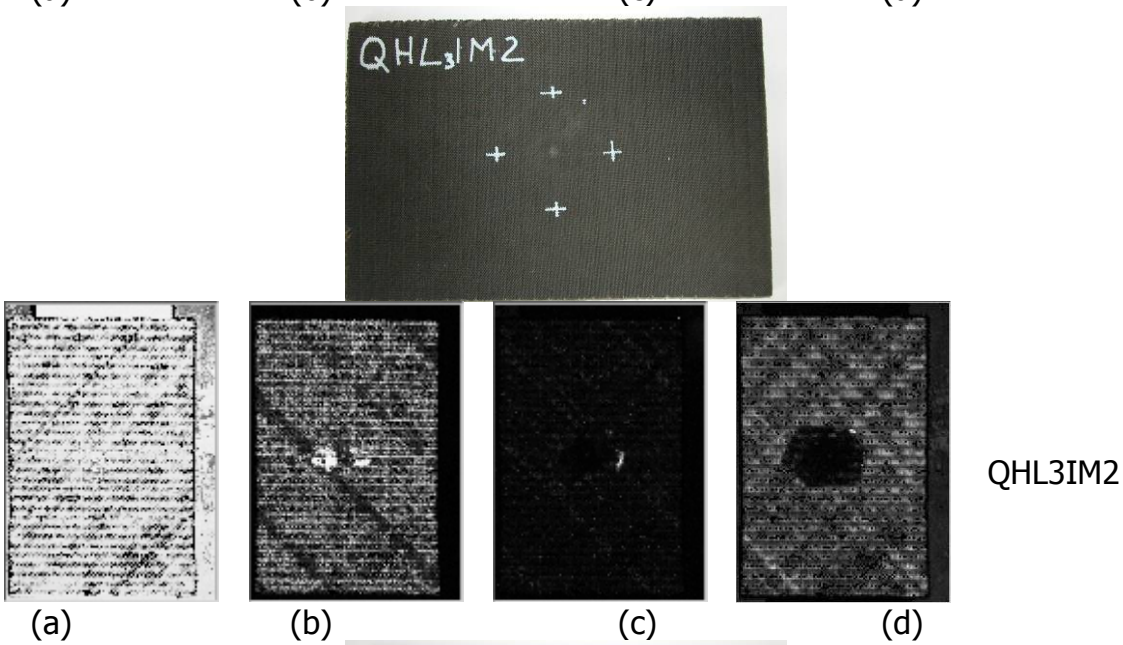

(a) (b) (c) (d)

QHL3IM2

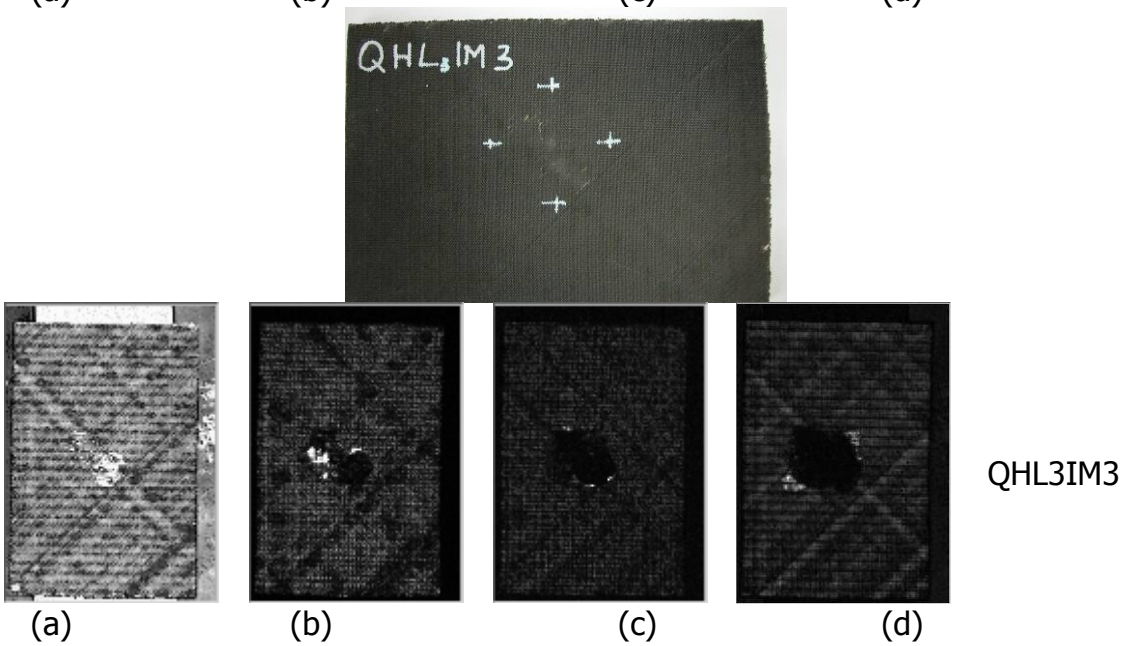

(a) (b) (c) (d)

QHL3IM3

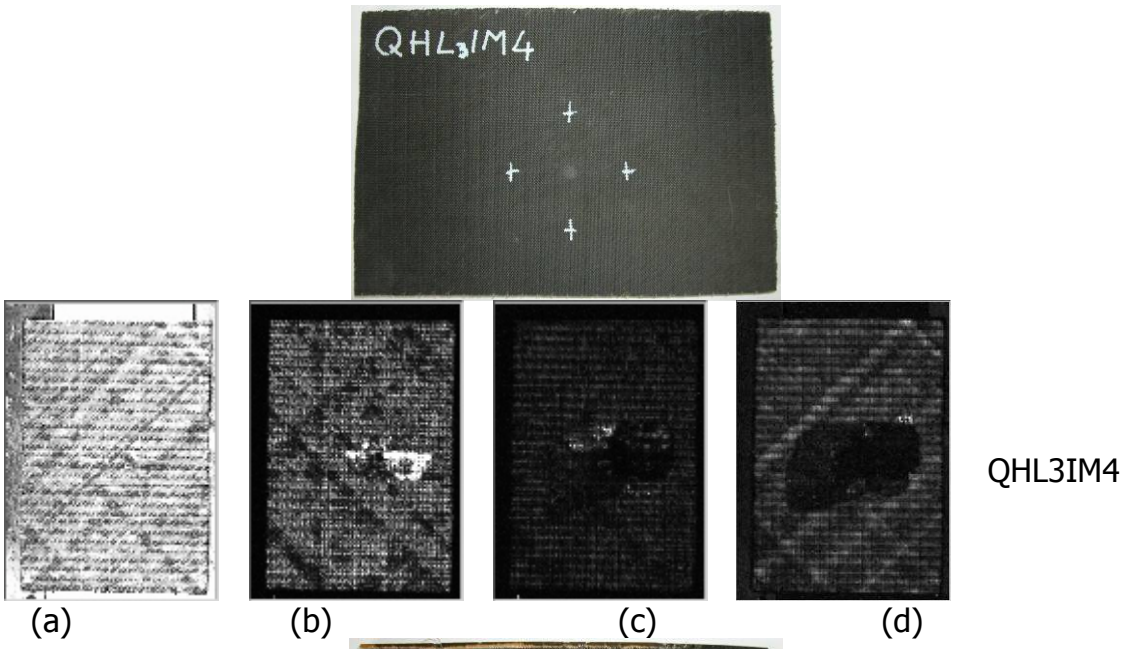

(a) (b) (c) (d)

QHL3IM4

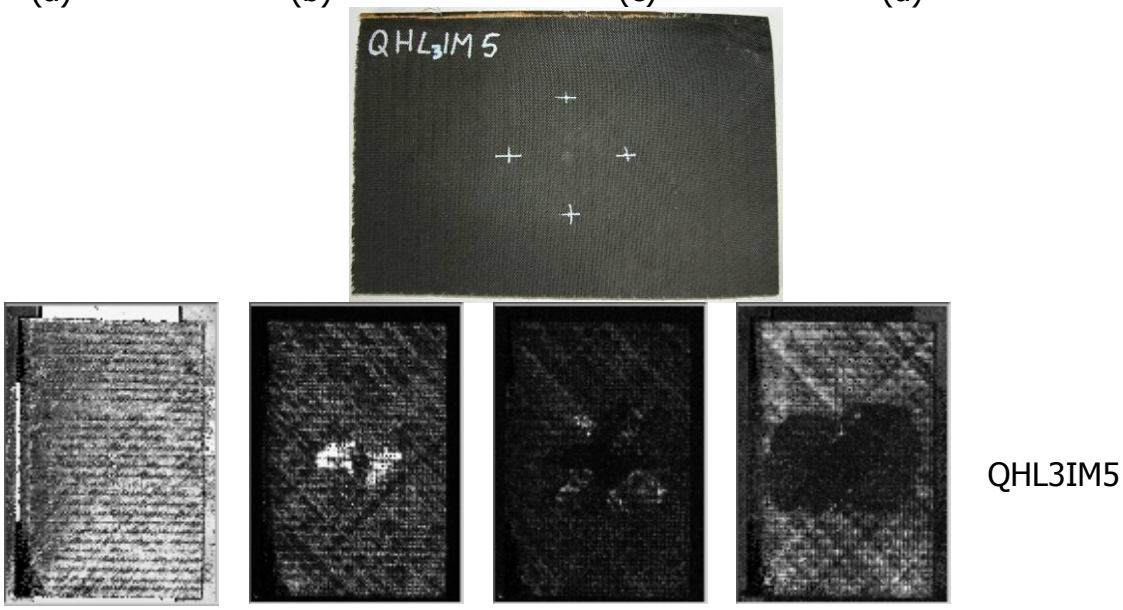

(a) (b) (c) (d)

QHL3IM5

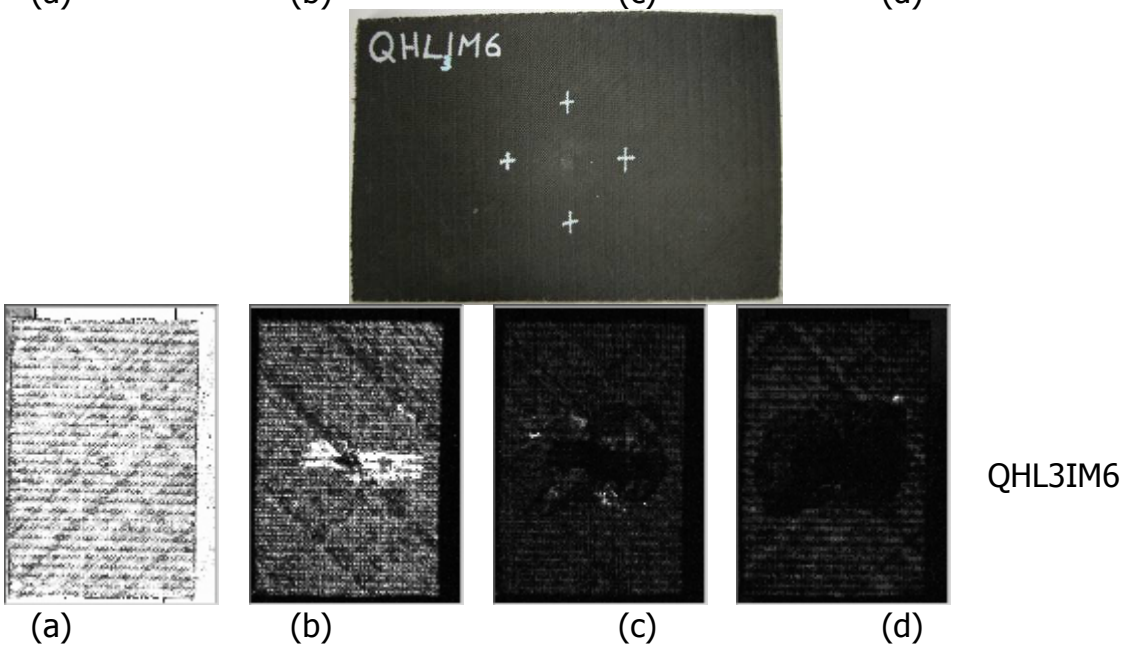

(a) (b) (c) (d)

QHL3IM6

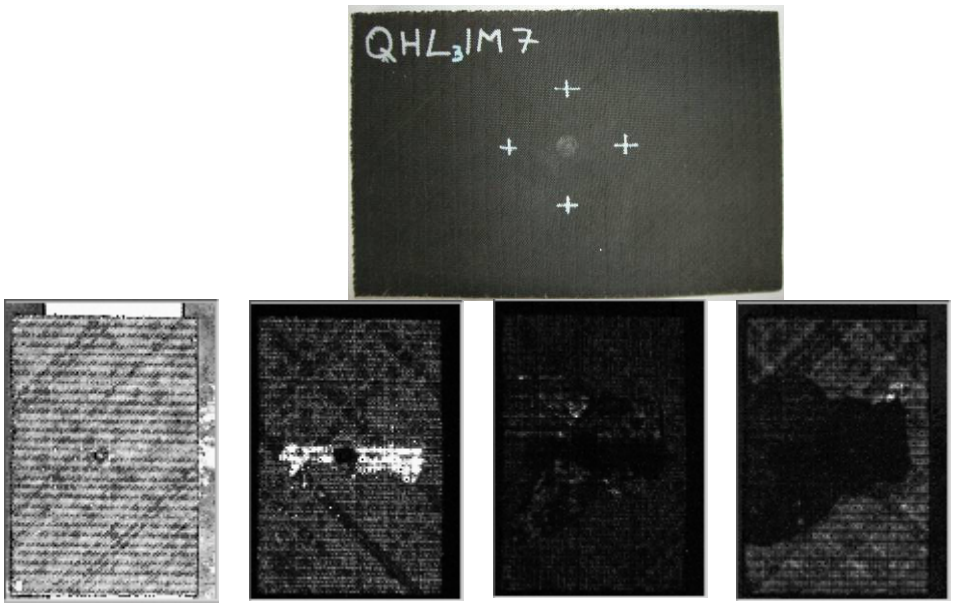

(a) (b) (c) (d)

QHL3IM7

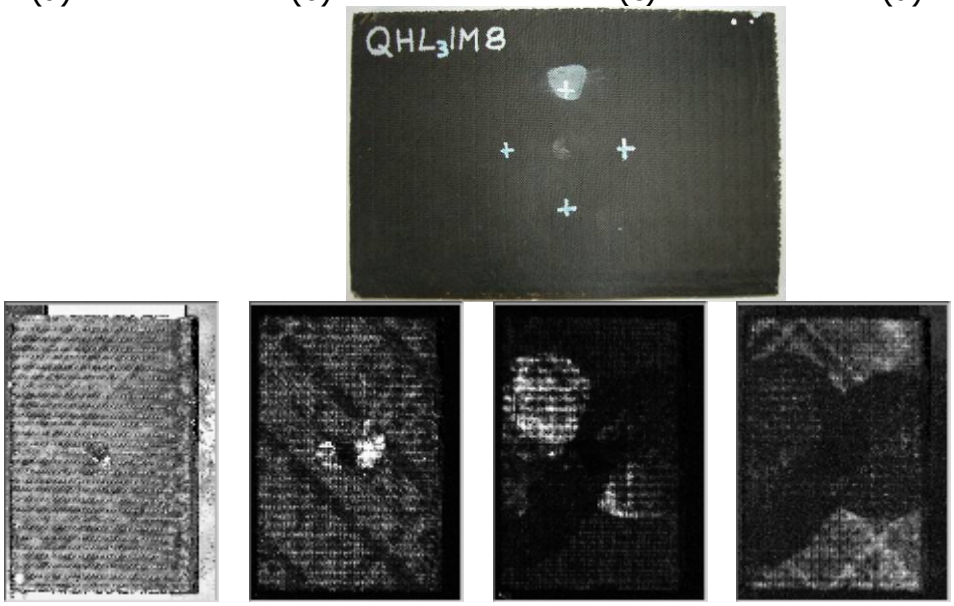

(a) (b) (c) (d)

QHL3IM8

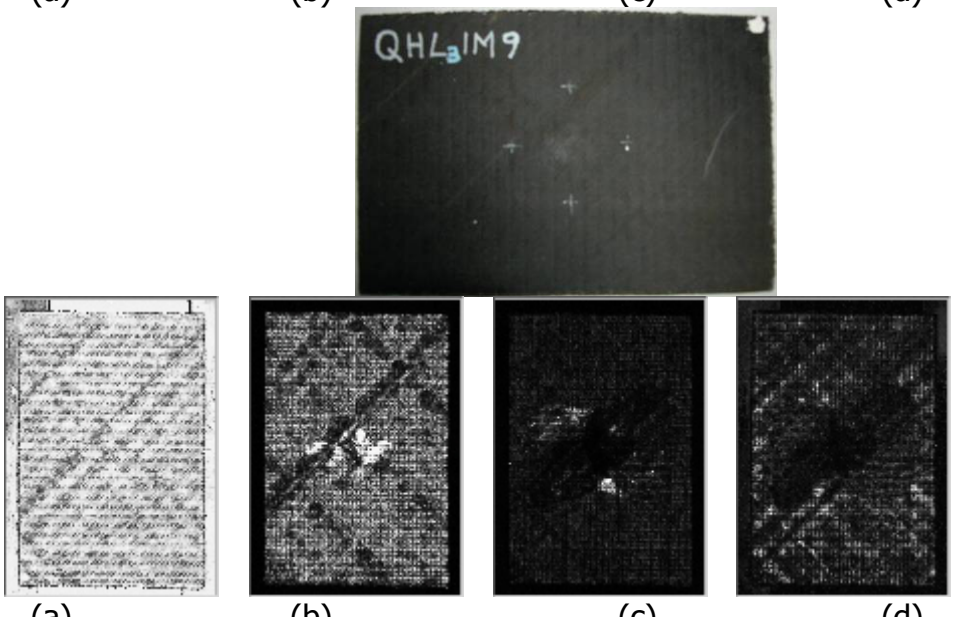

(a) (b) (c) (d)

QHL3IM9

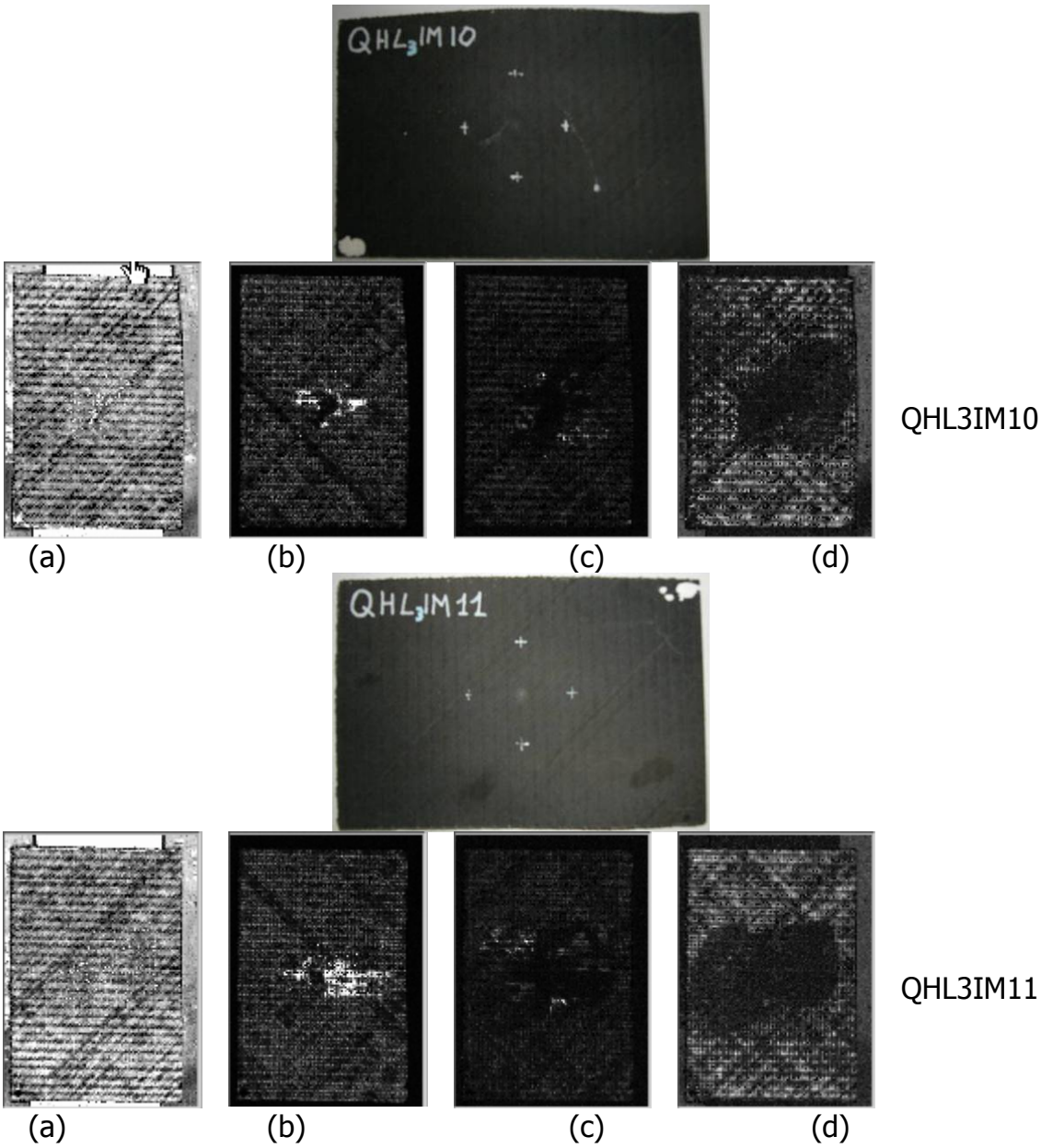

Figure III.24: Quadriaxial laminates impacted with different energies

III.3.6 Experiment Management Control

All test planning and execution was registered in log files. This log files are giving us the opportunity to evaluate the system reliability during diverse number of continuous experiments. This log file system can be useful in order to implement a cost management control, due to possibility to remember all times necessary to a Full Volume Ultrasonic Nondestructive Scan (FV-SCAN). In the Table III.13 is reported one of this log tables.

Table III.13
Management control log file

Non Impacted Laminates	Predicted	Executed	Start time	End time	Comments	Total time ore
QLLIM1-1	28-oct-04	09-nov-04	15.15	17.03	(Realignment) - ok	1.48
QLLIM2-1	28-oct-04	29-oct-04	11.24	13.48	ok	2.24
QLLIM3-1	01-nov-04	09-nov-04	9.31	11.48	(Realignment) - ok	2.17
QLLIM4-1	29-oct-04	29-oct-04	13.56	16.21	Verify - ok	2.25
QLLIM5-1	01-nov-04	02-nov-04	10.17	13.02	Ok	2.45
QLLIM6-1	29-oct-04	10-nov-04	13.29	15.47	(Realignment) - ok	2.18
QLLIM7-1	02-nov-04	02-nov-04	13.11	15.18	ok	2.07
QLLIM8-1	02-nov-04	02-nov-04	15.28	17.19	ok	1.51
QLLIM9-1	29-oct-04	29-oct-04	8.00	11.02	ok	3.02
QLLIM10-1	03-nov-04	03-nov-04	9.09	11.18	ok	2.09
QLLIM11-1	03-nov-04	11-nov-04	9.54	11.41	(Realignment) - ok	1.47
Image processing	11-nov-04	11-nov-04	12.52	17.35	ok	4.43

set 1 Complete

Impacted Laminates	Predicted	Executed	Start time	End time	Comments	Total time
QHL3IM1-1	15-nov-04	15-nov-04	10.02	12.21	ok	2.19
QHL3IM2-1	16-nov-04	16-nov-04	9.48	12.04	ok	2.16
QHL3IM3-1	17-nov-04	17-nov-04	11.33	13.50	ok (Fuse N. 25 brake down)	2.17
QHL3IM4-1	17-nov-04	17-nov-04	15.24	17.41	ok	2.17
QHL3IM5-1	18-nov-04	18-nov-04	9.51	11.36	ok	1.45
QHL3IM6-1	18-nov-04	18-nov-04	12.17	14.34	ok	2.17
QHL3IM7-1	18-nov-04	19-nov-04	8.49	11.08	ok	2.19
QHL3IM7bis-1	19-nov-04	18-nov-04	15.37	17.49	ok	2.12
QHL3IM8-1	19-nov-04	19-nov-04	11.33	13.50	ok	2.17
QHL3IM9-1	19-nov-04	19-nov-04	14.39	16.56	ok	2.17
QHL3IM10-1	22-nov-04	22-nov-04	8.42	10.58	ok	2.16
QHL3IM11-1	22-nov-04	22-nov-04	12.58	15.16	ok	2.18
Image processing	22-nov-04	22-nov-04	11.52	18.25	ok	6.33

set 2 Complete

Non Impacted Laminates	Predicted	Executed	Start time	End time	Comments	Total time
QOL3IM1-1	23-nov-04	23-nov-04	8.43	11.01	ok	2.18
QOL3IM2-1	23-nov-04	23-nov-04	12.47	15.25	ok	2.38
QOL3IM3-1	23-nov-04	23-nov-04	16.25	18.43	ok	2.18
QOL3IM4-1	24-nov-04	24-nov-04	8.45	9.24	ok (Fuse N. 25 brake down)	0.39
QOL3IM4bis-1	24-nov-04	24-nov-04	9.36	11.24	ok	1.48
QOL3IM5-1	24-nov-04	24-nov-04	13.04	15.23	ok	2.19

QOL3IM6-1	24-nov-04	24-nov-04	16.50	19.11	ok	2.21
QOL3IM7-1	25-nov-04	25-nov-04	8.33	10.53	ok	2.20
QOL3IM8-1	25-nov-04	25-nov-04	11.04	13.23	ok	2.19
QOL3IM9-1	25-nov-04	25-nov-04	13.41	16.01	ok	2.20
QOL3IM10-1	26-nov-04	26-nov-04	8.29	10.48	ok	2.19
QOL3IM11-1	26-nov-04	26-nov-04	11.47	14.07	ok	2.20
Image processing	26-nov-04	14-dec-04	10.20	15.50	ok	5.30

set 3 Complete

Non Impacted Laminates	Predicted	Executed	Start time	End time	Comments	Total time
QML3IM1-1	29-nov-04	29-nov-04	12.54	15.14	ok	2.20
QML3IM2-1	29-nov-04	01-dec-04	9.00	11.18	ok	2.18
QML3IM3-1	29-nov-04	01-dec-04	11.35	13.52	ok	2.17
QML3IM4-1	30-nov-04	01-dec-04	14.06	16.26	ok	2.20
QML3IM5-1	01-dec-04	02-dec-04	8.42	11.05	ok (Fuse N. 25 brake down)	2.23
QML3IM6-1	01-dec-04	02-dec-04	12.21	14.41	ok	2.20
QML3IM7-1	02-dec-04	03-dec-04	8.31	10.50	ok	2.19
QML3IM8-1	02-dec-04	03-dec-04	11.34	13.59	ok	2.25
QML3IM9-1	02-dec-04	06-dec-04	9.40	11.31	ok	1.51
QML3IM10-1	03-dec-04	06-dec-04	11.43	13.32	ok	1.49
QML3IM11-1	03-dec-04	06-dec-04	13.44	16.04	ok	2.20
Image processing	03-dec-04	14-dec-04	15.51	18.25	ok	2.34

set 4 Complete

Impacted Laminates	Predicted	Executed	Start time	End time	Comments	Total time
QLL3IM1-1	06-dec-04	09-nov-04	15.15	17.03	ok	1.48
QLL3IM2-1	06-dec-04	06-dec-04	16.34	18.52	ok	2.18
QLL3IM3-1	06-dec-04	07-dec-04	8.38	11.01	ok	2.23
QLL3IM4-1	06-dec-04	07-dec-04	11.15	13.33	ok	2.18
QLL3IM5-1	07-dec-04	07-dec-04	13.40	16.00	ok	2.20
QLL3IM6-1	07-dec-04	07-dec-04	16.15	18.35	ok	2.20
QLL3IM7-1	07-dec-04	09-dec-04	9.33	11.19	ok	1.46
QLL3IM8-1	09-dec-04	09-dec-04	13.52	16.10	ok	2.18
QLL3IM9-1	09-dec-04	10-dec-04	8.54	11.10	ok	2.16
QLL3IM10 incomplete-1	09-dec-04	10-dec-04	13.13	13.52	ok (Fuse N. 25 brake down)	0.39
QLL3IM10-1	09-dec-04	10-dec-04	13.59	16.18	ok	2.19
QLL3IM11-1	10-dec-04	10-dec-04	16.29	18.44	ok	2.15
Image processing	15-dec-04	15-dec-04	11.15	15.37	ok	4.22

set 5 Complete

Impacted Laminates	Predicted	Executed	Start time	End time	Comments	Total time
QML3IM1-1	10-dec-04	23-nov-04	8.43	11.01	ok	2.18
QML3IM2-1	10-dec-04	13-dec-04	11.23	13.58	ok	2.35

QML3IM3-1	10-dec-04	13-dec-04	14.53	17.20	ok	2.27
QML3IM4-1	13-dec-04	14-dec-04	8.46	11.01	ok	2.15
QML3IM5-1	13-dec-04	14-dec-04	11.55	14.09	ok	2.14
QML3IM6-1	13-dec-04	14-dec-04	14.27	16.50	ok	2.23
QML3IM7-1	14-dec-04	15-dec-04	8.41	11.03	ok	2.22
QML3IM8-1	14-dec-04	15-dec-04	11.21	13.54	ok	2.33
QML3IM9-1	14-dec-04	15-dec-04	15.32	17.54	ok (Fuse N. 25 brake down)	2.22
QML3IM10-1_bad	15-dec-04	16-dec-04	8.29	10.38	Stopped at 150/155	2.09
QML3IM10-1	15-dec-04	16-dec-04	16.43	18.27	Ok	1.44
QML3IM11-1	15-dec-04	16-dec-04	10.50	12.32	Ok	1.42
Image processing	15-dec-04	17-dec-04	11.40	18.06	ok – Other PC used	6.26

set 6 Complete

Impacted Laminates	Predicted	Executed	Start time	End time	Comments	Total time
QOL3IM1-1	16-dec-04	09-nov-04	15.15	17.03	ok	1.48
QOL3IM2-1_bad	16-dec-04	16-dec-04	12.45	14.10	Power switch shut down	1.25
QOL3IM2-1	16-dec-04	16-dec-04	14.22	16.36	ok	2.14
QOL3IM3-1	16-dec-04	17-dec-04	9.01	11.20	ok	2.19
QOL3IM4-1	16-dec-04	17-dec-04	11.50	14.10	ok	2.20
QOL3IM5-1	17-dec-04	17-dec-04	14.30	16.50	ok	2.20
QOL3IM6-1	17-dec-04	17-dec-04	17.00	19.20	ok	2.20
QOL3IM7-1	17-dec-04	20-dec-04	8.41	11.03	ok	2.22
QOL3IM8-1	20-dec-04	20-dec-04	11.21	13.54	ok	2.33
QOL3IM9-1	20-dec-04	20-dec-04	15.32	17.54	ok (Fuse N. 25 brake down)	2.22
QOL3IM10-1	20-dec-04	21-dec-04	10.09	12.28	ok	2.19
QOL3IM11-1	21-dec-04	21-dec-04	12.39	15.04	ok	2.25
Image processing	21-dec-04	21-dec-04	15.15	19.37	ok	4.22

set 7 Complete

III.3.7 Conclusions

An innovative 3D UT NDE system, based on complete UT waveform detection and processing, was utilized to carry out the full volume-scanning of impacted biaxial and quadriaxial NCF composite laminates. The measurement and comparison of the volumetric damage development in the advanced composites made by the RIFT technology was performed through UT image analysis.

The results obtained showed that the biaxial NCF laminates performed better than the quadriaxial ones in terms of internal damage development. Moreover, by comparing the NCF laminates with classical composite laminates subjected to the same impact conditions, in NCF material it is possible to observe a much more reduced and circumscribed delamination damage.

III.4. Glass fiber reinforced propylene (GFRP) bonding

III.4.1 Introduction

Polymer matrix composite materials present a large number of applications in various industrial fields where high mechanical properties and low specific weight are requested. The most common composite materials for structural and non-structural applications utilize a thermoset matrix such as epoxy, polyester, etc. Composite materials with a thermoplastic matrix are less utilised because of not yet solved problems regarding their fabrication technology and specific behaviour aspects (e.g. high temperature resistance).

The collaborative research activities between the Department of Materials and Production Engineering of the University of Naples Federico II and the ENEA Research Centre of Brindisi focus on the application of thermoplastic matrix composite materials in the fabrication of parts for the rail transportation industry.

In particular, the quality evaluation of bonded joints in terms of mechanical strength and structural integrity was carried out to verify the possibility to employ commercial adhesive types to realise bonded joints between panels made of thermoplastic composite materials for internal furnishing elements of rail carriages.

The mechanical resistance of a bonded joint depends on various factors:

- bonding surface;
- thickness of the adhesive;
- properties of the adhesive;
- adhesion of the bond on the two joining surfaces;
- elastic properties of the joint.

In this work, glass fibre reinforced propylene (GFRP) matrix composite panels were utilised. Like other thermoplastic resins, this matrix material presents an insufficient chemical affinity with most of the available commercial adhesives. Accordingly, the joint geometrical parameters have been purposely set up and two adhesive types were selected as those presenting the best requirements for these composite materials. The joint quality was assessed by destructive tensile testing and ultrasonic (UT) nondestructive evaluation (NDE) on single-lap bonded joints.

III.4.2 Materials and Mechanical testing

Glass fibre reinforced thermoplastic polypropylene resin (commingled TWINTEX cloth) panels with weft-warp configuration 0°/90° for an average thickness of 2.5 mm were used to obtain the experimental samples. Panels were fabricated by hot press forming at the CETMA Laboratories, Brindisi, Italy.

For the mechanical characterisation of the adhesives, the ASTM D 5868 standard was considered. This standard provides for the single-lap sample scheme reported in Figure III.25. The single-lap samples were cut from the panels according to the scheme shown in Figure III.26. Two series of samples were fabricated:

- 1st series - obtained by sample cutting with a diamond coated blade;
- 2nd series - obtained by sample cutting with abrasive water-jet process.

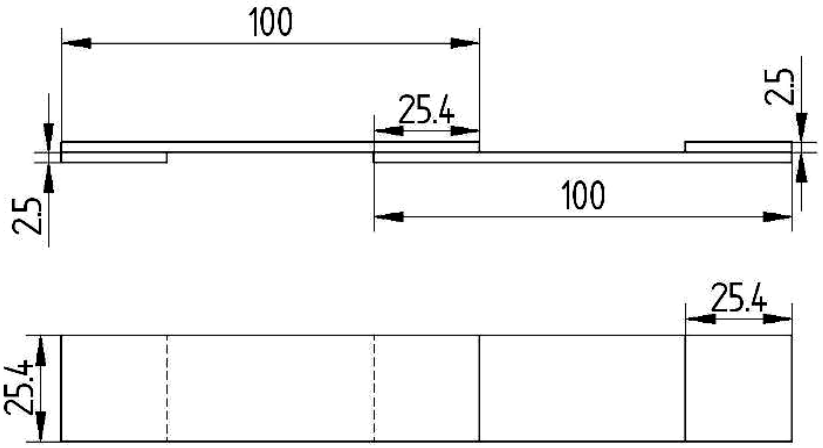

Figure III.25: Geometry and dimensions of single-lap joint.

The 2nd series samples were prepared because the traditional diamond saw cutting can easily damage the thermoplastic matrix due to local temperature increase, even when using a refrigerating fluid. As a matter of fact, the abrasive water-jet cutting process does not produce a temperature increase in the cutting area.

Two commercial structural acrylic bi-component adhesives were considered:

- 3M Scotch-Weld type 8005 (lower work life: 3 min)
- 3M Scotch-Weld type 8010 (higher work life: 12 min)

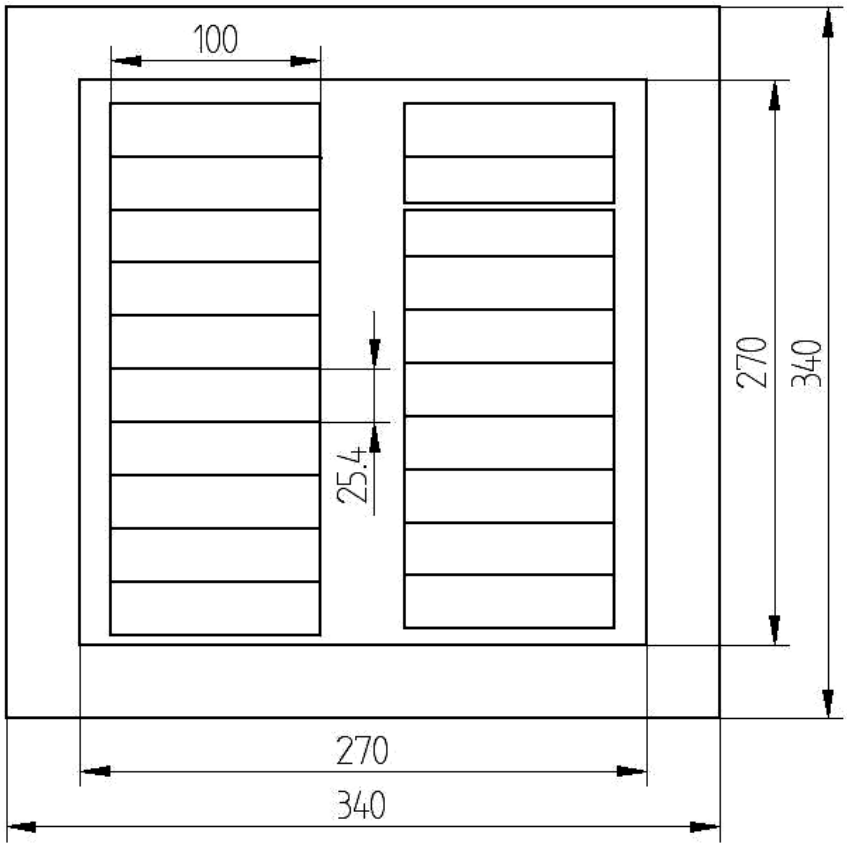

Figure III.26: GFRP panels and cutting scheme.

A suitable manual applicator EPX type was used to obtain the correct components mixture (ten parts by volume of base material and one part of catalytic material). The theoretical bonding area (see Figure III.25) is 25.4 mm x 25.4 mm, with adhesive

thickness varying between 0.25 mm and 0.30 mm. The adhesive layer thickness variation is the consequence of the non uniform thickness of the composite panels and the bonding procedure carried out by sandwiching a distancing insert amid the two glass plates between which the samples to be joined are positioned. During bonding, some differences due to adhesive properties were found. Both adhesives require a time period after mixing the two components. Technical specifications indicate that for the 8005 adhesive the time of application must be lower than 2.5 – 3 minutes while for the 8010 adhesive type the application must occur before 10 – 12 minutes. Beyond application time, the adhesive assumes a gelatinous consistency with a high viscosity that makes the adhesive unusable.

Bonding tests allowed to verify the application time suggested in the technical documentation for each adhesive type. The nominal application times (adhesive work life) resulted overrated and their actual values are ≈ 50% of the suggested times. In the 1st series samples, the bonding was obtained with the adhesive at room temperature (≈ 22°C). To increase the adhesive application time for the 2nd series samples and have available enough time to realise a perfect alignment between panels, adhesive cartridge and panels were kept in a low temperature environment (a common refrigerator was used). Moreover, for both adhesive types, a 24 h curing time at 22°C was applied before mechanical testing. Reinforcement tabs were bonded on the single-lap sample extremities (see Figure III.25) for sample alignment during tensile testing on a MTS Alliance RT/50 electro mechanical machine with a 50 kN load cell. The tensile tests were carried out under displacement control and at a constant transverse velocity of 5 mm/min.

III.4.3 Ultrasonic testing

Before mechanical testing, all single-lap joint samples were subjected to a volumetric UT scanning procedure (FV-Scan) using the custom made software package Robotest© v2.0. Pulse-echo volumetric UT scans were carried out with focused, high frequency (5 or 10 MHz) immersion transducers with focal distance 50 or 100 mm. In this work, the 100 mm (50 mm) nominal focal length UT probe was set at 95.7 mm (45.7 mm) from the single-lap joint sample front surface to focus the UT beam at mid-joint. Water and GFRP material UT speeds were 1483 m/s and 2562 m/s, respectively.

In this work, UT testing was carried out using the Full Volume Scan (FV-Scan) procedure. This type of scan consists in detection and digitization of the whole UT waveform for each material interrogation point during scanning. At the end of scan, UT data are saved in volumetric files containing the whole set of complete UT waveforms. From the UT volumetric file, UT images for any segment of the UT signal, i.e. for any portion of the material thickness, can be obtained and analyzed. The software also allows to retrieve single UT waveforms corresponding to any given in-plane location by mouse clicking on the UT image. The digital oscilloscope was set at 0.5 Volts/div, 0.5 μs/div and sampling frequency 100 MHz, resulting in 1000 samplings for each complete UT waveform. For each single-lap joint sample, a 40 mm x 40 mm area over the bonding was scanned according to the boustrophedon scheme with a 0.5 mm scan step.

III.4.4 Mechanical results

In Figures III.27 and III.28, the results of the tensile tests on the 1st and 2nd series single-lap samples are reported as stress vs. displacement curves. In Tables III.14 and III.15, maximum stress and elongation at failure are listed.

Table III.14
1st series single-lap joint samples tensile test results

Sample ID	Adhesive	Maximum stress (Mpa)	Elongation at failure (mm)	Adhesive thickness (mm)
P0a	8005	4.50	7.36	0.26
P0b	8005	4.98	3.28	0.29
P0c	8005	4.56	3.08	0.27
P1a	8005	4.54	5.94	0.29
P1b	8005	3.64	2.49	0.28
P1c	8005	7.61	7.22	0.26
P0d	8010	5.8	2.23	0.28
P0e	8010	7.08	3.50	0.28
P0f	8010	5.54	4.05	0.29
P1d	8010	5.96	4.82	0.29
P1e	8010	4.44	5.29	0.25
P1f	8010	5.48	2.62	0.28
P3d	8010	6.57	6.61	0.28
P3e	8010	3.90	3.04	0.27
P3f	8010	6.69	6.65	0.29

Table III.15
2nd series single-lap joint sample tensile test results

Sample ID	Adhesive	Maximum stress (Mpa)	Elongation at failure (mm)	Adhesive thickness (mm)
A1.1	8005	3.69	1.15	0.28
A1.2	8005	6.06	3.40	0.30
A1.3	8005	6.44	2.03	0.27
A2.1	8005	5.06	1.55	0.28
A2.2	8005	6.62	2.71	0.28
A1.4	8010	5.51	1.96	0.26
A1.5	8010	5.67	2.62	0.26
A1.6	8010	5.05	2.60	0.28
A3.1	8010	5.78	2.33	0.25
A3.2	8010	5.20	2.27	0.25

The 2nd series samples, prepared with an improved bonding procedure in comparison with the 1st series samples and cut by an abrasive water-jet process, present a higher repeatability in the tensile test results (Table III.15). In particular, the elongation at failure presents similar values for all tested samples, ranging between 1.15 and 3.40 mm. Moreover, the elongation at failure is notably reduced in comparison with the 1st series samples (Table III.15). This behaviour can be due to the fact that the adhesive and the bonding procedure used for the 1st series samples did not allow for a thorough polymerisation.

The maximum stress value is lower than 8 MPa whereas the value declared by the

adhesive producer is 13 MPa for both adhesive types.

By macroscopic analysis of the fractured samples, it can be seen that the fracture surfaces (see Figures III.29 and III.30) develop exclusively at the interface between the adhesive layer and the sample surface, without damaging the composite material fibres.

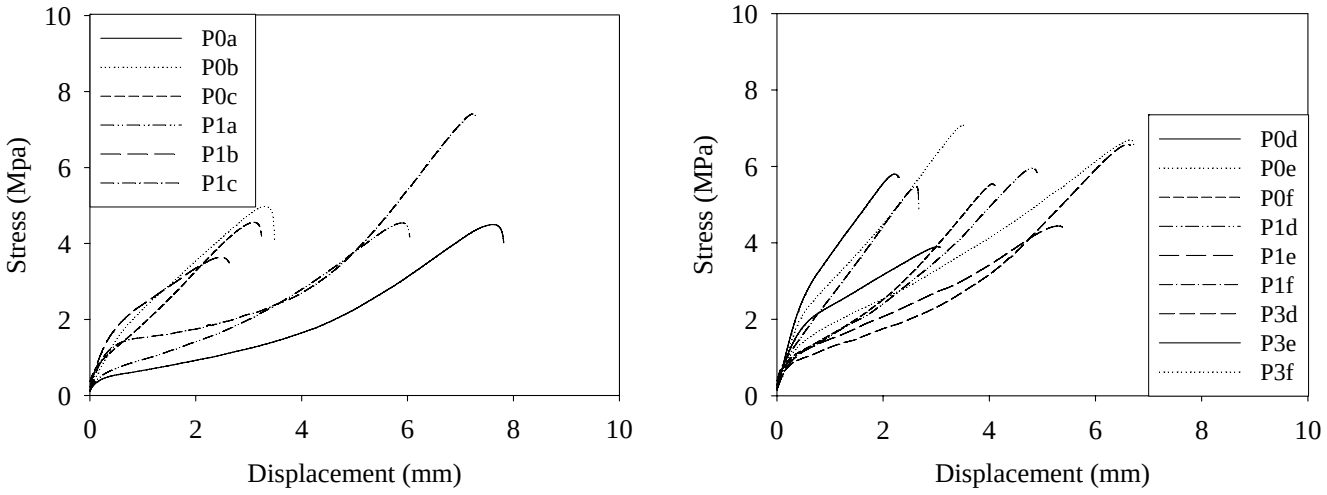

(a) (b)

Figure III.27: 1st series single-lap joint samples tensile tests:
(a) 8005 adhesive, (b) 8010 adhesive

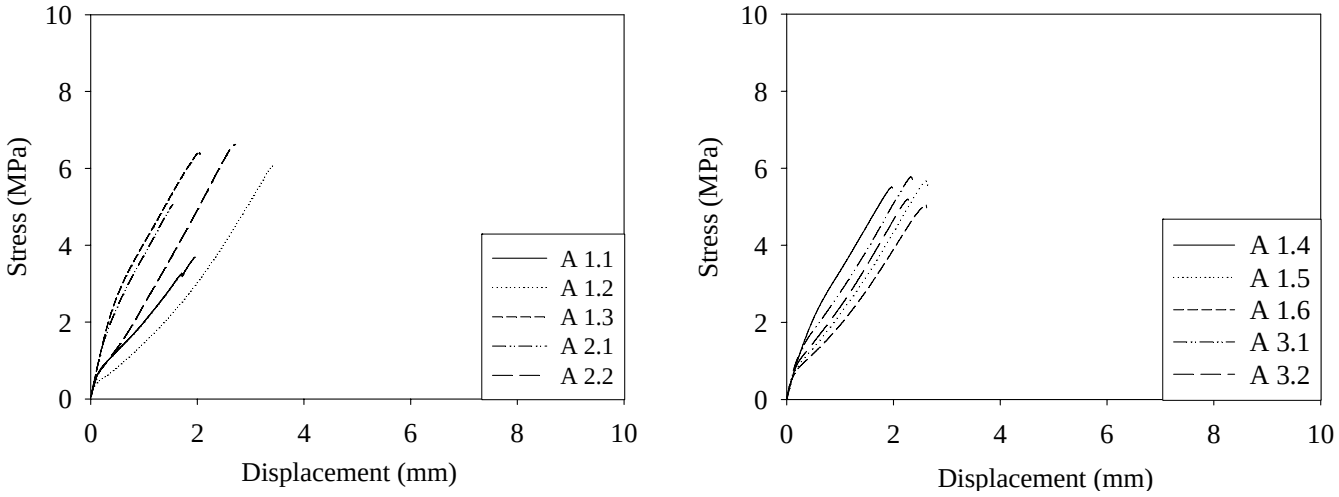

(a) (b)

Figure III.28: 2nd series single-lap joint samples tensile tests:
(a) 8005 adhesive, (b) 8010 adhesive

Figure III.29: 2nd series – Fracture surfaces of the single-lap joint samples bonded with the 8005 adhesive.

Figure III.30: 2nd series – Fracture surfaces of the single-lap joint samples bonded with the 8010 adhesive.

III.4.5 Ultrasonic testing results

In Figures III.31 – III.34, UT images from FV scans of 1st and 2nd series single-lap joint samples, bonded with the 8010 and 8005 adhesives, are reported.

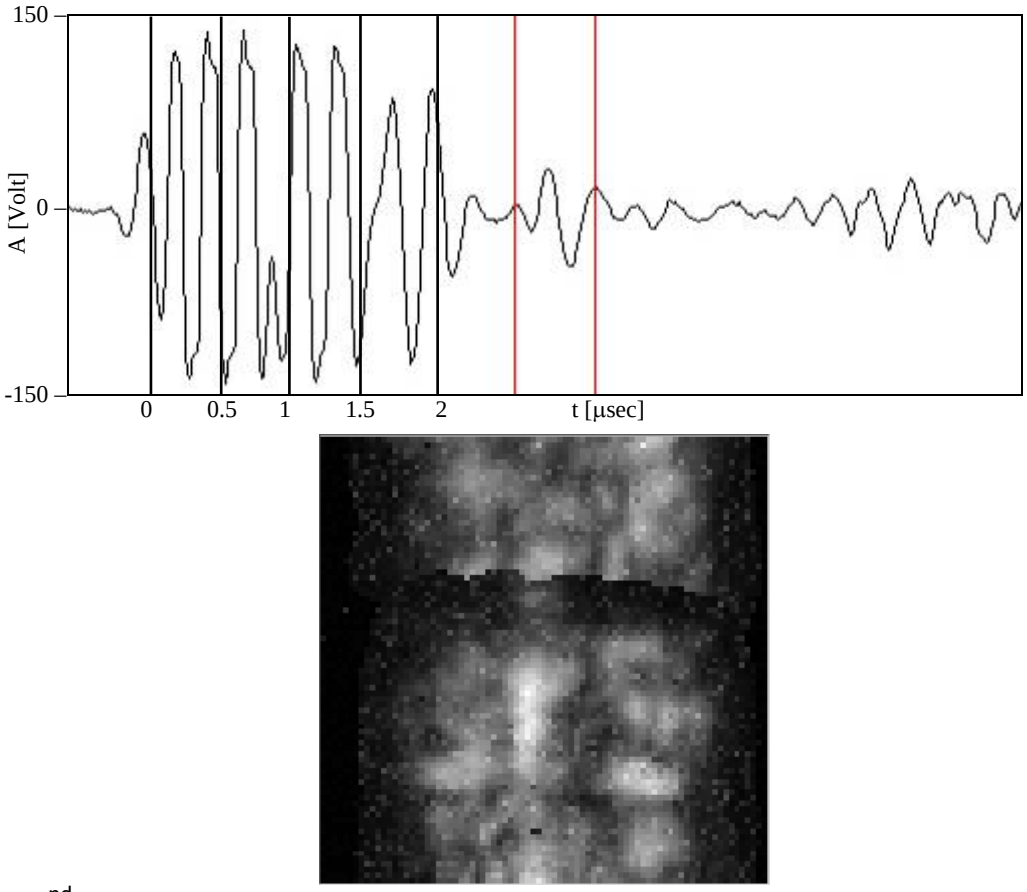

Figure III.31: 2nd series adhesive 8010, step 0.5 mm, frequency 5 MHz, scan area 40 x 40 mm^2

All UT images are obtained by time gating (vertical red lines) the UT signal portion corresponding to the joint interface, including adhesive thickness. Images display the in-plane UT portrayal of the entire bonded area. FV scans were carried out with 5 and 10 MHz probes. The lower frequency was used to account for the high UT attenuation in thermoplastic composites and the higher frequency to obtain improved resolution UT images.

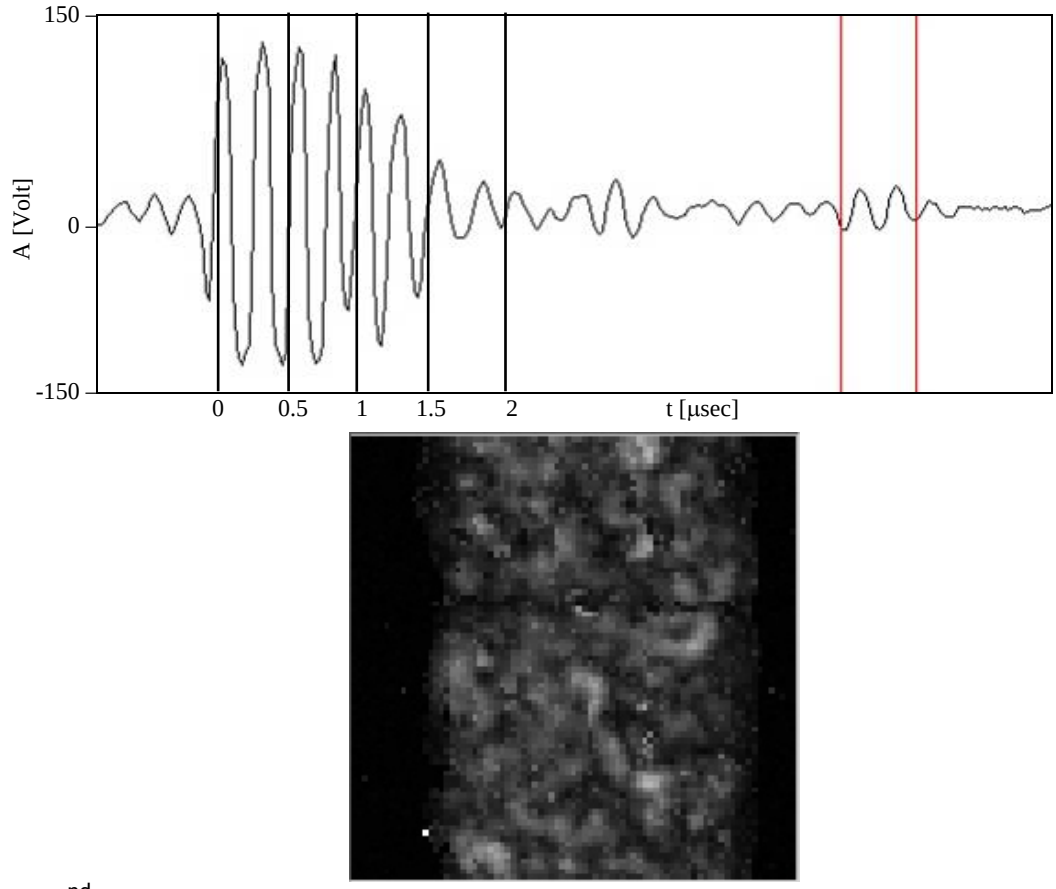

Figure III.32: 2nd series adhesive 8010, step 0.5 mm, frequency 10 MHz, scan area 40 x 40 mm^2.

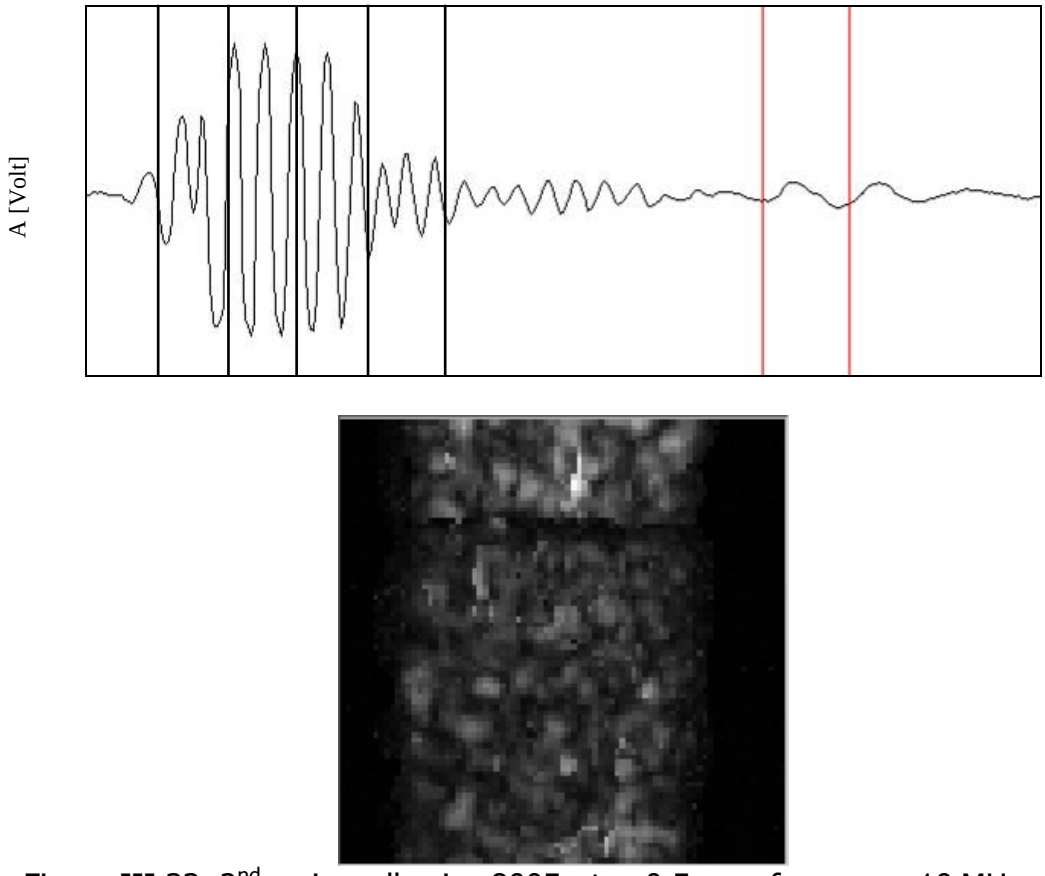

Figure III.33: 2nd series adhesive 8005, step 0.5 mm, frequency 10 MHz, scan area 40 x 40 mm^2.

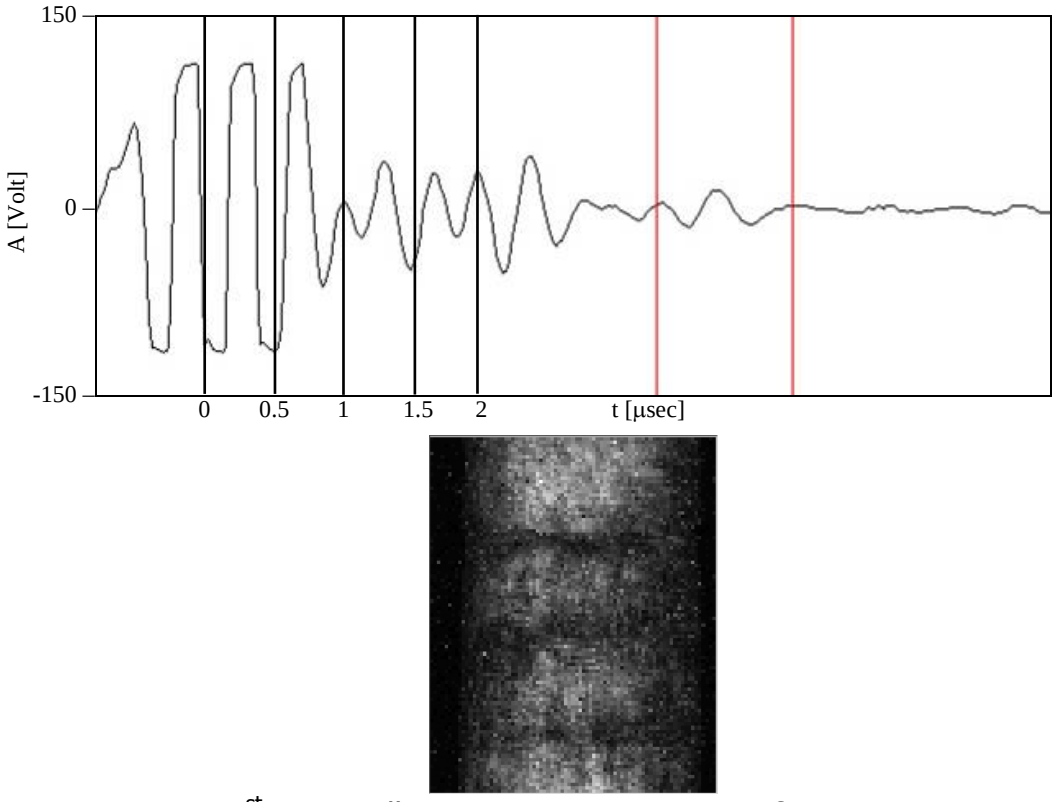

Figure III.34: 1st series adhesive 8005, step 0.5 mm, frequency 10 MHZ, scan area 40 x 50 mm^2.

As a matter of fact, the 5 MHz probe allowed for the complete UT signal penetration of the single-lap joints and bond area UT images could be reliably generated (see Figure III.31). The 10 MHz UT signal could not traverse the entire single-lap joint; in pulse-echo mode, this condition is generally not advised for UT scanning and the higher resolution due to higher frequency is not utilizable for image analysis.

However, though the UT signal could not reach the single-lap joint back surface, it reached and included the bonding area at mid-lap joint, as verified through time-of-flight thickness measurements: the joint interface is encountered by the signal at 1.7 μs and completely traversed at 2.4 μs from the front echo (Δmax = 0.7 μs). If the UT time gate is set over this time interval, the reliable generation of improved resolution UT images, illustrative of the bonding area, is achieved (Figures III.32 and III.34). Accordingly, the 10 MHz UT scans were considered for single-lap joint quality assessment through UT image analysis.

Figures III.31 and III.32 report UT images from 2nd series 8010 adhesive single-lap samples FV scanned with 5 MHz and 10 MHz UT probes, respectively. It can be easily seen that the resolution provided by the 10 MHz UT probe is decidedly superior.

Figures III.32 and III.33 show UT images from 10 MHz FV scans of 2nd series samples bonded with the 8010 and 8005 adhesive. No significant bond defect (non homogeneity, delamination, inclusions) is seen, suggesting the two adhesives yield the same bond quality. Figure III.34 shows the UT image from a 1st series sample bonded with 8005 adhesive and scanned with 10 MHz. Here, the joint area shows evident horizontal dark lines, revealing a prominent non homogeneity in the bond.

This low bond quality can be due to the procedure for 1st series samples preparation, where bonding was performed at room temperature and application time was the one suggested by the adhesive producer. As the actual adhesive work life was found

to be 50% shorter than the declared one, the 1st series samples may not have achieved a thorough adhesive polymerization in the joint, yielding the poor bond quality evidenced by the UT image analysis.

III.5. Insulated gate bipolar transistor (IGBT) assembly devices

III.5.1 Introduction

Insulated Gate Bipolar Transistor (IGBT) assembly devices are widely utilized for variable-speed drives in industry and are now increasingly gaining interest for railways transportation applications because of their recently enhanced capability to manage high blocking voltages and high currents. Raising power demands, higher power densities, higher switching speeds and augmented reliability constraints call for adequate IGBT design taking into consideration thermal aspects and the use of advanced materials.

During operation, the IGBT assembly device thermal joints are stressed by a very large number of temperature variation cycles (5 to 10 million cycles for 30 years service life of railway equipment) with amplitude > 40 °C. A critical aspect in IGBT assembly device thermal design is, therefore, the selection of joint materials with high temperature resistance and similar thermal expansion coefficient (TCE) to avoid IGBT assembly structure delamination and component cracking, ultimately resulting in the device catastrophic failure. Metal matrix composites (MMC) for IGBT assembly device construction can provide significant benefits to thermal design due to their relatively high temperature resistance and intrinsic capability to be adjusted, at the material design stage, to the required thermal behaviour.

The main concern in the inspection of IGBT assembly devices is the quality assessment of joint material integrity. Traditional inspection procedures are based on complex and expensive thermal resistance measurements that provide only limited accuracy.

In the present research work, an alternative quality assurance approach is proposed whereby a thoroughly non-destructive inspection (NDI) method, based on ultrasonic (UT) testing, is applied to the IGBT assembly device at preset service time intervals. UT testing in the pulse-echo mode offers the advantage of using a single transmitter/receiver probe so that only one side of the IGBT assembly structure needs to be accessible. Moreover, by employing UT immersion scanning with full waveform acquisition and analysis, it is possible to inspect the entire volume of the IGBT assembly structure. This method appears, therefore, particularly suited for the NDI testing of thermal cycle stressed IGBT assembly devices.

III.5.2 IGBT assembly device structure

IGBT assembly layers

The structure of the IGBT assembly device under consideration is composed of various layers of different materials and thicknesses (Figure III.35). The baseplate is an aluminium matrix silicon carbide (AlSiC) particle reinforced MMC with particle volume fraction Vp = 63%. An aluminium nitride (AlN) ceramic layer, between two copper (Cu) layers, is placed on top of the AlSiC MMC baseplate. The bottom copper layer is soldered to the baseplate and the upper copper layer is soldered to the IGBT silicon (Si) chipset. The electrical emitter and gate contacts are made of Al pads wire bonded on the chipset. The IGBT assembly package (Figure III.36) is filled with silicone gel for electrical insulation, corrosion resistance and prevention of shear stress on the bond wires.

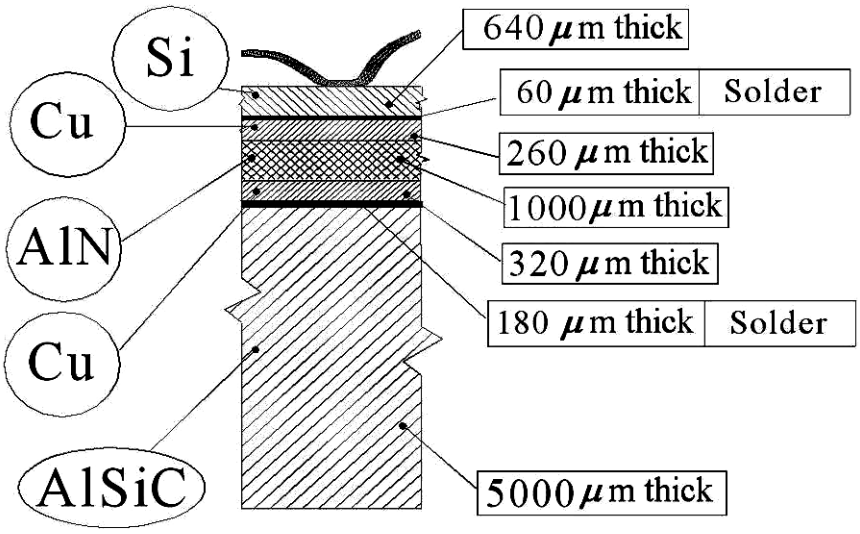

Figure III.35: IGBT assembly device structure (thickness in μm).
AlSiC = MMC baseplate; AlN = aluminium nitride ceramic layer; Cu = copper layers on top and bottom of the AlN ceramic layer; Si = silicon chipset.

IGBT assembly materials

The AlSiC MMC was chosen as baseplate material because of its thermal coefficient of expansion (TCE), matching the AlN ceramic layer TCE, and its sufficiently high thermal conductivity, κ, for efficient heat dissipation (Table III.16). Matching the AlSiC MMC baseplate TCE to other IGBT assembly materials can provide a more than twice longer service life by minimizing thermal stresses that cause high temperature cycle fatigue failure.

Table III.16
Main properties of IGBT assembly materials.

Material	Density (g/cm^3)	TCE (ppm/°C)	Thermal Conductivity (W/mK)	Bend Strengh (MPa)	Young's Modulus (GPa)
Si	2.3	4.2	151	-	112
AlSiC	3.0	6.5-9	170-200	450	290
Cu	8.96	17.8	398	330	131
Al	2.7	23.6	238	137-200	68
SiC	3.2	2.7	200-270	450	415
AlN	3.3	4.5	170-200	300	310
Alumina	3.98	6.5	20-30	300	350

The AlSiC TCE can be adjusted to IGBT design requirements by controlling the MMC SiC particle volume fraction, Vp: a Vp = 63% was selected for the baseplate providing a TCE = 8.39 ppm/°C (30° - 150°C) and a κ= 180 W/mK. IGBT assembly devices with AlSiC baseplates have equivalent power dissipation and more than two-fold higher reliability over the same devices with a Cu baseplate of traditional design (Cu TCE = 17 ppm/°C and a κ = 398 W/mK). The ceramic layer (Figure III.37) on the top of the AlSiC baseplate is made of AlN because of its remarkably high thermal conductivity as a ceramic material (Table III.16). The high thermal conductivity coupled with high dielectric strength leads to

its application as substrate and packaging for high power or high density microelectronic assembly.

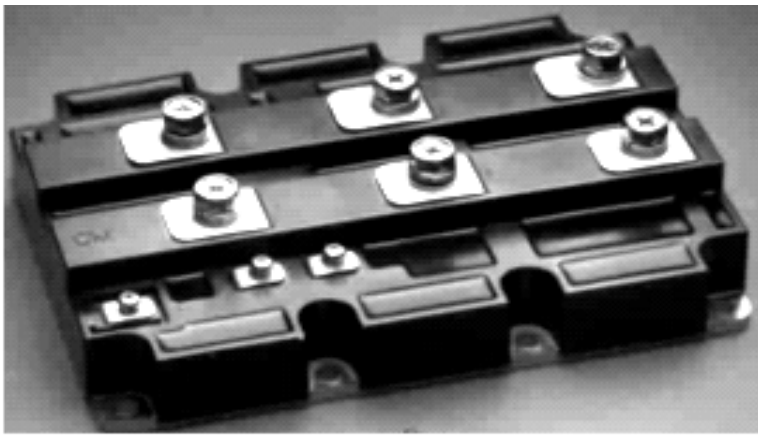

(a)

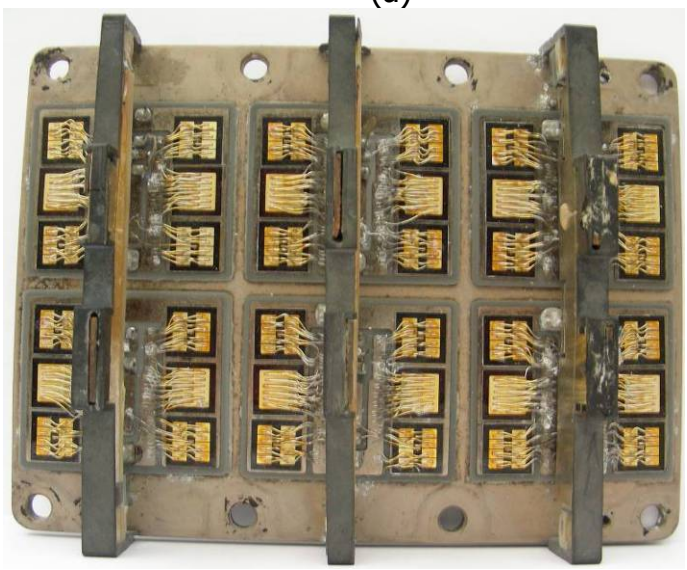

(b)

Figure III.36: IGBT assembly device: (a) external view, (b) internal view.

Figure III.37: Layout of the AlN ceramic layer.

IGBT thermo-mechanical cycling

The IGBT assembly device is a package basically made of 3 soldered layers (AlSiC MMC baseplate, AlN ceramic layer, Si chipset) that form two principal soldered joints:

- AlSiC MMC baseplate upper surface and AlN ceramic layer bottom side;
- AlN ceramic layer top side and IGBT Si chipset bottom surface.

IGBT assembly devices are traversed by a high variable electrical current intensity inducing a thermo-mechanical fatigue at the joint solders due to the different TCE of the AlSiC and AlN materials. The IGBT temperature increases during the accelerating and braking phases when the converter output current is high; the highest temperature attained in a cycle is 125 °C. IGBT assembly devices subjected to thermal fatigue cycling during service were submitted to the FV-Scan UT NDI procedure through the custom made software code ECUS Inspection©.

III.5.3 Results and discussion

UT FV-Scan NDI

The following assemblies were analysed:

(i) a new unsoldered Si chipset tablet (Figure III.38);
(ii) a sound IGBT assembly device after 750 h of accelerated thermal fatigue cycling (45000 cycles) (Figure III.40);
(iii) a failed IGBT assembly device after 750 h of accelerated thermal fatigue cycling (45000 cycles) (Figure III.42).

UT FV-Scans were performed on water immersed IGBT assemblies (see Table III.17). The UT focused probe was positioned in the water so that the UT signal, after travelling in water, entered the assembly, at focal distance and perpendicularly to the assembly plane:

a) from the bottom Cu layer side, in the case of the unsoldered chipset tablet;
b) from the AlSiC MMC baseplate, in the case of the IGBT devices.

The ECUS Inspection© software code allows for the generation of single or multiple UT images of any thickness portion of the internal structure of the examined assembly by processing the volumetric file containing the complete UT waveforms detected during the FV-Scan.

Table III.17
UT FV Scan settings.

	Transducer type	Scan size (mm)	Scan step (mm)
Chipset tablet	2” focused, 15 MHz	X = 62 Y = 52	0.1
Sound IGBT device	2” focused, 15 MHz	X = 189 Y = 143	0.5
Failed IGBT device	2” focused, 15 MHz	X = 191 Y = 141	0.7

To obtain UT images, it is first necessary to select and retrieve a typical UT waveform from the volumetric file. Then, a time gate is set on this waveform to identify the assembly thickness to be imaged. The time gate can be divided into a number of equal sub-gates to obtain multiple images of selected thickness portions. As the time axis orientation corresponds to the UT propagation in the assembly thickness direction, the sub-gate width identifies the assembly thickness portion to be imaged. One image is generated for each sub-gate and each image represents the internal structure of the corresponding portion of the assembly thickness.

Chipset tablet

The unsoldered IGBT 6-chip tablet and its layered structure are shown in Figure III.38. In Figure III.39.a, the typical UT waveform of the chipset tablet UT volumetric file is reported. The UT waveform entered the chipset tablet from the bottom Cu layer side after travelling in water. Thus, the 1st peak from the left is the front echo reflected by the front surface of the bottom Cu layer (water - bottom Cu layer interface: 1st interface encountered by the UT signal). The 2nd peak is the echo reflected by the interface between bottom Cu layer and AlN ceramic layer. The 3rd peak is totally contained in the AlN ceramic layer material. The interface between AlN ceramic layer and upper Cu layer is comprised between the 4th and the 5th peak. The interface between upper Cu layer and Si chip is comprised between the 6th and the 7th peak. The 8th peak is the back echo reflected by the back surface of the Si chip (Si chip – water interface: last interface encountered by the UT signal).

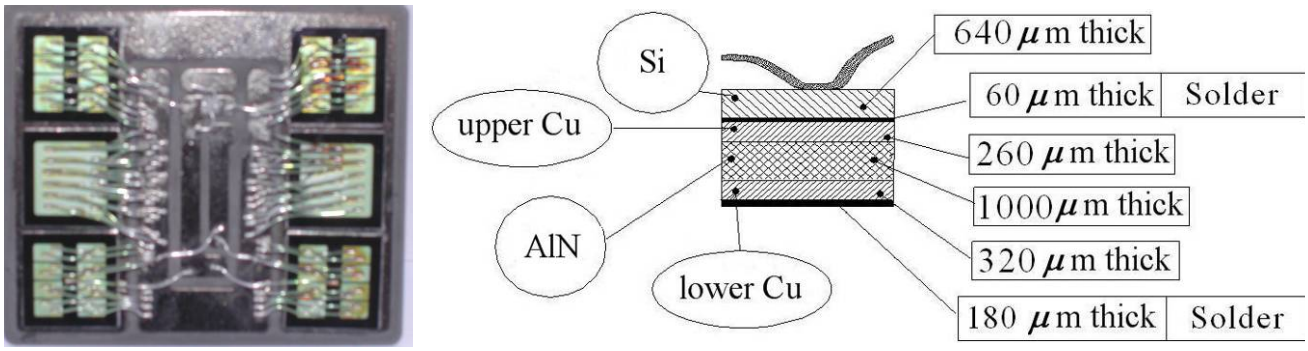

(a) (b)

Figure III.38: (a) Unsoldered IGBT 6-chip tablet; (b) layered structure of the chipset tablet – solder layer between AlSiC and lower Cu layers included (thickness in μm).

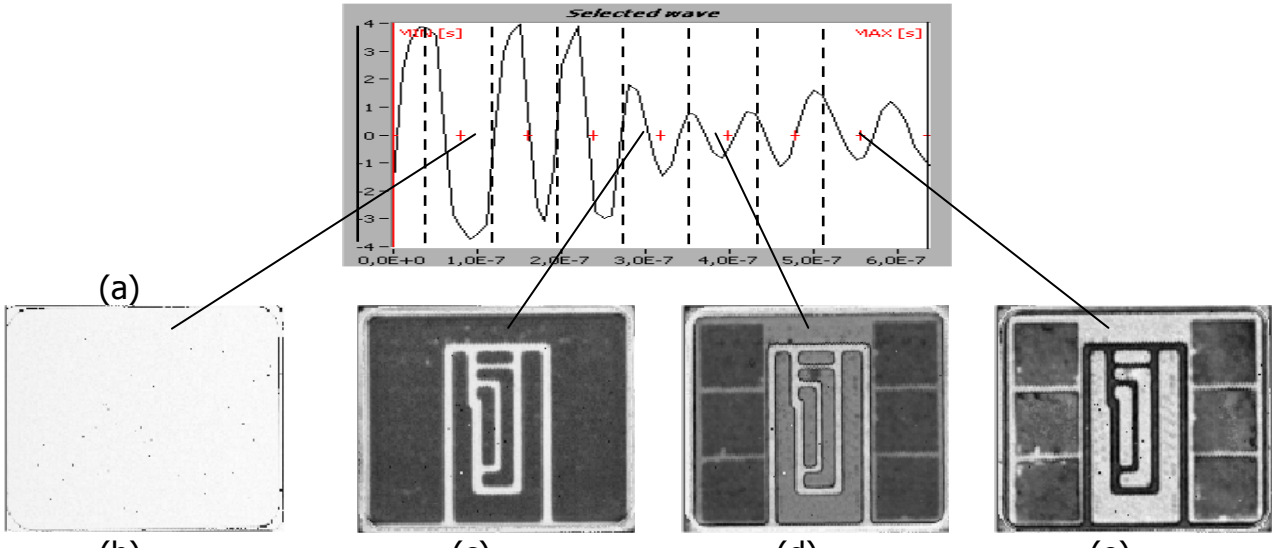

(a)

(b) (c) (d) (e)

Figure III.39: (a) Chipset tablet typical UT waveform with application of time sub-gates (b–e) UT images for selected time sub-gates.

The total time distance between front and back echoes is 0.55 μs; this is the time it takes the UT signal to traverse to and fro the complete chipset tablet layered thickness.

The UT waveform was divided into eight equal time sub-gates of 0.08 μs width so that each sub-gate contained only one peak.

Multiple UT images were generated and, after image analysis, four were considered significant: 2nd sub-gate image of the bottom Cu layer – AlN ceramic layer interface (Figure III.39.b); 5th sub-gate image of the AlN ceramic layer – upper Cu layer interface (Figure III.39.c); 6th sub-gate image of to the upper Cu layer – Si chipset interface (Figure III.39.d); 8th sub-gate image of to the Si chip back surface (Figure III.39.e).

The thickness of the chipset tablet layers was measured through a micrometer and the time-of-flight (TOF) between UT echoes corresponding to the chipset tablet layer interfaces was evaluated through UT waveform analysis. The same was done on unsoldered zones of the AlSiC baseplate. On the basis of thickness and TOF values, the UT velocity of each chipset tablet layer material and of the AlSiC MMC was calculated through equation III.2 and reported in Table 3.

$$V = 2\,d / TOF \qquad \text{(III.4)}$$

Table III.20
UT characterization of IGBT chipset tablet layers and baseplate

Assembly module layer material	Thickness, d (μm)	Time-of-flight, TOF (μs)	UT velocity, V (m/s)
Si chips	640	0.15	8300
Upper soldered layer	60	0.03	4650
Upper Cu layer	260	0.11	4650
AlN ceramic layer	1000	0.18	11100
Lower Cu layer	320	0.14	4650
Lower soldered layer	180	0.08	4650
AlSiC MMC	5000	1.13	8850

IGBT assembly devices

In Figures III.40 and III.42, the sound and failed IGBT devices subjected to UT FV-scan are shown.

In Figures III.41 and III.43, the typical UT waveforms of the sound and failed IGBT volumetric files are reported.

The UT waveforms entered the IGBT assembly devices from the AlSiC baseplate side.

The total time distance between the front echo (AlSiC MMC baseplate front surface) and the back echo (Si chipset back surface) is 1.68 μs; this is the time it takes the UT signal to traverse to and fro the complete IGBT assembly layered structure thickness.

Within this time window, two time sub-gates were selected to obtain information on the principal soldered joints: AlSiC/Cu/AlN joint and AlN/Cu/Si chipset joint.

The AlSiC MMC baseplate thickness is 5 mm and its UT velocity, measured through equation III.2, is 8850 m/s. Thus, the baseplate TOF is 1.13 μs. On the basis of this measurement and the previous chipset tablet UT waveform analysis, the AlSiC/Cu/AlN soldered joint can be inspected by:

(a) setting on the UT waveform a time sub-gate of width 0.12 μs, starting at TOF = 1.13 μs from the front echo and ending at TOF = 1.25 μs,
(b) generating the corresponding UT image (Figures III.41.a and III.43.a).

The AlN/Cu/Si chipset soldered joint can be inspected by:

(a) setting on the UT waveform a time sub-gate of 0.12 μs starting at TOF = 1.62 μs from the front echo and ending at TOF = 1.74 μs,

(b) generating the corresponding UT image (Figures III.41.b and III.43.b).

In Table III.21, the time sub-gate specifications for IGBT soldered joint UT image generation are summarized.

Table III.21
Time sub-gates for IGBT soldered joint UT image generation.

IGBT soldered joint	Time sub-gate start TOF	Time sub-gate end TOF	Time sub-gate width
AlSiC/Cu/AlN	1.13 μs	1.25 μs	0.12 μs
AlN/Cu/Si chipset	1.62 μs	1.74 μs	0.12 μs

Figure III.40: Photo of the sound IGBT device.

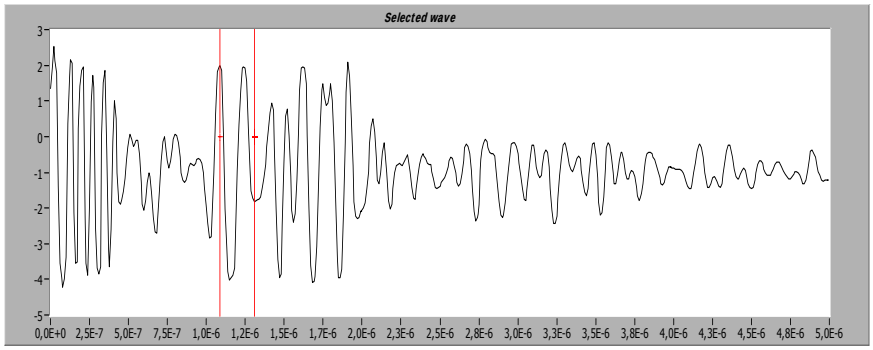

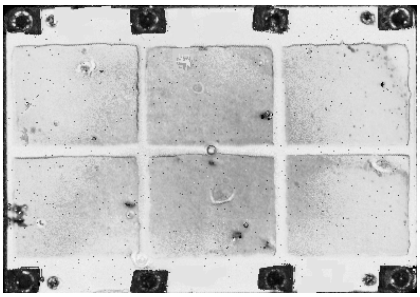

(a) AlSiC/Cu/AlN joint

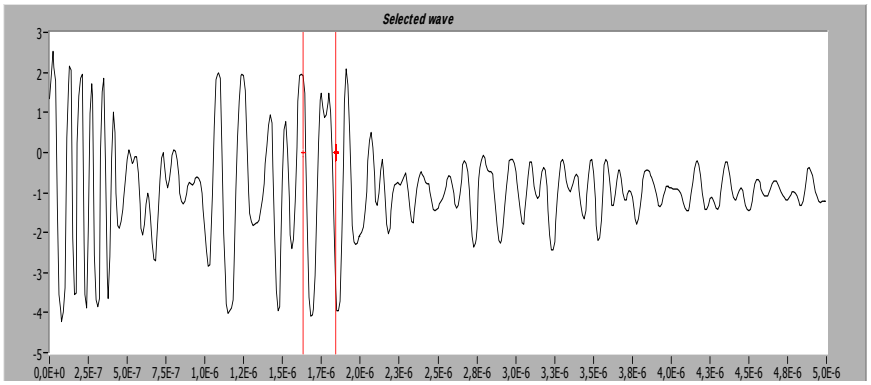

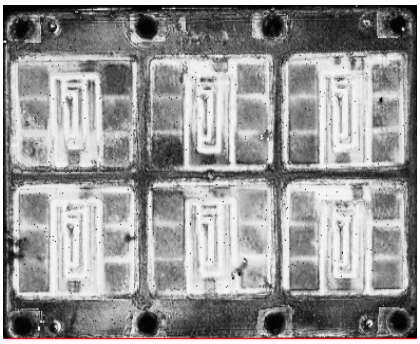

(b) Si chipset back surface

(c) Si chipset back surface detailed upper right chip

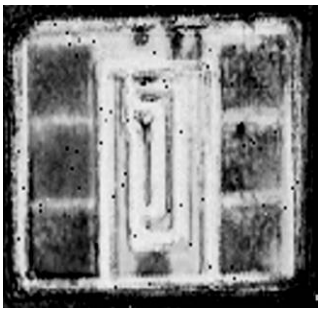

Figure III.41: Sound IGBT assembly device.

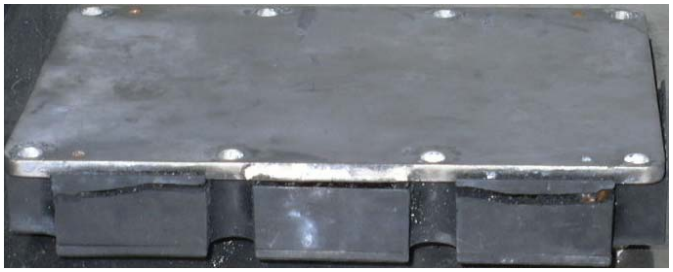

Figure III.42: Photo of the failed IGBT device.

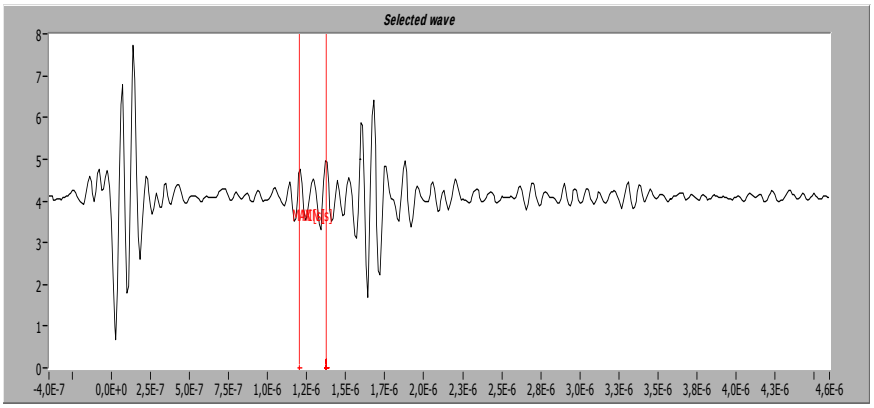

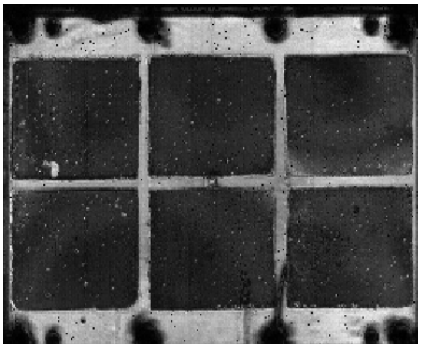

(a) AlSiC/Cu/AlN joint

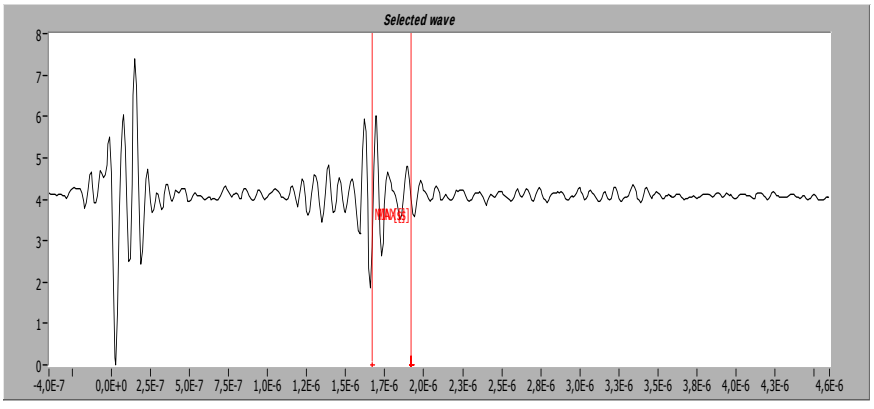

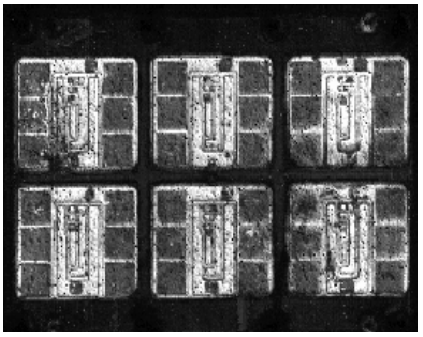

(b) Si chipset back surface

(c) Si chipset back surface detailed upper left chip

Figure III.43: Failed IGBT assembly device.

III.5.4 UT image analysis

Chipset tablet

Figure III.39.b illustrates the interface between the bottom Cu layer and the AlN ceramic layer; the two layers can be judged perfectly bonded as no solution of continuity is evidenced in the UT image.

Figure III.39.c depicts the interface between the AlN ceramic layer and the upper Cu layer; the geometrical pattern of the Cu layer is accurately described, indicating a faultless bond between the two layers.

Figure III.39.d portrays the upper Cu layer – Si chipset interface; the six Si chips are perfectly delineated, including their sharp corners, indicating the flawless soldering of the AlN/Cu/Si chipset joint.

Figure III.39.e reports the UT image obtained from a time sub-gate set on the Si chipset tablet back echo. All details of the chipset tablet are again clearly shown, confirming the flawlessness of the chipset tablet assembly interfaces, and even signs of the electrical contacts soldered on top of the Si chips can be detected in the image (small dots on the Si chip images).

The excellent results obtained from the UT image analysis are not surprising as the unsoldered chipset tablet under examination was a brand new one ready for the soldering process on the IGBT assembly device.

IGBT assembly devices

Figures III.41.a and III.43.a show the UT images of the AlSiC/Cu/AlN soldered joint in the sound and failed IGBT device, respectively.

From Figure III.41.a, it can be noticed that the rectangular base of all six chipset tablets is accurately imaged in the sound IGBT assembly device (Figure III.41.a). In reverse, the failed IGBT assembly device presents three chipset tablets with ill defined corners:

(a) lower right and left corners of the upper right chipset tablet,
(b) upper right corner of the lower central chipset tablet,
(c) lower right corner of the lower left chipset tablet (Figure III.43.a).

This indicates a partial delamination that, though limited to a very small area and not affecting the IGBT performance, are a very good example of the resolution provided by the UT FV scan method. Further stressing could however extend the delamination from the corners, which are the most critical locations, to much larger areas.

Figures III.41.b and III.43.b report the UT images of the AlSiC/Cu/AlN soldered joint in the sound and failed IGBT device, respectively.

Figure III.43.c shows a chipset tablet from the failed IGBT assembly device with several ill defined or missing features: (a) deficient rectangular shape of the lower left Si chip (delamination damage); (b) incomplete upper Cu layer pattern where the lower left Si chip wire bonds are located; (c) crack development in the lower right Si chip. These types of damage were clearly identified in two out of six chipset tablets of the failed device, while the rest of the chipset tablets displayed only minor or negligible damage conditions.

From the figures, it can be noted that in both cases the Si chips are fairly well delineated and, accordingly, appear well soldered to the dielectric substrate. Thus, no delamination can be diagnosed for the AlN/Cu/Si chipset soldered joint in the failed IGBT assembly device whose breakdown should be attributed to different electrical mechanisms. It is worth noticing that also in Figure III.43.b a rounding of the corners of the upper left, lower central and lower left chipset tablets is clearly evidenced, confirming the conclusion reached through UT image analysis of Figure III.43.a.

III.5.5 Conclusions

AlSiC metal matrix composite baseplate IGBT devices for railway traction applications, subjected to temperature fluctuations during service, were non-destructively evaluated through UT testing. The use of AlSiC as IGBT baseplate material allows for optimal thermal management design due to its high temperature resistance, sufficiently high thermal conductivity and thermal expansion coefficient that can be designed to match the one of adjacent assembly materials, thus providing for a much longer service life.

Under thermal fatigue conditions, the most critical parts of the IGBT assembly device are the thermal joints of its assembly structure that can undergo a thermo-mechanical failure (inter-layer delamination and layer cracking), leading to the IGBT assembly device ultimate breakdown. The quality and integrity of the IGBT assembly soldered joints were assessed through the analysis of UT images generated from UT volumetric files obtained by pulse-echo immersion scanning with full waveform acquisition (FV-Scan method); this technique allowed for the UT 2½ D axial tomography of the IGBT assembly structure.

UT image analysis of the sound IGBT assembly device showed no evidence of delamination or cracking in the two principal soldered joints: (a) between AlSiC baseplate and dielectric AlN ceramic layer, and (b) between AlN ceramic layer and Si chipset. UT image analysis of the failed IGBT assembly device evidenced only a partial delamination at the most critical locations of the chipset tablet soldered joints (corners). No delamination or cracking was revealed for the soldered joint between AlN ceramic layer and Si chipset.

III.6. Experimental heat pipe prototype for IGBT applications

III.6.1 Introduction

A non-destructive quality control procedure for a prototype heat pipe module for the cooling of Insulated Gate Bipolar Transistor (IGBT) devices for railway traction applications is presented. The heat pipe module is made of aluminum matrix silicon carbide (AlSiC) particle reinforced metal matrix composite (MMC) baseplate with cooper and steel tubes brazed in it. An ultrasonic (UT) non-destructive evaluation procedure was carried out according to the full volume scanning method, allowing for the UT axial tomography of the prototype heat pipe module internal structure. The quality of the brazing process of the different tubes in the AlSiC heat pipe module was verified and critically assessed through UT image analysis.

III.6.2 Heat pipe prototype model design for IGBT assembly device

The selection of the AlSiC MMC as baseplate material for IGBT devices is basically recommended by the fact that its thermal coefficient of expansion (TCE) matches the TCE of the insulating AlN ceramic layers soldered on the baseplate to carry the silicon chip sets in the IGBT assembly. Moreover, the AlSiC material displays a sufficiently high thermal conductivity, κ for efficient heat dissipation (Table III.22).

An AlSiC composition with reinforcing particle content by volume V_p = 63% was selected for the heat pipe prototype model under consideration providing a TCE = 8.39 ppm/°C (30° - 150°C) and a κ= 180 W/mK. The selected AlSiC MMC microstructure is fully dense with no void space, creating a hermetic material (see Figure III.44).

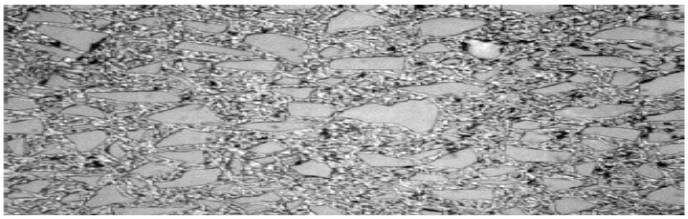

Figure III.44: Optical micrograph of polished AlSiC-9 microstructure showing discrete SiC particulate (dark contrast) in a continuous Al metal phase (bright contrast).

Table III.22

Main properties of IGBT assembly materials

Material	Density g/cm^3	TCE ppm/°C 25-150 °C	Thermal Conductivity W/mK	Bend Strengh MPa	Young's Modulus GPa
Si	2.3	4.2	151		112
AlSiC (V_p = 60% SiC)	3.0	6.5-9	170-200	450	290
Cu	8.96	17.8	398	330	131
Al	2.7	23.6	238	137-200	68
SiC	3.2	2.7	200-270	450	415
AlN	3.3	4.5	170-200	300	310
Alumina	3.98	6.5	20-30	300	350

The prototype heat pipe module is an AlSiC block of 190 mm x 140 mm (Figure III.45) with four tubes with nominal diameter 15 mm and thickness 1 mm brazed in it. The tube center is positioned at 12.5 mm from the AlSiC block upper surface and the four tubes are encountered starting at 4 mm from the AlSiC block upper surface. Two copper and two steel tubes were alternatively brazed in the AlSiC block in order to allow for the comparative evaluation of the suitability of two different materials for IGBT heat pipe module application. The heat pipe module is located under the IGBT device and realizes a heat transfer between high temperature areas (IGBT device) and low temperature areas (lower free surface of the heat pipe module). A refrigerant liquid is introduced in the tubes and the different temperature areas change the phases from liquid to gas in the heat pipe module upper zone (caused by the heat transfer from the high temperature IGBT device) and from gas to liquid in the heat pipe module lower zone (caused by condensation due to the cold heat pipe module lower free surface). These heat transfer phenomena allow for the cooling of the IGBT device with high efficiency.

Figure III.45: Prototype AlSiC MMC heat pipe module.

The purpose of this research work is to assess the quality of the brazing between the different tubes and the AlSiC MMC block. In order to subject the prototype heat pipe module to the same conditions as the real service ones, different temperature cycles were applied to it. The heat pipe prototype module is placed on the mobile floor of a heating/cooling chamber and with a vertical displacement it is transferred from a -40°C environment to a +125°C environment for 80 temperature cycles with cycling time equal to 45 minutes. In this way, it is possible to simulate the thermal loads to be experienced by the heat pipe module assembled in the IGBT device under real service conditions.

Ultrasonic NDE system

Pulse-echo immersion ultrasonic (UT) testing was utilized for the nondestructive evaluation (NDE) of the prototype heat pipe module. A volumetric type of UT NDE approach (Full Volume Scan), based on complete waveform acquisition and analysis allowing for the UT axial tomography of the heat pipe prototype module, was used to evaluate the accuracy of the positioning and the quality of the brazing of the four tubes in the AlSiC block. The UT NDE system utilised in this work consists of a purposely designed hardware configuration and a custom made software code, named "ECUS Inspection", developed in the LabView environment .

III.6.3 Hardware configuration

The UT immersion transducer used is a 15 Mhz, highly damped, focused probe. To obtain the maximum resolution from the UT NDE and to capture the maximum number of refracted waves from the cylindrical surface of the tubes, the UT waveform focal spot was positioned at a 1 mm from the upper surface of the AlSiC block (Figure III.46). The UT scans parameters for different thermal cycling states (0, 1 and 2) are reported in Table III.23.

The focal spot of the UT wave is present on the upper surface and does not present any deviation. If we change the focal spot position in the internal of the AlSiC MMC a refraction will be present (see Figure III.46) at the interface between the water and the AlSiC MMC. In order to obtain the maximum resolution from the UT information and to capture the maximum number of refracted waves from the cylindrical surface of the tubes we have positioned the UT wave spot at a distance equal to 1 mm from the upper surface.

This change in the focal length can be predicted by equation III.5. Given the focal length and material path, this equation can be used to determine the appropriate water path to compensate for the focusing effect in the test material.

$$WP = F - MP\left(c_{tm}/c_{w}\right), \tag{III.5}$$

where:

WP = Water Path
MP = Material Depth
F = Focal Length in Water
c_{tm} = Sound Velocity in the Test Material
c_{w} = Sound Velocity in Water

In our case the 15MHz probe focalized at 49 mm under the interface water – AlSiC, the focal point will be present at an effective distance equal to 3.75 mm.

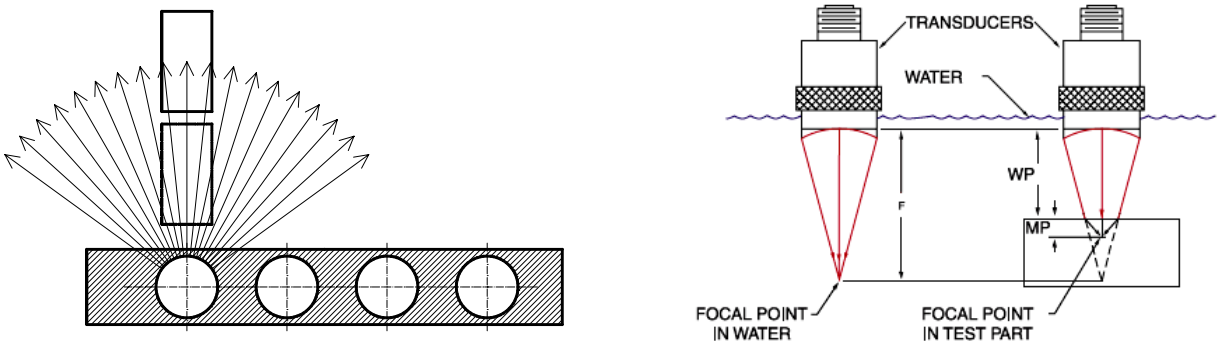

Fig. 4: Setting up the focal distance of the UT transducer

The used software package was "ECUS Inspection". This is a custom made software code developed in the LabView environment with the scope to control the UT probe displacement in the x-y plane (scan) and provide for the complete UT signal detection, storage and analysis (for details see Chapter II).

Table III.23
UT scan parameters

Scan size	Focal distance	Step Size	Gain dB	State
140 mm x 185 mm	1 mm	0.5 mm	62	Cicl. 0
140 mm x 185 mm	1 mm	0.5 mm	68	Cicl. 0
140 mm x 185 mm	1 mm	0.7 mm	66	Cicl. 1
140 mm x 185 mm	1 mm	0.4 mm	75	Cicl. 2
140 mm x 185 mm	1 mm	0.4 mm	58	Cicl. 2

III.6.4 UT NDE results and discussion

The heat pipe prototype module was investigated before and after the two thermical cycles Elaborating the UT signals obtained during the scanning of the upper respectively lower part of the heat pipe prototype model were obtained the signals and the respectively images presented in this paragraph.

If we consider the positioning of the tubes and their cylindrical symmetry for the signal interpretation relatively to the upper part of the module we will use only one time window superior to 1.3 μs (see Figure III.47). Investigating this part of the UT wave, we obtained the corresponding image where it is possible to observe the longitudinal positioning of the four tubes (see Figure III.48).

In the Figure III.48 is presented the view of the tubes from the upper part before the first thermal cycle. It is possible to observe the good quality of the brazing for the continuity of the white stripes that are representing the different tubes. With a more detailed analysis can be evidenced two possible brazing errors for the cooper tubes (red marked in Figure III.48). If this is a true consideration, this micro error presence will influence the brazing quality of the cooper tubes during the first thermal cycle by a relative detachment in those corresponding areas.

By using *negative* option in the "ECUS Inspection©" software package (see Figure III.49) it is possible to observe that the brazing of the first lower cooper tube is presenting a diminishing in the central part (black) and on the third tube the presence of grey parts are indicating a low connection between the AlSiC base and the Cooper tube.

In the case of the lower part scan (Figure III.50) it is possible to observe that the time gate is around 1.5 μs. The difference between the 1.3 μs (upper scan) and 1.5 μs (lower scan) is due to the non symmetry of the cooper tubes in the AlSiC MMC.

By analysing the images (Figures III.50 and III.51) it is possible to observe that before the first thermal cycle are present discontinuous areas, even if they are small, in the case of the cooper tubes. By analysing the images is possible to conclude that is possible to observe, in the case of the negative image, small white areas included in the black area that is the representation of the brazed tubes.

After the first and second thermal cycles and the elaboration of the respective UT signals (Figures III.53 and III.53) it is possible to observe that suspected areas regarding brazed cooper tubes is a reality and it is possible to notice the white areas (tube area) being interrupted by black areas (graduate displacement of the brazed areas in the evidenced red zone)

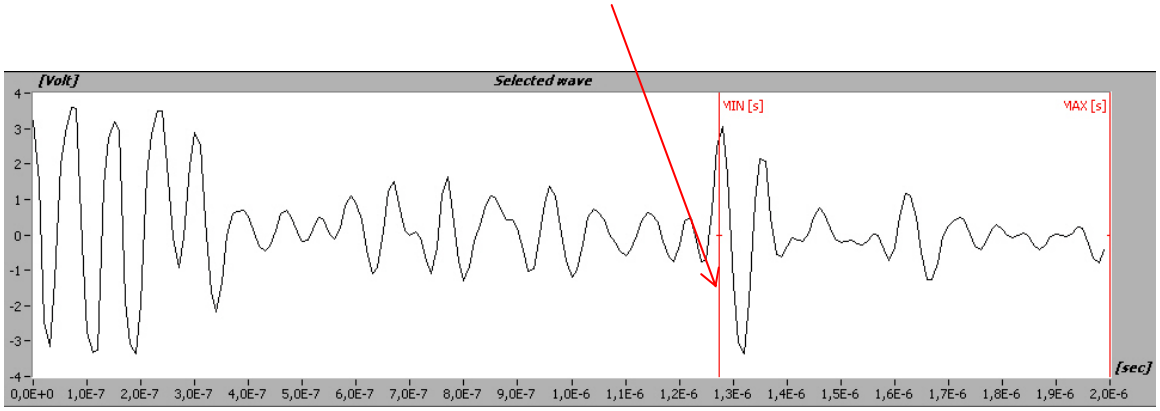

Figure III.47: Heat pipe prototype module corresponding UT wave (up).

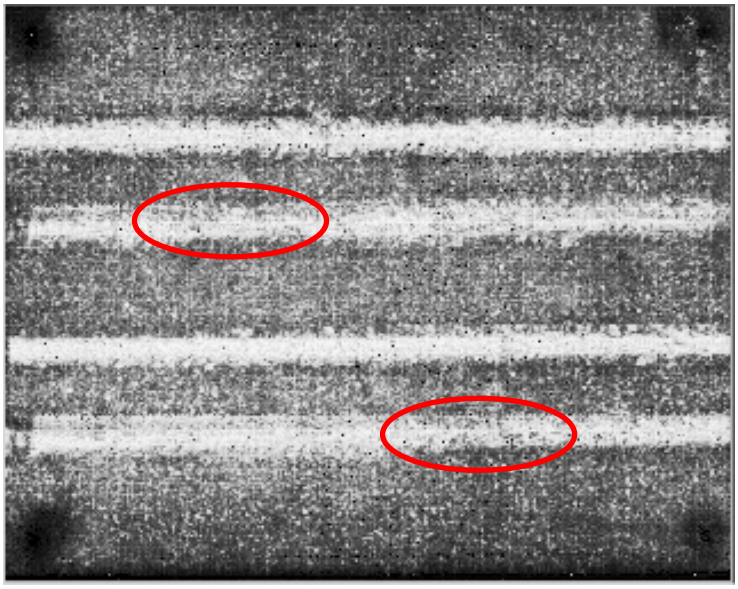

Figure III.48: UT image of the upper part of the heat pipe prototype module before the first thermal cycle.

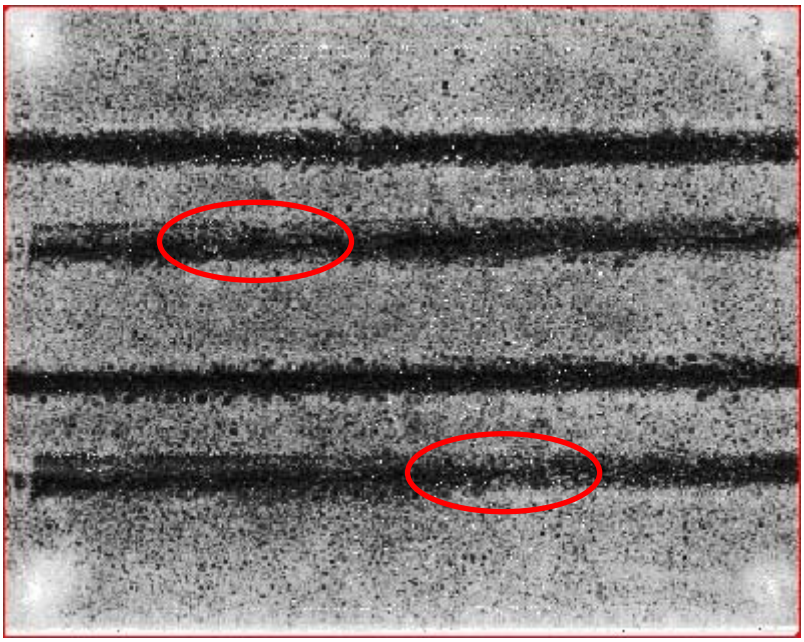

Figure III.49: Negative image of the upper part of the heat pipe prototype module before the first thermal cycle.

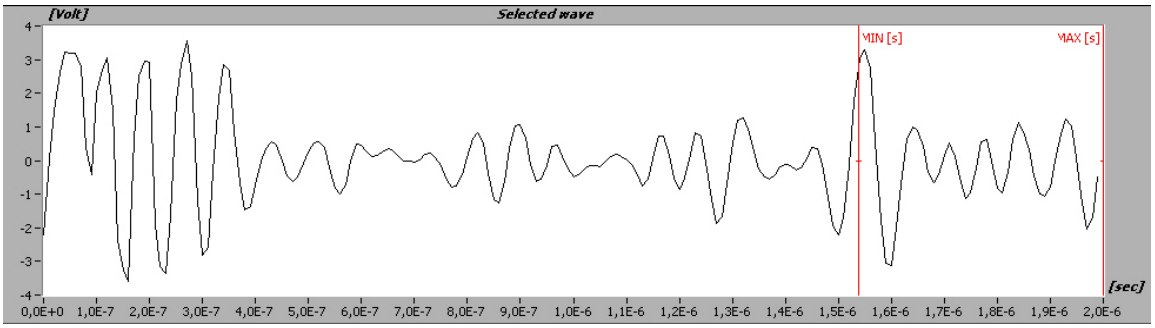

Figure III.50: Heat pipe prototype module corresponding UT wave (down) before first thermal cycle

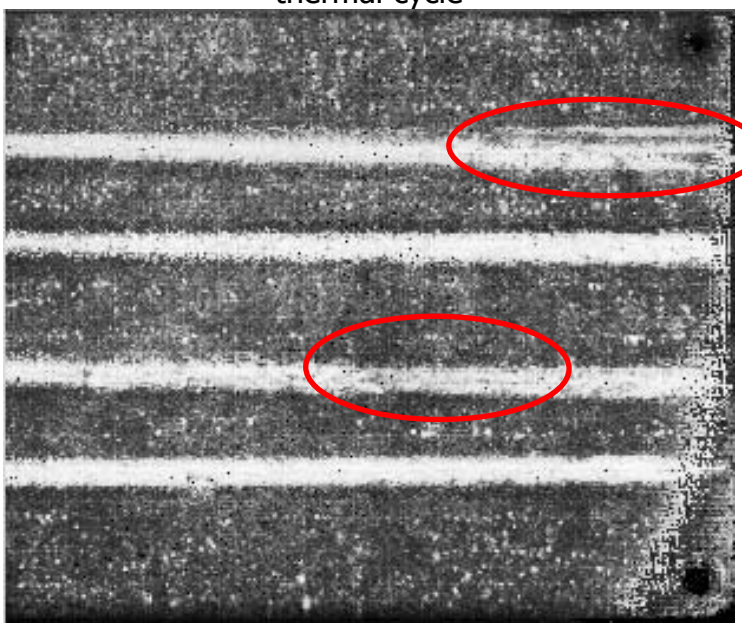

Figure III.51: UT image of the lower part of the heat pipe prototype module before the first thermal cycle

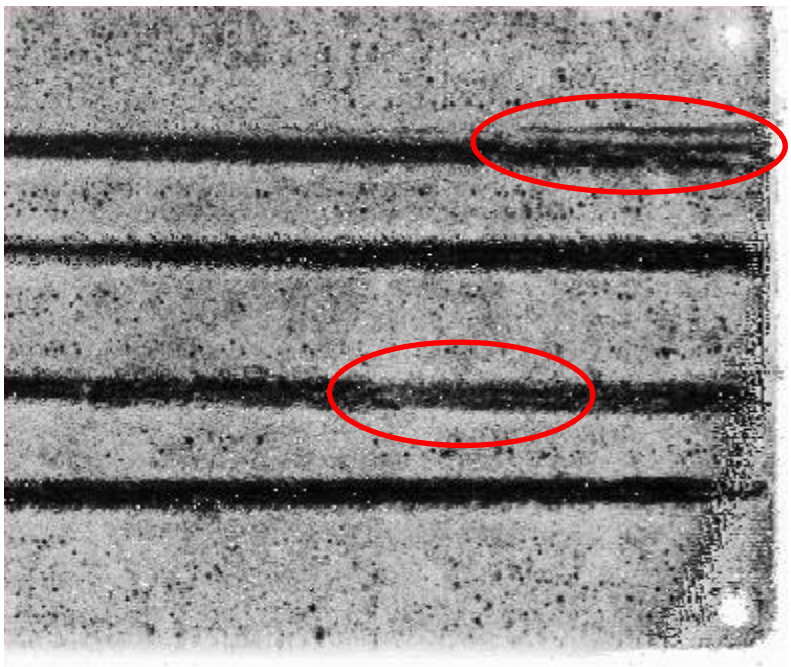

Figure III.52: Negative image of the lower part of the heat pipe prototype module before the first thermal cycle

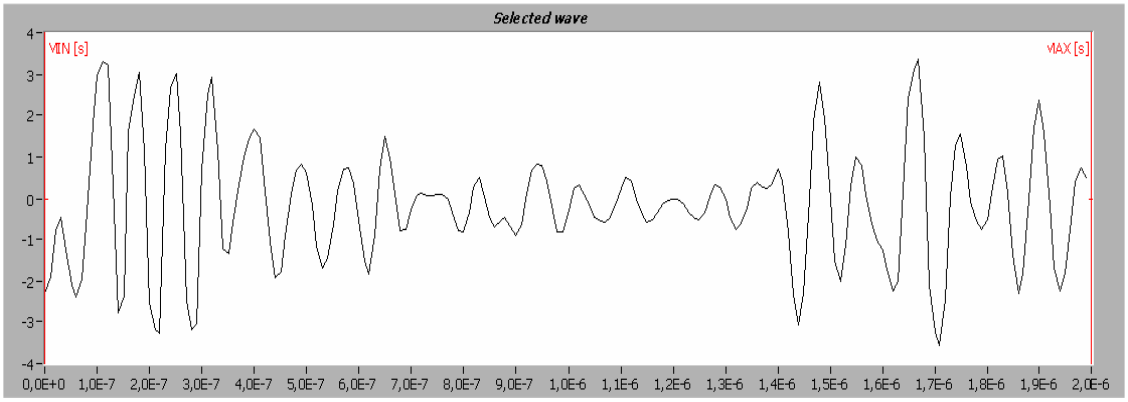

Figure III.53: Heat pipe prototype module corresponding UT wave (up) for the first thermal cycle.

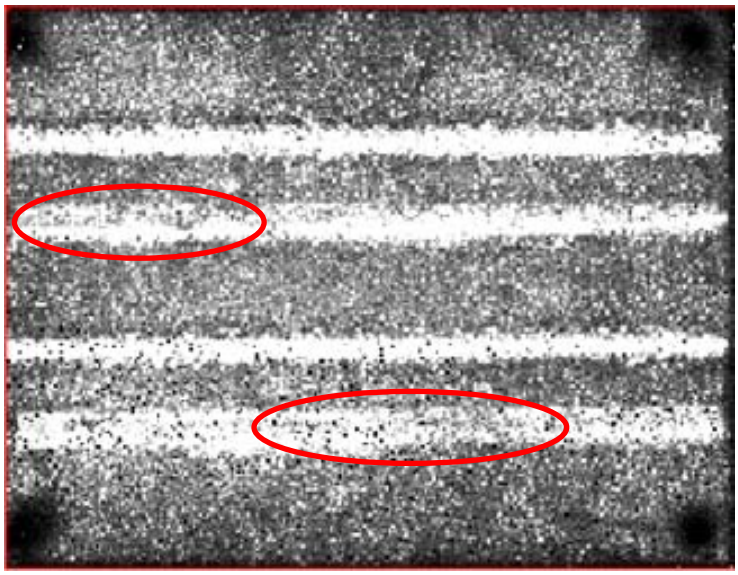

Figure III.54: UT image of the up part of the heat pipe prototype module for the first thermal cycle (80 cycles).

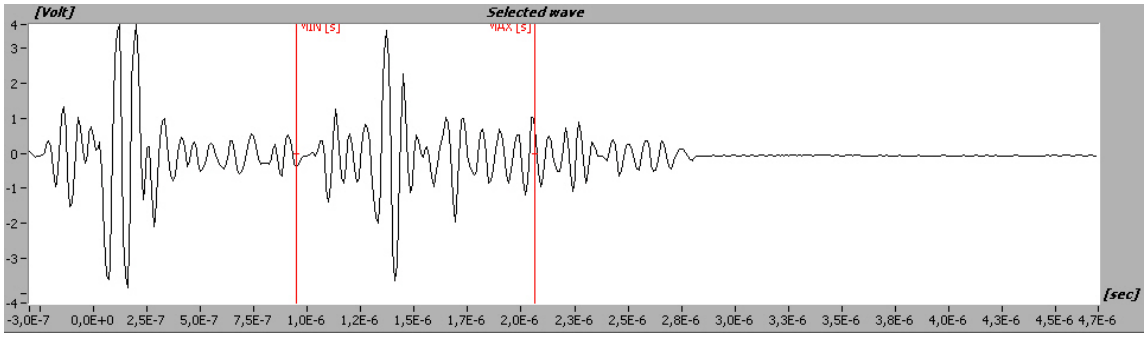

Figure III.53: Heat pipe prototype module corresponding UT wave (up) for the second thermal cycle.

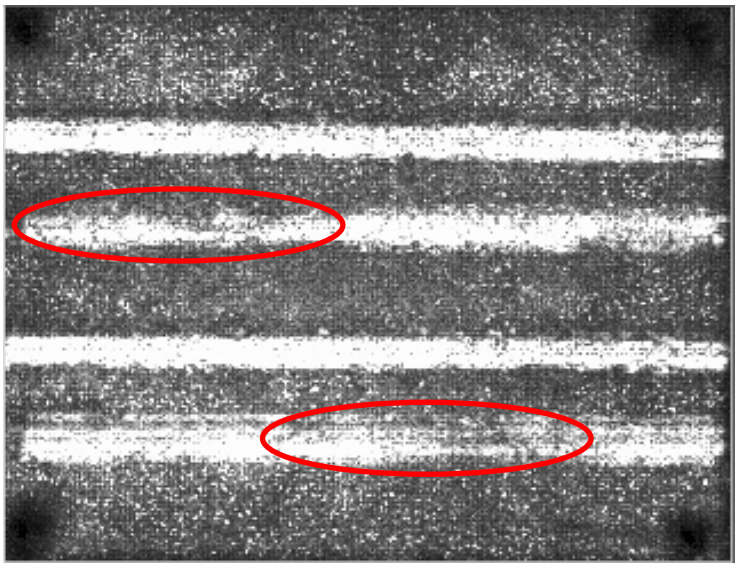

Figure III.54: UT image of the up part of the heat pipe prototype module for the second thermal cycle (160 cycles).

III.6.5 Conclusions

The UT NDE technique was shown to be effective in the quality verification of the AlSiC heat pipe module. Despite the cylindrical shape of the AlSiC – tube interface, over 30% of the brazed surface could be evaluated.

Though the copper tubes are more desirable because of their higher heat transfer properties, the quality of the steel tube brazing was shown to be superior. The copper tubes display initial brazing defects that increase with increasing number of thermal cycles

III.7. Copper 99.99% brazed assembly

III.7.1 Introduction

A non-destructive quality control procedure for an accelerometer prototype made of brazed cell assemblies for medical applications is presented. The component cells are made of pure copper 99.99% LeCuivre France. An ultrasonic (UT) non-destructive evaluation procedure was carried out according to the full volume scanning method, allowing for the UT axial tomography of the build-up assembly. The quality of the brazing process of the 99.99 % copper plates was verified and critically assessed through UT image analysis.

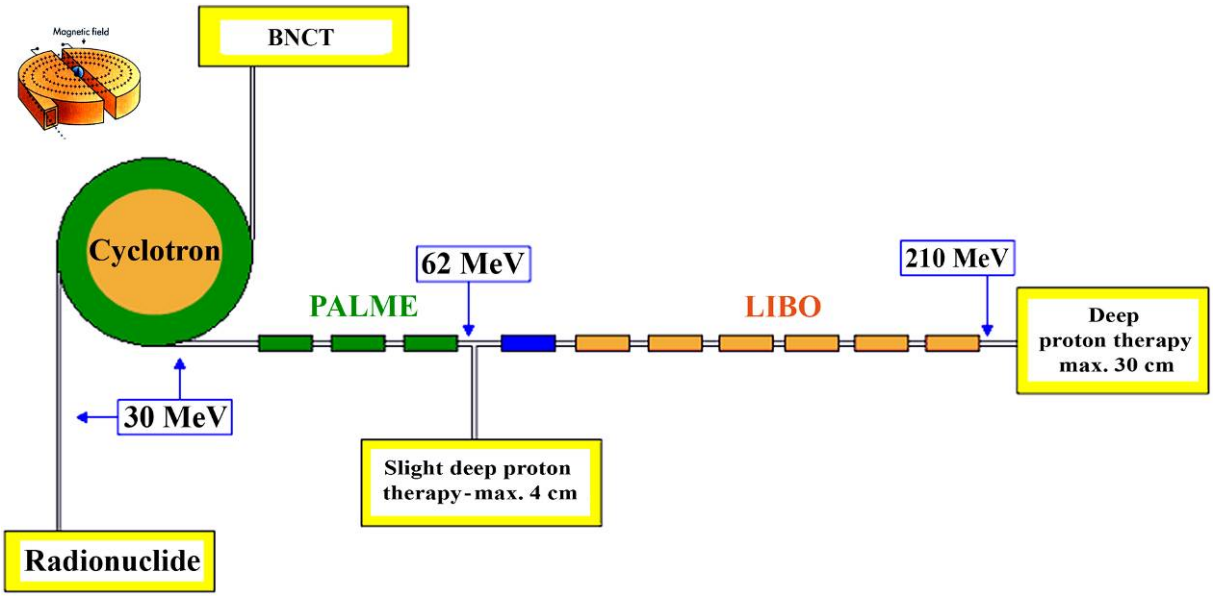

Figure III.55: Acceleration state scheme.

In Figure III.55 is presented the scheme of a prototype accelerometer for proton therapy use. It is possible to observe a 30 MeV cyclotron. The first level of acceleration from 30 MeV to 62 MeV is called PALME, which was used and tested at INFN National South Laboratories from Catania. The second level of acceleration is called LIBO and at the maximum amplified energy that can be reached is equal to 210 MeV.

The protons up to 30 MeV are used also for the radionuclide production, and also by using a different line can be used for Boron Neutron Capture Therapy (BNCT).

The protons from 62 MeV up to 210 MeV are used for the slight deep proton therapy and deep proton therapy.

The accelerometer cells under examinations are part of the LIBO acceleration segment. The LIBO acceleration segment is made of multiple brazed assembly cells. Each assembly cell is made out of four Back-to-back accelerating cells that are brazed as showed in Figure III.56.

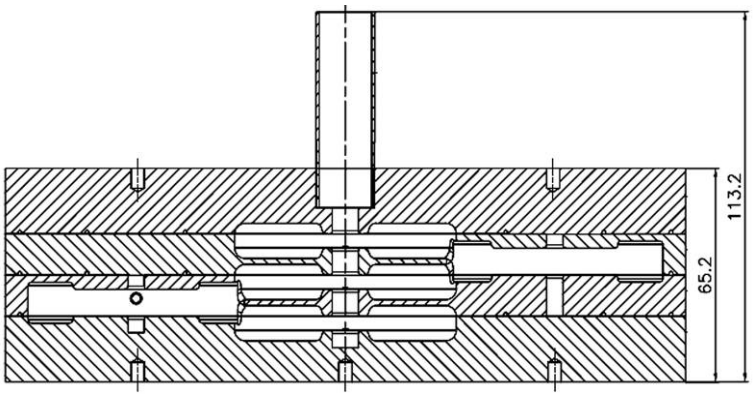

Figure III.56: Back-to-back accelerating cells.

III.7.2 Cell brazed assembly structure

The accelerometer cells are made of Oxygen Free High Conductivity (OHFC) 99.99% LeCuivre (France) C10200 that presents the following characteristics: is high ductility, high electrical and thermal conductivity, high impact strength, good creep resistance, ease of welding, and low volatility under high vacuum (see Table III.24). Physical properties of the OFHC C10200 copper are presented in Table III.25.

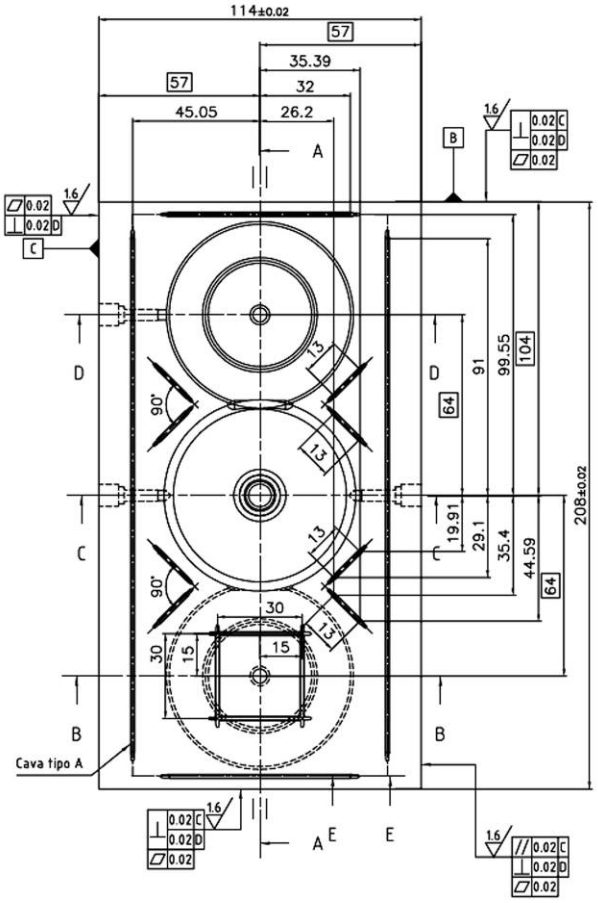

(a)

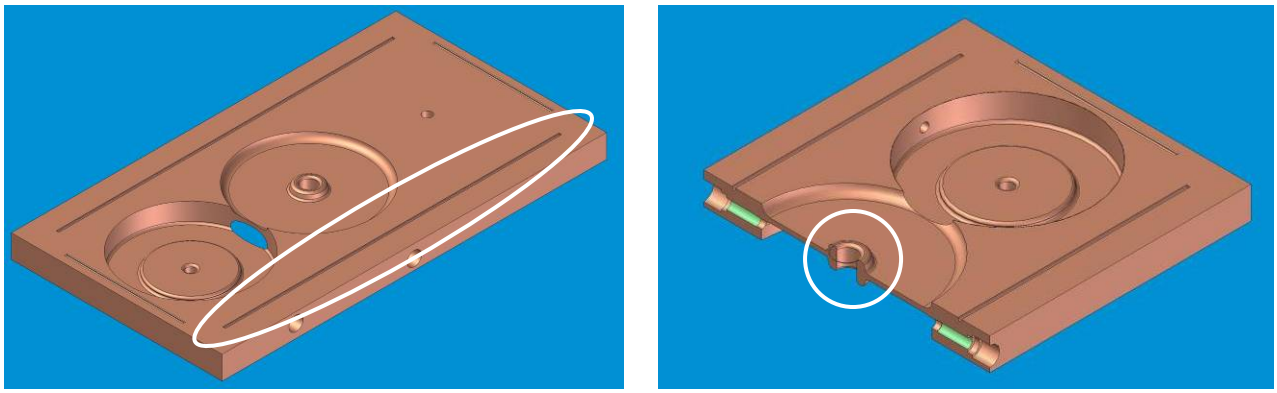

(b) (c)

Figura III.57: Back-to-back accelerating cell.

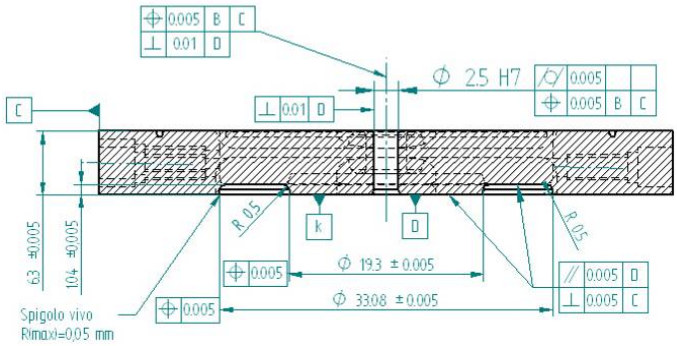

(a)

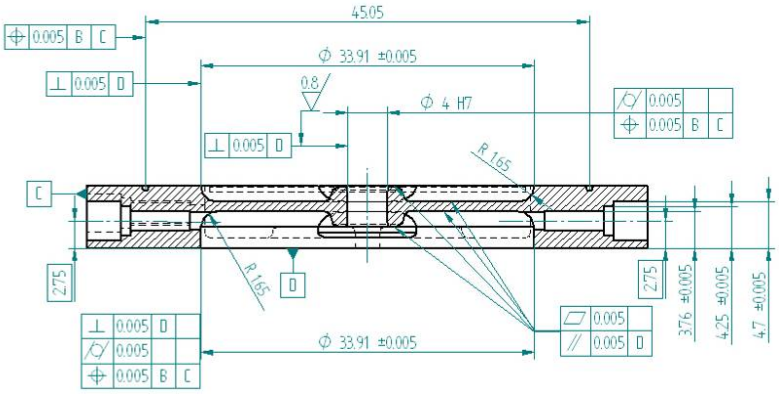

(b)

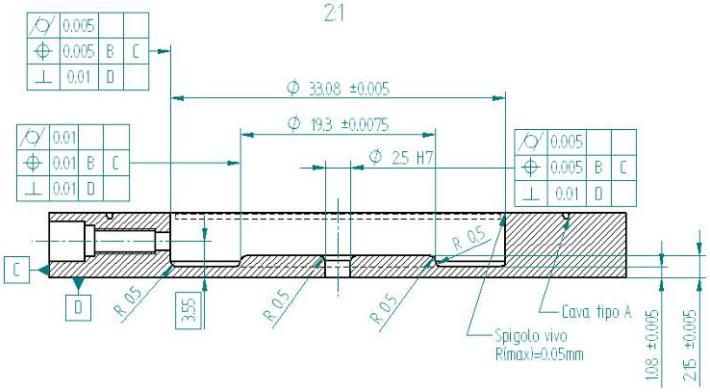

(c)

Figure III.58: Geometric dimensions of OFHC Back-to-back accelerating cell: a) B-B section, b) C-C section, c) D-D section.

In the Figure III.57 is possible to observe a 2d sketch (Figure III.57.a), a 3D CAD model (Figure III.57.b) and a "nose" section (Figure III.57.c). It is possible to observe in both images the brazing channels and the complex geometry of the so called "nose". Their importance in the final assembly is due to the high vacuum quality obtained between cavities. The back-to-back accelerating cell geometrical characteristics are shown in Figure III.58.

In order to control the brazing by ultrasonic means an assembly with two back-to-back cells of 208 mm x 114 mm x 12.6 mm and 208 mm x 114 mm x 5 mm was built.

Table III.24
Fabrication properties of OFHC 99.99% Copper

Joining Technique	**Suitability**
Soldering	Excellent
Brazing	Excellent
Oxyacetylene Welding	Fair
Gas Shielded Arc Welding	Good
Capacity for Being Cold Worked	Excellent
Capacity for Being Hot Formed	Excellent
Forgeability Rating	65/100
Machinability Rating	20/100
Most commonly used Tempers	H00, M20

Table III.25
Physical properties of OFHC 99.99% Copper

Physical property	SI value
Melting Point - Liquidus	1083 °C
Melting Point - Solidus	1083 °C
Density	8.94 gm/cm^3 @ 20 °C
Specific Gravity	8.94
Electrical Resistivity	1.71 microhm-cm @ 20 °C
Electrical Conductivity	0.591 MegaSiemens/cm @ 20 °C
Thermal Conductivity	391.1 W/m · ^{o}K at 20 °C
Coefficient of Thermal Expansion	16.9 ·10^{-6} per ^{o}C (20 - 100 °C)
Coefficient of Thermal Expansion	17.3 ·10^{-6} per ^{o}C (20 - 200 °C)
Coefficient of Thermal Expansion	17.6 ·10^{-6} per ^{o}C (20 - 300 °C)
Specific Heat Capacity	393.5 J/kg · ^{o}K at 293 °K
Modulas of Elasticity in Tension	117000 MPa
Modulus of Rigidity	44130 MPa

III.7.3 UT brazing inspection

The assembly of two back-to-back cells with a total 17.6 mm height was investigated and the UT signals were obtained. The respectively UT images are presented in this paragraph.

Table III.26
Scanning data

Scanning area (X-Y) [points]	Focal Distance [mm]	Scanning Step [mm]	UT Probe	Inspection side
212x120	25	1	25 MHz	12 mm
212x120	25	1	25 MHz	5 mm

Two UT NDE FV scan tests were carried out from both sides of the assembly cell 12 mm and 5 mm and the scanning values are reported in Table III.26.

Using Robotest v2.0 software package is possible to divide the full signal in 16 intervals, by setting up the first gate in correspondence of the front echo and the last time gate in correspondence of the back echo (see Figure III.59). Figure III.60 presents the relative 16 images of the brazed assembly cell and it is possible to observe in the case of the section 10, 11 and 12 the passage of the UT signal through the brazing layer. The quality of the brazing is confirmed by the same grey tones present in the brazing canal areas.

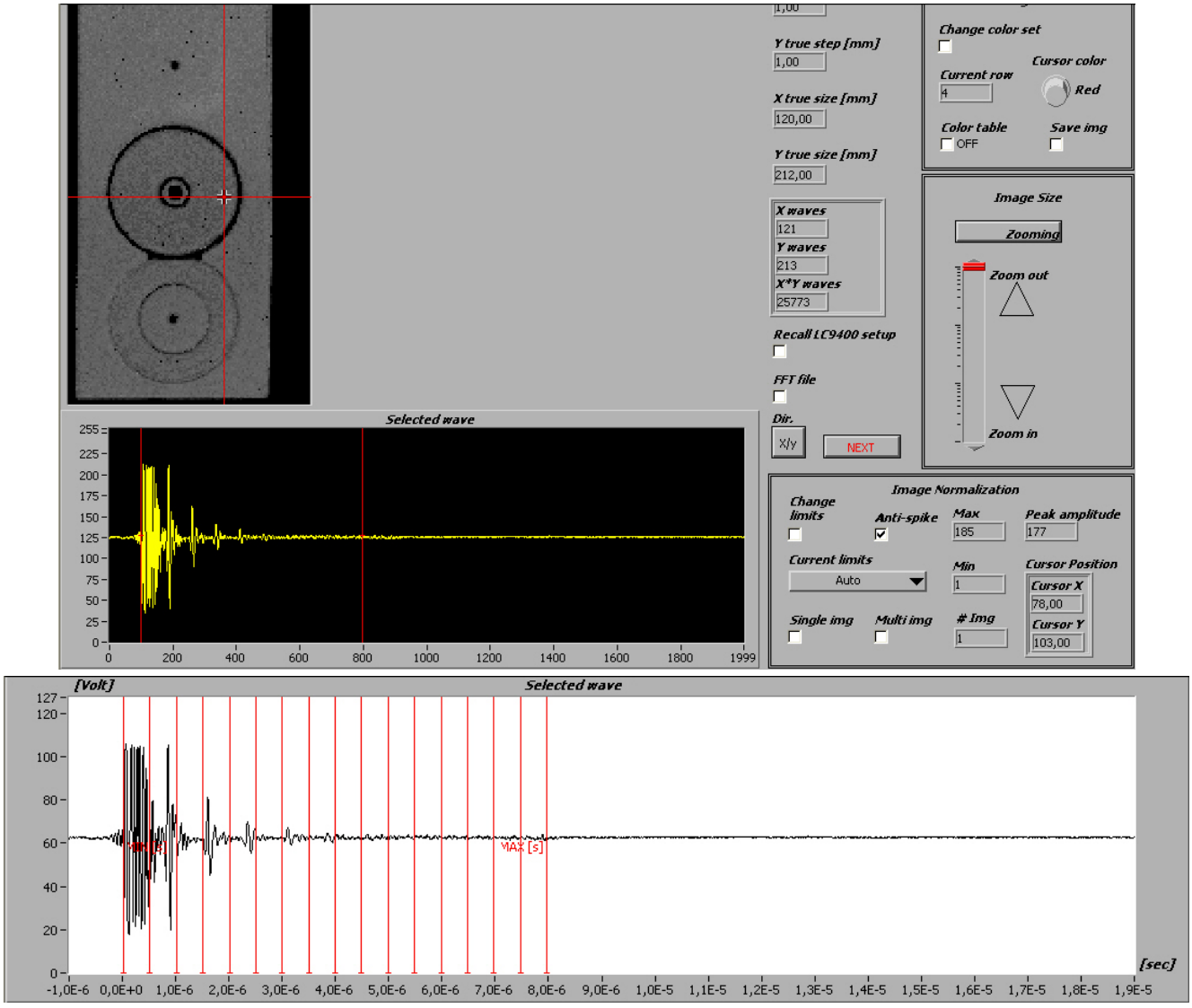

Figure III.59: UT signal selection for the 12.6mm side scan

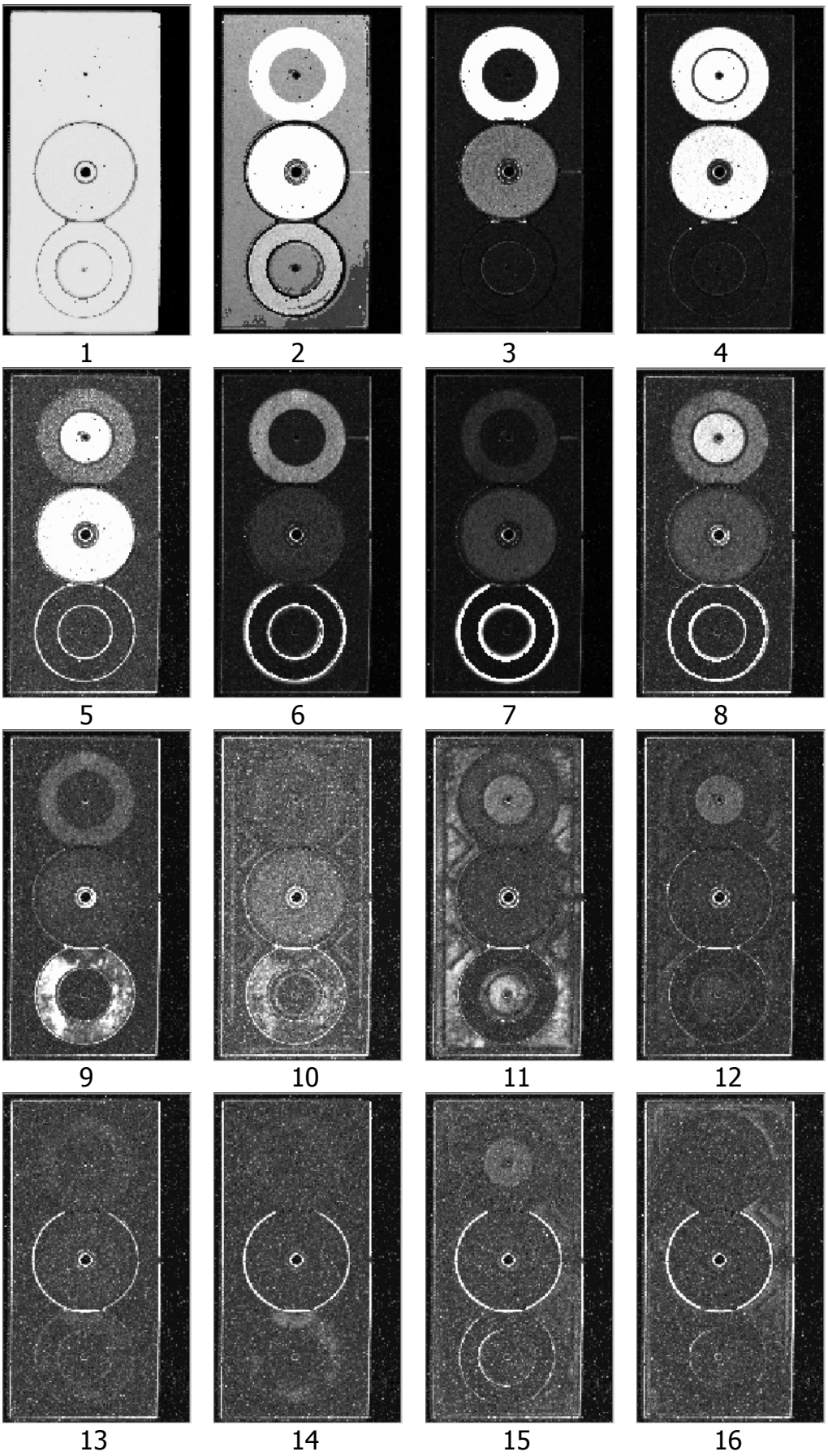

Figure III.60: Sequence layer by layer in the 12.6 mm side scan. Image 11 is characteristic for the brazing layer inspection between the copper plates.

The scanning result from the 5 mm side is presented in the Figure III.61.a along with a 3D view based on UT reconstruction (Figure III.61.b) and the C-Scan result of the same plate carried out at CERN Geneva (Figure III.61.cIt is possible to observe the higher quality of the UT image obtained through the FV-scan technique (Figure III.61.a) in comparison with the conventional UT C-scan image obtained at CERN Geneva (Figure III.61.c). However, in both cases the same brazing defects is evidenced at the upper side of the UT image as well as minor defects in the lower part of the UT image.

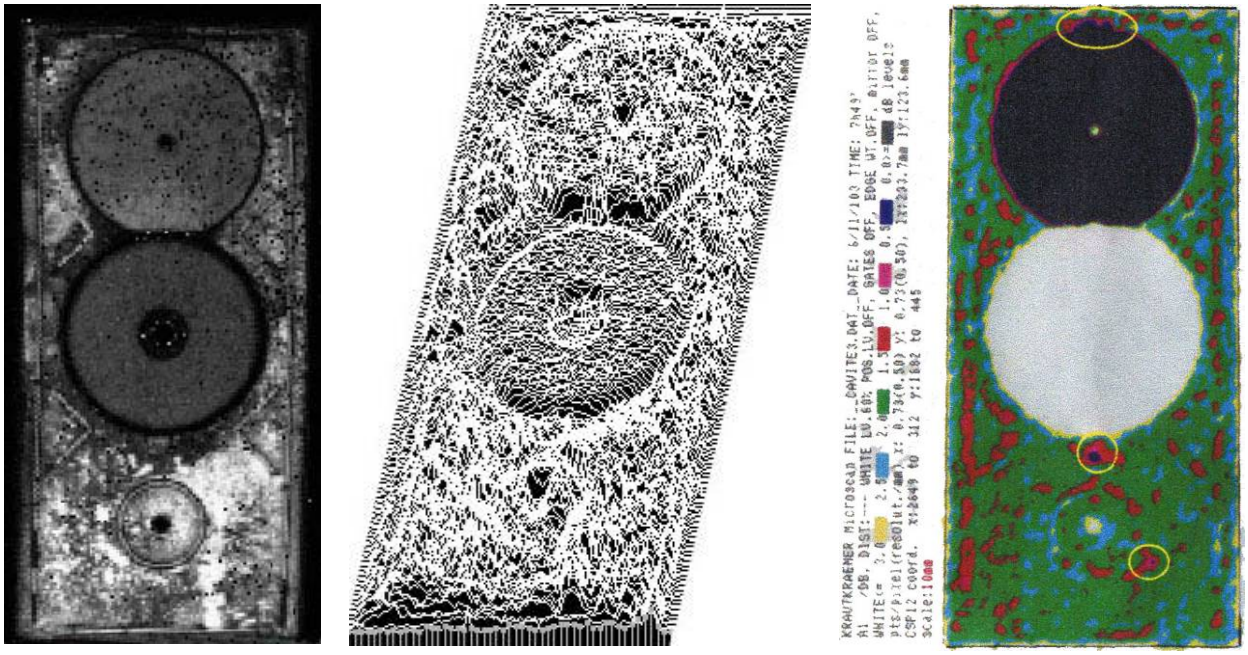

(a) (b) (c)

Figure III.61: 5 mm side ultrasonic images:
(a) FV-scan UT image of the brazing interface, (b) 3D model of the scan (a), (c) CERN Geneva C-Scan UT image of the brazing interface

III.8. Turbine blade geometrical characterisation

III.8.1 Introduction

A non-destructive quality control procedure for a turbine blade, product serial number FRE103072 (see Figure III.62) made by Europea Microfusioni Aerospaziali (EMA) Morra De Sanctis, made of nickel based alloy through micro casting fusion is presented. In Figure III.63 sections of the high-precision engine blade for aircraft engine turbines are reported.

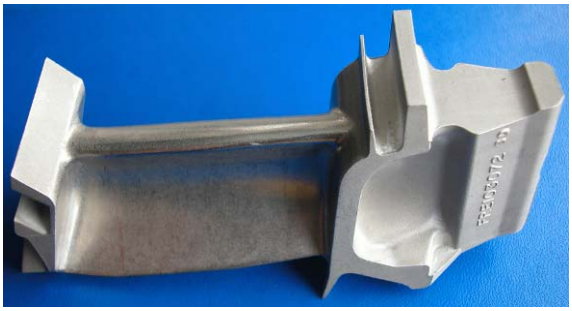

Figure III.62: High-precision engine blade for aircraft engine turbines serial # FRE103072.

From the section reported in Figure III.63 it is possible to observe the channel network used for the cooling flow through the turbine blade during work regime. Also can be noticed the presence inside the channels of multiple profiles that are blocking the laminar flaw of the cooling liquid. The result is a better thermal exchange between the turbine blade and the cooling.

From the quality point of interest, on the turbine blade must be carried out a series of controls as: dimensional controls (general dimensioning, airfoil profile control) on the external profile and on the internal channel profile. These procedure followed is made through CMM machines by controlling the needed information in three critical sections for the external sections. In the case of internal profile inspection ultrasonic methods are used. The UT controls are involving manual wall thickness and cooling channels diameter inspection.

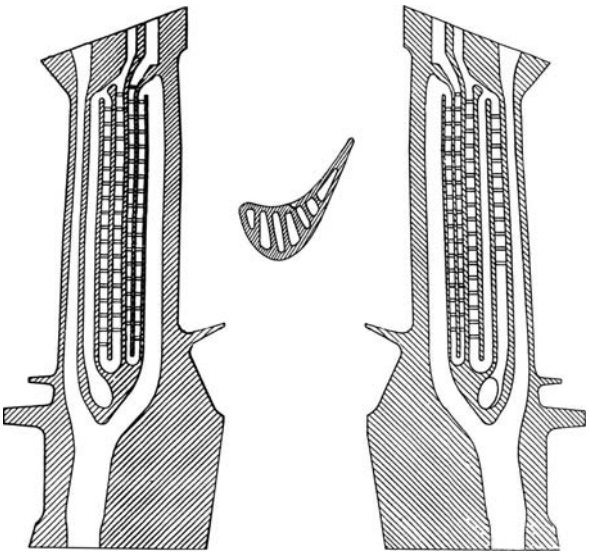

Figure III.63: Turbine blade construction design.

Due to the complex geometry of the turbine blade and in order to finalize the ultrasonic non destructive inspection Robotest v2.0 and the 6 axis Staubli RX60 robotic arm were used. Robotest v2.0 realises first of all a preliminary scanning in order to learn the piece geometry and after an ultrasonic Full Volume Scan type will be carried out.

During this paragraph the use of the plug-ins special created for this research work presented in Chapter II will be recalled.

Each single scan is divided in 3 phases:

- Adaptive scan, during this scan the software is learning the piece external geometry by retrieving from UT signals the information needed to reconstruct the area of scan. The learning scan will use as major importance the focal distance value of the UT probe by considering the maximum amplitude of the signal that guaranties the orthogonal condition between the UT probe and the surface in cause.
- Measuring scan, during this scan the UT scanning system will realise an ultrasonic Full Volume Scan type by following the point matrix obtained during the adaptive scan, but with lower value for the scanning steps.
- The third phase is the UT wave signal interpretation in order to generate UT images, measurements of wall thickness and the necessary turbine blade profile.

In our case we have realised two successive UT scans. The first one was a scan with the x axis value distance major than the y axis value (Scan A). Scan B is referring to a scan with the y axis dimension greater than the x axis dimension. Both scan parameters are presented in the Table III.27.

Table III.27
San A and Scan B parameters

Turbine blade code FRE103072	Scan A	Scan B
X axis scanning step	0.1 mm	0.1 mm
Y axis scanning step	0.1 mm	0.1 mm
X axis number of steps	60	140
Y axis number of steps	150	70
UT probe frequency	25 MHz	25 MHz
Focal distance	25 mm	25 mm
Sampling rate	100 MHz	100 MHz
Samples for each UT wave	400	5000
Total number of scanning points	9210	10010

III.8.2 Scanning area A results

During area A scan the major importance of the results is the one in y axis direction as is possible to observe in Figure III.64. The inspected area is 15 mm (y axis) x 6 mm (x axis). This scan gave us the opportunity to realise a good inspection of the turbine blade cooling channels. In Figure III.64 is indicated the inspected scanning area.

In the case of the first scan the low number of samples for each UT wave (400 points/UT wave) is contributing in a better visualisation of the turbine blade internal cooling channels, and due to improved software graphical engine the 2D or 3D/4D visualisation is optimised.

In order to optimize the image quality an over sampling equals to 2% of the total number of scanned points is realised.

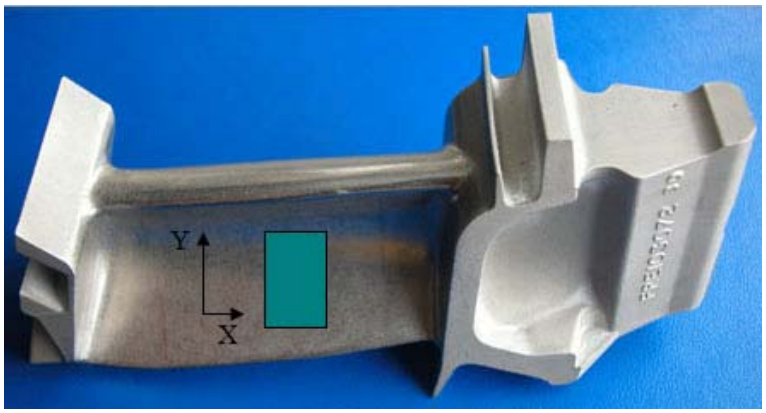

Figure III.64: Scanning area A; X and Y represents UT scan axis.

Figure III.65 reports the zoomed in image in false colours obtained after the first scan. This image is obtained from one of the plug-in presented in Chapter II and at the base of this image is the UT scan file generated through RoboTest v2.0 software package. In yellow colour are visible all the turbine blade internal cooling channels and with red colour the separation profiles between the cooling channels.

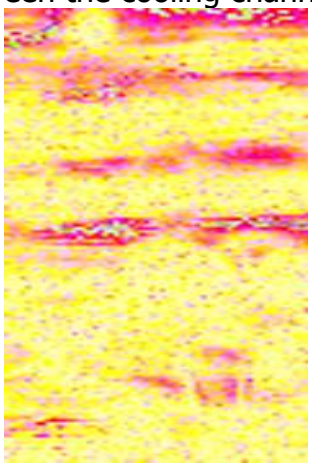

Figura III.65: Scanning area A: Zoomed in false colour image (C-Scan obtained from a FV-Scan).

By using the 3D signal processing pack from RoboTEST v2.0 on the UT signal files, 4D point clouds were obtained and analysed. During the UT signal analyse the 3D information concerning the frontal surface points were reported along with the information regarding the wall thickness (Figure III.66) and the amplitude of the back echoes (Figure III.67).

The point of clouds were graphical represented by associating for each 3D point a grey tone choose from a gray scale created from the 4th dimension (wall thickness or back echo amplitude) information. In Figures III.66 and III.67 internal cooling channels of the turbine blade can be recognised. Also, it is possible to observe in the internal part of the channels multiple profiles that are blocking the laminar flow of the cooling liquid.

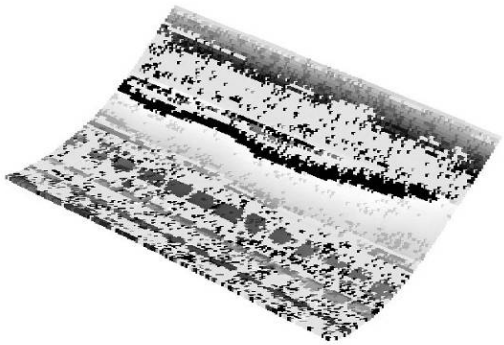

Figure III.66: Scanning area A: 4D wall thickness result (D-Scan);
The black tone area is corresponding to lower values of the wall thickness.

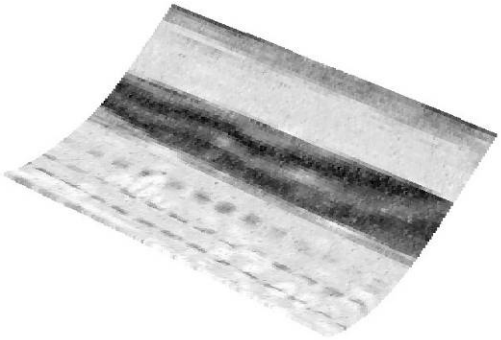

Figure III.67: Scanning area A: 4D back echo amplitudes result (C-Scan).

III.8.3 Scanning area B results

During area B scan the profile inspection (long x axis) was carried out. The inspected area is 7 mm wide (Y axis direction) and 14 mm long (X axis direction) (se Figure III.68). In order to obtain major information about the turbine blade profile a 5000 points/wave sampling was used. This high number of sampling points is rendering the UT profile processing heavier, and will take more time to elaborate the acquired data.

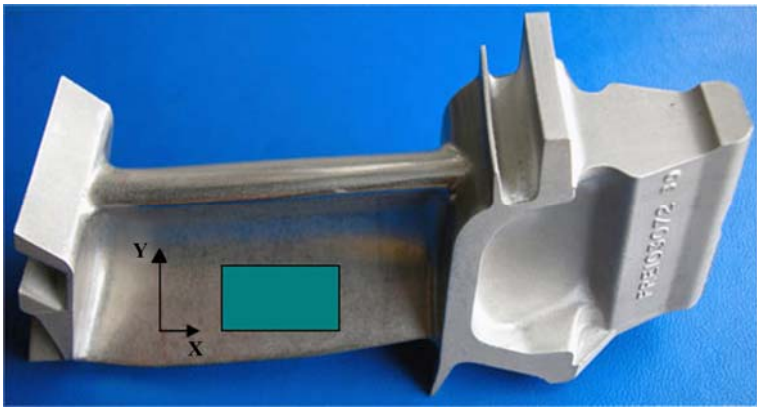

Figure III.68: Scanning area B; represents UT scan axis.

From scanning area B, 13 sections in XZ plane were obtained. They were numbered from 0 to 12 and they were disposed as reported in Figure III.69.

The graphics in Figure III.70 are showing the external turbine blade profile obtained directly from adaptive scanning (white points or lines) and wall-thickness retrieved for each section (red points or lines).

The points and lines courses are representing different wall-thickness variations corresponding to the internal channels profiles of the turbine blade. When the wall thickness is constant the cooling channels geometrical dimensions can be obtained.

The software packages used in this case are some plug-ins developed in LabView (see Chapter II). Those were realised as interactive software, where we can choose the profile for each of 13 sections desired and just by selecting with the pointer the needed section we can retrieve all the necessary information about the wall-thickness in millimetres.

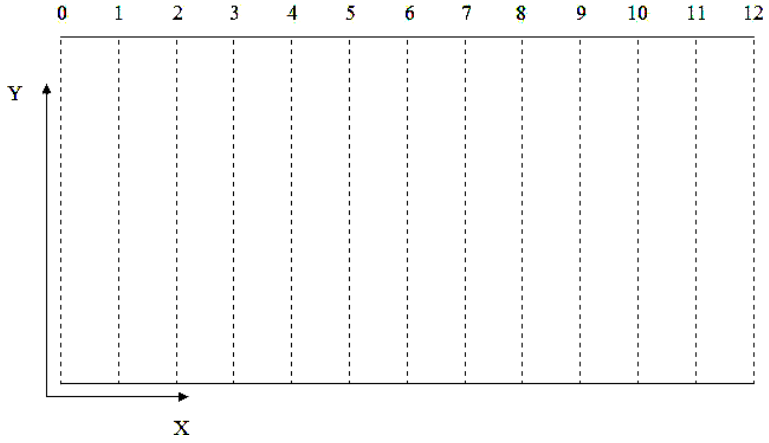

Figura III.69: Scanning area B sectioned by 13 XZ sections numbered from 0 to 12.

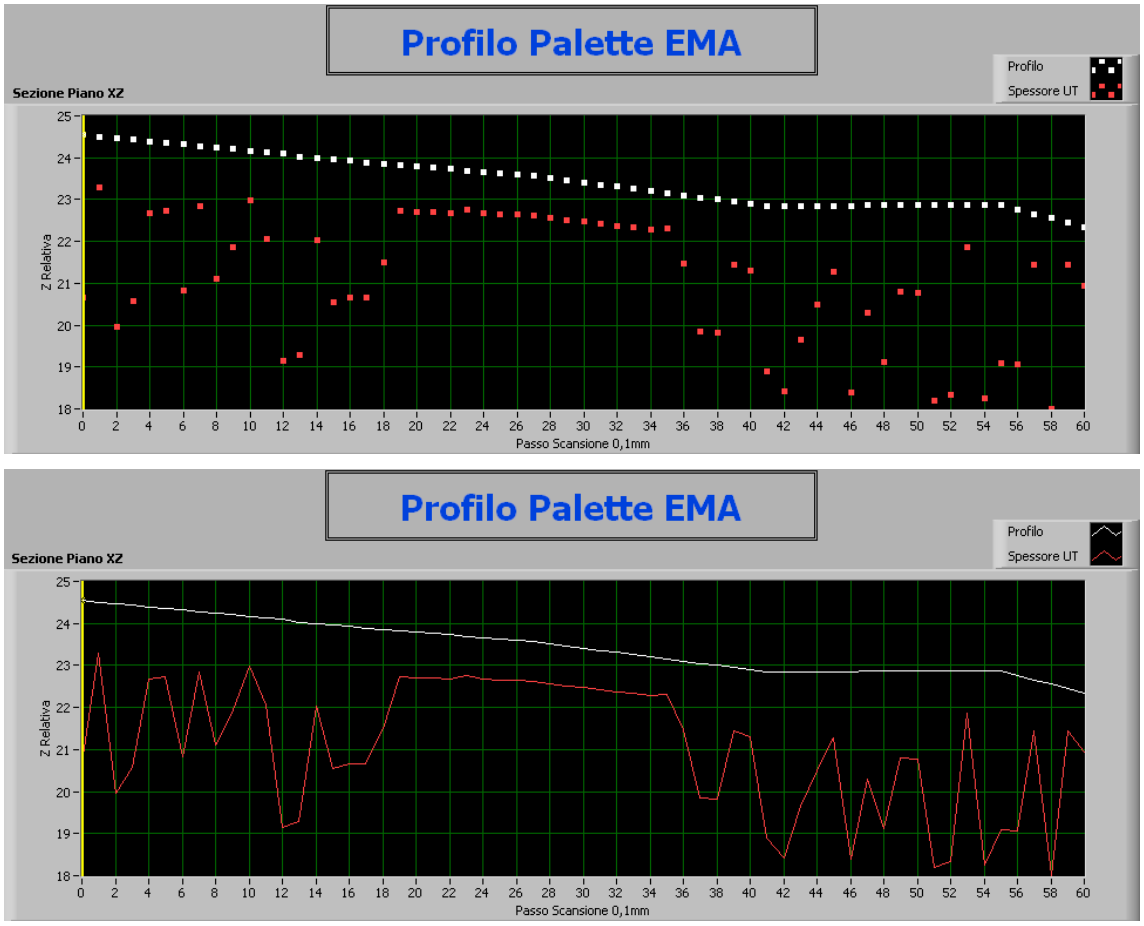

Figure III.70: Section 0 of the surface scan area B. White points/lines present the external profile characterisation. Red points/lines wall-thickness characterisation.

Chapter IV

Advanced Methods for Process Monitoring

IV.1 Introduction

Turning, drilling, milling and grinding are material removal processes widely used in many industrial sectors. In some of them, such as the car or the aerospace industry, the geometrical accuracy and surface finish requirements have been strongly increased in recent years. To meet these new needs, conventional machine tools have been replaced by numerical control machine tools (NCMT) to eliminate the variability introduced by the operator and to obtain better quality parts

On the other hand, in order to increase productivity and reduce manufacturing costs, NCMT have been associated with other components, mainly robots and computers, in flexible and computer-integrated manufacturing systems able to operate automatically during long periods of time. Such advanced manufacturing systems demand an optimal performance at all machining stages. This includes just in time tool change when the tool has reached a certain wear level.

However, the predetermined moment to perform the tool change is, in general, not easy to predetermine. To reduce costs, it is desirable to utilize the tool life as thoroughly as possible but this depends, case by case, on the required geometrical and surface accuracy levels.

The availability of a tool condition monitoring (TCM) techniques allowing for the on-line control of tool wear state and proper actions to counteract any decrease in machining performance caused by worn out tools or unexpected catastrophic tool failure, is becoming a critical requirement in order to optimize and improve the manufacturing process efficiency.

Development and implementation of tool condition monitoring systems has been the study subject of many researchers during the last years. Particularly, acoustic emission (AE) generated by friction between tool and work piece during the cutting process has been analyzed by a large number of authors and employed, in different ways, to develop systems allowing for the on-line tool wear monitoring.

However, standard solutions for industrial applications have not been found yet. This is mainly due to the complexity of tool wear mechanisms and the possibility to select among different alternatives in each step of the establishment of a tool wear monitoring procedure, so that not only one solution is possible.

The object of this research work is to verify the state of the different cutting tools during cutting process. Two different tool conditions were considered: fresh and worn, and different cutting parameters were varied. The sensor monitoring approach was based on the detection and analysis of audible sound signals generated by the cutting process.

The detected audible sound signal was processed in the frequency domain by a Real – Time spectrum analyser LARSON DAVIS 2800 model. This instrument provided a number of signal parameters that were analysed by:

- Graphical analysis;
- Neural Network processing.

IV.2 Audible sound system

The following instrumentation and software packages were utilized in the research work:

- Larson Davis Noise Analyser
- Spectrum Pressure Level (OS Dos)
- Noise and Vibration Works (OS Windows)
- CA Cricket Graph III (OS Mac)
- NWorks by Neural Ware (OS Mac)

IV.2.1 Larson Davis noise analyser

The analyser utilized is the Larson Davis 2800 Analyser, which allows carrying out two types of acquisition: Real-Time Normal mode, or Sound Level Meter (SLM) Mode. The differences between these two acquisition modes is that the SLM mode provides us the same FFT data as the Real – Time Normal mode, but it also provides a series of signal characterization parameters: SUM (LIN), SUM (A), SLOW, SLOW MIN, SLOW MAX, FAST, FAST MIN, FAST MAX, IMPULSE, LEQ, SEL, PEAK, Tmax3, Tmax5.

The SLOW parameter values, Figure IV.1 represent the values of the RMS SLOW level, along with the MIN and MAX values of the RMS Slow level, since the last data reset. The averaging time of the SLOW detector is 1 second.

The FAST parameter values, Figure IV.2 represent the values of the RMS Fast level along with the MIN and MAX values of the same RMS level, with the averaging time of the FAST detector set at 1/8 (0.125) seconds.

The MIN and MAX values of the RMS SLOW and RMS FAST are maintained over each measurement period.

The IMPULSE level, Figure IV.3, has an averaging time of 0.035 seconds, but is characterized by a very slow decay rate (3dB/sec), which means that we obtain an average value larger than the real value because the signal decays very slowly, and during acquisition we can't have the minimum and medium values.

LEQ (Equivalent Level), Figure IV.4, is a parameter used for the analysis of time-varying acoustic signals. It represents the steady level, which, integrated over the measurement period, would produce the same energy as the actual signal. The time used for calculation is the time elapsed since the last data reset.

SEL (Single Event Level) is similar to LEQ, except that is represents the steady signal which, integrated over a one second period, would produce the same energy as the signal integrated over the elapsed time since the last data reset.

Along with the LEQ and SEL integrated level, the 2800 analyser produces the maximum PEAK level that has occurred since last data reset. The PEAK detector has a rise time of 50 microseconds.

The Taktmaximal 3 and 5 (Tmax3, Tmax5) is an integrated level, which is based on a German standard.

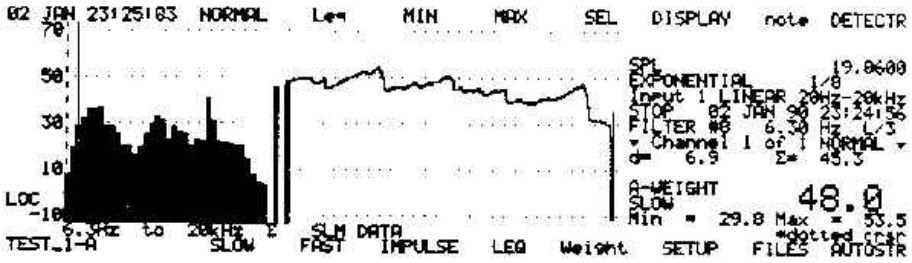

Figure IV.1: SLOW Display.

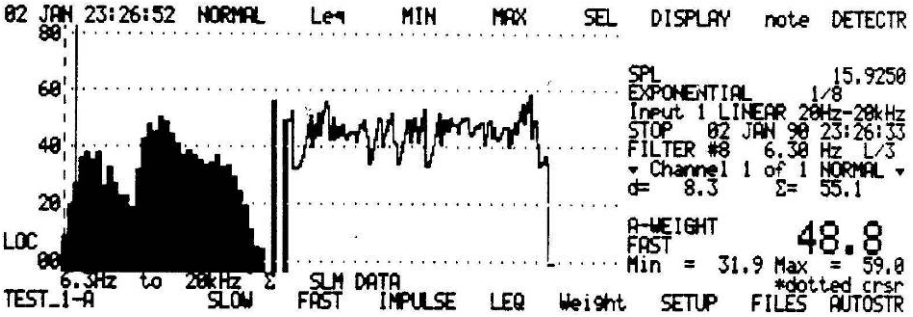

Figure IV.2: FAST Display.

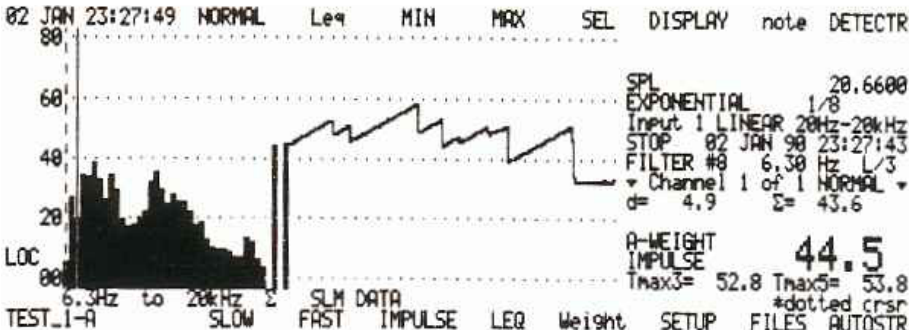

Figure IV.3: IMPULSE Display (slow decay rate).

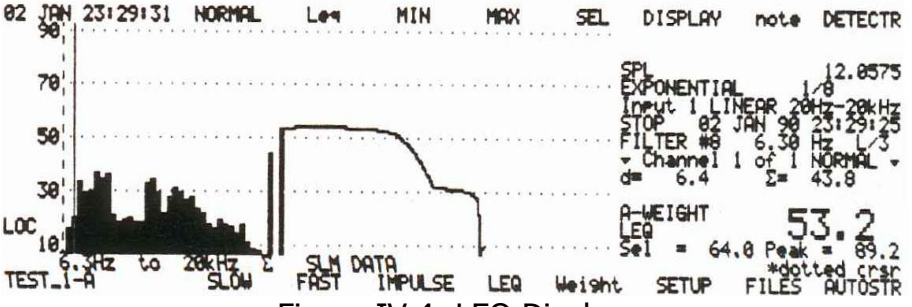

Figure IV.4: LEQ Display.

In the default settings of the Model 2800, the frequency analysis function is configured as follows:

- Microphone Input: CHANNEL 1
- Analog Filtering: 20Hz highpass and 20KHz lowpass filters
- Digital Filtering: 1/3 Octave Bandwidths
- Averaging Type: Exponential
- Averaging Time: 1/8 second (corresponds to SLM FAST)
- Units: SPL (Sound Pressure Level)

In the next paragraph the Setup procedure of the 2800 Analyser will be presented. The Back and Right Side Panel of the 2800 Analyser are shown in Figure IV.5.

First the microphone must be connected to the CHANNEL 1 input; with the power switched OFF. This type of analyser is equipped and with a removable NiCd packs battery.

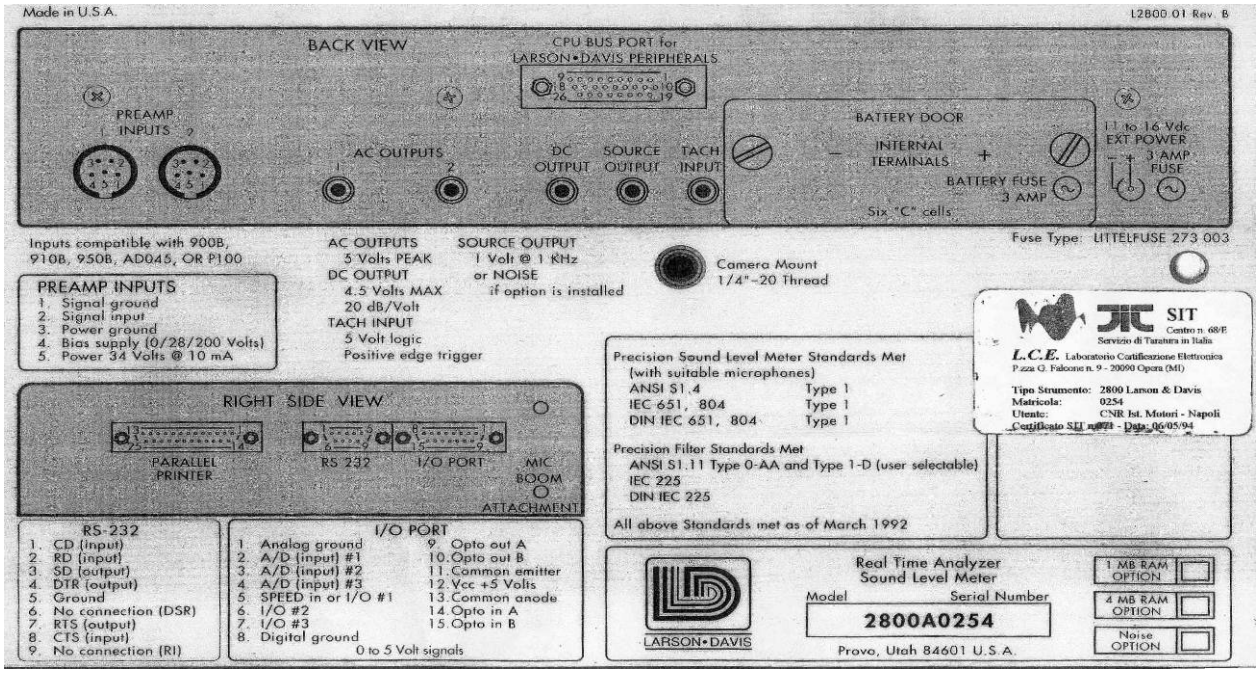

Figure IV.5: Back and Right side Panel of LD Model 2800.

After this procedure, the analyser will be turned ON. The initialisation of the system will take place, and the analyser is ready to acquire.

To create the files for each measurement, we enter the FILES menu. In this window, we can see time and date, the free and used memory on the upper left corner, and in the part "MEMORY" we can see the INITIAL file with the size equal at 256 byte. To create the new file, we must push the "CREATE" button (letter A), than; in the upper right corner we must introduce the name of the file. To save the file, we must push the "EXIT" button, and we will see the new file that have the initial size of 256 bytes.

To rename or erase the file we must push the "RENAME" or "DELETE" buttons (letter J respectively I). To re-enter the principal menu, we will push "EXIT" button. Finally we must see the name of the file in use, in the lower left corner.

To select the transfer rate, we must push "SCREEN/SYSTEM" button, and after this we will select the "I/O" button (letter I), and we will select the velocity of transfer from 300, 600, 1200, 2400, 4800, 9600, 19200, by pushing the buttons (letter J, K, L, M, N, O, P). After this, a message like "RS232 9600 baud selected" will appear for a short period of time in the upper right corner of the display. To exit to the principal menu we push the "EXIT" button. When we are exiting from a menu, the changes are automatically refreshed.

To change the FFT setup, we must enter the "SYSTEM", and then the "FILTER", menu (letter G). We will see a representation as shown in the Figure IV.6. In this menu we have the opportunity to select the number of lines that the selected interval will be divided into, by pushing the buttons "100line, 200line, 400line, 800line", corresponding to the letters I, J, K, L.

In this menu, we have the opportunity to change frequency zoom interval by entering the "FFTZOOM" menu (letter M), as shown in the Figure IV.7.

Once selected the preferred interval, we can return to the FILTER menu by pressing one time the "EXIT" button, or for exiting to the principal menu, the same button two times.

To store the data in automatic mode, we must set-up the "AUTOSTORE" menu (letter P). Once entered in this menu, we will push the "BYTIME" button (letter B). After this, we will modify the "ENDSTAR" (letter D) and "DELTA" (letter C) values.

By pushing the "ENDSTAR" button, we will see in the upper right corner the "END TIME = 000010.000", this one being the default end time. With the NUMPAD existing on the 2800 Analyser, we will set-up this parameter, and to update the modifications, we will push the "EXIT" button.

By pressing the "DELTA" button, we can set the time between two successive measures, and in the upper right corner we will see "DELTA TIME = 000000.1000", this being the default delta time. To make the changes we will push the "EXIT" button.

To acquire in the SLM mode, we must push the "SLM" button. The 2800 Analyser is ready to make the acquisitions.

To start or stop the acquisition, it is necessary to push "RESET/R/S" button, on the lower left corner of the analyser.

For any new experiment, we must create a new measure file.

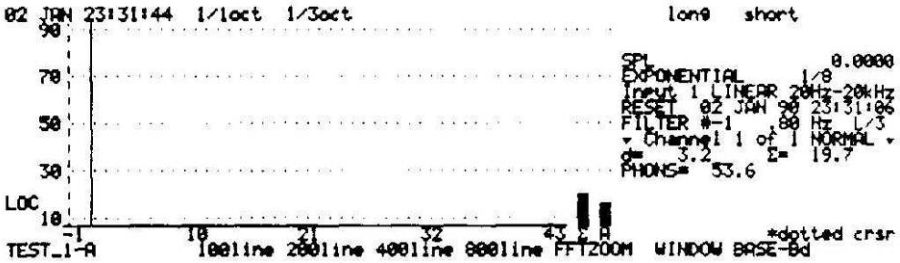

Figure IV.6: FILTER menu.

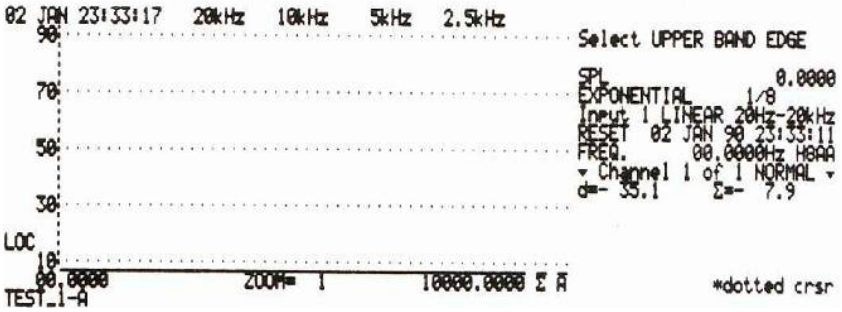

Figure IV.7: FFTZOOM.

Table IV.1

The values for the interval for each zoom level

ZOOM VALUE (letter)	Frequency interval
1 (A)	0 – 20000 Hz
2 (B)	0 – 10000 Hz
4 (C)	0 – 5000 Hz
8 (D)	0 – 2500 Hz
16 (E)	0 – 1250 Hz
32 (F)	0 – 625 Hz
64 (G)	0 – 312.5 Hz
128 (I)	0 – 156.25 Hz
256 (J)	0 – 78.125 Hz
512 (K)	0 – 39.0625 Hz

In our case, the following setup of the 2800 Analyser was utilized:

1. We created 8 files for each measurement, 4 for fresh blade and 4 for worn blade, 2 for each type of work material, aluminium alloy and low carbon steel;
2. We selected the velocity of transfer of 9600, the same velocity must be imposed to the personal Computer used for transferring the files, see paragraph 1.2.2;
3. We set the FFT filter to 800 lines, and a FFTZOOM equal at 2. This filter gives an interval from 0 to 10.000 Hz, divided into 800 sub-intervals with a step of 12.5Hz.
4. The measurements were Auto Stored, By Time, with the end time equal to 10 seconds, and the step equal to 1 second.

IV.2.2 Spectrum Pressure Level (Dos)

This software, SPL Dos, allows us to load the measurement from the 2800 Analyser, and to view them.

The transfer from the 2800 Analyser, is made following the procedure:

1. The serial port of the 2800 Analyser, and the COM1 of the PC would be connected with a serial cable, which is available with the Analyser;
2. Once connected, we will open the SPL program, entering the DOS command "C:\SPL\SPL.EXE"
3. With the program running, we will make a new archive which will be *.LD3 format, by accessing the "ARCHIVE" menu, "FRESH ARCHIVE", and now we must write the name of the archive, Ex: "archive_name. LD3"
4. Once the archive is made, we must insert the measurements, from the 2800 Analyser by following the next steps:
    i. "LOAD MEASUREMENTS" menu;
    ii. It will appear a window where we impose the transfer velocity, the same as the one in the 2800 Analyser, Ex: 9600;
    iii. The third window that will appear is the window where we should load the records;
    iv. For loading the rest of the measurements we will follow the procedure from 4.i.;
    v. After all the measurements have been loaded; we will save them all, and will quit this program.
5. For transferring to the next program, we must copy the archive *.LD3 to a external mass storage.

IV.2.3 Noise and Vibration Works

This version of Noise and Vibration Works, is 1.26, and this one is used for obtaining the numerical values from the files in *.LD3 format, which cannot be available directly to the 2800 Analyser. Those numerical values will give us the possibility to observe the graphics displayed in real-time when we are acquiring with the analyser.

To get the tables with the values we need to pursue the next procedure:

I. Copy in a directory the *.LD3 archive;

II. Open the N.W.WIN program from the Windows Start menu, Programs, N.W.WIN;
III. Once opened from "Analyser" menu, we make the option for "2800/2900/3000" analyser, because we have used the 2800 Analyser;
IV. It will appear a window with the selected analyser. In the "Measurements" menu of this window, we will choose the "load DOS archive";
V. It will appear a window, with all the measurements, loaded from 2800 Analyser, to the SPL program. We will load all the measurements, at end of this, we will see a FFT graphic in the main window of the N.W.WIN;
VI. Once loaded, all the measurements, we will go in THE "VISUALISATION" menu, and we will opt for "VIEW NUMBERS" MENU, or directly by pressing F4 button;
VII. It will disappear the window with the graph, and will appear a window which is composed of one TIME column, one OVERLOAD column, 800 columns with the values for each 12.5 Hz, from 0 to 10000 Hz, and at the end the columns with the parameters SUM (LIN), SUM (A), SLOW, SLOW MIN, SLOW MAX, FAST, FAST MIN, FAST MAX, IMPULSE, LEQ, SEL, PEAK, Tmax3, Tmax5; see results paragraph;
VIII. We will transfer this table to Microsoft Word by making COPY and PASTE, and will save the file as *.TXT format;
IX. After all the dataset is transferred we will close the program N.W.WIN.

IV.2.4 CA Cricket Graph III

The Cricket Graph has helped us to make the graphics elaboration of the numerical values obtained from the 2800 Analyser.

This program has the possibility to make the transpose of the rows with the columns, and to load the first row in the column titles.

These options will be selected when we must make the graphs. For checking those options, we must enter in the "OPTIONS" menu, "PREFERENCES" and "TEXT FILE I/O …". It will appear a window where in the lower side will see those two options. If we are preparing the tables, we must NOT select these options.

Once we have view this options, we will load the *.TXT file saved with the Microsoft Word. It will appear the same table like the one in N.W.Win program. From this table, we will eliminate the "OVERLOAD" column, and the "FIRST SECOND" row, by accessing twice the "DATA" menu, "DELETE".

After this operation, we will CUT the last columns with the parameters, describing the signal, and we will PASTE those columns in a new Cricket Graph document.

We save the file as *.TXT format, Ex.: file_name_PA.TXT, in our case "SNA1PA.TXT".

Attention, for saving the file as *.TXT file, we must select in "SAVE AS" window, the "TXT" options, and the name of the file will include the ". TXT".

Once made this operation, we will have a file with 802 columns, and 10 rows. This file will be saved as *.TXT format file.

The same procedure will be done for all the 8 tables.

To calculate the maximum values of the different intervals, chosen by us, ex: 0-250Hz, 250-500 Hz, 500-1000 Hz, 1000-2500 Hz, 2500-5000 Hz, 5000-10000Hz, we must put in the same file, alternating, the tables with 802 columns, of the same material, for

the first and second experiment, for fresh and worn blade, and at the end of the table we must enter the formula for calculating the max values.

To visualize the maximum values, we must double click in the first cell of the column, where we will put those values, and write the max formula "=COLMAX (CF: CL)", where CF is the first column and CL is the last column of the desired interval. In the next table we will see the frequency interval and the formula for the same interval.

Table IV.2
The formulas syntaxes for the maximum values for every frequency interval

Frequency Interval	Cricket Graph Formula
0-250 Hz	=COLMAX (C2: C22)
250-500 Hz	=COLMAX (C23: C42)
500-1000 Hz	=COLMAX (C43: C82)
1000-2500 Hz	=COLMAX (C83: C202)
2500-5000 Hz	=COLMAX (C203: C402)
5000-10000 Hz	=COLMAX (C803: C802)

When we finish all this we will "CUT" the maximum values, and we will "PASTE" those values in an Excel worksheet, and the file will be saved as *.TXT format. Once finished with preparing this files we can start with the graphics.

To utilize the tables for the graphs, we must select from "TEXT FILE I/O…" proprieties, the "transpose the rows with the columns", and to "load first row in the column titles".

For the first graphics we will use the table with the 802 columns and 10 rows. After opening those files, we will observe that we have 801 rows and 10 columns, in the columns we have the time, and in the rows we have the frequency.

Accessing the "GRAPH" menu, "FRESH GRAPH", "LINE", we will make the graphics. In the window that will appear, we must select the vertical and horizontal axes, in our case it will be the frequency in the logarithmic scale, and SEC2, fresh blade, first and second experiment. For all the seconds we will follow the same procedure, and at the end we will have the graphics of Figure IV.18 for aluminium alloy and Figure IV.24 for low carbon steel.

The next graphics will be the maximal values function of logarithmic frequency. Those one it will be the "SCATTER" graph type and the table are the maximum values without making the "transpose the rows with the columns" option. The graphics are showed in the Figure IV.19 for aluminium alloy, and Figure IV.25 for low carbon steel.

The third type of graph has on base the same table like the previous one but with the "transpose the rows with the columns", and to "load first row in the column titles" active. This graphics will contain the interpolation of the frequency intervals, with the superior intervals for the same material, for fresh and worn blade. For example, in a graphic we will have the interpolation of the 0-250 Hz interval with 250-500Hz interval from the fresh blade, and the 0-250 Hz interval with 250-500 Hz interval from the worn blade.

These graphics are presented in Figure IV.20 for the aluminium alloy and Figure IV.26 for low carbon steel, and in total we will have 15 graphs, where we will see the discriminations from the fresh and worn blade, at different frequency intervals.

Cricket Graph will be used after the Neural Network elaborations.

The graphics that we will make are the "LINE" type graphs, and will contain the Success Rate (SR%) function of the Learning Steps for all the threshold error, Figure IV.23 for aluminium alloy and Figure IV.29 for low carbon steel. Next will be the Success Rate (SR%) vs. threshold error, for all the learning steps, Figure IV.22 for aluminium alloy and Figure IV.28 for low carbon steel, and the graph of the Output Values of the Neural Networks vs. Identification Input for fresh and worn blade, at learning step 12000, for aluminium alloy, and 10000 for low carbon steel. This graphics are visualized in the Figure IV.21 for aluminium alloy and Figure IV.27 for low carbon steel.

IV.2.5 NWorks by Neural Ware

Also referred to as connectionist architectures, parallel distributed processing, and neuromorphic systems, an artificial neural network (ANN) is an collections of mathematical models that emulate some of the properties of biological nervous systems and draw on the analogies of adaptive biological learning. The key element of the ANN paradigm is the novel structure of the information processing system. It is composed of a large number of highly interconnected processing elements that are analogous to neurons and are tied together with weighted connections that are analogous to synapses.

Learning in biological systems involves adjustments to the synaptic connections that exist between the neurons. This is true of ANN's as well. Learning typically occurs by example through training, or exposure to a trusted set of input/output data where the training algorithm iteratively adjusts the connection weights (synapses). These connection weights store the knowledge necessary to solve specific problems.

There are multitudes of different types of ANN's. Some of the more popular include the multilayer perceptron which is generally trained with the backpropagation of error algorithm, learning vector quantization, radial basis function, Hopfield, and Kohonen, to name a few. Some ANN's are classified as feedforward while others are recurrent (i.e., implement feedback) depending on how data is processed through the network. Another way of classifying ANN types is by their method of learning (or training), as some ANN's employ supervised training while others are referred to as unsupervised or self-organizing. Unsupervised algorithms essentially perform clustering of the data into similar groups based on the measured attributes or features serving as inputs to the algorithms.

The ANN's major applications are:

- Artificial Intelligence
- Automobile Controls
- Character Recognition
- Forecasting / Market Prediction
- Image Understanding
- Logistics
- Optimization
- Quality Control
- Robotics
- Visualization

In the full sense, a neural network, it's a computer architecture (comprising software, hardware or both) modelled on the way the human brain processes sensory stimuli. Most traditional computer programs use statements that take the form, "if this, then that." A solution is achieved via a series of deductive steps, with given instructions executed one at a time. Neural networks, on the other hand, are inductive programs; they take in a great amount of information all at once and then draw a conclusion. The

programmer first gives the system some training data with known conclusions. That helps the program learn the correct solutions by example. The more data fed into the computer-which may or may not be a traditional digital computer-the better the results. A neural network involves large numbers of sensing and processing nodes that continuously interact one with another. Between each pair of nodes sits a non-linear transfer function, such as a numerical weight, that helps determine the final conclusion. As the neural net learns through the input of data, the weights are tweaked for a better solution. Ultimately, the network learns the solution itself.

The software package used is the NWorks by Neural Ware 4.05 Macintosh version. The learning steps were 1000, 2000, 4000, 6000, 8000, 10000, 12000, and the train was made for all with two steps.

To run the program will select the program shortcut from desktop, and it will appear a window as shown in Figure IV.8.

After the program is launched, we must select the folder that contains the learning and testing file. This is possible by accessing the "FILE" menu, "CURENT FOLDER…" and the window showed in Figure IV.9 will appear. We will select the folder with all the dataset, and at finished we will select "FOLDER" option. In our case it was selected the second two, first experiment (21), aluminium alloy piece.

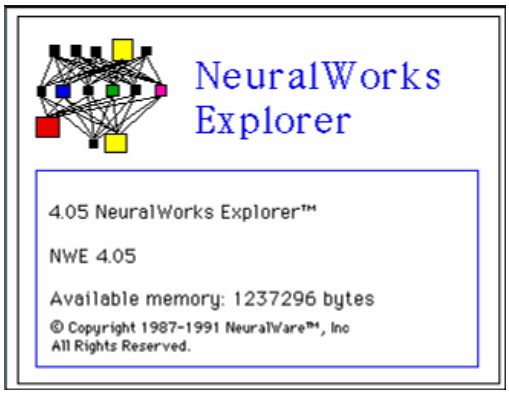

Figure IV.8 Neural Network Explorer.

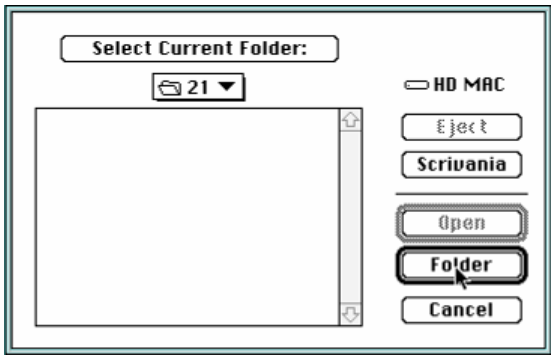

Figure IV.9 Select Folder Window.

After this operation we will enter the "NETWORK" menu "BACK PROP BUILDER", we will have the window, which contains the ANN's settings Figure IV.10. The learning rule is the "CUM-DELTA" the transfer rule is "SIGMOID", the input, hidden and output values are 6-3-1 and the files used in the learning and testing process are "s21a.nna" and "s21t.nna". Also in the main window Figure IV.11, will be present and the RMS error graph.

Once set-up up will start the learn process of the ANN, and that is doing by selecting from "RUN" menu "LEARN…" options. In the window that will appear will insert 1000, which is the learning step. This step will be used until the network has reached 2000 learning steps. From that point we have choose to make the learning step equal at 2000. In this case we have 1000, 2000, 4000, 6000, 8000, 10000, 12000 learning steps for each network. The network after each learning step we will be tested, "RUN" menu "TEST" option, where we will insert the value 2 for each learning step.

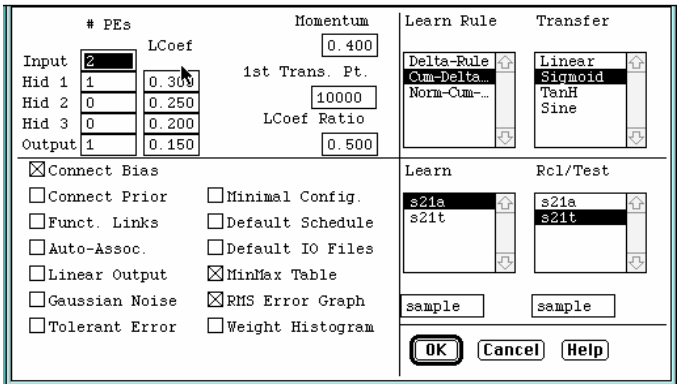

Figure IV.10: Back propagation builder menu.

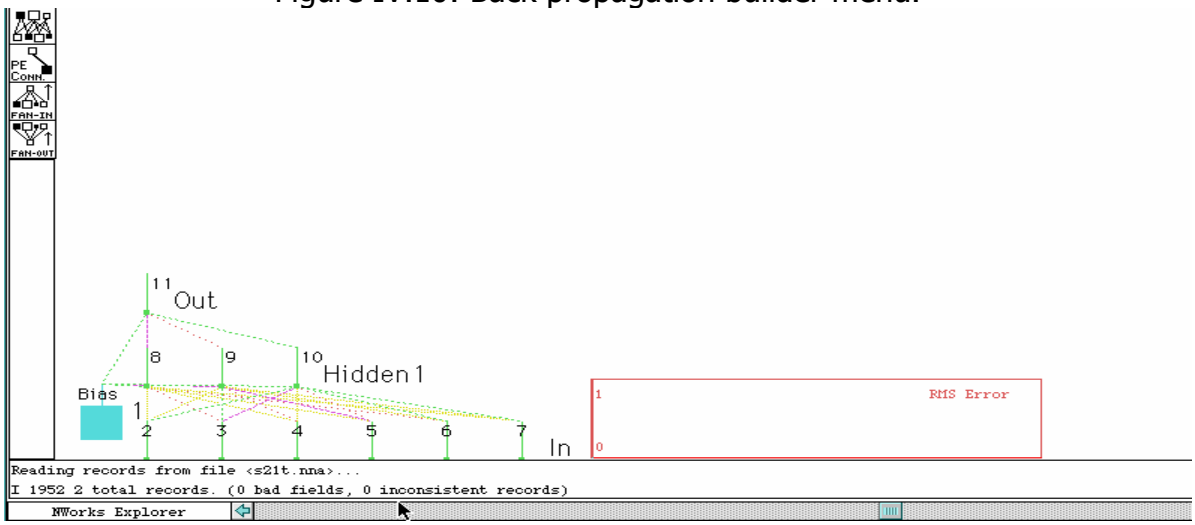

Figure IV.11: Main window of NWorks by Neural Ware 4.05.

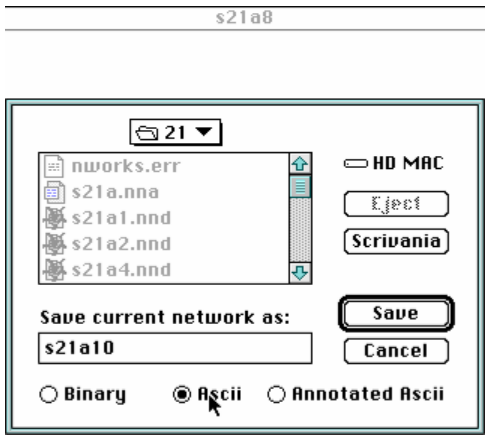

Figure IV.12: Network saved at step 10000.

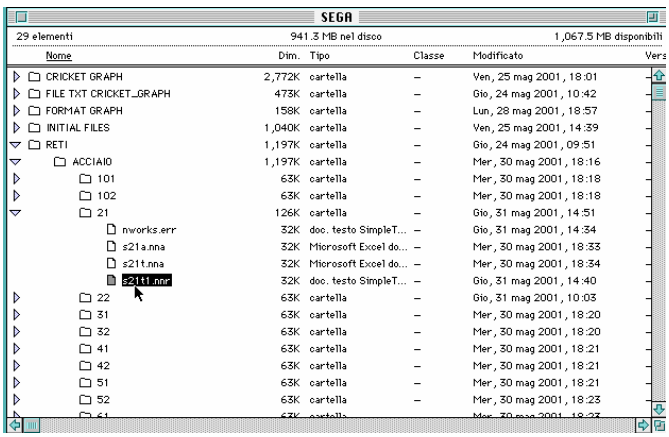

Figure IV.13: Test file saving at step 1000.

The test file is giving us the value that we will must insert in test menu, because the number of the rows in this file is equal at the number inserted.

The learning file is that, which not contains the rows in the testing files, but it contains the rows from first and second experiment, fresh and worn tool.

Once made the learning and testing the network will be saved, with the name of the learning file in the format *.NND, Figure IV.12, and the answer file of the network will be saved with the name of the testing file format *.NNR, Figure IV.13.

After the saving of the entire network and test file, we will put in a document the output of ANN and the desired output of the same learning step, and we will calculate the Success Rate (%) for each learning step and threshold.

IV.3 Experimental applications

IV.3.1 Band saw cutting tests

The cutting tests were performed with a SENAS 300 band saw, Figure IV.14, with a cutting speed of 1750 mm/sec, a feed rate of 4.35 mm/sec. Diamond coated fresh and worn blades with a cut kerf equal at 1.5 mm., were used (Figure IV.15).

The work materials used was an Al alloy plate (Figure IV.16) and a low C steel plate (Figure IV.17) with a thickness of 3.3 mm, a length of 144 mm for Al and 203 for low C steel, and a width of 107 mm and 94 mm respectively.

Figure IV.14: SENAS 300 band saw machine.

Figure IV.15: Diamond coated fresh blade.

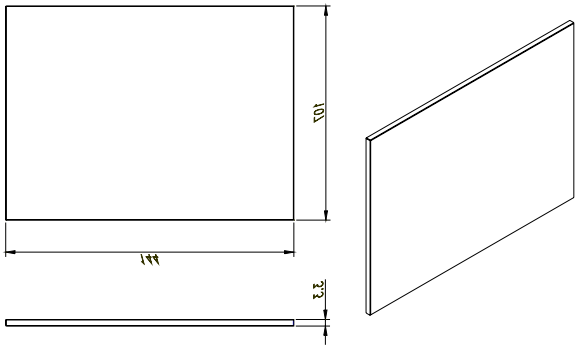

Figure IV.16: Aluminium alloy plate.

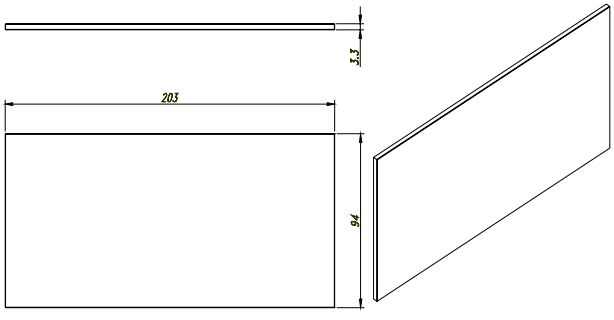

Figure IV.17: Low carbon steel plate.

IV.3.2 Results

FFT Processing

In order to present the results for the whole cutting test duration (10 seconds), pairwise plots of maximal signal amplitude for each selected frequency interval were constructed. In our case were selected six frequency intervals:

- 0 – 250 Hz.
- 250 – 500 Hz.
- 500 – 1000 Hz.
- 1000 – 2500 Hz.
- 2500 – 5000 Hz.
- 5000 – 10000 Hz.

The maximum signal amplitude was evaluated for each frequency interval and for each second of cutting test, for fresh and worn blade.

Neural Network Data Processing

In order to process the audible sound signal data in higher dimension feature spaces, a neural network based approach was carried out. A 6-3-1 Neural Network was developed with 6 input nodes in the input layer, 3 nodes in the hidden layer and 1 node in the output layer for the fresh and worn blade classification.

The Neural Network characteristics parameters are:

- Momentum - 0.4
- Lcoef.Ratio - 0.5
- Learn Rule - CUM - DELTA
- Transfer Rule - SIGMOID
- Epoch Size - 6

Training set for each work material was constructed by forming 6–features input patterns containing the maximum signal amplitudes for each frequency interval, each tool state and each second of the cutting test.

For the training and testing of the Neural Network, a "Leave - K - Out" procedure with K=2 was utilized. For the learning process of the Neural Network a total of learning steps between 1000 and 12000 was utilized (Figure IV.22, IV.28). For the Success Rate determination threshold values variable between 0.1 and 0.5 was utilized (Figure IV.23, IV.29).

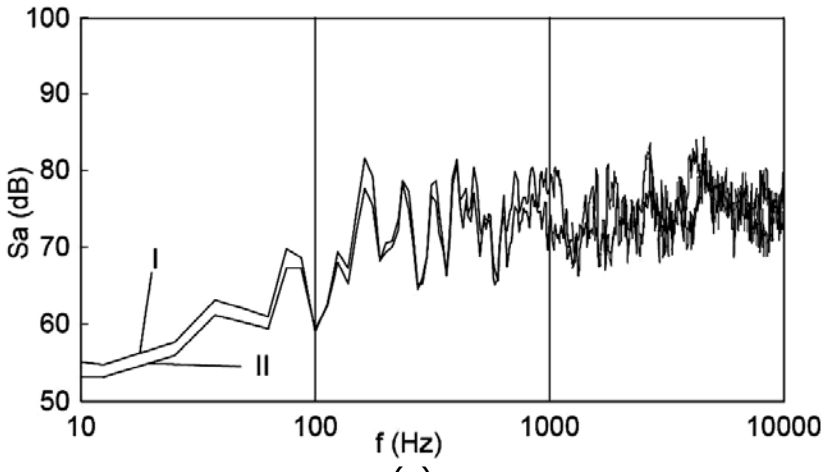

(a)

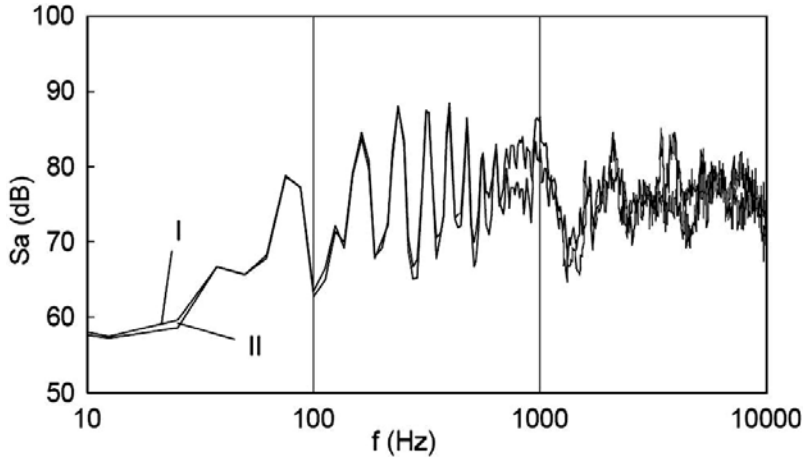

(b)

Figure IV.18: 2024 Al alloy – Signal amplitude Sa (dB) vs. frequency f (Hz) for second # 2, I and II test. (a) fresh blade (b) worn blade.

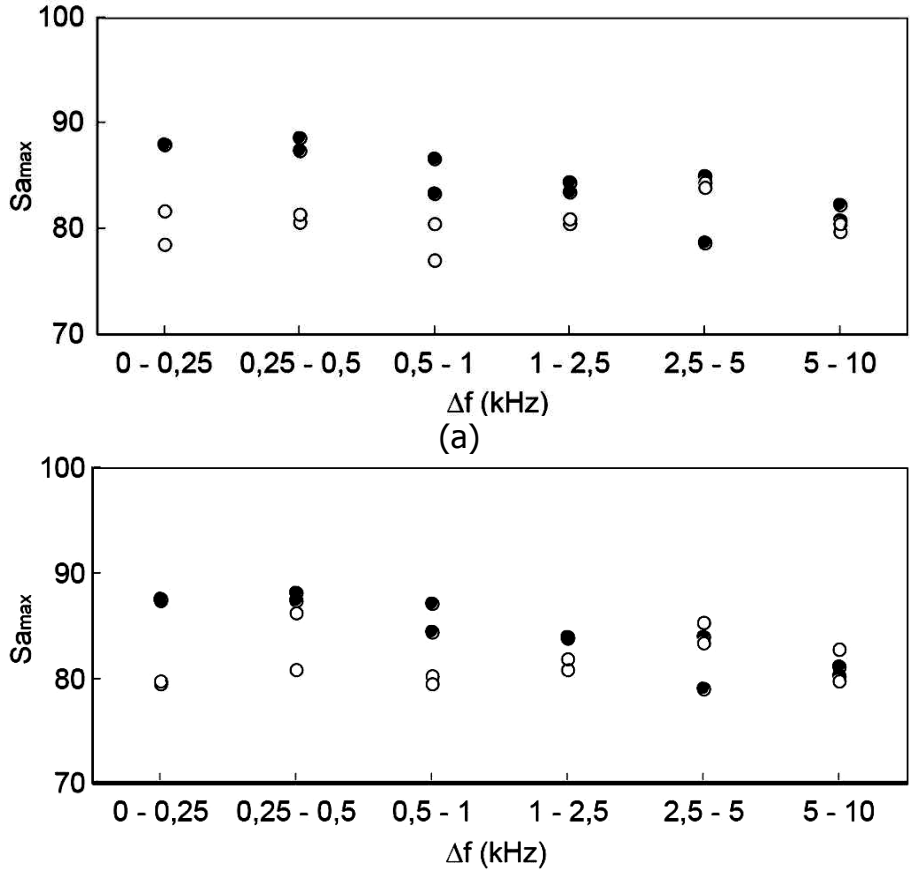

Figure IV.19: Al alloy, maximum signal amplitude Samax (dB) vs. selected frequency Df (Hz) intervals for fresh and worn blades, I and II test: (a) second # 2, (b) second # 3. White symbols = actual output for fresh blade, Black symbols = actual output for worn blade.

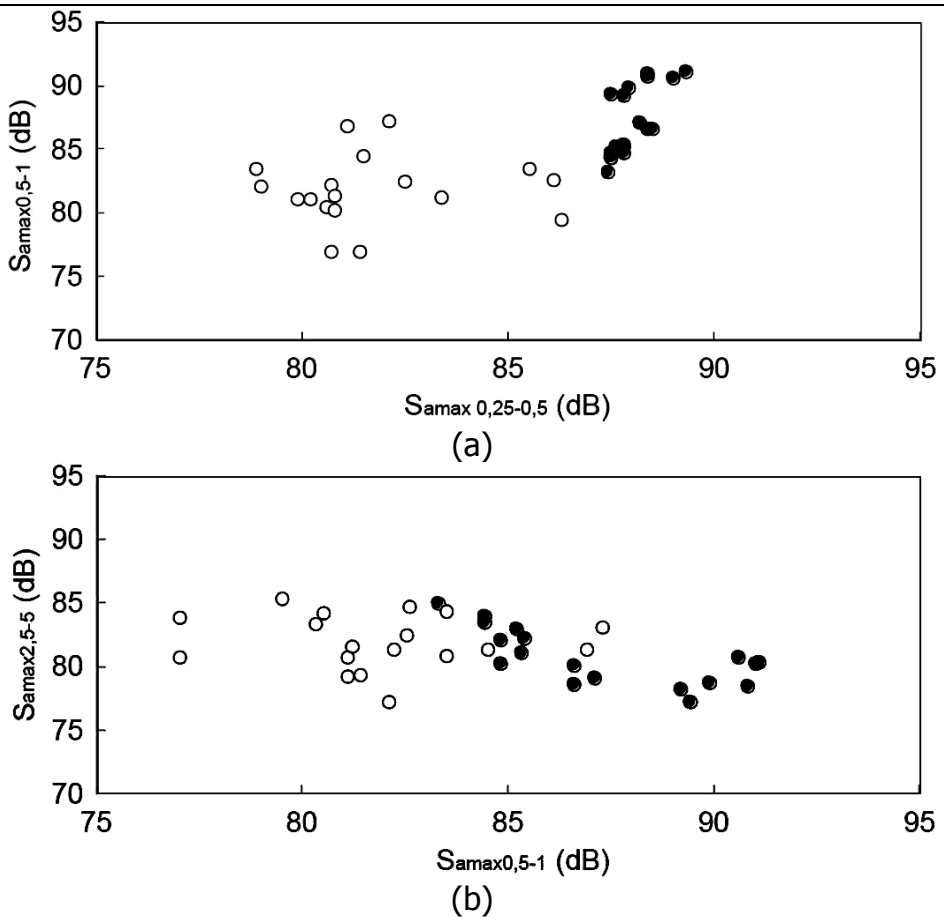

Figure IV.20: 2024 Al alloy, Pairwise plots of maximum amplitude signals for fresh and worn blade, for the whole cutting test duration, I and II test: (a) 0.5/1 kHz freq. int. vs. 0.25/0.5 kHz freq. int., (b) 2.5/5 kHz freq. int. vs. 0.5/1 kHz freq. int. White symbols = actual output for fresh blade, Black symbols = actual output for worn blade.

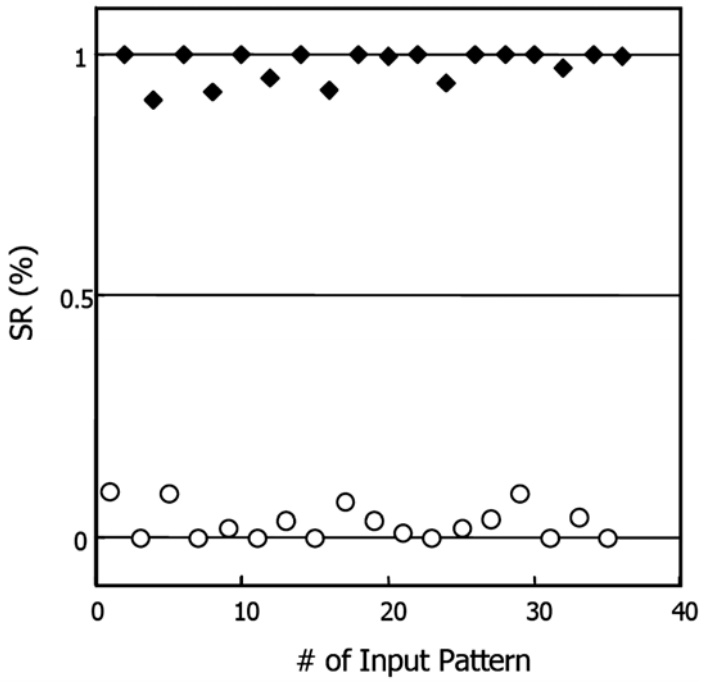

Figure IV.21: NN output vs. # of input pattern. 2024 Al alloy (10000 learning steps). o Fresh blade, ◆ worn blade, 0/1= desired output for fresh/worn blade.

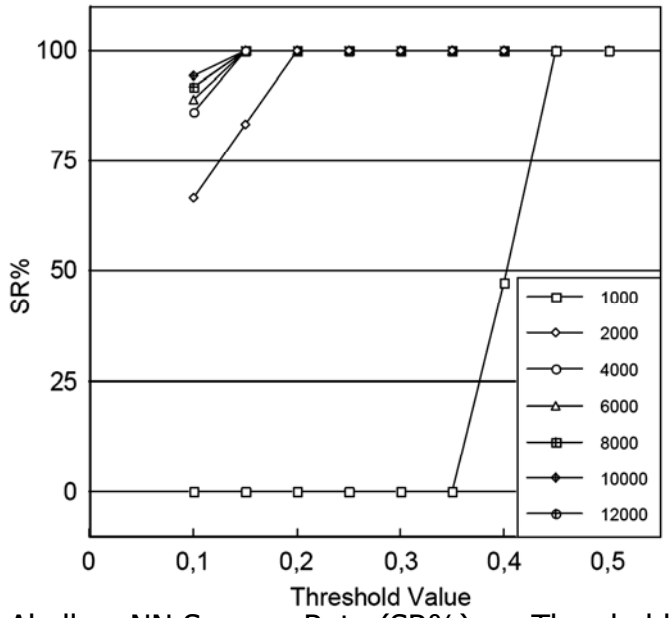

Figure IV.22: 2024 Al alloy, NN Success Rate (SR%) vs. Threshold Value for different learning steps.

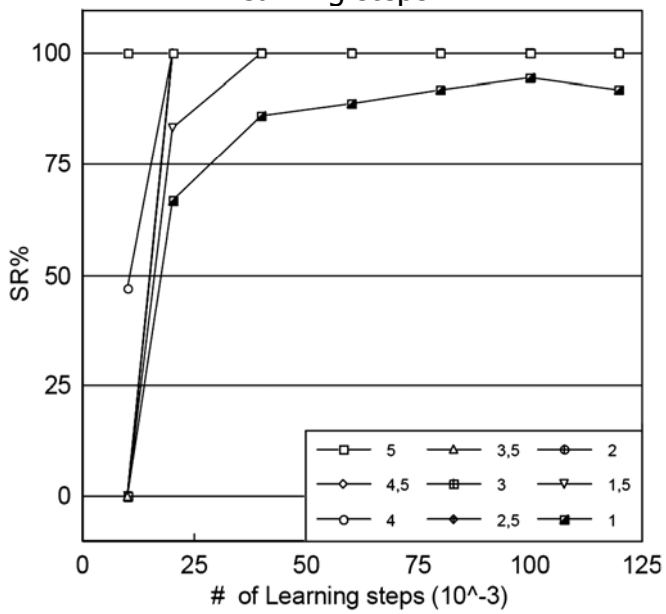

Figure IV.23: 2024 Al alloy, NN Success Rate (SR%) vs. # of learning steps, for different threshold values.

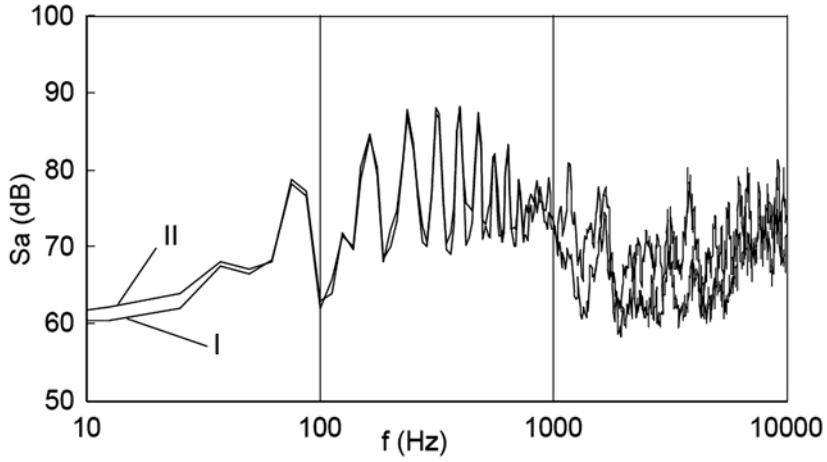

(a)

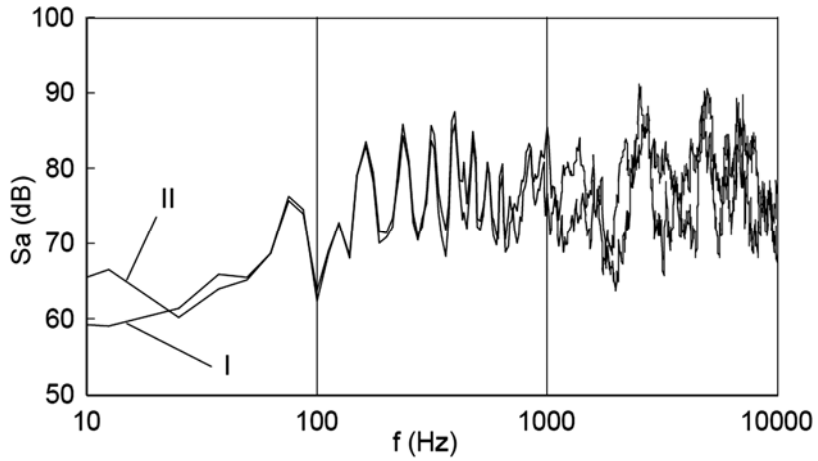

(b)

Figure IV.24: Low C steel – Signal amplitude Sa (dB) vs. frequency f (Hz) for second # 2, I and II test. (a) fresh blade, (b) worn blade.

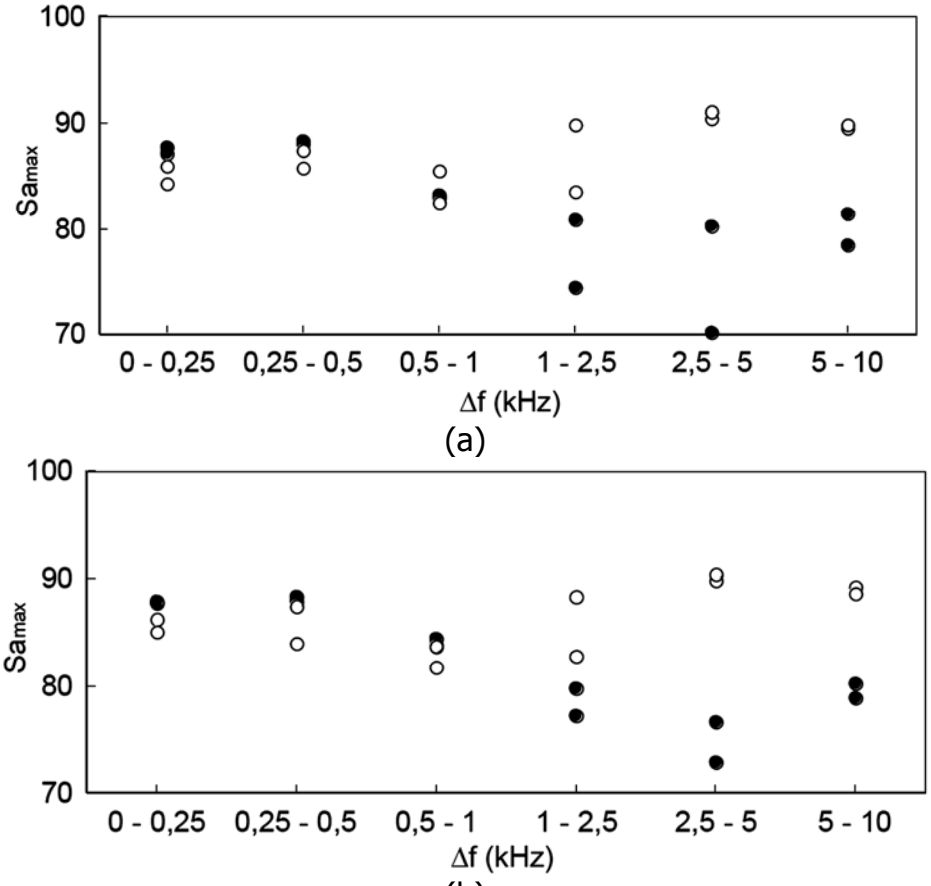

Figure IV.25: Low C steel, maximum signal amplitude Sa_{max} (dB) vs. selected frequency Df (Hz) intervals for fresh and worn blades, I and II test: (a) second #2, (b) second #3. White symbols = actual output for fresh blade, Black symbols = actual output for worn blade.

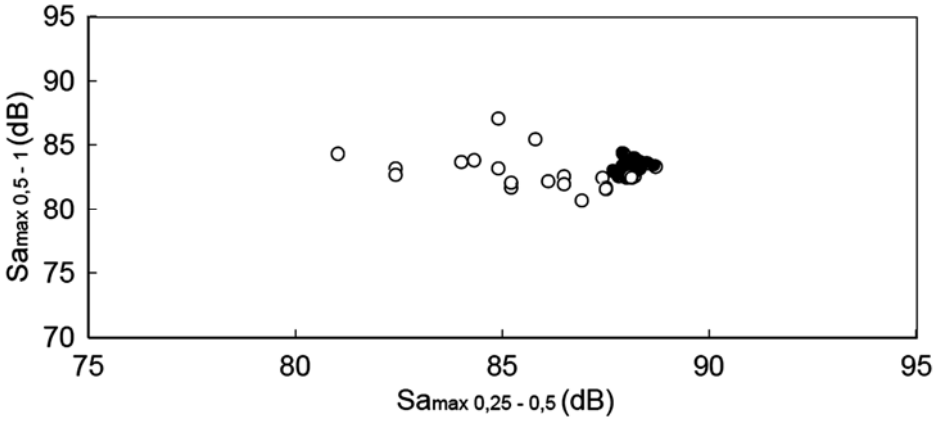

(a)

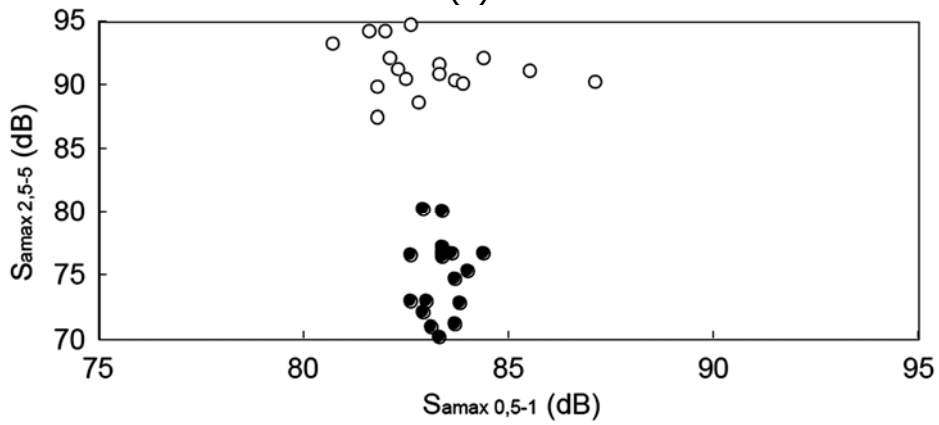

(b)

Figure IV.26: Low C steel, pairwise plots of maximum amplitude signals for fresh and worn blade, for the whole cutting test duration, I and II test: (a) 0.5/1 kHz freq. int. vs. 0.25/0.5 kHz freq. int., (b) 2.5/5 kHz freq. int. vs. 0.5/1 kHz freq. int. White symbols = actual output for fresh blade, Black symbols = actual output for worn blade.

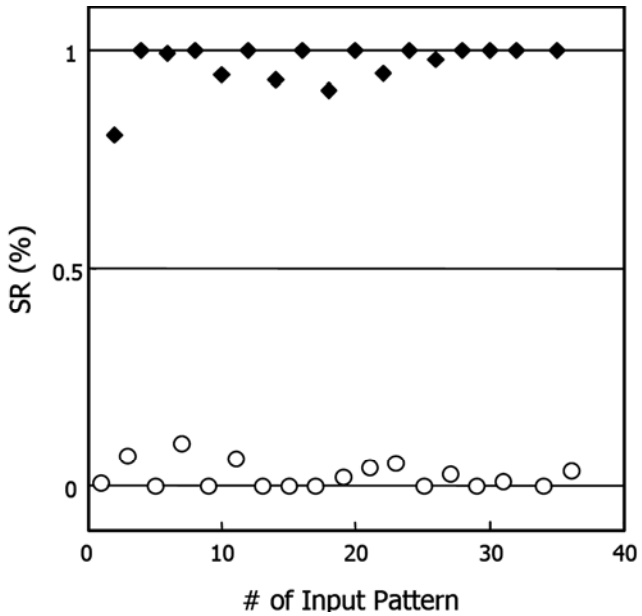

Figure IV.27: NN output vs. # of input pattern. Low C steel (12000 learning steps). o Fresh blade, ◆ worn blade, 0/1= desired output for fresh/worn blade

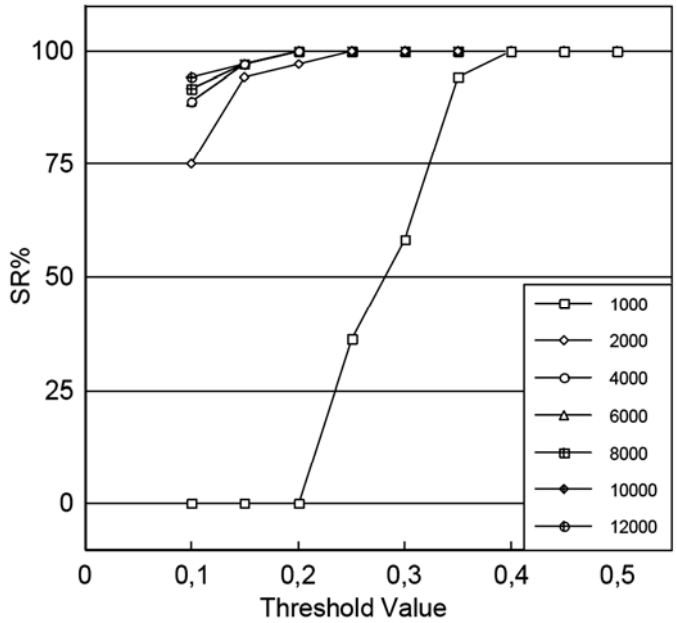

Figure IV.28: Low C steel, NN Success Rate (SR%) vs. Threshold Value for different learning steps.

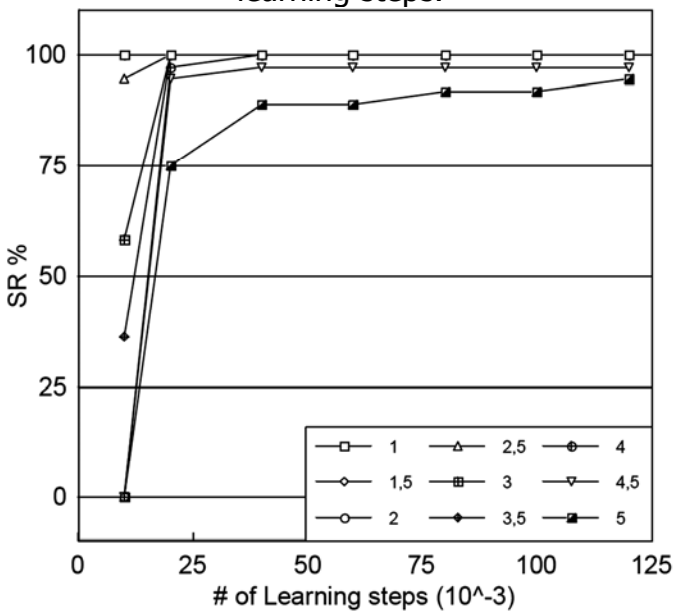

Figure IV.29: Low C steel, graph of the Succe0ss Rate (SR %) function of the learning steps for threshold error.

IV.3.3 Discussions

Graphical analysis

From Figure IV.19 and IV.24, it can be noted that, in the case of Al alloy, the separation between fresh and worn blade data points occurs for low frequency ranges (f<2500 Hz) (Figure IV.19). On the contrary, in the case of low C steel, fresh and worn blade data points separation is verified for high frequency ranges (f>1000 Hz) (Figure IV.24).

In the Figure IV.20 and IV.26, it can be seen that the pairwise of plots of low frequency intervals allows for an excellent, linear separation between fresh and worn blade data points, in the case of Al alloy (Figure IV.20). In the case of low C steel (Figure

IV.26), data points separation is steel verified though the group separability is linear not as good for Al alloy.

Neural Network analysis

In the Figure IV.21 and IV.27, the Neural Network output is reported vs. # of input patterns for the work materials. From the figure, it can be clearly seen that the Success Rate in the identification of the state blade, fresh and worn, is 100 % for both work materials.

In Figure IV.22 and IV.28, the Neural Network Success Rate for both work materials is reported vs. threshold value for different # of learning steps (variable between 1000 and 12000) and vs. # of learning steps for different threshold values (variable between 0.1 and 0.5)(Fig.1.23 and IV.29).

Only for low # of learning steps and threshold values, a real significant reduction of Neural Network success rate is verified.

These conditions however represent a uselessly severe condition of Neural Network audible sound data processing for fresh and worn blade identification.

IV.3.4 Milling process monitoring

Introduction

This research work reports a first approach to the development of a process monitoring system based on audible sound sensors for a milling process. The aim is to characterize the audible sound signals emitted for different cutting conditions during machining.

The main contribution of this work is that signal analysis is carried out independently of the noise generated by the milling machine used for the cutting tests and the environment; in fact, particular attention was paid to protect the sensor from the chips and to isolate the experiments from environmental noise that could contaminate the detected signals.

The classification of audible sound signal features for process monitoring was carried out by graphical analysis and parallel distributed data processing using a supervised neural network (NN) approach.

Materials and experimental procedures

The workpiece material was a T4 - 6065 aluminium alloy in the form of 100 x 200 x 40 mm plates. The cutting tests were performed on a DORMAC FU-100 milling machine using a 5-teeth milling cutter.

Cutting tests consisted in longitudinal milling with the following cutting conditions: spindle rotation speed S = 800 rpm, feed rate f = 80 mm/min (f/NZ = 0.02 mm/tooth), depths of cut d = 0.5 mm and d = 1 mm.

The audible sound monitoring system was composed by a Larson Davis 2800 Spectrum Analyser, a standard Larson Davis preamplifier model PRM 900B, a ½" free field high sensor and a ½" pre-polarized microphone.

A sound level meter (SLM) instrument is a device designed to measure and display the broadband sound pressure level of an audible signal. The spectrum analyser utilised

can perform sound level meter functions and frequency analysis functions simultaneously, with the spectral data displayed along with the SLM measurements.

All audible sound signals detected by the Larson Davis 2800 Spectrum Analyser were transferred and off-line analysed on a PC. The experimental layout is shown in Figures IV.30 and IV.31.

Figure IV.30: Experimental layout

Figure IV.31: Microphone protected by a plastic mesh.

The distance between the ½" pre-polarized microphone and the cutting point was fixed so that, during each machining test, it was approximately equal to 85 mm.

Particular attention was paid to protect the microphone from the chips by means of a plastic mesh (Figure IV.31) and to isolate the experiments from environmental noise

that could contaminate the detected signals. For each cutting condition, three audible sound signal specimens were recorded. In this way, it was possible to verify the repeatability of the monitoring tests. In addition, the noise of the milling machine running unloaded was recorded, three times as well, in order to characterize the audible sound signals without the noise generated by both machine and environment.

The spectrum analyser was set at 800 lines acquisition mode and a Fast Fourier Transformation (FFT) zoom equal to 2, which means that the capture interval was from 0 to 10000 Hz and this frequency interval was divided into 800 lines yielding a 12.5 Hz step.

The audible sound signal (Figure IV.32) was detected in sound Level Meter mode providing for the same FFT data file as the Real-Time Normal mode plus a series of signal parameters such as [16]: SUM (LIN) SUM (A), SLOW, SLOW MIN, SOLW MAX, FAST, FAST MIN, FAST MAX, IMPULSE, LEQ, SEL, PEAK, Tmax3 and 5.

The measurements were automatically saved, using the "by time" option, with end time equal to 10 seconds and step equal to 1 second. The transfer velocity was set at 9600 Baud, which is the same as the velocity set on the PC used for file transfer.

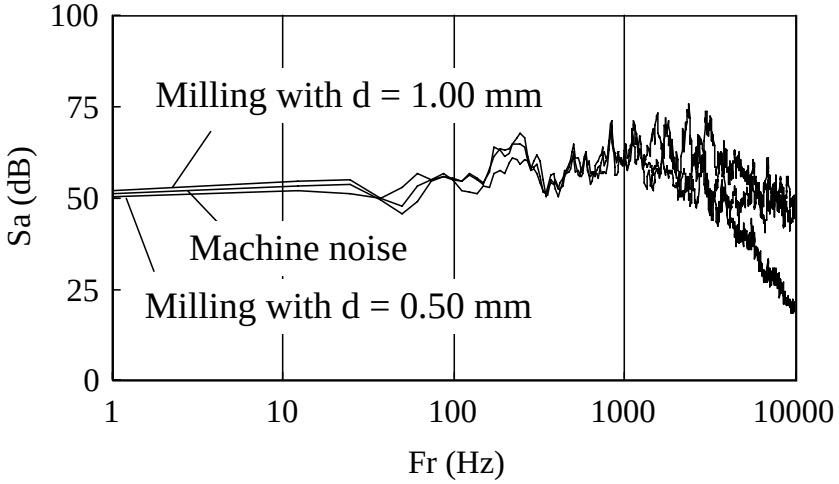

Figure IV.32: Signal amplitude, Sa, vs. frequency, Fr, of audible sound signals during the 5th second of unloaded machine running test and machining tests with d = 0.5 mm and d = 1.0 mm and the same S = 800 rpm and f = 80 mm/min conditions.

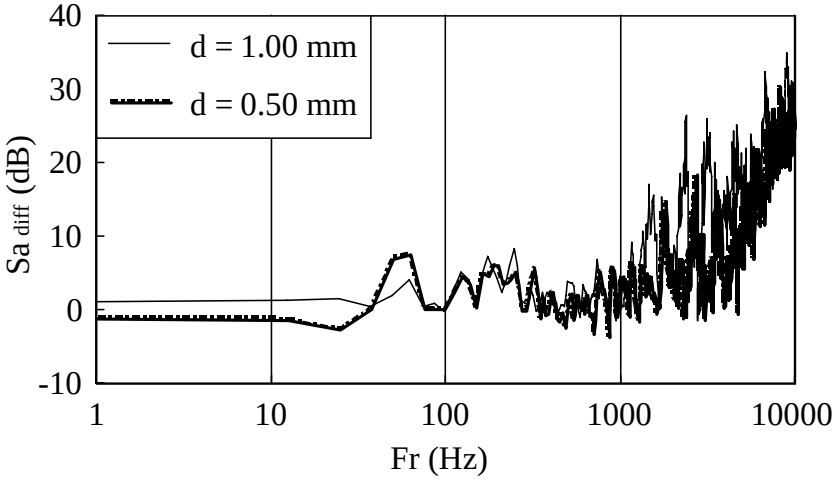

Figure IV.33: Signal amplitude, Sa diff, vs. frequency, Fr, of audible sound signals during the 5th second of machining tests with d = 0.5 mm and d = 1.0 mm and the same S = 800 rpm and f = 80 mm/min conditions.

The audible sound signal was detected in Fast level mode. This acquisition mode produces the display and the recording of the RMS Fast level, along with the minimum and maximum values of the RMS Fast level for each test duration. The averaging time of the Fast detector is 1/8 s. For graphical analysis, Spectrum Pressure Level Noise and Vibrations Works (OS Windows) software packages were used. For NN data processing, the Neural Network Explorer software package was used.

IV.3.5 Results and discussion

The audible sound signals were detected in Sound Level Meter mode. Test repeatability was verified by analysing the difference between the signals recorded under the same test conditions (three repetitions) and dividing it by 800 (lines of acquisition of the spectrum analyser). In all cases, repeatability error was less than 5%.

A reference for the machine and environment noise signal was evaluated as the average of the 3 signals obtained from each of the unloaded machine running tests. Figure IV.32 shows an example of noise reference signal; in the figure, the signal amplitude, Sa, is reported vs. frequency, Fr, for the 5th second of the unloaded machine running test with S = 800 rpm and f = 80 mm/min. In the same figure, the machining sound signals for two depths of cut values, d = 0.5 mm and d = 1 mm, are also reported for the 5th second of machining test under the same S and f conditions.

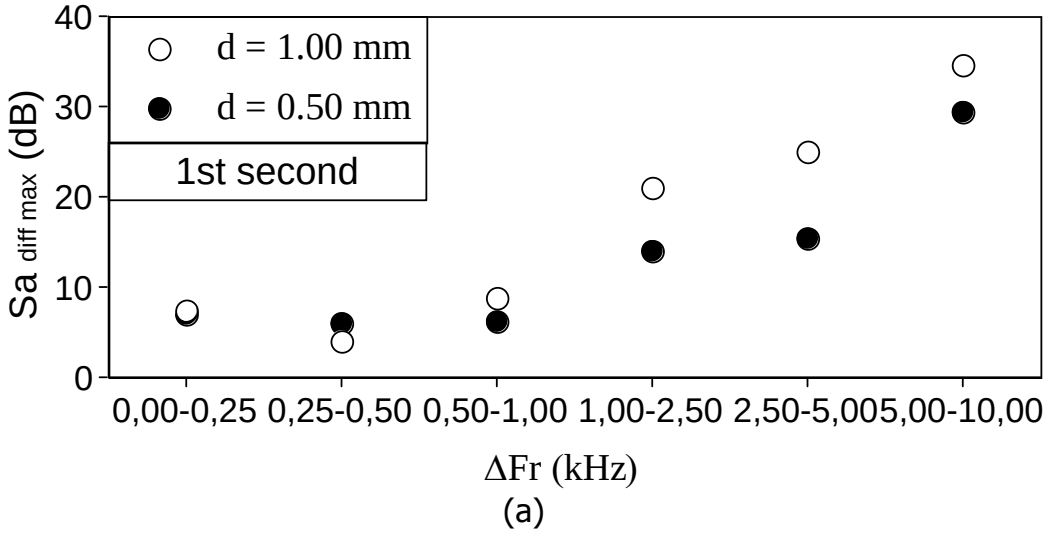

(a)

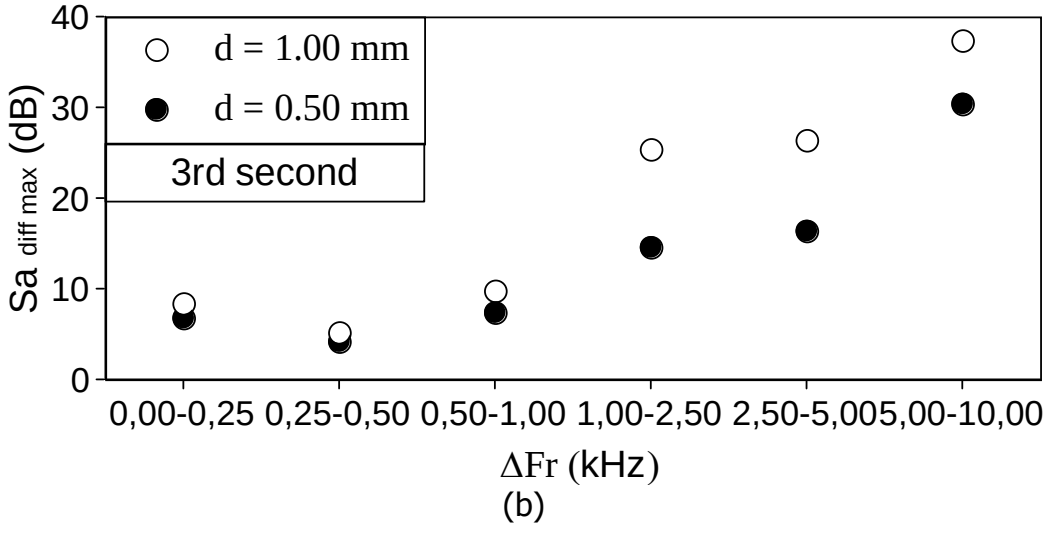

(b)

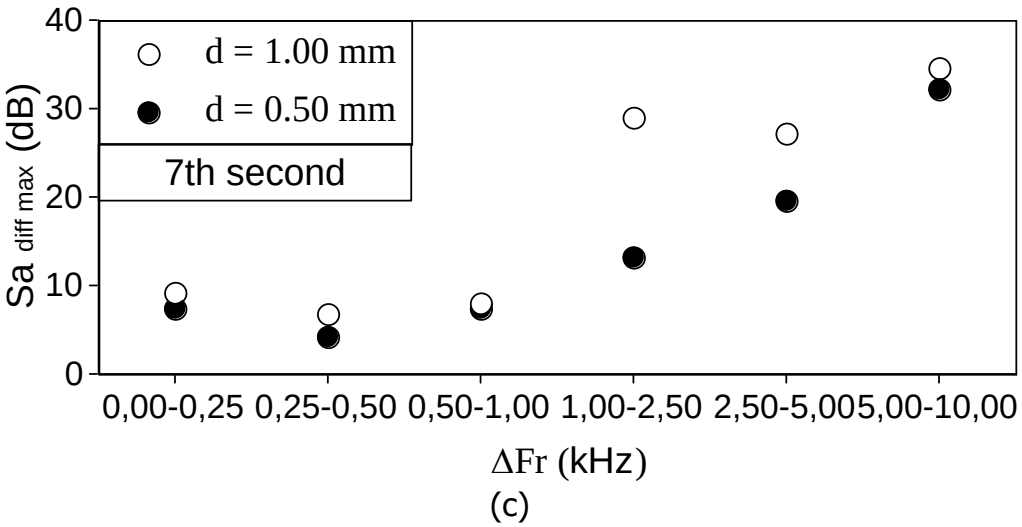

(c)

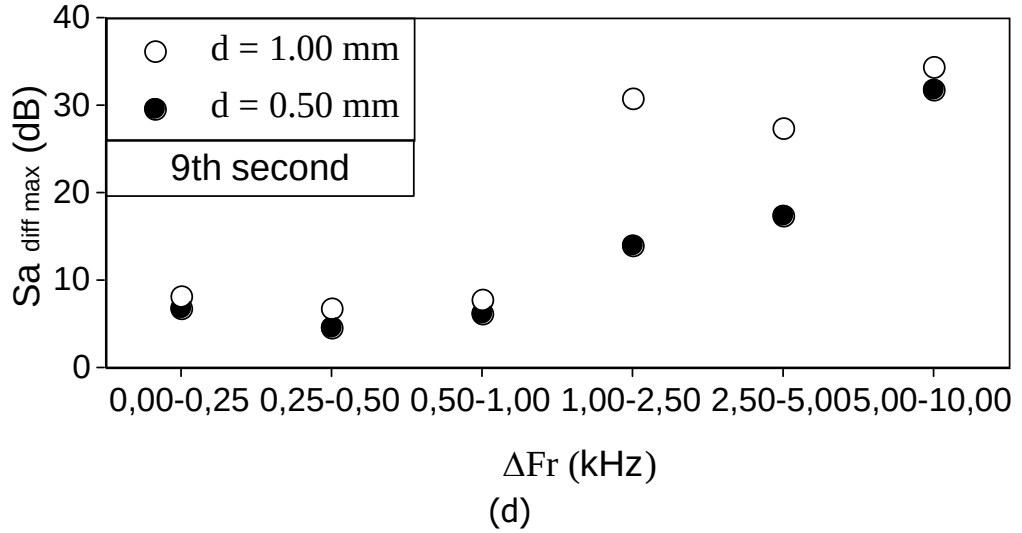

(d)

Figure IV.34: Difference signal maximum amplitude, Sa diff max, vs. frequency intervals, ΔFr, for the: (a) 1st second, (b) 3rd second, (c) 7th second and (d) 9th second

The noise reference signals were subtracted from audible sound signals detected during machining tests to obtain difference signals for classification analysis. All calculations were carried out on difference signals (Figure IV.33).

FFT signal processing

The maximum amplitude of the difference signal was evaluated for each frequency interval and each second of cutting test. The six frequency intervals selected for audible sound signal processing are: 0-0.25, 0.25-0.5, 0.5-1, 1-2.5, 2.5-5, 5-10 kHz. Figure IV.34 reports four examples of the difference signal maximum amplitude, Sa diff max, versus frequency intervals, ΔFr, during the 1st, 3rd, 7th and 9th second of each test. The figure shows that it is possible to discriminate audible sound signals obtained from machining with different depths of cut values using frequency intervals higher than 1 kHz.

Graphical representation of data in a 6 dimensions feature space is not feasible. Thus, the results are presented in a 2 dimensions feature space by pair-wise plotting of frequency interval maximum signal amplitude, as shown in Figure IV.35 for (a) two low frequency intervals, (b) two medium frequency intervals, and (c) two high frequency intervals. From the figure, it can be seen that, for the high frequency intervals, the

separation between cluster points characteristic of the two depths of cut values is excellent.

The same can be seen if the difference signal maximum amplitude is plotted versus depth of cut, as in Figure IV.36 where the difference signal maximum amplitudes for low, medium and high frequency intervals are reported. At low frequencies (0-0.25 kHz), the Sa diff max value is ≈ 10 dB for both values of depth of cut. In this case, it is impossible to discriminate the depth of cut value. However, at high frequencies (2.50-5.00 kHz), the Sa diff max value is ≈ 10 dB for d = 0.50 mm and ≈ 30 dB for d = 1.00 mm; in this case, depth of cut discrimination is feasible.

Neural network data processing

A supervised NN data processing was utilized for pattern recognition using the 6-component feature vectors containing the difference signal maximum amplitudes for the 6 frequency intervals. A three-layer feed-forward back-propagation NN was built with configuration: input layer = 6 nodes, hidden layer = 3 nodes determined by "cascade learning procedure", output layer = 1 node.

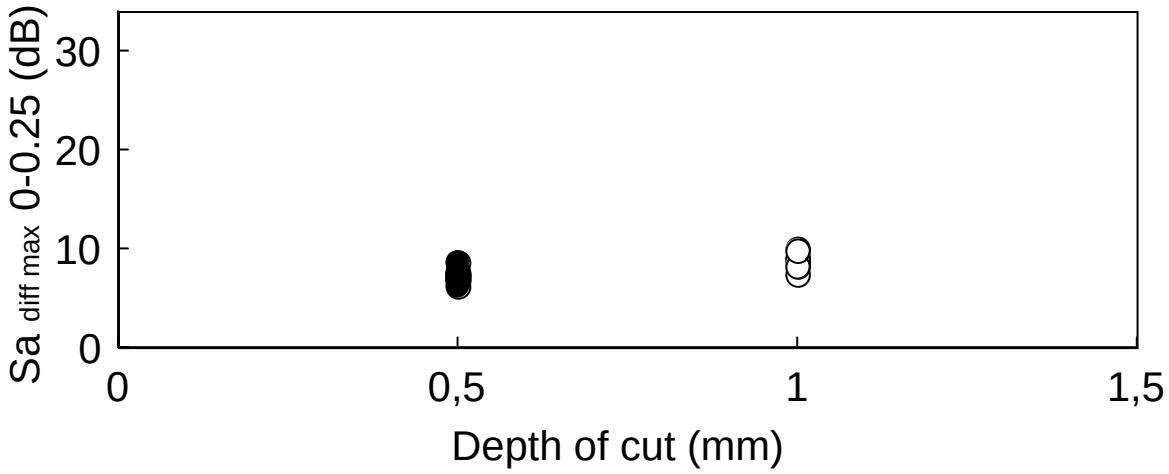

(a)

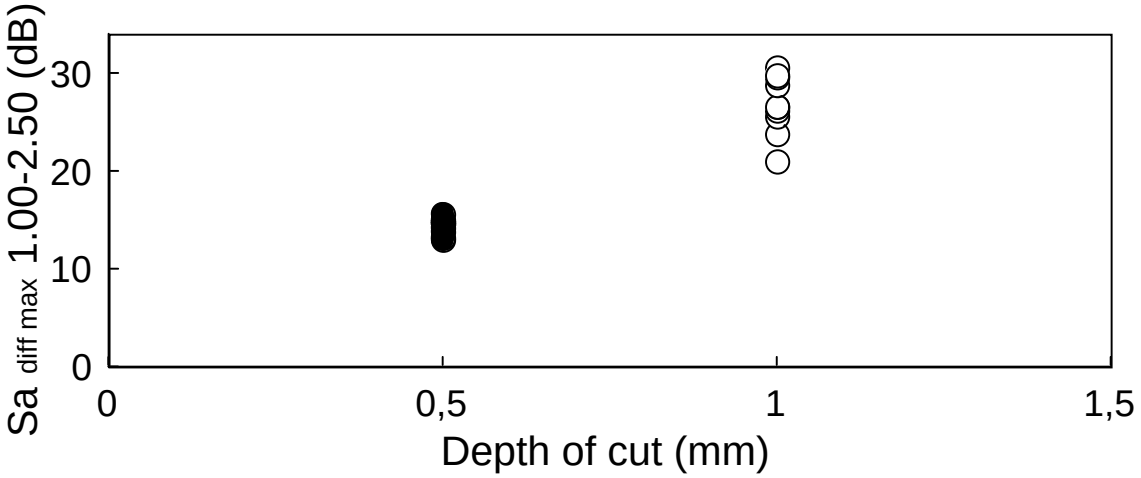

(b)

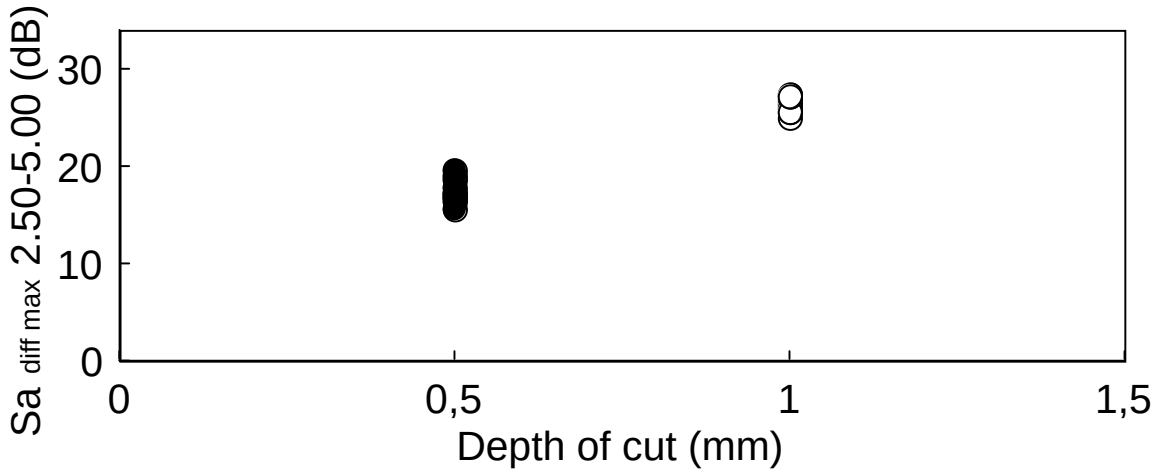

(c)

Figure IV.36: Difference signal maximum amplitude vs. depth of cut: (a) low frequency intervals, (b) medium frequency intervals, (c) high frequency intervals.

The 6-3-1 NN was trained and tested according to the leave-k-out procedure with k = 2, using a number of learning steps comprised between 1000 and 14000. In Figure IV.37, the NN output is reported versus the number of input patterns for 12000 and 14000 number of learning steps. From this figure, it can be seen that the NN success rate (SR) in the identification of depth of cut is 100% in both cases, though it improves with increasing number of learning steps. Figure IV.38 reports the NN SR vs. number of learning steps for different threshold values. From the figure, it can be seen that the NN SR is approximately 85% starting from 2000 learning steps. Figure IV.300 reports the NN SR as a function of threshold value for variable numbers of learning steps. From the figure, it can be seen that the NN SR start decreasing gradually only below threshold values 0.3, except in the case of the lowest number of learning steps (i.e. 1000) for which a rapid SR reduction is expectedly verified.

IV.3.6 Conclusions

Audible sound energy generated during milling of T4-6056 Al alloy plates was detected and analysed in the frequency domain by a real-time spectrum analyser. Signal analysis was carried out by suppressing the noise generated by the machine and the environment from the signal emitted during machining for different depths of cut values. Classification of audible sound signal features was performed in two-dimensions by graphical analysis and in a multi-dimensional space by parallel distributed data processing using a supervised NN approach to identify the process conditions on a sensor monitoring basis. Graphical examinations showed that the discrimination of the depth of cut is possible only with reference to high frequency ranges. On the other hand, the supervised NN data processing proved that the classification of depth of cut can be reliably achieved independently of frequency.

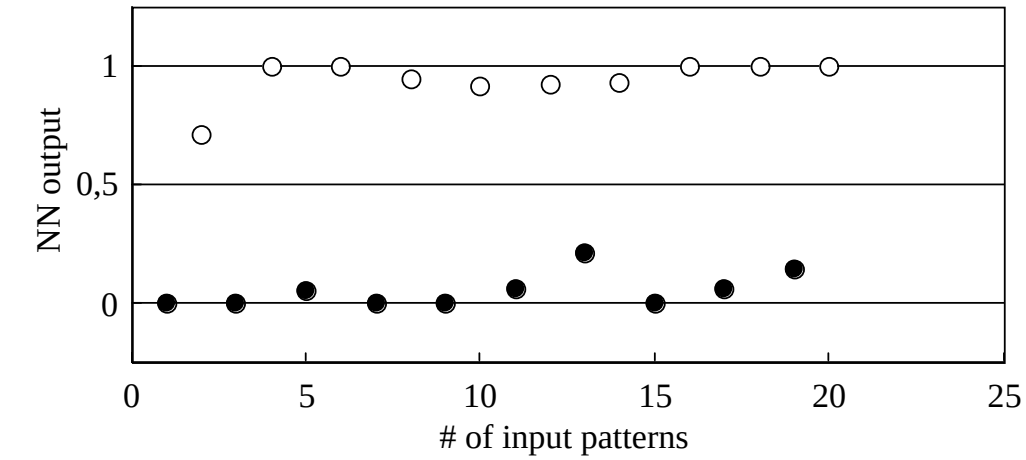

(a)

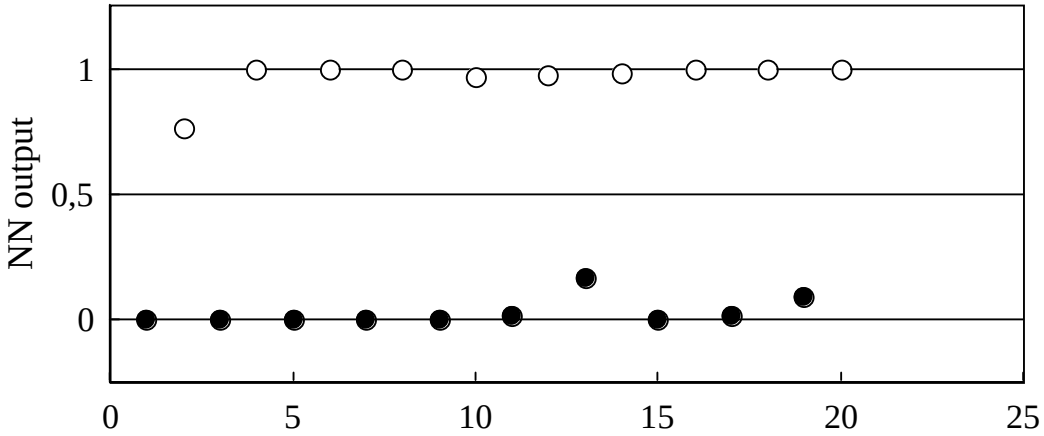

(b)

Figure IV.37: Actual NN output vs. # of input patterns for:
(a) 12000 and (b) 14000 learning steps.
● Actual output 0.50 mm o Actual output 1.00 mm

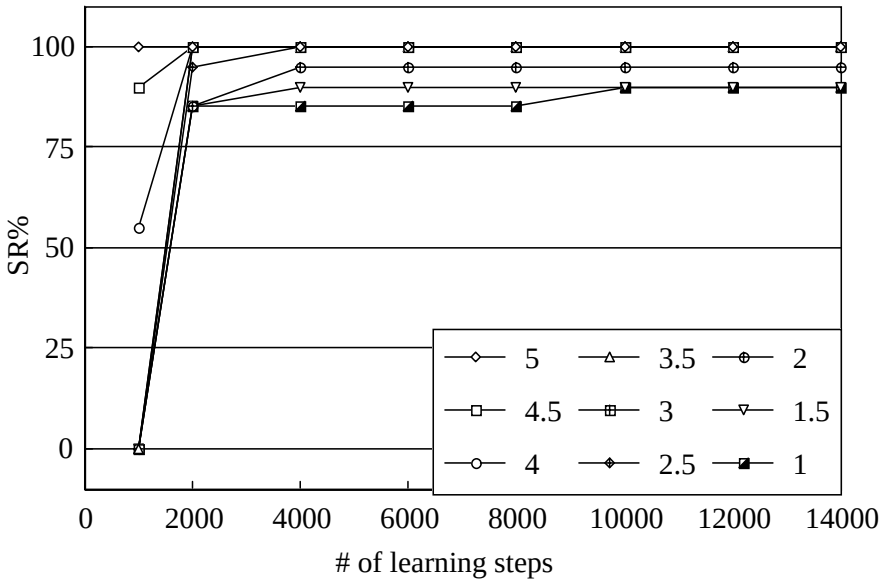

Figure IV.38: NN success rate vs. number of learning steps for different threshold values.

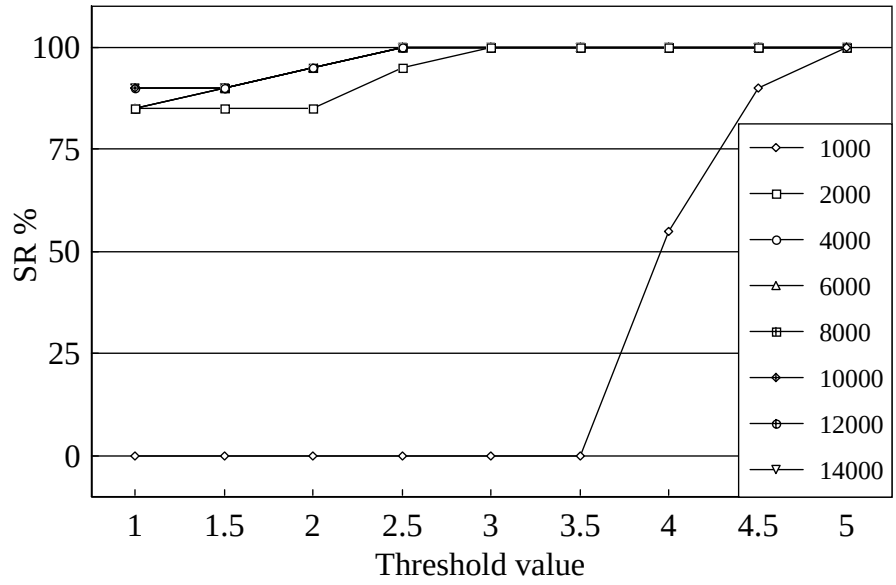

Figure IV.39: NN success rate vs. threshold value for different numbers of learning steps.

Bibliography

Chapter I.1

[1] ASM International Metals Handbook Ninth Edition, Nondestructive Evaluation and Quality Control, Volume 17.
[2] ASNT Nondestructive Testing Handbook, Second Edition, Special Nondestructive Testing Methods, Volume 9.
[3] ASNT Nondestructive Testing Handbook, Second Edition, Electromagnetic Testing, Volume 4.

Chapter I.2

[4] ASTM E 165 Standard Practice for Liquid-Penetrant Inspection Method.
[5] ASTM E 270 Standard Definitions of Terms Relating to Liquid-Penetrant Inspection.
[6] ASTM E 1208 Standard Method for Fluorescent Liquid-Penetrant Examination Using the Lipophilic Post-Emulsification Process.
[7] ASTM E 1209 Standard Method for Fluorescent-Penetrant Examination Using the Water-Washable Process.
[8] ASTM E 1210 Standard Method for Fluorescent-Penetrant Examination Using the Hydrophilic Post-Emulsification Process.
[9] ASTM E 1219 Standard Method for Fluorescent-Penetrant Examination Using the Solvent-Removable Process.
[10] ASTM E 1220 Standard Method for Visible-Penetrant Examination Using the Solvent-Removable Process.
[11] ASTM E 1135 Standard Test Method for Comparing the Brightness of Fluorescent Penetrants.
[12] ASTM D 2512 Compatibility of Materials with Liquid Oxygen (Impact-Sensitivity Threshold Technique).
[13] AMS 2647 Fluorescent Penetrant Inspection--Aircraft and Engine Component Maintenance.
[14] ASME SEC V ASME Boiler and Pressure Vessel Code Section V, Article 6.
[15] MIL-STD-6866 Military Standard Inspection, Liquid Penetrant.
[16] MIL-STD-410 Nondestructive Testing Personnel Qualifications & Certifications.
[17] MIL-I-25135 Inspection Materials, Penetrant.
[18] MIL-I-25105 Inspection Unit, Fluorescent Penetrant, Type MA-2.
[19] MIL-I-25106 Inspection Unit, Fluorescent Penetrant, Type MA-3.
[20] MIL-STD-271 (Ships) Nondestructive Testing Requirements for Metals.

Chapter I.3

[21] Radiography & Radiation Testing, 1985, Nondestructive Testing Handbook, American Society for Nondestructive Testing, 3/2.
[22] Halmshaw, R., 1987, Nondestructive Testing, Edward Arnold Publishers.
[23] Link, R., Nuding, W., Sauerwein, K., 1984, Br. J. Nondestructive Testing, 26: 291-295.
[24] Brixner, L.H., 1987, Mater. Chem. Phys., 16: 253-281.
[25] Daum, W., Rose, P., Heidt, H., Builtjes, J.H., 1987, Br. J. Nondestructive Testing, 29: 79-82.
[26] Nondestructive Testing Personnel Qualification and Certification, Supplement A, Radiographic Testing Method, ASNT-TC-1A, American Society for Nondestructive Testing.
[27] Radons, J., 1917, Uber die bestimmung von funktionen durch ihre Integralwerte langs gewisser Mannigfaltigkeiten. Saechsische Akademie der Wissenschaften, Leipzig, Berichte uber di Verhandlungen, 69: 262-277.
[28] Bracewell, R.N., 1956, Strip Integration in Radio Astronomy, Aust. J. Phys., 9: 198-217.
[29] Cormack, A.M., 1963, Representation of a Function by Its Line Integrals, With Some Radiological Applications, J. Appl. Phys., 34: 2722-2727.
[30] Kuhl, D.E., Edwards, R.Q., 1963, Image Separation Radioisotope Scanning, Radiology, 80: 653-662.
[31] DeRosier, D.J., Klug, A., 1968, Reconstruction of Three-Dimensional Structures from Electron Micrographs, Nature, 217: 130-134.
[32] Hounsfield, G., 1973, Computerized Transverse Axial Scanning Tomography: 1. Description of System, Br. J. Radiol., 46: 1016.
[33] Johns, C., Gillmore, J., 1989, CAT Scans for Industry, Quality,:26-28.
[34] Ter-Pergossian, M., Phelps, M.M., Brownell, G.L., 1977, Reconstruction Tomography in Diagnostic Radiology and Nuclear Medicine, University Park Press.
[35] Vinegar, H.J., 1986, X-Ray CT and NMR Imaging of Rocks, J. Petro. Tech., March: 257-259.
[36] Rothwell, W.P., 1985, Vinegar, H.J., Petrophysical Application of NMR Imaging, Appl. Opt., 24/3, Dec.
[37] Shuck, R., Jones, S., 1989, Magnetic Resonance Imaging From Medicine to Industry, Adv. Imag., 4/2: 20.
[38] Ellingson, W.A., Ackerman, J.L., Sawicka, B.D., Groenemeyer, S., Kriz, R.J., 1987, Applications of Nuclear Magnetic Resonance Imaging and X-Ray Computed Tomography for Advanced Ceramics Materials, in Proceedings of the Advanced Ceramic Materials and Components Conference (Pittsburgh, PA), April.
[39] Lale, P.G., 1959, The Examination of Internal Tissues, Using Gamma Ray Scatter With a Possible Extension to Megavoltage Radiography, Phys. Med. Biol., 4.
[40] Strecker, H., 1982, Scatter Imaging of Aluminum Castings Using an X-Ray Beam and a Pinhole Camera, Mater. Eval., 40/10: 1050-1056.
[41] Bossi, R.H., Friddell, K.D., Nelson, J.M., 1988, Backscatter X-Ray Imaging, Mater. Eval., 46: 1462-1467.
[42] Wang, S.Y., Agral, S., Gryte, C.C., 1984, Computer-Assisted Tomography for the Observation of Oil Displacement in Porous Media, J. Soc. Pet. Eng., 24: 53.

[43] Wang, S.Y. and all, 1984, Reconstruction of Oil Saturation Distribution Histories During Immiscible Liquid-Liquid Displacement by Computer Assisted Tomography, AIChE J., 30/4: 642-646.
[44] Wellington, S.L., Vinegar, H.J., 1985, CT Studies of Surfactant-Induced CO2 Mobility Control, Paper 14393, presented at the 1985 Annual Technical Conference and Exhibition, Las Vegas, Society of Petroleum Engineers, Sept.
[45] Vinegar, H.J., Wellington, S.L., 1987, Tomographic Imaging of Three-Phase Flow Experiments, Rev. Sci. Instrum., 58/1: 96-107.
[46] Wellington, S.L., Vinegar, H.J., 1987, X-Ray Computerized Tomography, J. Petro. Tech., 39/8: 885-898.
[47] Withjack, E.M., 1987, Computed Tomography for Rock-Property Determination and Fluid-Flow Visualization, Paper 16951, presented at the 1987 SPE Annual Technical Conference and Exhibition, Dallas, Society ofPetroleum Engineers, Sept.
[48] Withjack, E.M., 1988, Computed Tomography Studies of 3-D Miscible Displacement Behavior in a Laboratory Five-Spot Model, Paper 18096, presented at the 1988 SPE Annual Technical Conference and Exhibition, Houston, Society of Petroleum Engineers.
[49] Maylotte, D.H., Kosky, P.G., Spiro, C.L., Lamby, E.J., 1983, Computed Tomography of Coals, U.S. DOE Contract DE-AC21-82MC19210.
[50] Lowrey, A.R., Friddell, K.D., Cruikshank, D.W., 1985, Nondestructive Evaluation of Aerospace Composites Using Medical Computed Tomography (CT) Scanners, Paper presented at the ASNT Spring Conference, Washington, D.C., American Society for Nondestructive Testing, March.
[51] Buckley, R.G., Michaels, K.J., 1985, Computed Tomography: A Powerful Tool in Solid Motor Exit Cone Evaluation, Paper presented at the ASNT Spring Conference, Washington, D.C., American Society for Nondestructive Testing, March.
[52] Elson, B.J., 1984, Computerized X-Ray to Verify MX Motors, Aviat. Week Space Technol., 149, 16 April.
[53] Armistead, R.A., 1988, CT: Quantitative 3D Inspection, Adv. Mater. Process., March: 42-48.
[54] Tonner, P.D., Tosello, G., 1986, Computed Tomography Scanning for Location and Sizing of Cavities in Valve Castings, Mater. Eval., 44: 203
[55] Sawicka, B.D., Tapping, R.L., 1987, CAT Sc|anning of Hydrogen Induced Cracks in Steel, Nucl. Instr., Methods.
[56] Taylor, T., Ellingson, W.A., Koenigsberg, W.D., 1986, Evaluation of Engineering Ceramics by Gamma-Ray Computed Tomography, Ceram. Eng. Sci. Proc., 7: 772-783.
[57] Blumenfeld, S.M., Glover, G., 1981, Spatial Resolution in Computed Tomography, in Radiology of the Skull and Brain, Technical Aspects of Computed Tomography, C.V. Mosby Company, 5.
[58] Yester, M.W., Barnes, G.T., 1977, Geometrical Limitations of Computed Tomography (CT) Scanner Resolution, Appl. Opt. Instr. Med. VI, Proc. SPIE, 127: 296-303.
[59] Joseph, P.M., 1978, Image Noise and Smoothing in Computed Tomography (CT) Scanners, Opt. Eng., 17: 396-399.
[60] Barrett, H.H., Swindell, W., 1981, Radiological Imaging: The Theory of Image Formation, Detection, and Processing, Academic Press.
[61] Cohen, G., DiBianca, F.A., 1979, The Use of Contrast-Detail-Dose Evaluation of Image Quality in Computed Tomography Scanners, J. Comput. Asst. Tomogr: 189.

[62] American Society for Testing and Materials, 1989, Standard Guide for Computed Tomography (CT) Imaging.
[63] Hanson, K.M., 1977, Detectability in the Presence of Computed Tomography Reconstruction Noise, Appl. Opt. Instr. Med. VI, Proc. SPIE, 127: 304.
[64] Chew, E., Weiss, G.H., Brooks, R.H., DiChiro, G., 1978, Effect of CT Noise on the Detectability of Test Objects, Am. J. Roentgenol., 131: 681.
[65] Joseph, P.M., 1978, Artifacts in Computed Tomography, Phys. Med. Biol., 23: 1176-1182.
[66] Brooks, R.H., and all, 1979, Aliasing: A Source of Streaks in Computed Tomograms, J. Comput. Asst. Tomgr., 3/4: 511-518.
[67] Chesler, D.A., and all, 1977, Noise Due to Photon Counting Statistics in Computed X-Ray Tomography, J. Comput. Asst. Tomgr., 1/1: 64-74.
[68] Hanson, K.M., 1979, Detectability in Computed Tomographic Images, Med. Phys., 6/5.
[69] McDavid, W.D., Waggener, R.G., Payne, W.H., Dennis, M.J., 1975, Spectral Effects on Three-Dimensional Reconstruction from X-Rays, Med. Phys., 2/6: 321-324.
[70] Joseph, P.M., Spital, R.D., 1978, A Method for Correcting Bone Induced Artifacts in Computed Tomography Scanners, J. Comput. Asst. Tomogr., 2/3: 100-108.
[71] Cline, H.E., Lorensen, W.E., Ludke, S., Crawford, C.R., Teeter, B.C., 1988, Two Algorithms for the Three-Dimensional Reconstruction of Tomograms, Med. Phys., 15/3: 320-327.
[72] Alvarez, R. E., Macovski, A., 1976, Energy Selective Reconstructions in X-Ray Computerized Tomography, Phys. Med. Biol., 21: 733-744.
[73] Tam, K.C., 1988, Limited-Angle Image Reconstruction in Non-Destructive Evaluation, in Signal Processing and Pattern Recognition in Nondestructive Evaluation of Materials, NATO ASI Series Vol F 44, Springer-Verlag.
[74] Brooks, R., DiChiro, G., 1976, Principles of Computer Assisted Tomography (CAT) in Radiographic and Radioisotopic Imaging, Phys. Med. Biol., 21: 689-732.
[75] Herman, G.T., 1979, Image Reconstruction from Projections: Implementation and Applications, Springer-Verlag.
[76] Herman, G.T., 1980, Image Reconstruction from Projections: The Fundamentals of Computerized Tomography, Academic Press.
[77] Flannery, B.P., Deckman, H.W., Roberge, W.G., D'Amico, K.L., 1987, Three-Dimensional X-Ray Microtomography, Science, 237, 18 Sept: 1439-1444.
[78] Ramachandran, G.N., Laksh-minarayanan, A.V., 1971, Three-Dimensional Reconstruction from Radiographs and Electron Micrographs: III. Description and Application of the Convolution Method, Indian J. Pure Appl. Phys., 9: 997.
[79] Shepp, L.A., Logan, B.F., 1974, The Fourier Reconstruction of a Head Section, Trans. IEEE, NS-21: 21-43.
[80] Gordon, R., Bender, R., Herman, G.T., 1970, Algebraic Reconstruction Techniques (ART) for Three-Dimensional Electron Microscopy and X-Ray Photography, 29: 471-481.
[81] Gilbert, P., 1972, Iterative Methods for the Three-Dimensional Reconstruction of an Object from Projections, J. Theor. Biol., 36: 105-117.
[82] Herman, G.T., Lent, A., 1976, Iterative Reconstruction Algorithms, Comput. Biol. Med., 6: 273-294.
[83] Berger, H., 1976, Practical Applications of Neutron Radiography and Gaging, STP 586, American Society for Testing and Materials.
[84] Neutron Radiography Issue, At. Energy Rev. 1977, 15/2: 123-364.

[85] Tyufyakov, N.D., Shtan, A.S., 1979, Principles of Neutron Radiography, Amerind Publishing, (translated from the Russian).
[86] Von der Hardt, P., Rottger, H., 1981, Neutron Radiography Handbook, D. Reidel Publishing.
[87] Barton, J.P., Von der Hardt, P., 1983, Neutron Radiography, D. Reidel Publishing.
[88] Bryant, L.E., McIntire, P., 1985, Radiography and Radiation Testing, in Nondestructive Testing Handbook, ASTM, 3.
[89] Barton, J.P., Farny, G., Person, J.L., Rottger, H., 1987, Neutron Radiography, ASTM, Standard Practices for Thermal Neutron Radiography of Materials, E 748, D. Reidel Publishing.
[90] Berger, H., 1988, Some Recent Developments in X-Ray and Neutron Imaging Methods, Nondestructive Testing, Pergamon Press, 1: 155-162.
[91] Ridal, A., Ryan, N.E., 1987, Neutron Radiography, Proceedings of the Second World Conference (Paris, June 1986): 463-470.

Chapter I.4

[92] Krautkramer, A.J., Krautkramer, H., 1969, Ultrasonic Testing of Materials, 1st ed, Springer-Verlag.
[93] Ensminger, D., 1973, Ultrasonics, Marcel Dekker.
[94] Bar-Cohen, Y., 1986, NDE of Fiber Reinforced Composites-A Review, Mater. Eval., 44/4: 446-454
[95] Bar-Cohen, Y., 1987, Nondestructive Characterization of Defects Using Ultrasonic Backscattering, in Ultrasonic International 87, Conference Proceedings, Butterworth: 345-352
[96] Halmshaw, R., 1987, Nondestructive Testing, Edward Arnold: 143, 198, 211.
[97] Bar-Cohen, Y., Mal, A.K., 1989, Leaky Lamb Waves Phenomena in Composites Using Pulses, in Review of Progress in Quantitative NDE, Plenum Press, 8.
[98] Mal, A.K., Bar-Cohen, Y., 1988, Ultrasonic Characterization of Composite Laminates, in Wave Propagation in Structural Composites, Proceedings of the Joint ASME and SES meeting, , American Society of Mechanical Engineers, AMD-90: 1-16.
[99] Grills, R.H., Tsao, M.C., 1987, Nondestructive Testing With Portable Ultrasonic Imaging System, in Corrosion Monitoring in Industrial Plants Using Nondestructive Testing and Electromechanical Methods, STP 908, American Society for Testing and Materials: 89-101.
[100] Lloyd, E.A., 1974, Non-Destructive Testing of Bonded Joints--A Case for Testing Laminated Structures byWide-Band Ultrasound, Non-Destr. Test., Dec.: 331-334.
[101] Highmore, P.J., 1974, Non-Destructive Testing of Bonded Joints--The Depth Location of Non-Bonds in Multi-Layered Media, Non-Destr. Test., Dec.: 327-330.
[102] Garland, W.E., Ritter, P.O., Fee, J.K., 1969, Applications of Ultrasonic Inspection to Composite Materials, in Proceedings of the 7th Symposium on Nondestructive Evaluation of Components and Materials in Aerospace and Nuclear Applications, Western Periodicals Company: 226-238.
[103] Bar-Cohen, Y., Mal, A. K., Ultrasonic NDE of Adhesive Bonding, in Ultrasonic Testing, ASNT Handbook, American Society for Nondestructive Testing, to be published, 8.
[104] Lautzenheiser, C.E., Pickett, A.G., Whiting, A.R., Wilson, A.W., 1965, Ultrasonic Studies of Fatigue Crack Initiation and Propagation, Paper presented at the Spring Convention, Los Angeles, American Society for Nondestructive Testing, Feb.

[105] Lautzenheiser, C.E., Whiting, A.R., Wylie, R.E., 1966, Crack Evaluation and Growth during Low-Cycle Plastic Fatigue-Nondestructive Techniques for Detection, Mater. Eval., May: 241-248.
[106] Cook, J.F., Aldrich, D.A., Anderson, B.C., Scown, V.S., 1984, Development of an Automated Ultrasonic Inspection System for Verifying Waste Container Integrity, Mater. Eval., Dec.
[107] Pao, Y.H., Sachse, W., Fukuoka, H., 1984, Acoustoelasticity and Ultrasonic Measurement of Residual Stresses, in Physical Acoustics: Principles and Methods, Academic Press, 17: 61-143.
[108] Clark, A.V., Moulder, J.C., Mignogna, R.B., DelSanto, P.P., 1987, Comparison of Several Ultrasonic Techniques for Absolute Stress Determination in the Presence of Texture, National Bureau of Standards.

Chapter I.5

[109] Cielo, P., 1988, Optical Techniques for Industrial Inspection, Academic Press: 243.
[110] Hildebrand, B.P., Brenden, B.B., 1972, An Introduction to Acoustical Holography, Plenum Press.
[111] Hildebrand, B.P., Davis, T.J., Boland, A.J., Silta, R.L., 1984, A Portable Digital Ultrasonic Holography System for Imaging Flaws in Heavy Section Materials, IEEE Trans., SV-31/4: 287-294.
[112] Hildebrand, B.P., Collins, H.D., 1972, Evaluation of Acoustical Holography for the Inspection of Pressare Vessel Sections, Mater. Res. Stand., 12/12, Dec: 23-32.
[113] MacDonald, D.E., Kietzman, E.K., 1987, Comparative Evaluation of Acoustic Holography Systems, Report NP-5130, Electric Power Research Institute.
[114] Tolansky, S., 1948, Multiple-Beam Interferometry of Surfaces and Films, Clarendon Press.

Chapter I.6

[115] Burrows, M.L., 1964, A Theory of Eddy Current Flaw Detection, University Microfilms, Inc.
[116] Dodd, C.V., Deeds, W.E., Spoeri, W.G., 1971, Optimizing Defect Detection in Eddy Current Testing, Mater. Eval., March: 59-63.
[117] Dodd, C.V., Deeds, W.E., 1968, Analytical Solutions to Eddy-Current Probe-Coil Problems, J. Appl. Phys., 39/6, May: 2829-2838.
[118] Halmshaw, R., 1987, Nondestructive Testing, Edward Arnold.
[119] Brown, R.L., 1967, The Eddy Current Slide Rule, in Proceedings of the 27th National Conference, American Society for Nondestructive Testing, Oct.
[120] Libby, H.L., 1971, Introduction to Electromagnetic Nondestructive Test Methods, John Wiley & Sons.
[121] Franklin, E.M., 1982, Eddy-Current Inspection-Frequency Selection, Mater. Eval., 40/Sept: 1008.
[122] Wilcox, L.C., Jr., 1966, Prerequisites for Qualitative Eddy Current Testing, in Proceedings of the 26th National Conference, American Society for Nondestructive Testing, Nov.
[123] Foerster, F., 1959, Principles of Eddy Current Testing, Met. Prog., Jan: 101.

[124] Franklin, E.M., 1986, Eddy-Current Examination of Breeder Reactor Fuel Elements, in Electromagnetic Testing, Vol 4, Nondestructive Testing Handbook, American Society for Nondestructive Testing: 444.
[125] Ghent, H.W., 1981, A Novel Eddy Current Surface Probe, AECL-7518, Atomic Energy of Canada Limited, Oct.
[126] Nondestructive Testing: A Survey, 1973, NASA SP-5113, National Aeronautics and Space Administration.
[127] Hagemaier, D., Bates, B., Steinberg. A., 1986, On-Aircraft Eddy Current Inspection, Paper 7680, McDonnell Douglas Corporation, March.
[128] Schmidt, T.R., 1984, The Remote-Field Eddy Current Inspection Technique, Mater. Eval., 42/Feb.
[129] Fisher, J.L., Cain, S.T., Beissner, R.E., 1987, Remote Field Eddy Current Model, in Proceedings of the 16th Symposium on Nondestructive Evaluation (San Antonio, TX), Nondestructive Testing Information Analysis Center.
[130] Lord, W., Sun, Y.S., Udpa, S.S., 1987, Physics of the Remote Field Eddy Current Effect, in Reviews of Progress in Quantitative NDE, Plenum Press.
[131] Atherton, D.L. Sullivan, S., 1986, The Remote-Field Through-Wall Electromagnetic Technique for Pressure Tubes, Mater. Eval., 44/Dec.
[132] Palanissimy, S., 1987, in Reviews of Progress in Quantitative NDE, Plenum Press.
[133] Kilgore, R.J., Ramchandran, S., 1989,NDT Solution: Remote-Field Eddy Current Testing of Small Diameter Carbon Steel Tubes, Mater. Eval., 47/Jan: 219-228.
[134] Cheu, Y.F., 1984, Automatic Crack Detection With Computer Vision and Pattern Recognition of Magnetic Particle Indications, Mater. Eval., Nov.

Chapter I.7

[135] Miller, R.K., McIntire, P., 1987, Nondestructive Testing Handbook, Acoustic Emission Testing, American Society for Nondestructive Testing, 5/2: 275-310.
[136] Drouillard, T.F., Glenn, T.G., 1985, Production Acoustic Emission Testing of Braze Joint, J. Acoust. Emiss., 1/2: 81-85.
[137] Vahaviolos, S.J., 1974, Real Time Detection of Microcracks in Brittle Materials Using Stress Wave Emission (SWE), IEEE Trans., Vol PHP-10/3, Sept: 152-159.
[138] Pärtzel, K.H., 1988, Acoustic Emission for Crack Inspection During Fully Automatic and Manual Straightening of Transmission Shafts, in Proceedings of the Acoustic Emission Symposium, Deutsche Gesellschaft für Metallkunde: 157-164.
[139] Miller, R.K., McIntire, P., 1987, Acoustic Emission Testing, Nondestructive Testing Handbook, American Society for Nondestructive Testing, 5/2: 167-186, 187-193.
[140] Parry, D.L., 1975, Industrial Application of Acoustic Emission Analysis Technology, in Monitoring Structural Integrity by Acoustic Emission, STP 571, American Society for Testing and Materials: 150-183.
[141] Miller, R.K., McIntire, P., 1987, Acoustic Emission Testing, Nondestructive Testing Handbook, American Society for Nondestructive Testing, 5/2: 421-424, 434-443, 226-259, 333-339, 267-271
[142] Fowler, T.J., 1988, Recent Developments in Acoustic Emission Testing of Chemical Process Equipment, in Progress in Acoustic Emission IV, Proceedings of the Ninth International Acoustic Emission Symposium, The Japanese Society for Non-Destructive Inspection: 391-404.

[143] Cole, P.C., 1988, Acoustic Emission, in The Capabilities and Limitations of NDT, Part 7, The British Institute of Non-Destructive Testing.
[144] Miller, R.K., McIntire, P., 1987, Acoustic Emission Testing, Nondestructive Testing Handbook, American Society for Nondestructive Testing, 5/2: 278, 472-484, 213-219.
[145] McBride, S.L., 1989, Acoustic Emission Measurements on Rubbing Surfaces, in Proceedings of the World Meeting on Acoustic Emission (Charlotte, NC), Acoustic Emission Group, March.
[146] Miller, R.K., McIntire, P., 1987, Acoustic Emission Testing, Nondestructive Testing Handbook, American Society for Nondestructive Testing, 5/2: 402-408, 194-202.
[147] Pollock, A.A., Hsu, S.-Y.S., 1982, Leak Detection Using Acoustic Emission, J. Acoust. Emiss., 1/4: 237-243.
[148] Miller, R.K., McIntire, P., 1987, Acoustic Emission Testing, Nondestructive Testing Handbook, American Society for Nondestructive Testing, 5/2:58-61, 84-88.
[149] Scruby, C.B., 1985, Quantitative Acoustic Emission Techniques, in Research Techniques in Nondestructive Testing, Academic Press, 8: 141-210.
[150] Miller, R.K., McIntire, P., 1987, Acoustic Emission Testing, Nondestructive Testing Handbook, American Society for Nondestructive Testing, 5/2: 64-90.
[151] Pao, Y.H., 1978, Theory of Acoustic Emission, in Elastic Waves and Non-Destructive Testing of Materials, American Society of Mechanical Engineers, AMD-20: 107-128.
[152] Enoki, M., Kishi, T., Kohara, S., 1983, Determination of Microcracking Moment Tensor of Quasi-Cleavage Facet by AE Source Characterization, in Progress in Acoustic Emission III, Proceedings of the Eighth International Acoustic Emission Symposium, The Japanese Society for Non-Destructive Inspection: 763-770.
[153] Yuyama, S., Imanaka, T., Ohtsu, M., Quantitative Evaluation of Microfracture Due to Disbonding by Waveform Analysis of Acoustic Emission, J.Acoust. Soc. Am., 1988, 83/3: 976-983; 1987, 82/2: 506-512.
[154] Pollock, A.A., 1986, Classical Wave Theory in Practical AE Testing, in Progress in Acoustic Emission III, Proceedings of the Eighth International Acoustic Emission Symposium, The Japanese Society for Non-Destructive Inspection: 708-721.
[155] ASTM, Standard Method for Primary Calibration of Acoustic Emission Sensors, E 1106-86, Annual Book of ASTM Standards.
[156] Vahaviolos, S.J., 1986, 3rd Generation AE Instrumentation Techniques for High Fidelity and Speed of Data Acquisition, in Progress in Acoustic Emission III, Proceedings of the Eighth International Acoustic Emission Symposium, The Japanese Society for Non-Destructive Inspection: 102-116.
[157] Pollock, A.A., 1981, Acoustic Emission Amplitude Distributions, in International Advances in Nondestructive Testing, Gordon & Breach, 7: 215-239.
[158] Gorman, M.R., Rytting, T.H., 1983, Long Duration AE Events in Filament Wound Graphite/Epoxy in the 100-300 KHz Band Pass Region, in First International Symposium on Acoustic Emission from Reinforced Composites, The Society of the Plastics Industry.
[159] Fowler, T.J., 1986, Experience with Acoustic Emission Monitoring of Chemical Process Industry Vessels, in Progress in Acoustic Emission III, Proceedings of the Eighth International Acoustic Emission Symposium, The Japanese Society of Non-Destructive Inspection: 150-162.
[160] Miller, R.K., McIntire, P., 1987, Acoustic Emission Testing, Nondestructive Testing Handbook, American Society for Nondestructive Testing, 5/2: 340.

[161] Kaiser, J., 1953, Erkenntnisse und Folgerungen aus der Messung von Geräuschen bei Zugbeanspruchung von Metallischen Werkstoffen, Arch. Eisenhüttenwes., 24/1-2: 43-45.
[162] Dunegan, H.L., Tetelman, A.S., 1971, Acoustic Emission, Res. Dev., 22/5: 20-24.
[163] Miller, R.K., McIntire, P., 1987, Acoustic Emission Testing, Nondestructive Testing Handbook, American Society for Nondestructive Testing, 5/2: 426.
[164] Acoustic Emission Examination of Fiber-Reinforced Plastic Vessels, 1983, Boiler and Pressure Vessel Code, Article 11, Subsection A, Section V, American Society of Mechanical Engineers.
[165] Acoustic Emission Examination of Metallic Vessels During Pressure Testing, 1988, Boiler and Pressare Vessel Code, Article 12, Subsection A, Section V, American Society of Mechanical Engineers, Dec, Addendum.
[166] Heiple, C.R., Carpenter, S.H., 1987, Acoustic Emission Produced by Deformation of Metals and Alloys—a Review, J.Acoust. Emiss., 6/3: 177-204, 6/4: 215-237.
[167] Miller, R.K., McIntire, P., 1987, Acoustic Emission Testing, Nondestructive Testing Handbook, American Society for Nondestructive Testing, 5/2: 49-61, 55-57, 78.
[168] Dunegan, H.L., Harris, D.O., Tatro, C.A., 1968, Fracture Analysis by Use of Acoustic Emission, Eng. Fract. Mech., 1/1: 105-122.
[169] Palmer, I.G., Heald, P.T., 1973, The Application of Acoustic Emission Measurements to Fracture Mechanics, Mater. Sci. Eng., 11/4: 181-184.
[170] Chaskelis, H.H., Callen, W.H., Krafft, J.M., 1973, Acoustic Emission From Aqueous Stress Corrosion Cracking in Various Tempers of 4340 Steel, NRL Memorandum Report 2608, Naval Research Laboratory.
[171] Ashary. A., Meier. G.H., Pettit, F.S., 1982, Acoustic Emission Study of Oxide Cracking During Alloy Oxidation, in High Temperature Protective Coating, The Metallurgical Society: 105.
[172] Pollock, A.A., 1986, Acoustic Emission Capabilities and Applications in Monitoring Corrosion, in Corrosion Monitoring in Industrial Plants Using Nondestructive Testing and Electrochemical Methods, American Society for Testing and Materials: 30-42.
[173] Yuyama, S.H., 1986, Fundamental Aspects of Acoustic Emission Applications to the Problems Caused by Corrosion, in Corrosion Monitoring in Industrial Plants Using Nondestructive Testing and Electrochemical Methods, American Society for Testing and Materials: 43-47.
[174] Pantucek, P., Struth, U., Behavior of Thermal Barrier and of Corrosion Protective Coating Systems.
[175] Kuernes, I., Bunk, W.J.G., Wurm, J.G., Under Combined Thermal and Mechanical Loads (Mechanical Compatibility Problems and Potential Solutions), in Ceramic Coatings for Heat Engines, Advanced Materials Research and Development for Transport, MRS-Europe, Symposium IX (Nov 1985), 1986, Les Editions de Physique Vol IX, Les Ulis Cedex, France: 117-138.
[176] Hutton, P.H., 1974, Acceptance Testing Welded Ammunition Belt Links Using Acoustic Emission, in Monitorino Structural Integrity by Acoustic Emission, STP 571, American Society for Testing and Materials: 107-121.
[177] Cole, P.T., 1987 Acoustic Emission Technology and Economics Applied to Pressure Vessels and Storage Tanks, in Proceedings of the Fourth European Conference on Nondestructive Testing (London), Pergamon Press: 2892.
[178] Carlyle, J.M., Evans, R.S., Sherlock, T.P., 1989, Acoustic Emission Characterization of a Hot Reheat Line Rupture, Paper presented at the NDE Symposium at the ASME

Piping and Pressure Vessel Conference (Honolulu), American Society of Mechanical Engineers, June.
[179] Standard Practice for Acoustic Emission Monitoring of Structures During Controlled Stimulation, E 569-85, Annual Book of ASTM Standards, American Society for Testing and Materials.
[180] Weakland, D.P., Grabski, D.P., 1987, Consider Instrumented Inspection of Safety-Related Nuclear Systems, Power, 131/3, March: 61-63.
[181] Standard Test Method for Acoustic Emission for Insulated Aerial Personnel Devices, 914-85, Annual Book of ASTM Standards, American Society for Testing and Materials.
[182] Moore, K., Larson, C.A., 1984, Aerial Equipment Requires Thorough, Regular Inspection, Transmiss. Distrib., Jan: 23-27.
[183] Blackburn, P.R., Rana, M.D., 1986, Acoustic Emission Testing and Structural Evaluation of Seamless Steel Tubes in Compressed Gas Service, J. Pressure Vessel Technol. (Trans. ASME), 108/May: 234-240.
[184] Recommended Practice for Acoustic Emission Testing of Fiberglass Reinforced Resin (RP) Tanks/Vessels, 1987, The Society of the Plastics Industry.
[185] Recommended Practice for Acoustic Emission Testing of Fiberglass Reinforced Plastics Piping Systems, 1983, in First International Symposium on Acoustic Emission From Reinforced Plastics, The Society of the Plastics Industry, July (see also ASTM Standard Practice E 1118-86).
[186] Spanner, J.C., 1979, Acoustic Emission: Who Needs It-and Why?, in Advances in Acoustic Emission, Proceedings of the International Conference on Acoustic Emission (Anaheim, CA), Dunhart Publishers.

Chapter I.8

[187] Almond, D.P., Patel, P.M., Reiter, H., 1987, The Testing of Plasma Sprayed Coatings by Thermal Wave Interferometry, Mater. Eval., 45/April: 471-475.
[188] Balageus, D.L., Déom, A.A., Boscher, D.M., 1987, Characterization and Nondestructive Testing of Carbon-Epoxy Composites by a Pulsed Photothermal Method, Mater. Eval., 45/April: 461-465.
[189] Murphy, J.C., Watsel, G.C., 1986, Photothermal Methods of Optical Characterization of Materials, Mater. Eval., 44/Sept: 1224-1230.
[190] Potet, P., Jeanin, P., Bathias, C., 1987, The Use of Digital Image Processing in Vibrothermographic Detection of Impact Damage in Composite Materials, Mater. Eval., 45/April: 466-470.
[191] Baughn, T.V., Johnson, D.B., 1986, A Method for Quantitative Characterization of Flaws in Sheets by Use of Thermal Response Data, Mater. Eval., 44/June: 850-858.
[192] Henneke, E.G., II, Jones, T.S., 1979, Detection Damage in Composite Materials by Vibrothermography, in Nondestructive Evaluation and Flaw Criticality of Composite Materials, STP 696, R.B. Pipes, American Society for Testing and Materials.
[193] Sandor, B.I., Lohr, D.T., Schmid, K.C., 1987, Nondestructive Testing Using Differential Infrared Thermography, Mater. Eval., 45/April: 372-395.
[194] Huang, Y., Xu, J., Shih, C.H., 1980, Applications of Infrared Techniques to Research on Tensile Tests, Mater. Eval., 38/Dec: 76-78.
[195] Huang, Y., Li, S.X., Lin, S.E., Shih, C.H., 1984, Using the Method of Infrared Sensing for Monitoring Fatigue Process of Metals, Mater. Eval., 42/July: 1020-1024.

[196] Green, D.R., Hassberger, J.A., 1977, Infrared Electro-Thermal Examination of Stainless Steel, Mater. Eval., 35/March: 39-43.
[197] Newitt, J., 1987, Application of Specific Thermal Imaging, Mater. Eval., 45/May: 500-504.
[198] Infrared Thermal Testing, Product Showcase, 1987, Mater. Eval., 45/April: 403-414.
[199] Kaplan, H., Friedman, R., 1980, Two New Portable Infrared Instruments for Plant Inspection, Mater. Eval., 39/Feb: 175-179.
[200] Williams, J.H., Jr., Felenchak, B.R., Nagem, R.J., 1983, Quantitative Geometric Characterization of Two Dimensional Flaws Via Liquid Crystal Thermography, Mater. Eval., 41/Feb: 190-201, 218.
[201] Cielo, P., and all, 1987, Thermographic Nondestructive Evaluation of Industrial Materials and Structures, Mater. Eval., 45/April: 452-460.
[202] Williams, J.H., Jr., Nagem, R.J., A 1983, Liquid Crystal Kit for Structural Integrity Assessment of Fiberglass Watercraft, Mater. Eval., 41/Feb: 202-210.
[203] Papadakis, E.P., Chesney, H.L., Hurley, R.G., 1984, Quality Assurance of Aluminum Radiators by Infrared Thermography, Mater. Eval., 42/March: 333-336.
[204] Mansour, T.M., 1983, Nondestructive Thickness Measurement of Phosphate Coatings by Infrared Absorption, Mater. Eval., 41/March: 302-308.
[205] Feit, E., 1987, Infrared Thermography Saves Shelburne Middle School Time and Money, Mater. Eval., 45/April: 400-401.
[206] Cielo, P., Lewak, R., Balageas, D.L., 1985, Thermal Sensing for Industrial Quality Control, in Thermosense VIII, Society of Photo Interpretive Engineers, 581: 47-54.
[207] Tretout, H., Marin, J.Y., 1985, Transient Thermal Technique for IR NDT of Composite Materials, in IR Technology and Applications, , Society of Photo Interpretive Engineers, 590: 277-292.

Chapter II.1 – Chapter II.2

[208] Adept Net Ethernet for the adept Mv Controller, November 1996, User's Guide, Part # 00971-02000, Rev. A, U.S.A.
[209] Benedetto, S., Biglieri, E., Castellani, V., 1987, Digital Transmission Theory, Prentice-Hall Inc., NJ.
[210] Blitz, J., 1967, Fundamentals of Ultrasonics, Butterworts, Second edition.
[211] Bonavitacola, F., 1999, Controlli non Distruttivi di Tipo Ultrasonico e Con Correnti Parassite Mediante Software Labview, Tesi di Laurea, Dipartimento di Ingegneria dei Materiali e della Produzione, Universitá degli Studi di Napoli Federico II, A. A. 1998-1999
[212] Conte, E., 1996, Lezioni di teoria dei segnali, Liguori Editore, Napoli.
[213] Grennberg, A., Sandell, M., 1993, Estimation of subsample time delay differences in narrowbanded ultrasonic echoes using the Hilbert transform correlation, Research Report RR-32, Division of Signal Processing, Lulea University of Technology, Lulea, Sweden, December.
[214] Grennberg, A., Sandell, M., 1992, Experimental determination of the single point echo of an ultrasonic transducer using a tomographic approach, Proceedings of the 14th Annual International Conference of the IEEE Engineering in Medicine and Biology Society, Paris, France, November: 2151-2152.
[215] Krautkramer Branson Usip 12, 1985, Operation Manual, Id. Number 27976-2.910-2, W. Germany, November.

[216] LeCROY LC9400, 1986, Operato rs Manual, Serial Number 86286, Sping Valley, New York, USA.
[217] National Instruments, 1996, LabVIEW Analysis VI Reference Manual, Part Number 320538C-01, Austin, Tx, USA, January.
[218] National Instruments, 1996, LabVIEW Code Interface Reference Manual, Part Number 320539C-01, Austin, Tx, USA, January.
[219] National Instruments, 1996, LabVIEW Communication VI Reference Manual, Part Number 320587C-01, Austin, Tx, USA, January.
[220] National Instruments, 1996, LabVIEW Cross-Reference Manual, Part Number 321001A-01, Austin, Tx, USA, January.
[221] National Instruments, 1996, LabVIEW Instrument I/O VI Reference Manual, Part Number 320537C-01, Austin, Tx, USA, January.
[222] National Instruments, 1996, LabVIEW Tutorial Manual, Part Number 320998A-01, Austin, Tx, USA, January.
[223] National Instruments, 1996, LabVIEW User Manual, Part Number 320999A-01, Austin, Tx, USA, January.
[224] Nondestructive Testing Encyclopedia, www.ndt.net/article/az/ndtmain.htm
[225] Robot “RX” and “RX evoluzione in B” Armadio CS/B - CS/MB, 1999, Manuale Operatore, D.280.096.03.A, Settembre.
[226] Robot famille RX serie60 CS7B, 1999, Manuel D’istruction, D.280.099.01.A, June.
[227] Roth, Don J., 1999, 3-D surface depression profiling using high frequency focused air-coupled ultrasonic pulses, NASA technical memorandum; NASA/TM-1999-209053, July.
[228] Salvo, F., 2001, Tecniche Ultrasoniche Robotizzate di Diagnostica Tridimensionale e di Ingegneria Inversa, Tesi di Laurea, Dipartimento di Ingegneria dei Materiali e Della Produzione, Universitá degli Studi di Napoli Federico II, A. A. 2000-2001.
[229] Sciavicco, L., Siciliano, B., 2000, Robotica Industriale Modellistica e controllo di manipolatori, McGraw-Hill, Seconda edizione.
[230] Spada, M., 2003, Confronto tra Metodi Ottici ed Ultrasonici di Reverse Engineering per Applicazioni Industriali, Tesi di Laurea, Dipartimento di Ingegneria dei Materiali e della Produzione, Universitá degli Studi di Napoli Federico II, A. A. 2002-2003.
[231] V+ Language Version 13.0, July 1998, Reference Guide, Part # 00963-01000, Rev A, U.S.A.
[232] V+ Operating System Version 13.0, August 1998, Reference Guide, Part # 00963-02000, Rev. A, U.S.A.
[233] V+ Operating System Version 13.0, June 1998, User’s Guide, Part # 00963-02300, Rev. A, U.S.A.

Chapter III.1 – Chapter III.4

[234] Teti, R., 1990, Ultrasonic Identification and Measurement of Defects in Composite Material Laminates, Annals of CIRP, 39/1: 527-530.
[235] Teti, R., Lopresto, V., Buonadonna, P., Caprino, G., 2002, Ultrasonic NDE of Impact Damaged CFRP Laminates, 10th Eur. Conf. on Comp. Mat. (ECCM-10), Brugge, 3-7 June: paper n. 346.
[236] Teti, R., Buonadonna, P., 1998, Full Volume Ultrasonic NDE of CFRP Laminates 8th Eur. Conf. on Comp. Mat. (ECCM-8), Naples, 1-5 June: 317-324.
[237] Bracewell, R., 1986, The Fourier transform and its applications, Singapore: McGraw Hill.

[238] Bennett, J. M., Mattsson, L., 1999, Introduction to Surface Roughness and Scattering, 2nd ed. Optical Society of America, Washington.
[239] Bjuggren, M., Krummenacher, L., Mattsson, L., 1997, Characterization of Engineering Surfaces by Infrared Scattering, Opt. Eng. 36: 874-882.
[240] Church, E. L., 1983, The precision measurement and characterization of surface finish, Proc. SPIE 429: 86-95.
[241] Elson, J. M., Bennett, J. M., 1979, Vector scattering theory, Opt. Eng. 18/2: 116-124.
[242] Lebar, A., Junkar, M., 2001, Surface evaluation methods for advanced AWJ cutting techniques. Manuf. Syst. (Aachen), 31/2: 101-103.
[243] ASM Handbook, 2001, Composites, vol 21, ASM International.
[244] Shiuh-Chuan, H., 1999, Stress analysis of adhesively-bonded lap joints, Composite Structures 47: 673- 678.
[245] Teti, R., 1989, Digital Ultrasonic Nondestructive Evaluation of CFRP Composites by Complete Waveforms, 7th Int. Conf. on Comp. Mat., Guangzhou, 22-24 Nov: 649-656.
[246] www.panametrics.com, 2003, Ultrasonic Transducer Technical Notes: 32-40.
[247] Teti, R., Buonadona, P, 2002, 3D Surface Profiling through UT Reverse Engineering, 3rd CIRP Int. Sem. on ICME, Ischia, 28-30 June: 387-394.
[248] Teshima, T. and all, 1993, Estimation of Cutting Tool Life by Processing Tool Image Data with Neural Networks, Annals of CIRP, 42/1: 59-62.
[249] Liu, D., Malvern, L.E., 1987, Matrix cracking in impacted glass/epoxy plates, J. of Composite Materials, 21: 594-609.
[250] Caprino, G., Lopresto, V., 2004, Fracture surfaces of CFRP laminates statically loaded at the centre, Proc. of ECCM11, 31 May- 3 June Rhodes, Greece.
[251] Liu, D., 1988, Impact induced delamination: a view of bending stiffness mismatching, J. Compos. Mater., 22: 674-92.
[252] Abrate, S., 1998, Impact on Composite Structures, Cambridge University Press.
[253] Teshima, T., Shibasaka, T., Takuma, M., Yamamoto, A., 1993, Estimation of Cutting Tool Life by Processing Tool Image Data with Neural Network, Annals of the CIRP, 42/1: 59-62.

Chapter III.5 – Chapter III.7

[254] Hierholzer, M., and all, 1995, Characteristics of High Voltage IGBT Modules, IEEE Colloquium on IGBT Propulsion Drives, London, April: 1/1-1/5.
[255] Brunner, H., and all, 1995, 3300 V IGBT module for traction application, EPE 95, 6th Eur. Conf. on Power Electronics & Application, Sevilla: 56-59.
[256] Jung, M., and all, 1995, Development Trends for Traction Inverter with High Voltage IGBTs, IEEE Colloquium on IGBT Propulsion Drives, London, April.
[257] Fratelli, L., Giannini, G., 1996, Dual Voltage High Power Converter for a distrubuted power system in heavy traction using High Voltage IGBT , PESC 96, Vol. II, Baveno, June: 1414-1419
[258] Fratelli, L., Giannini, G., 1997, Power traction converter with 3.3 kV IGBT modules, EPE 97, 7th Eur. Conf. on Power Electronics & Applications, Session L3b, Trondheim, Sept.
[259] Coquery, G., and all, 1995, Reliability of the 400 A IGBT modules for traction converters: contribution of the power thermal fatigue influence on life expectancy, EPE 95, 6th Eur. Conf. on Power Electronics & Application, Sevilla: 60-65.

[260] Reliability of Advanced High Power Semiconductor Devices for Railway Traction Application, Brite-EuRam Project N. 95-2105.
[261] Novich, B.E., Adams, R.W., 1995, Aluminum/Silicon Carbide (AlSiC) Metal Matrix Composites For Advanced Packaging Applications, Int. Electronics Packaging Conference - IEPS, San Diego, Sept. 24-27: 220-227.
[262] Occhionero, M.A., Adams, R.W., Fennessy, K.P., Hay, R.A., 1999, Cost-Effective Manufacturing of Aluminum Silicon Carbide (AlSiC) Electronic Packages, Advanced Packaging Materials Symposium - IMAPS, Braselton, March: 14-17.
[263] Sumi, S., and all, 1989, Thermal fatigue failures of large scale package type power transistor modules, ISTFA '89 Symposium,: 309-322.
[264] Mitic, G., Sommer, K.-H., Dieci, D., Lefranc, G., 1998, The thermal impedance of new power semiconductor modules using AlN substrates, IEEE-IAS Industry Applications Conference: 1026-1030.
[265] CERAM Research Ltd, http://www.ceram.co.uk.
[266] Underwood, E.E., 1973, Applications of Quantitative Metallograhy, in Metals Handbook, ASM, 8th edition, 8: 37-47.
[267] Schutze, T., and all, Further Improvements in reliability of IGBT Modules, EUPEC GmbH & Co. KG.
[268] Berg, H., Wolfgang, E., 1998, Advanced IGBT modules for railway traction applications: reliability testing, Microelectronics Reliability 38, RAPSDRA: 1319-1323.
[269] Teti, R., Fratelli, L., 2003, Ultrasonic Nondestructive Evaluation Of Alsic Metal Matrix Composite Baseplate Igbt Devices, Advancing with Composites, Milan, 7-9 May: 157-169.
[270] Teti, R., 1987, Ultrasonic Inspection of Composite Materials, in Journées sur le Contrôle Qualité des Matériaux Composites, Bordeaux, 12-13 May: 205-219.
[271] Weber, S., Blake, R.A., Teti, R., Boncelet, C., 1988, Characterizing Porosity of Composite Laminates through Digitized Ultrasonic Waveform Processing, in XV Review of Progress in Quantitative NDE, University of California - San Diego, La Jolla, CA, July 31-Aug. 5: 1575-1580.
[272] Teti, R, Mattsson, L., Lebar, A., Junkar, M., 2005, Metrology Applications of Two-Dimensional Frequency Analysis for Micro-Features Characterisation, in 1st Int. Conf. On Munti-Material Micro Manufacture – 4M 2005, Karlsruhe, 29 June – 1 July, Paper ID: 70571.
[273] Teti, R., Baciu, I.L., 2006, Quality Management of IGBT Assembly Devices through Micro Feature Ultrasonic NDI, The 1st CIRP International Seminar on Assembly Systems, , Stuttgart, Germany, 15-17 November: 245-250.

Chapter IV

[274] Buonadonna, P., Tecniche Sensoriale di Monitoraggio dell'Usura degli Utensili in Tornitura, Graduate Thesis, University of Naples Federico II.
[275] Teti, R., 1989, Tool Wear Monitoring Through Acoustic Emission, Annals of the CIRP, vol. 38/1: 99-102.
[276] Teti, R., Bastioli, C., Romano, G., 1989, Acoustic Emission Analysis of GFR Thermoplastic Composites, Third Intl. Symposium on Acoustic Emission from Composite Materials, Paris: 119-128.

[277] Teti, R., Dornfeld, D., 1989, Modeling and Experimental Analysis of Acoustic Emission from Metal Cutting, J. Engineering for Industry, 111: 229-237.
[278] Harris, D.O., Tetelman, A.S., Darwish, F.A., 1972, Detection of Fiber Cracking by Acoustic Emission, Acoustic Emission, ASTM STP505: 238-249.
[279] Ono, K., 1979, Acoustic Emission Arising from Plastic Deformation and Fracture, Fundamentals of Acoustic Emission, K. Ono, ed., University of California-Los Angeles: 167-208.
[280] Teti, R., Acoustic Emission Testing of Glass Fiber Reinforced Plastic Components, J. of Acoustic Emission, 5/4: 156-160.
[281] Fowler, T.J., 1979, Acoustic Emission Testing of Fiber Reinforced Plastics, Proceeding Paper 15021, J. of Technical Council, ASCE, 105 (TC2): 281-289.
[282] Caprino, G., Halpin, J.C., Nicolais, L., 1979, Fracture Mechanics in Composites Materials, Composites, Oct.: 223- 227.
[283] Masounave, J., Lanteigne, J., Bassim, M.N., Hay, D.R., 1986, Acoustic Emissions and Fracture of Ductile Materials, Engineering Fracture Mechanics, 1/1: 105-122.
[284] Shawaky, A., Rosenberger, T., Elbestawi, M., 1998, In process monitoring and control of thickness error in machining hollows shafts, Mechatronics, 8: 301-322.
[285] Sokolowski, A., Kosmol, J., 2001, Selected examples of cutting process monitoring and diagnostics, Journal of Materials Processing and Techecnology, 113(1-3): 322-330.
[286] Lin, B., Zhu, M.Z., Yu, S.Y., Zhu, H.T., Lin, M.X., 2002, Study of synthesis identification in the cutting process with a fuzzy neural network, Journal of Materials Processing and Techecnology, 129 (1-3): 131-134.
[287] Brophy, B., Kelly, K., Byrne, G., 2002, AI-based condition monitoring of the drilling process, Journal of Materials Processing and Technology, 124(3): 305-310.
[288] CA-Cricket Graph III for Macintosh: Version 1.0 User Guide, 1992.
[289] Dornfeld, D.A., 1992, Monitoring of machining process - Literature Review, CIRP Annals, 41(1): 93-96.
[290] Cho, D.W., Lee, S.J., Chu, C.N., 1999, The state of machining process monitoring research in Korea International Journal of Machine Tools and Manufacturing, 39(11): 1697-1715.
[291] Govekar, E., Gradišek, J., Grabec, I., 2000, Analysis of acoustic emission signals and monitoring of machining processes, Ultrasonics, 38(1-8): 598-603.
[292] Byrne, G., Dornfeld, D.A., Inasaki, I., Ketteles, G., König, W., Teti, R., 1995, Tool Condition Monitoring (TCM) – The Status of Research and Industrial Application, CIRP Annals, 44(2): 541-567.
[293] D'Errico, G.E., 1997, Adaptive systems for machining process monitoring and control, Journal of Materials Processing and Techecnology, 64(1-3): 75-84.
[294] Tönshoff, H.K., Wulsferg, J.P., Kals, H.J., Köning, W., Van Luttervelt, C.A., 1988, Developments and Trends in Monitoring and Control of Machining Processes, CIRP Annals, 37(2): 611-622.
[295] Grabec, I., Govekar, E., Susic, E., Antolovic, B., 1998, Monitoring manufacturing processes by utilizing empirical modeling, Ultrasonics, 36(1-5): 263-271.
[296] Inasaki, I., 1998, Application of acoustic emission sensor for monitoring machining processes, Ultrasonics, 36(1-5): 273-281.
[297] Kopac, J., Sali, S., 2001, Tool wear monitoring during the turning process, Journal of Materials Processing and Techecnology, 113: 312-316.

[298] Fu, J.C., Troy, C.A., Mori, K., 1996, Chatter classification by entropy functions and morphological processing in cylindrical traverse grinding, Precision Engineering, 18(2-3): 110-117.
[299] Larson Davis Laboratory, 2800 Manual, Preliminary documentation 1/27/93.
[300] Lu, M.C., Kannatey-Asibu, Jr.E., 2000, Analysis of sound signal generation due to flank wear in turning, International ME2000 Congress & Exposition, Orlando, FL.
[301] Noise and Vibrations Works, References Manual version 1.22.
[302] Masory, O., 1991, Monitoring machining processes using multi-sensor readings fused by artificial neural network, Journal of Materials Processing and Techecnology, 28(1-2): 231-240.
[303] Huang, P.T., Chen, J.C., 1998, Fuzzy logic-base tool breakage detecting system in end milling operations, Computers & Industrial Engineering, 35(1-2): 37-40.
[304] Teti, R., 1995, A Review of Tool Condition Monitoring a Literature, CIRP Annals, 44(2): 659-666.
[305] Teti, R., Baciu, I.L., 2004, Neural Network processing of audible sound parameters for sensor monitoring of tool conditions, Intelligent Computation in Manufacturing Engineering, 4, Sorrento: 385-390.
[306] Teti, R., Baciu, I.L., Rubio, E.M., 2004, Neural network classification of audible sound signals for process monitoring during machining, Proc. of the 15th International DAAAM SYMPOSIUM: Intelligent Manufacturing and Automation: Globalisation- Technology-Men-Nature, Viena: 459-460.
[307] Wilcos, S.J., Reuben, R.L., Souquet, P., 1997, The use of cutting force and acoustic emission signals for the monitoring the tool insert geometry during rough face milling, International Journal of Machine Tools and Manufacturing, 32(4): 481-494.
[308] Spectrum Pressure Level (Spl 3100), Manual Version 0.98, Program Version 1.10.
[309] Masters, T., 1993, Practical Neural Networks Recipies in C++, Academic press, San Diego, CA.
[310] Clark, W.I., Shih, A.J., Hardin, C.W., Lemaster, R.L., McSpadden, S.B., 2003, Fixed abrasive diamond wire machining—part I: process monitoring and wire tension force, International Journal of Machine Tools and Manufacturing, 43(5): 523-532.
[311] Fahlman, S.E., Lebiere, C., 1990, An Empirical Study of Learning Speed in Back Propagation Networks, Carnegie Mellon Univ. Technical Report, CMU-CS: 88-162.